

Investigating the effects of weak extracellular fields on single neurons: a modelling approach

vorgelegt von
Master of Science
Aspart Florian
geb. in Perpignan, Frankreich

von der Fakultät IV – Elektrotechnik und Informatik
der Technischen Universität Berlin



zur Erlangung des akademischen Grades
Doktor der Naturwissenschaften
- Dr. rer. nat. -
genehmigte Dissertation

Promotionsausschuss:

Vorsitzender: Prof. Dr. Henning Sprekeler

Gutachter: Prof. Dr. Klaus Obermayer

Gutachter: Prof. Dr. Gaute T. Einevoll

Gutachter: Prof. Dr. Richard Kempter

Tag der wissenschaftlichen Aussprache: 30. November 2018

Berlin 2018

To my little ninjas,

*Tout doit tendre au bon sens : mais, pour y parvenir,
Le chemin est glissant et pénible à tenir;
Pour peu qu'on s'en écarte, aussitôt on se noie.
La raison pour marcher n'a souvent qu'une voie.*

Nicholas Boileau. L'art poétique, 1674

Abstract

In the past decades, the rise of transcranial current stimulation (tCS) has sparked an increasing interest in the effects of weak extracellular electric fields on neural activity. These fields, such as induced during tCS, have been shown to polarize the neuronal membrane and, consequently, to modulate the spiking activity. In this thesis, I follow a modelling approach to investigate how single neuron properties affect their polarization in response to weak extracellular fields and how this response translates into a change in spiking activity.

In the first part, I consider the effects of the somatic membrane polarization due to sinusoidal electric fields on neural activity. Using a canonical spatial neuron model, I investigate how this subthreshold membrane polarization leads to a modulation of the spike rate response to stochastic input currents. Importantly, I observe a resonance in the spike rate modulation, or in other words, an enhanced spike-field coherence. The resonance frequency depends on the location of the background synaptic input and on the somatic spike mechanism. Furthermore, I extend leaky and non-linear integrate-and-fire point neuron models to reproduce the dynamics of the spatially extended neuron model. To this end, I analytically derive additional model components to account for (i) two different locations of synaptic inputs and (ii) the somatic polarization due to weak electric fields. While retaining computational efficiency, the point neuron model extension successfully reproduces the original model response to synaptic input and to extracellular fields. The extended model is therefore well suited to investigate the effects of extracellular electric fields on the dynamics of large neuronal populations.

In the second part, I focus on the polarization of the dendritic arbor due to weak electric fields. Using a biophysically detailed model, I first investigate the frequency-dependent subthreshold sensitivity of L5 cortical pyramidal cells to sinusoidal electric fields. Importantly, I observe a strong resonance around 10-20Hz in the field sensitivity at the apical dendrites, which is absent at the soma or basal dendrites. To disentangle the relative roles of the cell morphology and active properties in this differential field sensitivity, I further consider simplified models, ranging from simple passive cable models to reconstructed cell models with simplified active properties. I attribute this differential polarization to (i) an increased sensitivity at the apical dendrites due to the morphology and (ii) the high density of active ion channels, especially h-type current, in the apical dendrites. Finally, I illustrate how the subthreshold polarization due to electric fields can modulate firing activity of pyramidal cells, notably their firing of somatic action potentials and dendritic calcium spikes.

Overall, this thesis provides an enhanced understanding of the effects of weak electric fields on neural activity and is, therefore, a further step towards improving the design of tCS protocols.

Zusammenfassung

In den letzten Jahrzehnten löste die zunehmende Verbreitung von transkranieller Stromstimulation (tCS) ein erhöhtes Interesse an den Auswirkungen schwacher extrazellulärer elektrischer Felder auf die neuronale Aktivität aus. Diese Felder, die während tCS induziert werden, sind dafür bekannt, die neuronale Membran zu polarisieren und somit die Spikingaktivität zu modulieren. In dieser Arbeit verfolge ich einen Modellierungsansatz, um zu untersuchen, wie die Eigenschaften einzelner Neuronen ihre Polarisation durch schwache extrazelluläre Felder beeinflussen und wie diese Polarisation in eine Veränderung der Feuerrate übersetzt wird.

Zunächst betrachte ich die Auswirkungen der somatischen Membranpolarisation durch sinusförmige Felder auf die neuronale Aktivität. Anhand eines kanonischen räumlichen ausgedehnten Neuronenmodells untersuche ich, wie diese unterschwellige Membranpolarisation zu einer Modulation der Feuerrateantwort auf stochastische Eingangsströme führt. Interessanterweise finde ich eine Resonanz in der Modulation der Feuerrate, also eine verstärkte Kohärenz zwischen Spikes und dem Feld. Die Resonanzfrequenz ist abhängig von der räumlichen Position des synaptischen Eingangstroms und vom somatischen Spike-Mechanismus. Darüber hinaus erweitere ich lineare und nichtlineare Integrate-and-fire Neuronenmodelle, um die Dynamik des räumlichen Neuronenmodells zu reproduzieren. Zu diesem Zweck leite ich analytisch zusätzliche Modellkomponenten ab, um zwei verschiedene Stellen von synaptischen Eingängen sowie die somatische Polarisation durch schwache elektrische Felder zu berücksichtigen. Das erweiterte Punkt-Neuronenmodell reproduziert erfolgreich die Antwort des ursprünglichen Modells auf synaptische Eingaben sowie auf extrazelluläre Felder und ist dabei rechnerisch viel effizienter. Das erweiterte Modell ist daher gut geeignet, die Auswirkungen extrazellulärer elektrischer Felder auf die Dynamik großer Neuronenpopulationen zu untersuchen.

In einem zweiten Schritt konzentriere ich mich auf die Polarisation des dendritischen Baums durch schwache elektrische Felder. Anhand eines biophysikalisch detaillierten Modells untersuche ich zunächst die frequenzabhängige Unterschwellenempfindlichkeit von L5 kortikalen Pyramidenzellen unter Einwirkung von sinusförmigen elektrischen Feldern. Wichtig ist, dass ich eine starke Resonanz um 10-20Hz in der Empfindlichkeit von apikalen Dendriten für Felder beobachte, die an den Soma- oder Basal-Dendriten fehlt. Um der relativen Rolle der Zellmorphologie und der aktiven Eigenschaften in dieser differentiellen Empfindlichkeit für Felder auf den Grund zu gehen, betrachte ich vereinfachte Modelle, die von einfachen passiven Kabelmodellen bis zu rekonstruierten Zellmodellen mit vereinfachten aktiven Eigenschaften reichen. Ich schreibe diese differentielle Polarisation (i) einer erhöhten Empfindlichkeit an den apikalen Dendriten aufgrund der Morphologie und (ii) der hohen Dichte an aktiven Ionenkanälen, insbesondere dem h-Typ-Strom, in den apikalen Dendriten zu. Schließlich veranschauliche ich, wie die unterschwellige Polarisation durch die Felder die Spikingaktivität von Pyramidenzellen modulieren kann, insbesondere deren Auslösen von somatischen Aktionspotentialen und dendritischen Kalziumspikes.

Insgesamt bietet diese Arbeit ein besseres Verständnis der Auswirkungen schwacher elektrischer Felder auf die neuronale Aktivität und ist daher ein weiterer Schritt zur Verbesserung des Designs von tCS-Protokollen.

Acknowledgements

First of all, I would like to thank my supervisor, Klaus Obermayer, for giving me the opportunity to write my thesis in his group. He provided me with a great academic environment for my doctorate and offered me a good compromise between scientific guidance and freedom. His comments were always straight to the point and valuable. Most importantly, he taught me scientific rigor. I am very grateful to Josef Ladenbauer too. Josef took me under his wings when I started my PhD, and even before, during the application process. At his side, I wrote my first paper. Josef taught me good scientific practice such as double checking all results and paying attention to small details. Without him, this thesis would not have been half as good. Furthermore, I would like to thank Michiel WH Remme with whom I collaborated on my second paper. Some people are great to work with, Michiel is definitely one of them. I learned a lot from him. Asking the right questions and providing his expertise on biophysics, Michiel highly improved the quality of that article. I am also thankful to Joram Keijser for his contribution to the evaluation of the pyramidal cell models (last section of chapter 3). Joram was a lab rotation student I was lucky to supervise. He achieved a great job in a short period of time. Thank you Joram and good luck for your own thesis.

I would like to thank all the other group members of the last four and a half years. I really enjoyed our fruitful scientific and everyday life discussions. I am particularly obliged to Sinem Balta, Franziska Oschmann, Michael Scholz and Caglar Cakan for proofreading part of this thesis. Sharing an office room with me, Sinem and Caglar enabled me not to be the smartest person in the room, thank you for that. I am also very grateful to all scientists I met at conferences or workshops and to the reviewers of my work, whose constructive critics helped me improve my work.

Last but not least, I would like to thank my friends (other than the ones above mentioned) and family for their support. I am particularly appreciative of my parents for giving me the chance to study. I would also like to thank my sister, Minus, for always helping me trying to take over the world. Finally, I am very grateful to my wife and sons for supporting me and for providing me with good reasons to disconnect out of office hours. Thank you Julia for these puzzling evenings. Thank you Linus for the sword play. Éclairs! And thank you Kupa for giving me, with your birth, a deadline for submitting this manuscript.

Contents

1	Introduction	1
2	The somatic doctrine: Extending point neuron models to account for electric field effects at the soma	9
2.1	Overview	9
2.2	Models presentation	10
2.3	Extending LIF point neuron models	13
2.3.1	The somatic input filter for the LIF model	14
2.3.2	The distal input filter for the LIF model	19
2.3.3	Effect of an extracellular electric field on the neuronal dynamics	21
2.4	Extension for EIF neuron models	27
2.5	Discussion	33
3	The dendritic doctrine: Fields effects on cortical pyramidal cells	39
3.1	Overview	39
3.2	Impact of the morphology on the field sensitivity	40
3.2.1	Field sensitivity of passive cable models	42
3.3	Impact of voltage-dependent membrane properties on the field sensitivity	50
3.3.1	Field sensitivity of a biophysical pyramidal cell model with experimentally constrained conductances	51
3.3.2	Field sensitivity of a pyramidal cell model with quasi-active channels	56
3.4	Modulation of pyramidal cells spiking activity by weak electric fields . .	65
3.5	Discussion	80
4	Conclusion	85
A	Cable equation subject to an electric field: derivation and solutions	87
A.1	Derivation of the equation for passive cables subject to an extracellular electric field	87
A.1.1	Cable equation	87
A.1.2	Boundary conditions	89
A.2	Derivation of the BS somatic membrane potential in response to synaptic inputs and a spatially uniform extracellular electric field	90
A.3	Derivation of the membrane polarization of a straight passive cable due to a spatially non-uniform electric field	93
B	Derivation of the quasi-active approximation	96
C	Supplementary information	99
C.1	Supplementary information for chapter 2	100
C.2	Supplementary information for chapter 3	101
	Bibliography	115

List of Figures

2.1	Diagram of the extended point neuron model	11
2.2	Impedance and filter for somatic inputs	16
2.3	Reproduction of spiking activity for somatic inputs using LIF type models	18
2.4	Distal input filter and reproduction of spiking activity using LIF type models	20
2.5	The field sensitivity of the BS model decreases with the field frequency	22
2.6	The eP model requires an equivalent input current whose amplitude increases with field frequency to account for the field effects	23
2.7	Spike rate modulation due to an electric field for somatic inputs	25
2.8	Spike rate modulation due to an electric field for distal dendritic inputs	26
2.9	Reproduction of spiking activity for somatic inputs using EIF type models	29
2.10	Reproduction of spiking activity for dendritic inputs using EIF type models	30
2.11	Spike rate modulation due to an electric field for somatic inputs using neuron models of the EIF type	31
2.12	Spike rate modulation due to an electric field for distal dendritic inputs using neuron models of the EIF type	32
3.1	In a passive pyramidal cell model subject to an electric field, soma and basal dendrites get oppositely polarized than apical dendrites. This later are the most responsive to low frequency stimulations	41
3.2	A passive pyramidal neuron exhibits a frequency resonance in its field sensitivity at the proximal dendrites	42
3.3	The polarization of a passive straight cable due to an extracellular field is anti-symmetric and decreases with the field frequency	45
3.4	Passive cables with an acute bending angle can display a resonance in their sensitivity to spatially uniform fields	47
3.5	The presence of several basal dendrites increases the field sensitivity at the apical dendrites while decreasing the field sensitivity at the soma and basal dendrites	49
3.6	The presence of a shunt at the soma induces an asymmetric field sensitivity, the apical dendrites being more sensitive than the soma and basal dendrites	50
3.7	Unlike the soma and basal dendrites, the apical dendrites of an active cell have an increased subthreshold response to AC fields of 10-20Hz . .	52
3.8	The hyperpolarization-activated inward current, I_h , is responsible for the frequency resonance in the sensitivity of apical dendrites to AC fields	53
3.9	The distribution of the resting membrane potential does not qualitatively affects the field sensitivity profile of the active cell at the apical dendrites	54
3.10	The field sensitivity of a pyramidal cell decreases in a high-conductance state	55

3.11	The quasi-active channel conductance distribution affects the cell field sensitivity depending of the local conductance at the considered location	59
3.12	While regenerative currents increase the cell sensitivity to low frequency fields, restorative currents decrease it and induce a resonance	60
3.13	The type of QA channel, with conductance distributed increasingly from the soma, affects more strongly the field sensitivity at apical dendrites than at the soma and basal dendrites	61
3.14	The type of QA channel, with conductance distributed decreasingly from the soma, affects the field sensitivity at the soma, apical and basal dendrites	61
3.15	The time constant of restorative currents determines the resonance frequency of the sensitivity to AC fields	62
3.16	The effects of the channel type on the field sensitivity are transposable to other pyramidal cell morphologies, cell 2	63
3.17	The effects of the channel type on the field sensitivity are transposable to other pyramidal cell morphologies, cell 3	63
3.18	I_h is a restorative current whose time constant increases with increasing rest membrane potential	64
3.19	The Hay et al. model is fitted to reproduce BAC firing and responses to somatic step current injection as recorded <i>in vitro</i>	66
3.20	Stimulus onset-dependent BAC firing behavior of the Hay et al. model due to non-initialized internal calcium concentration	67
3.21	Fixing the Hay et al. model does not strongly lower the reproduction accuracy of the original model	69
3.22	Positive electric fields delay the cell response to low amplitude step currents injected at the soma	70
3.23	Negative electric fields advance the initial spiking response of the cell to low amplitude step currents injected at the soma, resulting in a delayed spike after the initial burst	70
3.24	In case of a somatic step input current of high amplitude, positive DC fields delay the first spike after the initial burst and negative fields advance it	71
3.25	The modulation of the first interspike interval after stimulus onset by AC fields is very weak.	72
3.26	Weak AC fields modulate the response to onset of somatic step input currents in a field frequency and phase dependent manner	73
3.27	DC fields modulate the somatic pulse amplitude threshold to trigger an action potential	74
3.28	The modulation of the somatic pulse amplitude threshold by AC fields depends on the subthreshold somatic polarization and therefore on the field frequency	74
3.29	DC fields modify the timing of action potentials during BAC firing	75
3.30	DC fields mainly affect the timing of the last spike during BAC firing	76
3.31	Weak DC fields modulate the EPSP amplitude threshold to trigger BAC firing	77
3.32	The modulation of the EPSP amplitude threshold through AC fields does not decrease monotonically with the field frequency	78

3.33	Weak DC fields modulate the temporal precision for detecting coincidence between action potentials and afferent EPSPs	79
3.34	Weak AC fields modulate the temporal precision for detecting BAC stimuli in a field frequency-dependent manner	80
A.1	Schematic description of a passive cable and a ball-and-stick models subject to an extracellular electric field	88
C.1	In a passive cable with an obtuse bending angle, the length of the bent branch has little effects on the field sensitivity at both ends	101
C.2	In a passive cable with a right bending angle, the length of the bent branch mainly affects the field sensitivity at its end, without inducing a resonance	102
C.3	In a passive cable with an acute bending angle, the membrane time constant τ determines the resonance frequency	103
C.4	In a passive cable with an acute bending angle, the relative lengths of the main and bent branches determine the presence of a resonance; the membrane time constant determines the resonance frequency	104
C.5	Decreasing the membrane time constant reduces the frequency-dependence of the field sensitivity along bent cables	104
C.6	The presence of several basal dendrites parallel to apical dendrites increases the field sensitivity at the apical dendrites and can induce a resonance at the soma	105
C.7	Pyramidal cells present, at rest, a gradient of membrane potential which is not counterbalanced by the polarization due to weak DC fields	105
C.8	In an active pyramidal cell model, the field sensitivity presents a strong resonance around 10-20Hz at the apical dendrites but not at the soma or the basal dendrites	106
C.9	The field sensitivity of a pyramidal cell is less frequency-dependent in an high-conductance state	107
C.10	Results with a QA channel conductance distributed linearly increasingly with distance from the soma are transposable to the cell 2 morphology	108
C.11	Results with a QA channel conductance distributed linearly decreasingly with distance from the soma are transposable to the cell 2 morphology	108
C.12	Results with a QA channel conductance distributed linearly increasingly with distance from the soma are transposable to the cell 3 morphology	109
C.13	Results with a QA channel conductance distributed linearly decreasingly with distance from the soma are transposable to the cell 3 morphology	109
C.14	Increasing the neuron membrane surface reduces the sensitivity to DC fields	110
C.15	The transfer impedances between the apical dendrites and the soma are symmetric and are not affected by DC fields	110
C.16	Weak AC fields modulate the back-propagation of action potentials along the apical dendrite, as well as the peak of the calcium spike during BAC firing.	113

List of Acronyms

AC	Alternating current
AHP	After-spike hyperpolarization
AP	Action potential
BAC	Backpropagating action potential-activated calcium spike
BAP	Backpropagating action potential
BS	Ball-and-stick neuron model
CA1	Cornu Ammonis area 1 (region of the hippocampus)
CC BY	Creative common attribution license
CV	Coefficient of variation
DC	Direct current
EIF	Exponential integrate-and-fire
eP	Extended point neuron model
EPSP	Excitatory post-synaptic potential
FEM	Finite element methods
IF	Integrate-and-fire
IPSP	Inhibitory post-synaptic potential
LTD	Long-term depression
LTP	Long-term potentiation
MRI	Magnetic resonance imaging
P	Point neuron model
tACS	Transcranial alternating current stimulation
tCS	Transcranial current stimulation
tDCS	Transcranial direct current stimulation
TMS	Transcranial magnetic stimulation

Chapter 1

Introduction

Over two centuries ago, Aldini (1804) was already applying low-amplitude electrical stimulations on the brain. This interest for low-amplitude current stimulations went on through generations of physiologists, before being partially eclipsed by high intensity current stimulations during the 20th century (see Zaghi et al., 2010, for an historical review). Beginning of the XXIst century, the rise of transcranial magnetic stimulation (TMS) gave birth to a renewed interest for non invasive stimulation techniques. Among them, the effects of transcranial current stimulation (tCS) on brain activity has been widely investigated (Zaghi et al., 2010). Yet, the efficacy of tCS has been highly variable. Behind this variability lies a lack of understanding of tCS effects on neural activity at the microscopic level. This thesis aims at providing a theoretical basis for a better understanding of tCS effects on neural activity. Specifically, this thesis focuses on the effects of weak extracellular electric fields, as generated during transcranial current stimulations, on single neuron activity. To begin with, I first review the effects of tCS and the associated extracellular field.

Presenting transcranial current stimulation Transcranial current stimulation consists in the application of a weak electric current on a subject scalp (see Herrmann et al., 2013, for a review). This non-invasive stimulation technique has been derived in multiple variants, depending on the type of the applied current. The usual variants consist in the application of direct currents (DC), namely transcranial DC stimulation (tDCS), or of alternating currents (AC), typically sinusoidal, i.e. transcranial AC stimulation (tACS). Other variants can use, for example, Gaussian white-noise currents, namely transcranial random noise stimulation (tRNS) (Paulus, 2011), or a DC current with additional oscillations, i.e. slow oscillatory transcranial direct current stimulation (so-tDCS) (Ladenbauer et al., 2017).

In all variants, the applied currents are of low amplitude: typically 1mA. In fact, the stimulation intensities were long set below 2mA for safety reasons (Zaghi et al., 2010), albeit some recent studies use stronger (3mA) currents (McNickle and Carson, 2015, for example). Typical stimulations last from a couple of minutes to hours (Paulus, 2011).

Transcranial brain stimulation have been shown to modulate the brain activity and, sometimes, the associated cognitive capacities (Herrmann et al., 2013). Among others, Nitsche and Paulus (2000) showed that tDCS could change up to 40% the excitabil-

ity of motor cortex revealed by TMS¹. Applying low frequency tACS during sleep, Marshall et al. (2006) enhanced the retention of declarative memories in human. Transcranial current stimulation has also been used to improve rehabilitation after stroke, albeit without robust results (Schmidt et al., 2013). Nevertheless, a general effect of tCS on neural activity is difficult to deduce from existing literature (Zaghi et al., 2010). Indeed, the tCS studies usually apply different stimulation setups (e.g. electrodes position, stimulus intensity or current type) on different tasks and, consequently observe different results (Fröhlich et al., 2014). Overall, this high variability reflects a lack of basic understanding of the mechanism behind tCS action on neural activity.

tCS-induced extracellular electric fields Injecting an electric current on a subject scalp results in a current flowing through the brain. The distribution of the current within the brain can be estimated from structural magnetic resonance images (T1, T2) of the head using Finite Element Methods (FEM) (Neuling et al., 2012; Datta et al., 2012). In brief, the head is first segmented in several layers, e.g. skin, skull, cerebrospinal fluid (CSF), white and grey matter. To each layer is associated a conductivity value², whose anisotropy can be estimated from diffusion tensor imaging (Neuling et al., 2012). Finally, the distribution of the current is computed in these layers by solving the maxwell equations with current and voltage continuity between layers as boundary conditions. The maxwell equations are solved by dividing the space into small unit volumes, hence the name Finite Element Methods³.

FEM studies inform us that most of the applied current flows along the scalp instead of penetrating the brain. The current can be 10 times stronger in the scalp than in the brain Neuling et al. (2012). Similarly, most of the current penetrating the brain flows within the CSF and tDCS produces mostly a current tangential to the cortical surface (Rahman et al., 2013).

The tCS-induced current penetrating the brain is distributed broadly across the brain. Nevertheless, the distribution is not uniform: the current amplitude reaches a peak at a given location and is lower in the rest of the brain. In fact the exact current distribution strongly depends on the stimulation setup, i.e. the number of electrodes and their positions. For example, using the HD-tDCS electrode setup⁴ results in a current more densely distributed under the electrodes (Datta et al., 2012). Furthermore, the current distribution also depends on the subjects head morphology. Datta et al. (2012) found a 1.5 fold difference in the peak current distribution across different subjects. Nonetheless, the deeper cortical regions are usually not reached.

The current induced within the brain by tCS can be translated into a gradient of extracellular potential. In the following, I refer to this gradient as the extracellular

¹ Nitsche and Paulus (2000) applied TMS on the motor cortex and measured the ensuing motor-evoked potential in the right abductor digiti minimi muscle (the muscle pulling the hand little finger away from the others). They found tDCS to significantly modify the size of this motor-evoked potential.

² The conductivities are relatively constant in the 1-100Hz frequency range usually used in tACS (see Miranda et al., 2009, for a review)

³Note that this technique is also used in Electroencephalography (EEG) analysis to compute the lead-field matrix, which maps the brain activity at a given location to the recorded voltage at the electrodes (Vatta et al., 2010).

⁴ The HD-tCS setup consists of 4 cathode disk electrodes surrounding an anode center electrode. The conventional electrodes setup usually uses only 2 electrodes: one anode and one cathode.

electric field, or simply the extracellular field. From now on, I will mostly consider the generated extracellular field instead of the extracellular current.

During 1mA tCS, the extracellular field peaks at approximately 0.5 V/m (Neuling et al., 2012; Datta et al., 2009, 2012).

Despite variations in the tCS-induced field distributions, the field is usually assumed to be, locally, spatially uniform (Bikson et al., 2012a). In other words, the field orientation and strength do not change spatially at the scale of a local neuronal population. This means that the spatial derivative of the field, i.e. the second spatial derivative of the extracellular potential, is null. In the Cartesian system, this yields:

$$\vec{\nabla}(\nabla \cdot E(t)) = \frac{\partial E(t)}{\partial x} \vec{i} + \frac{\partial E(t)}{\partial y} \vec{j} + \frac{\partial E(t)}{\partial z} \vec{k} = 0$$

where E is the electric field, $\vec{\nabla}$ denotes the vector differential operator, and $\vec{i}, \vec{j}, \vec{k}$ the standard unit vectors in the direction of the x, y, z coordinates.

In practice this assumption implies that, at a given time t , the extracellular potential scales linearly along a given spatial direction. However the exact amplitude of the field can vary in time. This assumption of a spatially uniform field is crucial for most of the results presented in this thesis.

A common question about tCS-induced extracellular electric field is how they compare to endogenous electric fields, namely Local Field Potentials (LFP)⁵. The main difference between endogenous and tCS-induced fields lies in the spatial non-uniformity of the endogenous fields at the neuron scale. Indeed, the second derivative of the LFP, also known as Current Source Density, have troughs and maxima along the cell (Einevoll et al., 2013).

The amplitudes of tCS-induced and endogenous fields are of similar order of magnitude. In fact, the amplitude of endogenous fields depends on the considered rhythm and can be stronger than tCS fields. For example, Fröhlich and McCormick (2010) measured a peak amplitude of 2 V/m during slow-oscillation in primary visual cortex of anesthetized ferrets. Similarly, Anastassiou et al. (2010) reported, in rats CA1, a LFP of 2-3 V/m during theta (4-12Hz) oscillations and of 10-15V/m during hippocampal sharp waves, which are associated with high temporal frequencies (180-200Hz).

Polarization of single neuron due to weak extracellular fields With the rise of tCS, the effects of weak electric fields on neural tissue has known a regain of interest in the last 15 years. In a seminal work, Bikson et al. (2004) applied step, i.e. DC, fields in rat hippocampal slices. Using intracellular and voltage-sensitive dyes recordings, they found the field to polarize pyramidal cells. The induced polarization was not uniform over the whole cell; instead fields parallel to the cell somato-dendritic axis induced a polarization at the apical tree opposite to the polarization at the soma or basal dendrites. For this field orientation, the stronger polarization was measured at the tip of basal and apical dendrites.

Most importantly, Bikson et al. (2004) used a wide range of DC field amplitudes and found the polarization induced by weak subthreshold fields ($\leq |40|$ V/m) to scale

⁵The term LFP is somewhat confusing. In the literature, LFP usually denotes the extracellular potential and not the extracellular field. In other words, LFP refers to the potential measured at one electrodes (Einevoll et al., 2013) and not to its gradient, which would be the extracellular electric field.

linearly with the field amplitude. This linearity enables the definition of the sub-threshold field sensitivity, at a given location, as the polarization amplitude divided by the field amplitude. Bikson et al. (2004) reported an average field sensitivity of $0.12 \pm 0.05 \text{ mV} \cdot (\text{V/m})^{-1}$ at the soma for fields parallel to the somato-dendritic axis and no somatic polarization for orthogonal fields.

The DC somatic polarization is now known to depend on the cell morphology and on the field orientation with respect to the cell somato-dendritic axis (Radman et al., 2009). In this work, Radman et al. applied DC fields on slices of rats motor cortex, while recording intracellularly interneurons and pyramidal cells. After reconstructing the cells, they found the somatic polarization to correlate with the cell morphology and the field orientation. In particular, pyramidal cells displayed the strongest somatic polarization for fields parallel to their somato-dendritic axis⁶; the soma of symmetric cells, e.g. interneurons, was little polarized.

Compared to polarization through DC fields, the polarization induced by oscillating, i.e. AC, fields has received little attention. Deans et al. (2007) measured, *in vitro*, the somatic polarization of CA3 pyramidal cells due to AC fields with frequencies ranging from DC to 100Hz. For all considered field frequencies, the polarization amplitude scaled linearly with the field amplitude. Deans et al. reported an exponential decay of the somatic polarization with the field frequency. It is noteworthy, though, that the lowest field frequency they measured is 10Hz and that the exponential decay is not including the 0 Hz field (DC) (see Deans et al., 2007, Fig. 1C). Hence, Deans et al. measurements do not exclude a resonance of the somatic field sensitivity in the low frequency range (between 0 and 10Hz). To my knowledge, Deans et al. work is the only experimental study reporting the subthreshold sensitivity of pyramidal cells to AC fields for a wide range of frequencies (see Reato et al., 2013, Fig. 1E for a review); unfortunately they solely measured the polarization at the soma.

Modulation of neural activity due to weak electric fields So far, I reviewed studies investigating the subthreshold polarization of neuronal membranes due to electric fields. Still, a primordial question remains: how does this subthreshold polarization translates into a suprathreshold modulation, i.e. a modulation of neuronal spiking activity?

To address this question, Bikson et al. (2012b) theorized the *somatic* and the *terminal* doctrines. According to the somatic doctrine, weak electric fields modulate neural activity by polarizing the soma; this somatic polarization brings the somatic membrane potential closer or further away from the spiking threshold. The terminal doctrine then complements the somatic doctrine. The terminal doctrine assumes that the effects of electric fields is not solely located at the soma but at neuronal terminals too, e.g. at the dendrites, at the synapses and/or at the axon.

The earlier studies focused only on the effects of somatic polarization on the spiking activity. The somatic polarization due to electric fields has been shown to shift the spike timing (Radman et al., 2007). Using CA1 hippocampal slices, Radman et al. applied an intracellular current ramp at the soma of pyramidal cells. This suprathreshold ramp current brought the cells to fire at a regular time interval. The application of

⁶ In (Radman et al., 2009), the somato-dendritic axis corresponded to the vector between the soma and the cell center of mass. This measure enables the definition of a somato-dendritic axis for interneurons.

weak DC fields (from -30 to 30 V/m) changed the timing of action potentials (AP). While positive fields delayed an action potential, negative fields advanced its onset; the shift of the spike timing scaled linearly with the field amplitude. The application of an oscillating, i.e. AC, field (30 Hz) increased the coherence of spiking with the field oscillations. More specifically, the field changed the distribution of spike occurrences at a given phase of the field⁷.

Recently, an increasing number of experimental studies started investigating the effects of weak electric fields on the synaptic efficacy. Using rats motor cortex slices, Rahman et al. (2013) found weak electric fields parallel to the somato-dendritic axis to modulate the synaptic efficacy consistently with the somatic polarization⁸: the synaptic efficacy was increased by fields which depolarized the soma. In contrast, fields perpendicular to the somato-dendritic axis modulated the synaptic efficacy in a pathway-specific manner. This latter modulation was consistent with the terminal polarization, the hyperpolarization of afferent axons facilitating the synaptic efficacy. Note that, the polarization of axons terminals due to DC fields has been shown to significantly modulate the action potential dynamics (Chakraborty et al., 2017). Rahman et al. (2017) further reported a modulation of synaptic efficacy through DC fields during adaptation to ongoing activity. Additionally, weak DC fields have been shown to affect synaptic plasticity in CA1 of rat hippocampal slices (Kronberg et al., 2017). Measuring long-term potentiation (LTP) and depression (LTD) at Schaffer collateral synapses, Kronberg et al. analyzed the impact of $\pm 20\text{V/m}$ DC fields on the plasticity. Interestingly, they observed a bias towards potentiation: the fields tended to reduce LTD and enhance LTP. This effects could be observed with both field directions, i.e. with positive or negative fields.

Weak extracellular fields have also been shown to alter the input/output function of pyramidal cell, i.e., the likelihood of the cell firing a somatic spike in response to a given synaptic input. For example, the application of 10 Hz tACS resulted, *in vivo*, in a reduced spike frequency of MT (middle temporal area) neurons and in an increased broadband LFP (Kar et al., 2017). Interestingly, Lafon et al. (2017) observed an asymmetric change in input/output function due to DC fields of opposite directions. Using a 2 compartments neuron model, Lafon et al. related this asymmetry to the interplay between the somatic and terminal polarization. Indeed, while a depolarization of the soma increased the probability of an action potential, an hyperpolarization of the dendrites enhanced the driving force of the synaptic activity but reduced the probability of a dendritic spike. Field parallels to the somato-dendritic axis induced opposite polarizations at the soma and at the apical dendrites. In case of a depolarization of the soma (and therefore an hyperpolarization of the apical dendrites)⁹, these opposite polarizations had a synergistic effect and the spiking probability of the cell was increased. On the contrary, in case of an opposite field polarization, the effects at the soma and the apical dendrites would cancel out and the input/output function of the cell was little affected. As a consequence, (Lafon et al., 2017) concluded on an asymmetric effect of

⁷Note that, Radman et al. (2007) used only the timing of the first spike for this analysis.

⁸Rahman et al. (2013) used the terms *tangential* and *radial*, which refers to the field orientation compared to the cortical surface. Tangential fields are orthogonal to the somato-dendritic axis of pyramidal cells and radial fields parallel to this axis.

⁹Lafon et al. (2017) used the term *anodal* and *cathodal* stimulations for referring to fields generated close to, respectively, the positive and negative tCS electrodes. Cathodal fields hyperpolarize the soma and depolarize the apical dendrites. Anodal fields induce the opposite polarization.

DC fields, when taking into account both somatic and apical terminal polarizations. Yet, it is noteworthy that the electric fields applied by Lafon et al. (2017) in this study were rather strong (35 V/m).

Modelling the effects of extracellular fields on a cable In addition to relatively recent experimental works on the membrane polarization due to extracellular fields, modelling studies have been investigating the mechanisms behind this polarization for some time (see Miranda et al., 2009, for an exhaustive review). The extracellular field is usually modeled by setting a gradient of extracellular potential along the cell membrane (see Rattay, 1986; Tranchina and Nicholson, 1986; Plonsey and Altman, 1988; Rattay, 1998; Roth and Basser, 1990, for early works). Using this approach, Roth and Basser (1990) derived a modified cable equation which accounts for the presence of an extracellular electric field. For completeness, the derivation of this cable equation is reproduced in the Appendix A.1.

Rattay (1986) showed that the impact of an extracellular field on the membrane is determined by the second derivative of the extracellular potential, i.e. the gradient of the field itself¹⁰. Consequently, spatially uniform fields (i.e. fields with a spatial derivative being null) impact straight cables only at their extremities, leaving infinite cables unaffected. In a more recent work, Anastassiou et al. (Anastassiou et al., 2010) demonstrated that the membrane polarization in response to DC fields is stronger for spatially non-uniform electric fields than for uniform ones.

Interestingly, the membrane potential has been shown to raise faster in response to an electric field than in response to an injected input current (Cartee and Plonsey, 1992). It is noteworthy that the formulation of the cable equation in an electric field relies on an *open-circuit* model. Indeed, the current is allowed to flow between neighboring neurons without any constraint on local electric balance. In this case the neuron does not alter its surrounding extracellular potential, unlike what would be the case in a *closed-circuit* model (see Bédard and Destexhe, 2013, Fig. 5, for a better description of these two models and for a cable theory generalized to membranes embedded in complex extracellular media).

Despite the assumption of an *open-circuit* model, the cable equation is still a good approximation for the polarization of a cylinder due to an extracellular field (Malik, 2011, Chapt. 2). Malik used FEM to simulate the polarization of a finite cylinder in presence of a current flowing in the extracellular medium. He then compared this polarization obtained through FEM to the polarization of the same cylinder as predicted by the cable equation. The cable equation accurately predicted the polarization to DC and AC uniform fields as long as the membrane conductance was not too low and the cable was not compact, i.e. the cable length was not negligible compared to its characteristic space constant λ (see Fig. 2.11 and 2.12 in Malik, 2011).

Effects of tCS at the network level The effects of weak electric fields at the network level have received even less attention than the effects at the single cell level. In a seminal work, Fröhlich and McCormick (2010) showed that endogeneous electric fields,

¹⁰ In general, the contributions of Rattay mainly focus on suprathreshold stimulations of neural activity, i.e. stimulations aiming at triggering spikes, as observed during intracellular electric stimulations, e.g. deep brain stimulation. Nevertheless, his results on the membrane polarization are valid in case of weak extracellular fields.

i.e. LFP, may entrain neural activity. The authors recorded LFP during slow oscillations, i.e. Up and Down states, in primary visual cortex of anesthetized ferrets and injected the corresponding temporal traces of the field in cortical slices. They observed an entrainment of Multi-Unit Activity (MUA), i.e. local population spiking, due to the field. A similar entrainment was reported *in vivo* by Anastassiou et al. (2011). Applying weak DC and AC fields in rats hippocampal slices, Reato et al. (2010) successfully modulated carbachol-induced gamma oscillations (25-35Hz). They reported that DC fields of opposite directions induced opposite modulations of the ongoing activity, the amplitude of the modulation was not symmetric with the field amplitude though. The modulation due to AC fields depended on the field frequency. Low frequency fields ($\leq 12\text{Hz}$) modulated ongoing oscillations with the frequency of the field; the mean firing rate remained unaltered. On the contrary, higher frequency fields induced half harmonic oscillations. Interestingly, the slices were more responsive to weak AC fields than to DC fields. Reato et al. also reproduced their *in vitro* results using a network of interconnected Izhikevich point neuron models, to which they added an additional injected input current to account for the somatic polarization. More recently, (Reato et al., 2015) observed effects of tDCS-induced field on carbachol-induced gamma oscillations that outlasted the field stimulation.

Entrainment of ongoing neural activity through tCS has also been observed *in vivo* (Ozen et al., 2010). Applying very low frequency ($\leq 1.7\text{Hz}$) tACS on rats, Ozen et al. reported a phase locking of neuronal activity to the electric field; the percentage of phased-locked neurons increased with the stimulus intensity and depended on the ongoing activity. Importantly, they observed a phase-bias of neuronal spiking with electric fields as low as 1V/m .

Using voltage-sensitive dyes, Xu et al. (2014) reported the presence of both active and passive components in the neural population response to weak AC fields. The passive component simply corresponded to the membrane polarization of neurons due to the field. The active component was present only for low frequency fields and during the first few cycles after the field onset. This active component amplified the neural response to positive phase of the field. Xu et al. (2014) explained this active component as a network amplification effect, the activity of several neurons being modulated synchronously. Interestingly, the active component was only triggered for electric fields stronger than 4V/m , which is of higher amplitude than tCS-induced field.

Outline To summarize, how transcranial current stimulation modulates ongoing neural activity is still largely not understood. This lack of understanding impedes the design of optimal stimulation protocols. tCS is known to induce an extracellular electric field within the brain. This electric field polarizes the neuronal membranes and therefore modulates the neural activity. Nevertheless, the effects of non-stationary fields on neural activity still require further investigation (Reato et al., 2013). In this thesis, I focus on the effects of weak uniform electric fields, as induced during tCS, on single neuron activity. The thesis is divided in two chapters which follow respectively the somatic and dendritic doctrine (Bikson et al., 2012b)¹¹. While addressing the same topic, the two chapters are largely independent and can be read separately.

In the first chapter, I investigate the effects of somatic polarization induced by weak

¹¹ In the dendritic doctrine, I consider the effects of the dendritic polarization due to weak extracellular fields, leaving aside the axonal polarization.

electric fields on single neurons activity. In practice, I study these effects in a canonical neuron model, namely a ball-and-stick model, and I extend simple point neuron models to reproduce these effects. In the second chapter, I extend my focus from the somatic polarization to the dendritic polarization: I investigate the polarization of the dendritic tree of cortical pyramidal neurons. In particular, I consider the relative role of morphology and of active membrane properties on the dendritic polarization. Finally, I show how this polarization may affect the spiking behavior of pyramidal cells.

Chapter 2

The somatic doctrine: Extending point neuron models to account for electric field effects at the soma

2.1 Overview

As introduced in the precedent chapter, transcranial current stimulation induces weak extracellular electric fields within the brain. These electric fields have been shown to polarize the membrane of single neurons (Bikson et al., 2004; Radman et al., 2009; Deans et al., 2007), and therefore to modulate the neural activity. However, their effects on population spike rate and the mechanisms underlying these effects are largely unexplored.

Computation models are a useful tool to investigate the modulation of population spike rates due to extracellular fields. While multi-compartment neuron models, e.g. models with reconstructed morphology, can be used to investigate the effects of extracellular fields on single cells or small circuits (Tiganj et al., 2014), these models are too complex to be deployed in large populations. On the contrary, point (single-compartment) neuron models of the integrate-and-fire (IF) type are computationally more efficient and analytically tractable (Brunel, 2000). Point neuron models are therefore suitable for investigating the spike rate dynamics of large neuronal populations. Nevertheless, usual IF neuron models lack the spatial extent, e.g. the dendritic morphology, necessary to a biophysical description of the effects of electric fields. Besides, the neuronal response properties are strongly shaped by the dendritic morphology (Ostojic et al., 2015), even in the absence of electric fields.

In this chapter, we investigate the effects of weak electric fields on neural activity following the somatic doctrine. In other words, we focus on the somatic polarization due to weak extracellular fields and on the ensuing modulation of the spike rate dynamics of simple neuron models. Furthermore, we present an extended point neuron model which captures these effects and which can be used in large-scale simulations. Specifically, we first consider a canonical spatial neuron model, namely the ball-and-stick neuron model, exposed to *in vivo*-like fluctuating synaptic inputs and to an extracellular electric field. We then analytically extend leaky and exponential (Fourcaud-Trocmé et al., 2003) IF point neuron models to reproduce the subthreshold membrane dynamics of this spatial model for arbitrary parametrizations. Our extended model replicates (i) the impact of

a dendritic tree on the synaptic inputs integration and (ii) the effects of weak electric fields. Quantitatively comparing the spiking activity of the two models, we evaluate the extended point neuron model. Finally, we investigate the effects of a spatially uniform AC field on spike rate dynamics.

The results presented in this chapter have been previously published (Aspart et al., 2016)^{1 2}.

2.2 Models presentation

In the following, we formally introduce the neuron models used in this chapter. In brief, the ball-and-stick model is a spatially extended canonical model which consists of a lumped soma attached to a passive cable. The extended point (eP) neuron model is a simple integrate-and-fire point neuron model with additional model components. We derive the point neuron model extension in two steps.

To begin with, we analytically compute the subthreshold response of a ball-and-stick (BS) model at the soma, i.e. its somatic membrane potential response, to three perturbations. The perturbations include synaptic inputs located (i) at the soma or (ii) at the distal dendrite and (iii) a spatially homogeneous, but time-varying, extracellular electric field. This computation involves solving the cable equation in presence of an electric field (see Appendix A.1 and A.2).

We then seek to reproduce the ball-and-stick membrane response in the point neuron model through derivation of additional model components (see Fig. 2.1). The model components are two linear temporal filters (one for each synaptic location), which we apply to the "raw" synaptic input, and an additional input current to account for the field effects. The three model components are derived analytically and depend on the parameters of the BS model and on the extracellular field.

We first derive the extension for the leaky integrate-and-fire (LIF) neuron model (Section 2.3). Finally, we adapt our extension to a more refined model: the exponential integrate-and-fire (EIF) neuron model (Section 2.4).

Ball-and-stick model We follow the BS neuron model description used by Tuckwell (1988): a lumped-soma attached to a straight passive dendritic cable. In other words, we neglect the diameter of the soma compared to the dendritic cable length l . Consequently, the soma perceives a uniform extracellular potential, equal to the potential at the beginning of the cable. We further provides the BS model with a IF-type reset mechanism as well as an exponential spike initiation mechanism (see below).

The dynamics of its membrane voltage, when subject to synaptic inputs located at the soma, $I_s(t)$, and at the distal dendrite, $I_d(t)$, and to a spatially homogeneous extracellular field, $E(t)$, are determined by the cable equation:

$$c_m \frac{\partial V_{BS}}{\partial t} - g_i \frac{\partial^2 V_{BS}}{\partial x^2} + g_m V_{BS} = 0, \quad 0 < x < l, \quad (2.1)$$

¹ The authors contribution to the original article are (FA: F. Aspart, JL: J. Ladenbauer, KO: Klaus Obermayer): Conceptualization: JL FA. Funding acquisition: JL KO. Investigation: FA JL. Methodology: FA JL. Project administration: JL KO. Software: FA JL. Supervision: JL KO. Validation: FA JL. Visualization: FA JL. Writing – original draft: FA JL KO. Writing – review & editing: FA JL KO.

²The article is published under the Creative Commons Attribution License (CC BY 4.0).

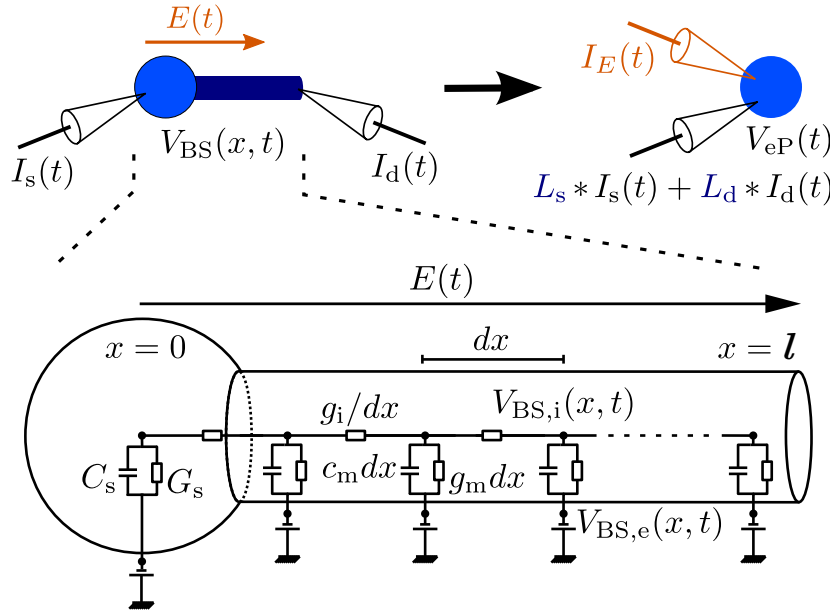


Figure 2.1: Diagram of the extended point neuron model

Top: Visualization of the ball-and-stick, BS, (*left*) and the extended point, eP, (*right*) neuron models. Both models receive synaptic input currents at the soma and the distal dendrite, $I_s(t)$ and $I_d(t)$, and are exposed to an external electric field $E(t)$. $L_s(t)$ and $L_d(t)$ denote the additional input filters describing the dendritic effects. $I_E(t)$ denotes the additional input current describing the field effect. $V_{eP}(t)$ and $V_{BS}(0, t)$ denote the corresponding membrane voltages (at the soma). *Bottom:* Electrical circuit diagram for the subthreshold dynamics of the BS model. For a description of the parameters and their values see Table C.1 in Appendix. Figure and caption adapted from (Aspart et al., 2016, CC BY 4.0)

with the boundary conditions at the soma ($x=0$) and at the dendritic end ($x=l$):

$$C_s \frac{\partial V_{BS}}{\partial t} - g_i \frac{\partial V_{BS}}{\partial x} + G_s V_{BS} - G_s \Delta_T e^{\frac{V_{BS} - V_T}{\Delta_T}} = I_s(t) - g_i E(t), \quad x = 0, \quad (2.2)$$

$$\frac{\partial V_{BS}}{\partial x} = \frac{I_d(t)}{g_i} + E(t), \quad x = l, \quad (2.3)$$

V_{BS} corresponds to the deviation of the membrane voltage from rest V_{rest} :

$$V_{BS}(x, t) := V_{BS,i}(x, t) - V_{BS,e}(x, t) - V_{rest}, \quad (2.4)$$

where $V_{BS,e}$ and $V_{BS,i}$ are the extra- and intracellular potentials. c_m is the membrane capacitance and g_m , g_i are respectively the membrane (radial) and the internal (axial) conductances of a dendritic cable segment of unit length. G_s and C_s denote the somatic membrane capacitance and leak conductance. The exponential term, with effective threshold voltage V_T and threshold slope factor Δ_T , corresponds to an approximate somatic sodium current during spike initiation (Fourcaud-Trocmé et al., 2003).

The cable equation due to the field (Eq. 2.1) and the boundary conditions at both ends (Eq. 2.2 and 2.3) due to synaptic inputs were already reported in the literature (Roth and Basser, 1990; Tuckwell, 1988). The boundary condition at the soma in presence of an electric field has not been derived before. For the sake of completion, the full derivation of these equations can be found in Appendix A.1.

We also provides the BS model with a IF-type spike mechanism. This mechanism is described by a reset condition at the soma:

$$\text{if } V_{BS}(0, t) \geq V_s \text{ then } V_{BS}(0, t) := V_r \quad (2.5)$$

We further include a short refractory period of length $T_{\text{ref}} = 1.5$ ms, during which we clamp the somatic membrane $V_{\text{BS}}(0, t)$ at the reset value V_r . We do not include any reset mechanism along the dendritic cable.

In the following, we define spike times as the times at which the somatic membrane voltage $V_{\text{BS}}(0, t)$ crosses the spike threshold V_s .

Point neuron models In our IF point neuron extension (eP model), the deviation, V_{eP} , of the membrane voltage from rest is determined by:

$$C_{\text{eP}} \frac{dV_{\text{eP}}}{dt} + G_{\text{eP}} V_{\text{eP}} - \alpha G_{\text{eP}} \Delta_T e^{\frac{V_{\text{eP}} - V_T}{\Delta_T}} = [L_s * I_s](t) + [L_d * I_d](t) + I_E(t), \quad (2.6)$$

G_{eP} and C_{eP} are the membrane leak conductance and capacitance. We set them to the same values as the somatic conductance and capacitance of the BS model: $C_{\text{eP}} = C_s$, $G_{\text{eP}} = G_s$. While this choice reduces the space of free parameters for the analysis, it enables us to determine the effects of adding a dendritic cable to a simple point neuron model.

L_s , L_d , I_E and α are the additional model components compared to usual point neuron models (Fourcaud-Trocmé et al., 2003). In brief, L_s and L_d are linear temporal filters to account for synaptic input at different locations (respectively the soma and the dendritic end). I_E is an equivalent input current to reproduce the polarization due to the field as observed in BS. Finally, the scaling factor α ensures an equal membrane response to the phenomenological spike initiating current (the exponential terms) in both models (BS and eP). More precisely it compensates the conductance difference in the BS and the eP model in response to the depolarizing current (see Section 2.4).

Similarly to the BS model, the eP model includes a reset condition:

$$\text{if } V_{\text{eP}} \geq V_s \text{ then } V_{\text{eP}} := V_r', \quad (2.7)$$

and a refractory period $T_{\text{ref}} = 1.5$ ms during which the membrane voltage V_{eP} is clamped to V_r' after each spike. Note that the eP and the BS model do not have the same reset value. In fact, we choose an elevated reset voltage for all point neuron models: $V_r' = (V_r + V_T)/2$, in order to imitate the remaining depolarization along the dendritic cable after each spike.

As mentioned above, we derive successively two versions of the extended point neuron model. First, we consider the leaky IF (LIF) version, where we neglect the exponential terms in Eqs. 2.2 and 2.6 by taking the limit $\Delta_T \rightarrow 0$ (and setting $V_s = V_T$). Subsequently, we treat the full exponential IF (EIF) versions of the BS and eP models. In the following sections, we detail the derivation of the point model extension components: the linear input filters $L_s(t)$, $L_d(t)$, the additional input current equivalent to the field effect, $I_E(t)$, and, in case of the EIF type models, the scaling factor α . The mathematical expressions of these model components are provided in Eqs. 2.14, 2.18 and 2.22, 2.23 (for the LIF case), and in Eqs. 2.26–2.30 (for the EIF case).

As a comparison, we also consider a point neuron model (of LIF and EIF type, respectively) without the extension, that is $L_s(t) = L_d(t) = \delta(t)$ and $\alpha = 1$. This model, which we refer as the P model, corresponds to the traditional IF point neuron model. We fit its parameters to best reproduce the activity of the BS model for equal synaptic inputs (see below for details).

Simulating the neuron models In the following, we simulate the BS neuron model using the NEURON simulation environment (Hines and Carnevale, 2001). Specifically, the model is integrated numerically using a finite difference space discretization, i.e. the dendritic cable is divided into 50 segments, and the implicit Euler (also known as backward Euler) time discretization scheme. We use fixed time steps of 0.05 ms for the LIF case and of 0.025 ms for the EIF simulation³. When mentioned, we apply a sinusoidal extracellular electric field to the BS model using the NEURON built-in “extracellular” mechanism.

We simulate the point neuron models (eP and P) using a self implemented forward Euler time discretization scheme with the same time step as for the BS model. The solution is implemented in Python and uses the “Numba” library for faster computation.

When mentioned, we investigate the models responses to *in vivo*-like fluctuating input currents. We describe these stochastic input currents using an Ornstein-Uhlenbeck process:

$$\frac{dI_x}{dt} = \frac{I_x^0 - I_x}{\tau} + \sigma_x \sqrt{\frac{2}{\tau}} \xi_x(t), \quad (2.8)$$

with mean I_x^0 , correlation time τ and standard deviation σ_x . The subscript $x \in \{s, d\}$ denotes the input location: “s” for a somatic input and “d” for an input located at the dendritic end. $\xi_x(t)$ denotes a Gaussian white noise process, i.e. with zero mean ($\langle \xi_x(t) \rangle = 0$) and delta autocorrelation ($\langle \xi_x(t) \xi_x(t + t') \rangle = \delta(t')$), $\langle \cdot \rangle$ being the expectation operator. In practice, we numerically integrate Eq. 2.8 using Gillespie’s method (Gillespie, 1996). In all presented simulations, the stochastic synaptic input is also integrated in NEURON and the same realization is shared across all neuron models, i.e. BS, eP and P.

We apply the linear filter $L_x(t)$ of the eP model offline in the Fourier domain. In other words, we take the fast Fourier transform (FFT) of $I_x(t)$, apply the filter in the frequency domain and then use the inverse FFT of the filtered signal $\hat{L}_x(\omega) \hat{I}_x(\omega)$, $x \in \{s, d\}$.

As an example, a clean source code for the implementation of all three model is freely available at https://github.com/nigroup/IF_extension.

2.3 Extending LIF point neuron models

We first consider the BS and eP models of the LIF type (i.e. $\Delta_T \rightarrow 0$, $V_s = V_T$). Therefore, the BS equation rewrites:

$$c_m \frac{\partial V_{BS}}{\partial t} - g_i \frac{\partial^2 V_{BS}}{\partial x^2} + g_m V_{BS} = 0, \quad 0 < x < l, \quad (2.9)$$

with the boundary conditions:

$$\begin{aligned} C_s \frac{\partial V_{BS}}{\partial t} - g_i \frac{\partial V_{BS}}{\partial x} + G_s V_{BS} &= I_s(t) - g_i E(t), & x = 0 \\ \frac{\partial V_{BS}}{\partial x} &= \frac{I_d(t)}{g_i} + E(t), & x = l \end{aligned}$$

³Varying the number of segments and/or the time step did not change the results obtained through numerical integration (neither the membrane voltage traces nor the spike trains).

The equation corresponding to the eP model of the LIF type is:

$$C_{\text{eP}} \frac{dV_{\text{eP}}}{dt} + G_{\text{eP}} V_{\text{eP}} = [L_s * I_s](t) + [L_d * I_d](t) + I_E(t), \quad (2.10)$$

Applying the Fourier transform in the temporal domain on Eq. 2.10 yields:

$$C_{\text{eP}} i\omega \hat{V}_{\text{eP}} + G_{\text{eP}} \hat{V}_{\text{eP}} = \hat{L}_s(\omega) \hat{I}_s(\omega) + \hat{L}_d(\omega) \hat{I}_d(\omega) + \hat{I}_E(\omega),$$

where $\omega = 2\pi f$ denotes an angular frequency and $\hat{\cdot}$ corresponds to the temporal Fourier transform.

From this equation, we obtain the membrane potential of the eP model in response to synaptic input currents and extracellular field:

$$\hat{V}_{\text{eP}}(\omega) = \frac{\hat{L}_s(\omega) \hat{I}_s(\omega) + \hat{L}_d(\omega) \hat{I}_d(\omega) + \hat{I}_E(\omega)}{C_{\text{eP}} i\omega + G_{\text{eP}}}. \quad (2.11)$$

The equations determining the membrane voltage of both models being linear (Eq. 2.9-2.10), we will in the following consider the membrane response to each perturbations, namely I_s , I_d and E , successively. To avoid ambiguity, we will denote the membrane potential variations due to each perturbations separately using the superscripts I_s , I_d or E .

2.3.1 The somatic input filter for the LIF model

Filter derivation We first consider the BS and eP neuron models (of the LIF type) simply subject to a synaptic input at the soma, I_s , i.e. in the absence of dendritic synaptic input ($I_d = 0$) and electric field ($E = 0$).

The subthreshold membrane response of the BS model is (see Appendix A.2 for the detailed derivation):

$$\hat{V}_{\text{BS}}^{I_s}(0, \omega) = \frac{\hat{I}_s(\omega)}{C_s i\omega + G_s + z(\omega) g_i \tanh(z(\omega)l)}, \quad (2.12)$$

$$z(\omega) = \sqrt{\frac{g_m + \sqrt{g_m^2 + \omega^2 c_m^2}}{2g_i}} + \text{sgn}(\omega) i \sqrt{\frac{-g_m + \sqrt{g_m^2 + \omega^2 c_m^2}}{2g_i}}, \quad (2.13)$$

Following from Eq. 2.11, the subthreshold membrane response of the eP model is:

$$\hat{V}_{\text{eP}}^{I_s}(\omega) = \frac{\hat{L}_s(\omega) \hat{I}_s(\omega)}{C_{\text{eP}} i\omega + G_{\text{eP}}}.$$

We design the linear synaptic input filter L_s in order to exactly reproduce in the eP model the somatic membrane response of the BS model, that is $\hat{V}_{\text{eP}}^{I_s}(\omega) = \hat{V}_{\text{BS}}^{I_s}(0, \omega)$. To this end, we set the filter equal to the ratio of impedances of both models:

$$\hat{L}_s(\omega) = \frac{C_{\text{eP}} i\omega + G_{\text{eP}}}{C_s i\omega + G_s + z(\omega) g_i \tanh(z(\omega)l)}, \quad (2.14)$$

where $z(\omega)$ is defined in Eq. 2.13.

To evaluate the necessity of the filter, we compare the eP and BS model to the P model (no dendritic filter, $\hat{L}_s(\omega) = 1$). The subthreshold response of the P model is:

$$\hat{V}_P^{I_s}(\omega) = \frac{\hat{I}_s(\omega)}{C_P i\omega + G_P}. \quad (2.15)$$

Comparing the equations for the membrane responses of the BS and the P model (respectively Eq. 2.12 and Eq. 2.15), the presence of an additional frequency-dependent term in the denominator of the BS model impedes the reproduction of the BS membrane response in the P model. Indeed, there is no set of parameters for the P model (i.e. C_P and G_P) such that $\hat{V}_P^{I_s}(\omega) = \hat{V}_{BS}^{I_s}(0, \omega)$ for all frequencies ω . Simple LIF point neuron model (i.e. the P model) can therefore only approximate the subthreshold somatic response of the BS model.

For comparison, we plot the impedances, $Z_m^{I_s}(\omega) := \hat{V}_m^{I_s}(\omega)/\hat{I}_s(\omega)$, $m \in \{\text{BS}|_{x=0}, \text{eP}, \text{P}\}$, of the three neuron models (Fig. 2.2A). The displayed impedance of the BS model corresponds to an arbitrary parameter set chosen as an example, nevertheless, choosing other parameters did not change qualitatively the following results. Here, the parameters of the P model are set to best reproduce the impedance of the BS model⁴. Despite this choice of best P parameters, the impedance of the P model deviates substantially from the BS one in the large frequencies. On the contrary, the impedance of the eP model successfully matches the one of the BS model. This is not surprising, since the input filter L_s was designed to this end.

We further look at the amplitudes and phases of the input filter $\hat{L}_s(\omega)$ for varying BS morphology (Fig. 2.2B-D). Regardless of the BS morphology, $\hat{L}_s(\omega)$ acts as a high-pass filter. It attenuates the low frequency somatic inputs and leave the higher frequency inputs (in comparison) unchanged. However, the BS morphology affects the filter shape. The bigger (e.g. longer and thicker) the dendritic compartment, the strongest is the attenuation in the low frequency range. On the contrary, the BS soma size mainly affects the higher frequency response: the bigger the soma, the more the filter attenuates high frequency inputs. For very small somas, the filter even enhance the high frequency responses ($L_s(\omega) > 1$ for $\omega = 10^4$).

Comparison of the models spiking activity After comparing the models impedances, and therefore their subthreshold membrane responses, we now focus on the suprathreshold activity of the models. More precisely, we analyze how well the eP and P neuron models reproduce the spiking activity of the BS model in response to an *in vivo*-like fluctuating input current at the soma $I_s(t)$. We describe this stochastic input current using an Ornstein-Uhlenbeck process, described in Eq. 2.8, with mean I_s^0 , correlation time τ and standard deviation σ_s .

To compare the spiking activity of the different neuron models in response to the somatic input, we use the spike trains coincidence factor Γ as defined by Gerstner and Kistler (2002)⁵. The spike trains coincidence factor between a reference

⁴In Fig. 2.2A, we first adjust the conductance of the P model, G_P , to match the steady-state somatic response of the BS model $Z_P^{I_s}(0) = Z_{BS}^{I_s}(0)$. We then select its capacitance C_P using grid search to minimize the mean squared distance between the impedance of both models ($Z_P^{I_s}$ and $Z_{BS}^{I_s}$) over the range of visualized input frequencies.

⁵In the paper, the authors refers to the coincidence factor as the "coincidence rate".

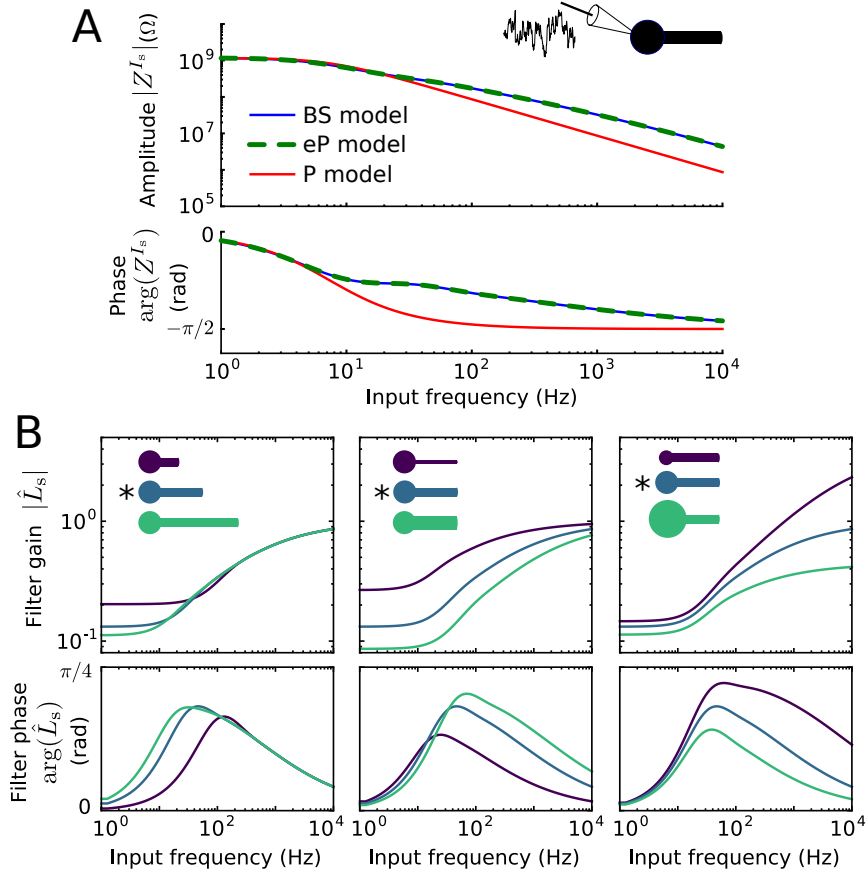


Figure 2.2: Impedance and filter for somatic inputs

(A) Impedances $Z_{\text{BS}}^{I_s}$, $Z_{\text{eP}}^{I_s}$, and $Z_{\text{P}}^{I_s}$ of the three neuron models as a function of input frequency. (B) Gain and phase of the input filter \hat{L}_s as a function of input frequency. The neuronal morphology varied as indicated, in terms of dendritic cable length ($350 \mu\text{m}$, $700 \mu\text{m}$, $1050 \mu\text{m}$), cable diameter ($0.6 \mu\text{m}$, $1.2 \mu\text{m}$, $1.8 \mu\text{m}$) and soma diameter ($5 \mu\text{m}$, $10 \mu\text{m}$, $15 \mu\text{m}$). * indicates the default parameter values. For all other parameter values used see Table C.1 in Appendix. Figure and caption adapted from (Aspart et al., 2016, CC BY 4.0)

and a compared spike train is defined as:

$$\Gamma_{\text{ref,comp}} = \frac{N_{\text{coinc}} - \langle N_{\text{coinc}} \rangle}{(N_{\text{ref}} + N_{\text{comp}})/2} \frac{1}{\mathcal{N}}, \quad (2.16)$$

where N_{ref} and N_{comp} are respectively the number of spikes in the reference and in the compared spike trains. N_{coinc} denotes the number of coincident spikes between both spike trains with temporal precision $\Delta = 3\text{ms}$. $\langle N_{\text{coinc}} \rangle = 2r\Delta N_{\text{ref}}$ corresponds to the expected number of coincidences if the compared spike train were generated by an homogeneous Poisson process with same spike rate $r = N_{\text{comp}}/T$, T being the spike train duration.

Due to the normalization factor $\mathcal{N} = 1 - 2r\Delta$, the coincidence factor ranges between 0 and 1. While $\Gamma_{\text{ref,comp}} = 1$ corresponds to spikes trains matching exactly (with temporal precision Δ), $\Gamma_{\text{ref,comp}} = 0$ indicates a pure chance coincidence levels.

We fit the P model parameters for each synaptic input realization (hence for each considered pair of I_s^0 , σ_s). For a given synaptic input, the P model parameters are optimized to best reproduce the BS spike train, in terms of spike coincidence⁶. As

⁶More precisely, we choose G_{P} to reproduce the steady-state subthreshold response of the BS

mentioned above, we set the membrane capacitance and conductance of the eP model to the same values as the BS somatic capacitance and conductance: $C_{\text{eP}} = C_s$, $G_{\text{eP}} = G_s$.

Fig. 2.3A displays the somatic membrane potential of the three models in response to weak (small I_s^0 , σ_s) and to strong (large I_s^0 , σ_s) somatic input currents $I_s(t)$. For both considered input currents, the eP model (green traces) successfully reproduces the somatic voltage dynamics of the BS model (blue traces). As a result, the spike times are well reproduced (see below for further analysis).

Note that, each spike introduces a mismatch between the BS and eP voltage traces. Indeed, we derived our model in the linear, i.e. subthreshold, regime. The reset associated to the spike introduces a non-linearity which breaks this assumption of linearity. Furthermore, after each spikes the membrane of the BS model is reset at the soma only; the dendritic cable remains polarized. As a result, the voltage traces of the eP and BS models diverge for short periods of time (typically around 10 ms) after each spikes. To account for this remaining polarization, we use an elevated reset voltage in the point neuron models compared to the BS one: $V_r' = (V_r + V_T)/2$. This intermediate voltage was chosen to minimize the distance between the spike-triggered voltage traces of the BS and the point neuron models (result not shown).

Compared to the eP model, the P model (red trace) fails to reproduce the fast fluctuations of the BS somatic membrane dynamics. This result is expected considering the impedance mismatch between both models in the high frequencies (cf. Fig. 2.2A).

We now compare how well both point neuron models reproduce the spiking activity of the BS model for a wide range of input parameters, i.e. for various mean I_s^0 and standard deviation σ_s (Fig. 2.3B-E). To this end, we quantify the spike trains similarity between two models using the above mentioned coincidence factor Γ (Eq. 2.16) with a precision of 3ms. Remember that we fit the P model to reproduce the BS spiking activity for each stochastic input realization. As a consequence, the presented coincidence factors, $\Gamma_{\text{BS,P}}$, correspond to the best possible results for a given BS spike train and might not generalize to other stochastic input realization with same parametrization. On the other hand, the parameters of the eP model remain constant across the diverse input parametrizations

For small spike rates, the eP model reproduces the BS spike trains very accurately ($\Gamma \geq 0.9$ for small I_s^0 and σ_s), see Fig. 2.3B,E. The model performance, i.e. the reproduction accuracy, decreases slightly for increasing σ_s (noise dominated input), but stronger for increasing I_s^0 (mean dominated input). Overall, $\Gamma_{\text{BS,P}}$ decreases with increasing spike rates. We attribute this phenomena to the mismatch in voltage traces observed earlier after each spikes. After each spike, the eP membrane potential deviates from the somatic membrane potential of the BS model for a transient period, whose duration does not depend on the spike rate. Consequently, these deviations have a stronger impact on the spike rate reproduction when the interspike intervals are shorter (for higher spike rates). Furthermore, when the input noise is low (small σ_s), the neuron models spike repetitively in a clock-wise manner. The mismatch in spike rates of the eP and BS models (even if it is rather low), together with the mismatches

model (as described above when displaying the models impedances). We then select C_P using grid search in order to maximize the coincidence factor Γ between the spike trains of the BS and P model neurons (for a simulation duration of circa 52s and the given pair of input (I_s^0 , σ_s) parameter values). Note that in order to optimize the use of the FFT (for the filter application) algorithm, the exact simulation duration is calculated to have a number of time sample (duration/time step) equals to a power of 2.

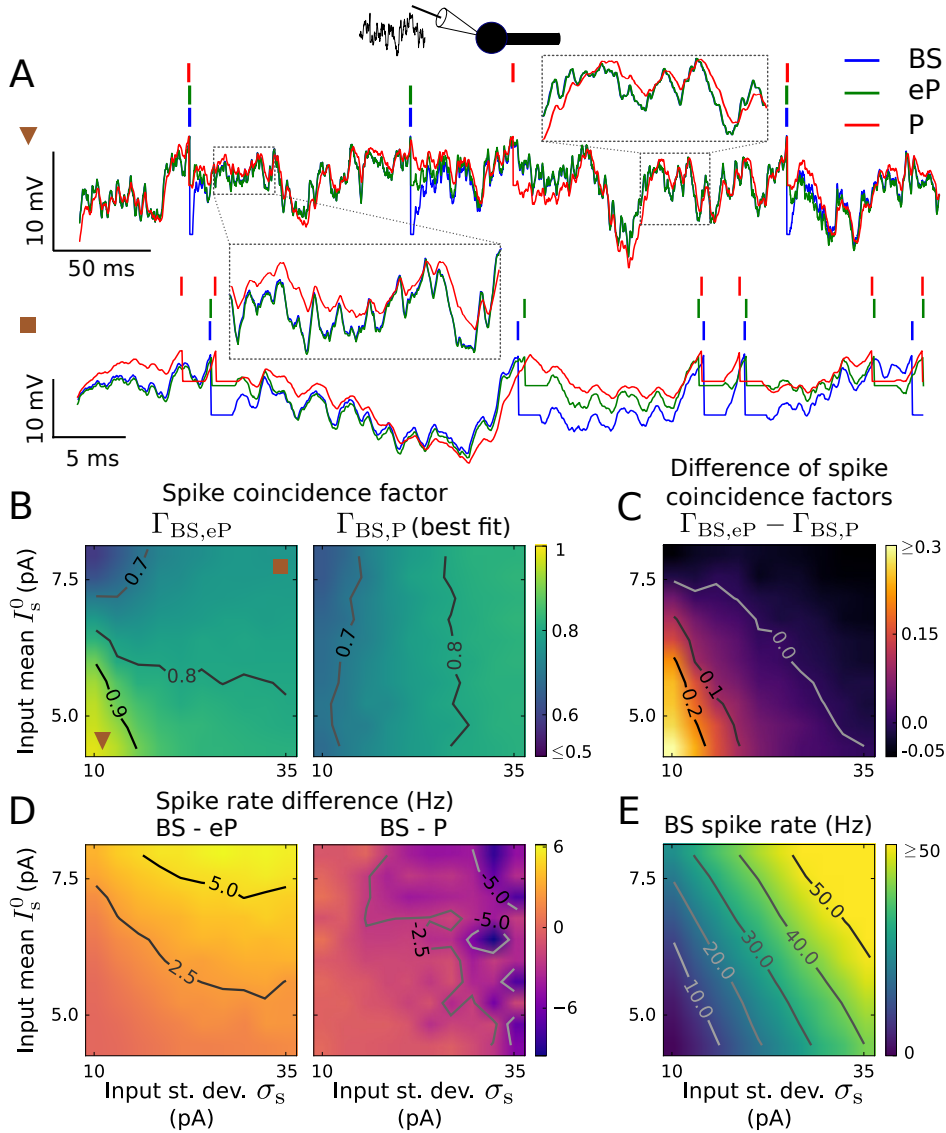


Figure 2.3: Reproduction of spiking activity for somatic inputs using LIF type models
 (A) Membrane voltage traces of the BS (blue), eP (green) and P (red) neuron models in response to a weak ($I_s^0 = 4.68$ pA, $\sigma_s = 11.94$ pA, top) and a strong input current ($I_s^0 = 7.69$ pA, $\sigma_s = 33.34$ pA, bottom). The parameter values of the P model were tuned independently to maximize the coincidence factor $\Gamma_{BS,P}$ for each set of input parameters. (B) Coincidence factor for the BS and eP model spike trains, $\Gamma_{BS,eP}$ (left), and for the BS and P model spike trains, $\Gamma_{BS,P}$ (right) as a function of input mean I_s^0 and standard deviation σ_s . (C) Difference $\Gamma_{BS,eP} - \Gamma_{BS,P}$ between the coincidence factors shown in B. (D) Spike rate difference of the BS and eP models (left) and of the BS and P models (right) as a function of I_s^0 and σ_s . (E) Spike rate of the BS neuron model. The input parameters used in (A) are indicated in (B). Results presented in (B)-(E) are averages over 6 noise realizations. The parameter values of the BS model are listed in Table C.1 in Appendix. Figure and caption adapted from (Aspart et al., 2016, CC BY 4.0)

in membrane potential after each reset, result in the neurons being out of phase and in a decreased coincidence factor. This explains the lower $\Gamma_{BS,P}$ for mean dominated inputs. Generally, The eP model slightly underestimates the spike rate of the BS model (Fig. 2.3D). Note that, the eP model performance, e.g. the spike coincidence and the spike rate reproduction, could be improved by fine tuning the reset voltage V_r' for a given input parametrization.

In comparison, the P model is considerably worse in reproducing the spike times for small spike rates and it performs only slightly better than the eP model for large spike rates (Fig. 2.3B,C). The P model slightly overestimates the BS spike rate (Fig. 2.3D). To conclude, the presented eP model outperforms the P model in the reproduction of the BS spiking activity, although we optimized the parameters of the P model for each input realizations.

In summary, adding a dendritic cable to a point neuron corresponds to high-pass filtering the somatic input currents. We therefore extended a point neuron model by adding a filter on somatic inputs. Our extended model, eP, accurately reproduces the sub- and suprathreshold responses of the BS model to somatic inputs. Most importantly, simulating the presented eP model requires at least 25 times less than simulating the BS model (measured on a single CPU code of a desktop computer).

2.3.2 The distal input filter for the LIF model

After considering somatic inputs, we now consider synaptic inputs at the distal dendrites. Besides the input location, we use the same setup as in the preceding section and the same analysis. To distinguish from the previous scenario, we denote the membrane response to the distal dendritic input with the superscript I_d . The somatic membrane response of the BS model to a distal input $I_d(t)$ can be expressed in the Fourier domain as (see Appendix A.2 for the full derivation):

$$\hat{V}_{\text{BS}}^{I_d}(0, \omega) = \frac{\hat{I}_d(\omega) \operatorname{sech}(z(\omega)l)}{C_s i\omega + G_s + z(\omega) g_i \tanh(z(\omega)l)}, \quad (2.17)$$

where $z(\omega)$ is given by Eq. 2.13.

Following from Eq. 2.11, the subthreshold membrane response of the eP model to distal input is:

$$\hat{V}_{\text{eP}}^{I_d}(\omega) = \frac{\hat{L}_d(\omega) \hat{I}_d(\omega)}{C_{\text{eP}} i\omega + G_{\text{eP}}}.$$

As previously done for the somatic input case, we derive the distal input filter \hat{L}_d in order to reproduce the somatic membrane dynamics of the BS model with eP model. In other words: $\hat{V}_{\text{eP}}^{I_d}(\omega) = \hat{V}_{\text{BS}}^{I_d}(\omega)$. This leads to the expression for the distal input filter:

$$\hat{L}_d(\omega) = \frac{(C_{\text{eP}} i\omega + G_{\text{eP}}) \operatorname{sech}(z(\omega)L)}{C_s i\omega + G_s + z(\omega) g_i \tanh(z(\omega)L)}. \quad (2.18)$$

We further choose $C_{\text{eP}} = C_s$, $G_{\text{eP}} = G_s$ for convenience.

Unlike the previous somatic input filter L_s , the distal input filter L_d exhibits low-pass properties for all considered BS morphologies (see Fig. 2.4A). The dendritic cable morphology affects the filter cutoff frequency: the longer or the thinner the cable, the lower the cutoff frequency. The soma size does not affect the filter shape. It is noteworthy, that the filter gain for high frequency dendritic input is much lower than the gain of the somatic input filter for low frequency (cf Fig. 2.2B). Therefore the filtering effects is much stronger for dendritic inputs than for somatic inputs.

We now evaluate the distal input filter in terms of reproduction of BS spiking activity, e.g. coincidence factor Γ and spike rates, in response to a stochastic input at the

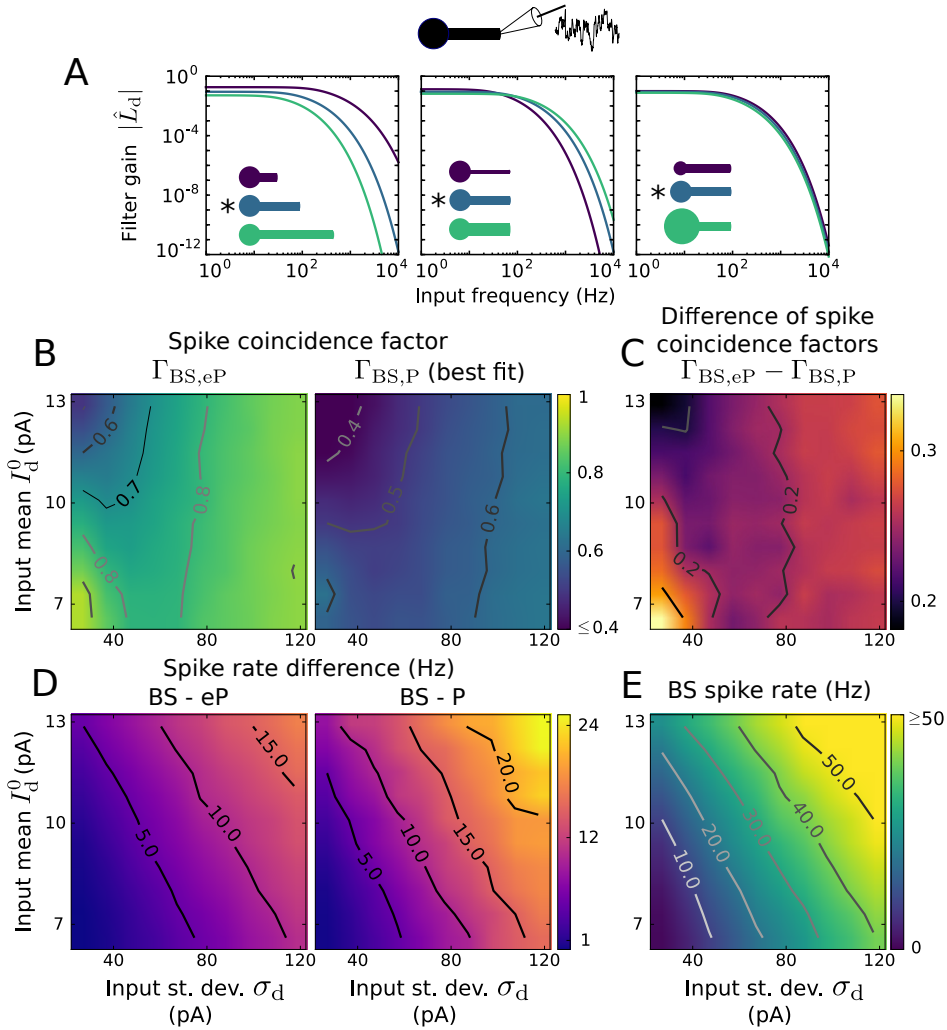


Figure 2.4: Distal input filter and reproduction of spiking activity using LIF type models (A) Gain and phase of the input filter \hat{L}_d as a function of frequency. The neuronal morphology varied as indicated, in terms of dendritic cable length (350 μm , 700 μm , 1050 μm), cable diameter (0.6 μm , 1.2 μm , 1.8 μm) and soma diameter (5 μm , 10 μm , 15 μm). * indicates the default parameter values. (B) Coincidence factor for the BS and eP model spike trains, $\Gamma_{BS,eP}$ (left), and for the BS and P model spike trains, $\Gamma_{BS,P}$ (right) as a function of input mean I_d^0 and standard deviation σ_d . (C) Difference $\Gamma_{BS,eP} - \Gamma_{BS,P}$ between the coincidence factors shown in (B). (D) Spike rate difference of the BS and eP models (left) and of the BS and P models (right) as a function of I_d^0 and σ_d . (E) Spike rate of the BS neuron model. Results presented in (B)-(E) are averages over 6 noise realizations. The default parameters values of the BS model are listed in Table C.1 in Appendix. Figure and caption adapted from (Aspart et al., 2016, CC BY 4.0)

dendritic end. We evaluate the response for various input mean I_d^0 and standard deviation σ_d values (Fig. 2.4B-E). For the sake of comparison, we again use the P model, i.e. without filter, whose parameters were optimized to reproduce the spike train of the BS model for each input realization (same fitting procedure as above).

For small spike rates, the eP model successfully reproduces the BS spike times ($\Gamma_{BS,eP} \geq 0.9$ for small I_d^0 and σ_d). Similarly as observed with the somatic input, the accuracy drops with increasing I_d^0 (see Section 2.3.1 for an explanation). Interestingly, the reproduction performance does not necessarily deteriorate as the spike rate increases. Indeed, the coincidence factor remains high, provided the noise intensity σ_d is sufficiently strong ($\Gamma_{BS,eP} \geq 0.8$ for $\sigma_d \geq 80$ pA, independently of I_d^0 in the considered range). The

eP model underestimates the spike rate of the BS model, though (Fig. 2.4D). Again, increasing the reset voltage value V_r' could potentially increase the spike rate reproduction, since the remaining dendritic polarization after each spike is stronger in case of distal input than in somatic input.

Importantly, the eP models outperforms the P model (with best fit parameters) for all considered distal inputs settings (Fig. 2.4B-D).

In summary, the dendritic cable act as a low-pass filter for distal dendritic inputs propagating through it. The presented eP model, i.e. the additional low-pass filter we derived, successfully reproduces the sub- and suprathreshold responses of the BS model to distal dendritic inputs. The computation speed-up of using the eP model for distal dendritic inputs remains the same as for somatic inputs.

2.3.3 Effect of an extracellular electric field on the neuronal dynamics

We now examine a neuron model subject to an extracellular electric field in addition to the synaptic inputs. To avoid ambiguity, we note the membrane voltages variation due to the field with the superscript E . Here, we restrict ourselves to the somatic doctrine. That is, we solely analyze the effects of the field on the subthreshold somatic membrane voltage and the resulting modulation of the spiking dynamics of the BS neuron. We further extend our extended point neuron model, eP, with an additional input current, whose expression is derived analytically in order to reproduce the field effects.

Field sensitivity We consider an electric field, $E(t)$, as induced during tACS. The field is oscillatory (more precisely sinusoidal), spatially uniform on the neuronal scale and of low amplitude (typically $\leq 2\text{V/m}$) (Bikson et al., 2012b):

$$E(t) = -\frac{\partial V_{\text{BS},e}}{\partial x}(t) = E_1 \sin(\varphi t)$$

where E_1 and φ are respectively the field amplitude and its angular temporal frequency. $V_{\text{BS},e}(x, t)$ is the extracellular potential.

The subthreshold somatic membrane voltage response of the BS model to this field, $V_{\text{BS}}^E(0, t)$, is ruled by the cable equation (Eqs. 2.1–2.3). It can be expressed in the temporal Fourier domain as (see Appendix A.2 for the full derivation):

$$\hat{V}_{\text{BS}}^E(0, \omega) = \frac{\hat{E}(\omega) g_i [\text{sech}(z(\omega)l) - 1]}{C_s i\omega + G_s + z(\omega) g_i \tanh(z(\omega)l)}, \quad (2.19)$$

where $z(\omega)$ is given by Eq. 2.13.

In the time domain, the BS somatic membrane dynamics is:

$$V_{\text{BS}}^E(0, t) = |A(\varphi)| \sin(\varphi t + \arg(A(\varphi))), \quad (2.20)$$

$$A(\varphi) = \frac{E_1 g_i [\text{sech}(z(\varphi)L) - 1]}{C_s i\varphi + G_s + z(\varphi) g_i \tanh(z(\varphi)l)}, \quad (2.21)$$

where $\arg(x)$ corresponds to the argument of the complex number x . Using this notation, we define the field sensitivity of the BS model at the soma as the ratio between

the amplitude of the somatic membrane response to the field and the amplitude of the field; in other words, the field sensitivity equals $|A(\varphi)|/E_1$.

Overall, the field sensitivity of the BS model decreases with increasing field frequency (Fig. 2.5, upper row). This means that the BS subthreshold response to field decreases when the field becomes faster.

The frequency-dependence of the field sensitivity varies quantitatively, but not qualitatively with the BS neuronal morphology. In particular, its dependence on the field frequency becomes stronger when the ratio between the sizes of the dendritic and somatic compartments increases. The cable length impacts the field sensitivity the most (see next Section 3.2.1 in next chapter for a more thorough analysis of this dependence). Importantly, the frequency-dependence and the amplitude of the BS model field sensitivity are similar to reported measurements on pyramidal cells in rat hippocampal slices (Deans et al., 2007).

The field frequency also affects the phase shift between the somatic subthreshold response and the field. The phase shift between the somatic membrane voltage and field oscillations also depends on the field frequency (Fig. 2.5, lower row). In the low frequencies, the membrane response and the field are anti-phased, the phase-shift then decreases with increasing frequency.

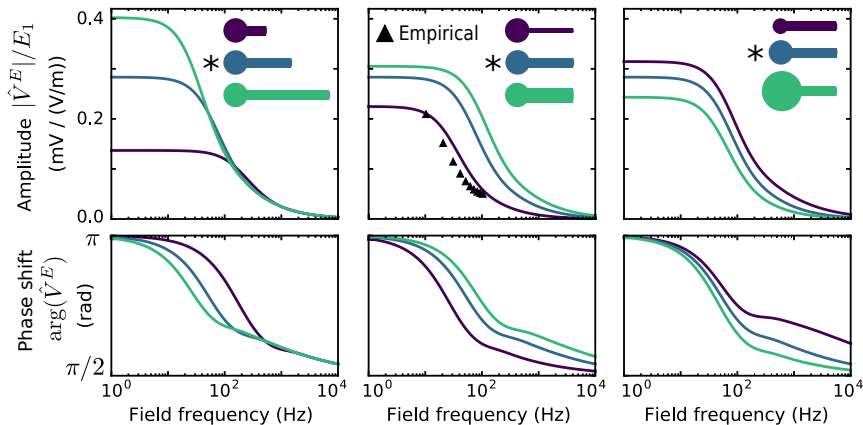


Figure 2.5: The field sensitivity of the BS model decreases with the field frequency

Neuron sensitivity to the field, i.e., the ratio between its somatic membrane voltage amplitude and the field amplitude, and phase shift between the oscillatory membrane voltage and the field. The neuronal morphology varied as indicated, in terms of dendritic cable length (350 μm , 700 μm , 1050 μm), diameter (0.6 μm , 1.2 μm , 1.8 μm) and soma diameter (5 μm , 10 μm , 15 μm). \blacktriangle indicate values obtained from electrophysiological recordings of rat hippocampal pyramidal cells (Deans et al., 2007). * indicates the default parameter values. For all other parameter values used see Table C.1 in Appendix. Figure and caption adapted from (Aspart et al., 2016, CC BY 4.0)

Equivalent input current Following from Eq. 2.11, the subthreshold membrane response of the eP model to an extracellular field, i.e. to the additional input current I_E equivalent to the field, is:

$$\hat{V}_{\text{eP}}^{I_d}(\omega) = \frac{\hat{I}_E(\omega)}{C_{\text{eP}}i\omega + G_{\text{eP}}}.$$

We choose the equivalent current, I_E , in order to guarantee an equal somatic membrane response in both models, i.e. $\hat{V}_{\text{eP}}(\omega) = \hat{V}_{\text{BS}}(0, \omega)$. This yields the analytical expression

of the current:

$$I_E(t) = |B(\varphi)| \sin(\varphi t + \arg(B(\varphi))), \quad (2.22)$$

$$B(\varphi) = \frac{E_1 g_i (C_{eP} \varphi + G_{eP}) [\operatorname{sech}(z(\varphi)l) - 1]}{C_s i \varphi + G_s + z(\varphi) g_i \tanh(z(\varphi)l)}, \quad (2.23)$$

Note that, although we consider only sinusoidal fields, this derivation is valid for spatially uniform fields with arbitrary temporal dynamics using the Fourier transform of the time-varying field (see for example the derivation done for simple straight passive cables in Appendix A.3).

The amplitude and phase (relative to the field) of the equivalent input current are displayed in Fig. 2.6. Interestingly, the amplitude of $I_E(t)$ increases with the field frequency. On the contrary, the field sensitivity of the BS model, and therefore of the eP model, decreases with the field frequency (Fig. 2.5). In practice, this means that the field sensitivity of the eP model decreases slower with increasing frequency than the eP subthreshold response to (unfiltered) input current does. In brief, the neuron model is more responsive to high frequency fields than to high frequency currents.

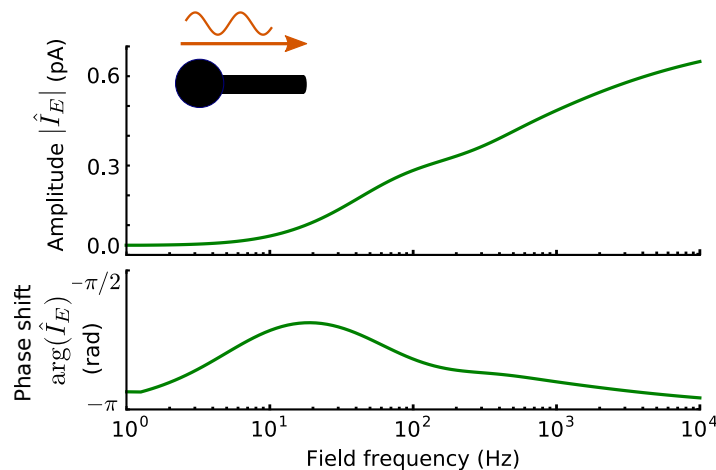


Figure 2.6: The eP model requires an equivalent input current whose amplitude increases with field frequency to account for the field effects

Input current I_E to reproduce the effect of a 1 V/m field in the eP model. In particular the equivalent current amplitude (top) and phase shift relative to the field (bottom) as a function of field frequency. For all parameter values used see Table C.1 in Appendix. Figure and caption adapted from (Aspart et al., 2016, CC BY 4.0)

Spike rate modulation We next investigate the frequency-dependent effects of electric fields on spiking activity in the BS and eP models. To this end, we simulate both neuron models with a noisy synaptic input either at the soma or at the distal dendrite and with an extracellular electric field. Note that, due to its low amplitude, the field alone does not elicit any spikes. On the contrary, we set the synaptic drive strong enough to induce stochastic spiking with rate r_0 . In this case, the subthreshold response of the BS model to combined synaptic input and electric field is:

$$\hat{V}_{BS}(0, \omega) = \hat{V}_{BS}^{I_s}(0, \omega) + \hat{V}_{BS}^{I_d}(0, \omega) + \hat{V}_{BS}^E(0, \omega),$$

where $\hat{V}_{\text{BS}}^{I_s}(0, \omega)$, $\hat{V}_{\text{BS}}^{I_d}(0, \omega)$ and $\hat{V}_{\text{BS}}^E(0, \omega)$ are defined in Eqs. 2.12, 2.17 and 2.19. The eP model response is:

$$\hat{V}_{\text{eP}}(\omega) = \frac{\hat{L}_s(\omega)\hat{I}_s(\omega) + \hat{L}_d(\omega)\hat{I}_d(\omega) + \hat{I}_E(\omega)}{C_{\text{eP}}i\omega + G_{\text{eP}}}.$$

The sinusoidal field leads to a modulation of the ongoing spiking rate. This modulation is sinusoidal and becomes apparent over many trials, i.e., over independent realizations of the synaptic input $I_s(t)$. Note that, the neuron spike rate averaged over many independent trials is equivalent to the spike rate of an uncoupled population of neurons, which individually receive independent stochastic inputs and are subject to the same oscillatory field.

To investigate this modulation of the population (or trial-averaged instantaneous) spike rate, we consider the same simulation setup as above. Each neuron model is subject to a stochastic synaptic input at the soma and to an oscillatory field $E(t) = E_0 \sin(\varphi t)$ ⁷. The sinusoidal spike rate modulation can be quantified as:

$$\text{spike rate}(t) = r_0 + r_1(\varphi) \sin(\varphi t + \psi(\varphi))$$

where r_0 is the baseline spike rate, $r_1(\varphi)$ the spike rate modulation amplitude and $\psi(\varphi)$ the phase difference between the field and the spike rate modulation. Importantly, both $r_1(\varphi)$ and $\psi(\varphi)$ depend on the field frequency. This definition of the spike rate modulation relates to the spike-field coherence measure used in the experimental literature.

In practice, we quantify the spike rate modulation at a given field frequency by building an histogram of the field phases at which the spikes are triggered⁸. We then fit this spike rate histogram with a sinusoid of the form $F(\phi) = r_0 + r_1 \sin(\phi + \psi)$, $\phi \in [0, 2\pi)$ being the phases of the spikes. We set r_0 to the histogram mean value and choose r_1 and ψ to minimize the square error. We use this computed value r_0 , r_1 and ψ to investigate the spike rate modulation due to the field.

In case of a synaptic input current located at the soma, the spike rate modulation of the BS model exhibits a clear resonance for field frequencies in the 15-50Hz range, i.e. in the beta and gamma frequency bands (Fig. 2.7). In other words, the spike rate oscillations are the largest for fields with frequency at the resonance. This is surprising since the resonance is absent in the subthreshold field sensitivity of the BS model (Fig. 2.5). This resonance is consistent across the considered spiking regimes, i.e. across the different somatic inputs parametrizations (in terms of I_s^0 and σ_s) (Fig. 2.7). Overall the resonance amplitude increases with the strength of the synaptic inputs and is the most prominent in case of the mean dominated input (large I_s^0 , small σ_s). When the baseline spike rate increases from a few spikes per second to about 60 Hz⁹, the resonance amplitude rapidly increases until it reaches a saturation point around $r_0 = 30$ Hz (Fig. 2.7, center plot). When the baseline spike rate increases, the resonance frequency shifts gradually from the beta to the gamma range.

The spike rate modulation and the field are anti-phased. Indeed, the phase shift ψ

⁷In the eP model the field is replaced by the equivalent input current $I_E(t)$ defined in Eq. 2.22.

⁸This spike rate histogram is computed using the spike phases from 944 trials of at least 26 s duration each. We disregard the first 2 s of each trials to avoid transients and consider only complete field cycles. We use 20 equally sized bins to build the histogram.

⁹To this end, we increase both the input mean and standard deviation simultaneously, starting from small values.

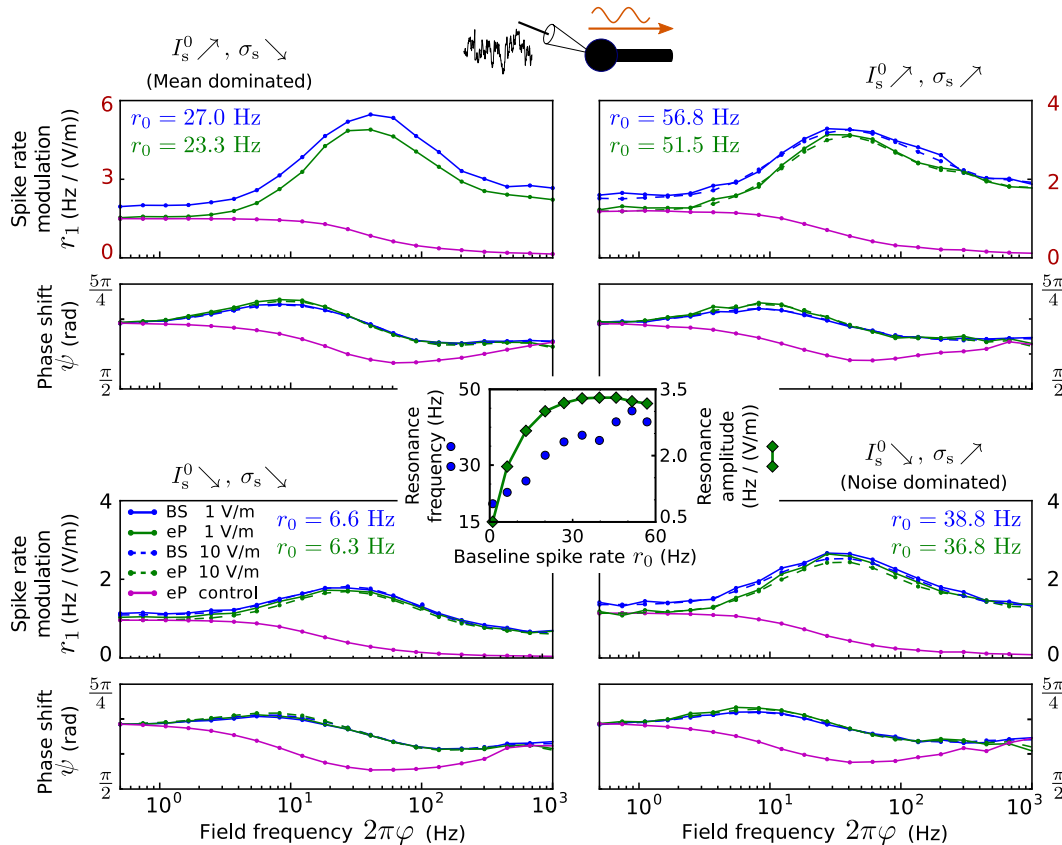


Figure 2.7: Spike rate modulation due to an electric field for somatic inputs

Top/bottom, left/right: Spike rate modulation of the BS (blue) and the eP (green) models due to an oscillating electric field as a function of its frequency, for different field amplitudes ($E_1 = 1$ V/m, solid lines; $E_1 = 10$ V/m, dashed lines) and somatic inputs: $I_s^0 = 7.69$ pA, $\sigma_s = 11.94$ pA (top left), $I_s^0 = 7.69$ pA, $\sigma_s = 33.34$ pA (top right), $I_s^0 = 4.68$ pA, $\sigma_s = 11.94$ pA (bottom left), and $I_s^0 = 4.68$ pA, $\sigma_s = 33.34$ pA (bottom right). Magenta lines show the spike rate modulation of the eP model for which I_E was given by $I_E(t) = I_1 \sin(\varphi t + \phi)$ with constant amplitude $I_1 = |B(0.5/(2\pi))|$, phase shift $\phi = \arg(B(0.5/(2\pi)))$, B from Eq. 2.23 and $E_1 = 10$ V/m. Note the different amplitude scales in the top panel. Results for larger field amplitude ($E_1 = 10$ V/m) are not displayed for the mean driven regime (top right), because spike rate modulation amplitudes exceeded the baseline rate in that case, which impedes the modulation quantification procedure. Center: Resonance frequency $\text{argmax}(r_1)$ and amplitude $\text{max}(r_1)$ of the spike rate modulation of the eP model as a function of baseline spike rate r_0 , which was changed by simultaneously increasing (I_s^0, σ_s) from (4.25 pA, 8.89 pA) to (8.12 pA, 36.40 pA). Figure and caption adapted from (Aspart et al., 2016, CC BY 4.0)

varies around π (Fig. 2.7), its exact value depending on the field frequency and the somatic input. This anti-phase relationship implies that the probability of spiking are the strongest at the troughs of the field oscillation. This anti-phase relationship is due to the field orientation we chose: in our convention, a positive DC field ($E(t) = E_0 > 0$) hyperpolarizes the somatic membrane voltage.

The spike rate modulation amplitude is proportional to the field amplitude. A field with an amplitude of 10 V/m modulates the spike rate 10 times more than a field of 1 V/m (see normalized spike rate modulation in Fig. 2.7). The phase shift between the field and the modulation is not affected by the field amplitude.

Importantly, the eP model successfully reproduces the spike rate dynamics, i.e. the spike rate modulation, of the BS model (Fig. 2.7). The reproduction performance is the best for low firing rate, as found above with the spike coincidence factor (Fig. 2.3).

We further examine the importance of the specific shape of the equivalent input current $I_E(t)$ in the reproduction accuracy. To this end, we consider a variant of the eP model, in which the derived equivalent input current from Eq. 2.22 is replaced with a sinusoidal input current whose amplitude and phase shift remain constant across the different field frequencies: $I_E(t) = I_1 \sin(\varphi t + \phi)$. The spike rate modulation due to this modified input current (Fig. 2.7, magenta line) lacks the typical resonance of the BS model. This highlights the importance of an equivalent input current whose amplitude increases with increasing field frequencies (as displayed in Fig. 2.6).

At last, we analyze the spike rate modulation due to the field when the background synaptic input is located at the distal dendrites (Fig. 2.8). Surprisingly, the modulation amplitudes increases monotonically with the field frequency over the whole range of considered frequencies (up to 1 kHz, see Discussion in Section 2.5 for an explanation). This increase is consistent in all considered input parametrizations (i.e. various I_d^0 and σ_d). As observed for somatic inputs, the modulation is the largest for mean dominated distal inputs (large I_d^0 , small σ_d), and the phase shift ψ also varies around π . The eP model again well reproduces the spike rate modulation of the BS model; this reproduction is not possible using an equivalent input current $I_E(t)$ with an amplitude independent on the field frequency.

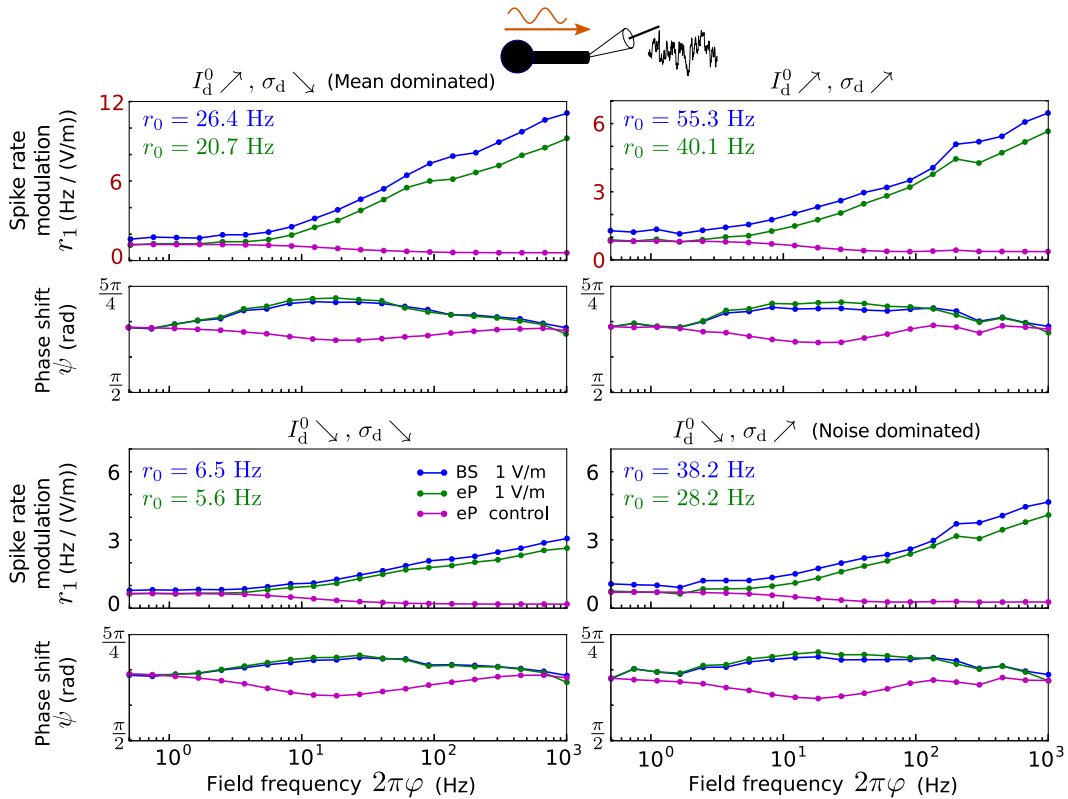


Figure 2.8: Spike rate modulation due to an electric field for distal dendritic inputs

Spike rate modulation of the BS (blue) and the eP (green) models due to an oscillating electric field as a function of its frequency, for different distal dendritic inputs: $I_d^0 = 12.44$ pA, $\sigma_d = 33.04$ pA (top left), $I_d^0 = 12.44$ pA, $\sigma_d = 111.2$ pA (top right), $I_d^0 = 7.03$ pA, $\sigma_d = 33.04$ pA (bottom left), and $I_d^0 = 7.03$ pA, $\sigma_d = 111.2$ pA (bottom right). Magenta lines show the spike rate modulation of the eP model for which I_E was given by $I_E(t) = I_1 \sin(\varphi t + \phi)$ with constant amplitude $I_1 = |B(0.5/(2\pi))|$ and phase shift $\phi = \arg(B(0.5/(2\pi)))$ with B from Eq. 2.23 and $E_1 = 10$ V/m. Note the different amplitude scales in the upper panel. Figure and caption adapted from (Aspart et al., 2016, CC BY 4.0)

In summary, we extended a point neuron model of the LIF type to reproduce the subthreshold membrane dynamics of the BS neuron model. In spite of being derived for the subthreshold regime, the extended point neuron model successfully reproduces the spiking dynamics of the BS neuron model in response to synaptic inputs and to an extracellular electric field. Furthermore, we found weak electric fields to modulate the spike rate response to stochastic synaptic input. Importantly, this spike rate modulation exhibits a resonance at a field frequency which depends on the location of the input current.

2.4 Extension for EIF neuron models

The analysis and model extension presented so far applies to neuron models of the LIF type. In other words, we considered only capacitive and leak currents through the neuronal membrane. We now consider more refined neuron models: neuron models of the exponential integrate-and-fire (EIF) type (Fourcaud-Trocmé et al., 2003). That is, the BS and eP models includes an exponential term which approximates the voltage-dependent sodium current, which is responsible for the spike initiation. We follow the same strategy as in the precedent section with LIF neurons to derive and evaluate the model extensions for neuron models of the EIF type.

EIF model derivation The EIF versions of the BS and eP models are described respectively by Eqs. 2.1–2.3 and Eq. 2.6. In order to reuse the same techniques as for the LIF model, we first linearize the exponential term around the baseline voltage value V_0 in Eqs. 2.2 and 2.6. From the linearized equations, we derive the model components of the eP model, namely $L_s(t)$, $L_d(t)$, α and $I_E(t)$.

Specifically, we analytically calculate the subthreshold somatic membrane voltage response of the linearized BS model, using the temporal Fourier transform. This yields the four response components:

$$\hat{V}_{\text{BS}}(0, \omega) = \hat{V}_{\text{BS}}^{I_s}(0, \omega) + \hat{V}_{\text{BS}}^{I_d}(0, \omega) + \hat{V}_{\text{BS}}^{\Delta_T}(0, \omega) + \hat{V}_{\text{BS}}^E(0, \omega) \quad (2.24)$$

where $V_{\text{BS}}^{I_s}$, $V_{\text{BS}}^{I_d}$ and V_{BS}^E are the somatic membrane response to synaptic inputs at the soma (I_s) and at the dendrites (I_d) and to the electric field E . Note the additional term $V_{\text{BS}}^{\Delta_T}$ which corresponds to the somatic membrane response to the (linearized) exponential term. These four components are explicitly expressed as (see Appendix A.2 for their full derivation):

$$\begin{aligned} \hat{V}_{\text{BS}}^{I_s}(0, \omega) &= \frac{\hat{I}_s(\omega)}{X(\omega)}, & \hat{V}_{\text{BS}}^{\Delta_T}(0, \omega) &= \frac{2\pi\delta(\omega)G_s e^{\frac{V_0 - V_T}{\Delta_T}} (\Delta_T - V_0)}{X(\omega)}, \\ \hat{V}_{\text{BS}}^{I_d}(0, \omega) &= \frac{\hat{I}_d(\omega) \operatorname{sech}(z(\omega)l)}{X(\omega)}, & \hat{V}_{\text{BS}}^E(0, \omega) &= \frac{\hat{E}(\omega)g_i [\operatorname{sech}(z(\omega)l) - 1]}{X(\omega)}, \end{aligned}$$

where $\operatorname{sech}(x) = \cosh(x)^{-1}$ denotes the hyperbolic secant function and:

$$X(\omega) = C_s i\omega + G_s \left(1 - e^{\frac{V_0 - V_T}{\Delta_T}} \right) + z(\omega) g_i \tanh(z(\omega)l).$$

Similarly, we linearize the exponential term of the full EIF eP model (Eq. 2.6) around the steady-state somatic voltage value; this yields:

$$C_{\text{eP}} \frac{\partial V_{\text{eP}}}{\partial t} + G_{\text{eP}} \left(1 - \alpha e^{\frac{V_0 - V_T}{\Delta_T}} \right) V_{\text{eP}} = G_{\text{eP}} \alpha e^{\frac{V_0 - V_T}{\Delta_T}} (\Delta_T - V_0) + [L_s * I_s](t) + [L_d * I_d](t) + I_E(t)$$

We then apply the temporal Fourier transform:

$$\begin{aligned} C_{\text{eP}} i\omega \hat{V}_{\text{eP}} + G_{\text{eP}} \left(1 - \alpha e^{\frac{V_0 - V_T}{\Delta_T}} \right) \hat{V}_{\text{eP}} = \\ 2\pi\delta(\omega) G_{\text{eP}} \alpha e^{\frac{V_0 - V_T}{\Delta_T}} (\Delta_T - V_0) + \hat{L}_s(\omega) \hat{I}_s(\omega) + \hat{L}_d(\omega) \hat{I}_d(\omega) + \hat{I}_E(\omega) \end{aligned}$$

This equation can be easily solved to obtain:

$$\hat{V}_{\text{eP}}(\omega) = \frac{\hat{L}_s(\omega) \hat{I}_s(\omega) + \hat{L}_d(\omega) \hat{I}_d(\omega) + 2\pi\delta(\omega) G_{\text{eP}} \alpha e^{\frac{V_0 - V_T}{\Delta_T}} (\Delta_T - V_0) + \hat{I}_E(\omega)}{C_{\text{eP}} i\omega + G_{\text{eP}} \left(1 - \alpha e^{\frac{V_0 - V_T}{\Delta_T}} \right)} \quad (2.25)$$

Finally, we obtain the explicit expressions for the components of the eP model (L_s , L_d , α and I_E) by requiring equal subthreshold responses of the eP and BS models: $\hat{V}_{\text{eP}}(\omega) = \hat{V}_{\text{BS}}(0, \omega)$. The resulting expressions of the eP model components are:

$$\hat{L}_s(\omega) = \frac{C_{\text{eP}} i\omega + G_{\text{eP}} \left(1 - \alpha e^{\frac{V_0 - V_T}{\Delta_T}} \right)}{C_s i\omega + G_s \left(1 - e^{\frac{V_0 - V_T}{\Delta_T}} \right) + z(\omega) g_i \tanh(z(\omega)l)}, \quad (2.26)$$

$$\hat{L}_d(\omega) = \frac{\left[C_{\text{eP}} i\omega + G_{\text{eP}} \left(1 - \alpha e^{\frac{V_0 - V_T}{\Delta_T}} \right) \right] \text{sech}(z(\omega)l)}{C_s i\omega + G_s \left(1 - e^{\frac{V_0 - V_T}{\Delta_T}} \right) + z(\omega) g_i \tanh(z(\omega)l)}, \quad (2.27)$$

$$\alpha = \frac{G_s}{G_s + \tanh(l/\lambda) g_i / \lambda}, \quad (2.28)$$

$$I_E(t) = |B(\varphi)| \sin(\varphi t + \arg(B(\varphi))), \quad (2.29)$$

$$B(\varphi) = \frac{E_1 g_i \left[C_{\text{eP}} i\varphi + G_{\text{eP}} \left(1 - \alpha e^{\frac{V_0 - V_T}{\Delta_T}} \right) \right] [\text{sech}(z(\varphi)l) - 1]}{C_s i\varphi + G_s \left(1 - e^{\frac{V_0 - V_T}{\Delta_T}} \right) + z(\varphi) g_i \tanh(z(\varphi)l)}, \quad (2.30)$$

where φ refers to the angular temporal frequency of the sinusoidal electric field and $z(\omega)$, expressed in Eq. 2.13, is the same as for the LIF case.

The scaling factor α ensures the reproduction of the somatic membrane response to the spike initiating current. In other words, α guarantees that the spike initiation current, described by the exponential term $V_{\text{BS}}^{\Delta_T}$, induces an equal steady state membrane potential in both BS and eP models.

It is noteworthy, that the two synaptic filters present the same qualitative dependence on the input frequency in the EIF and the LIF neurons (compare Eqs. 2.26 and 2.27 with Eqs. 2.14 and 2.18).

Reproduction performance of the extended EIF model We now compare the suprathreshold response of the eP and the BS model to synaptic inputs and to electric fields. We perform the same analysis as for the LIF case. In particular, we use the same simulation techniques as mentioned above.

We use the eP model components derived after linearizing the exponential term around the rest membrane potential: $V_0 = V_r$. Linearizing around a different value did not considerably improve the following results¹⁰. Note that, while the model components are computed after linearization, the exponential current in the BS, eP and P models are not linearized during the simulations.

To begin with, we assess how well the eP model reproduces the BS spiking activity in response to a synaptic input at the soma (Fig. 2.9). To this end, we compute the spike coincidence factor between the eP and BS model for a range of somatic input parameter values (I_s^0 and σ_s). This range is chosen to obtain a similar spike rates as for the LIF case in Fig. 2.3¹¹.

Despite the linearization approximation during the model derivation, the eP model

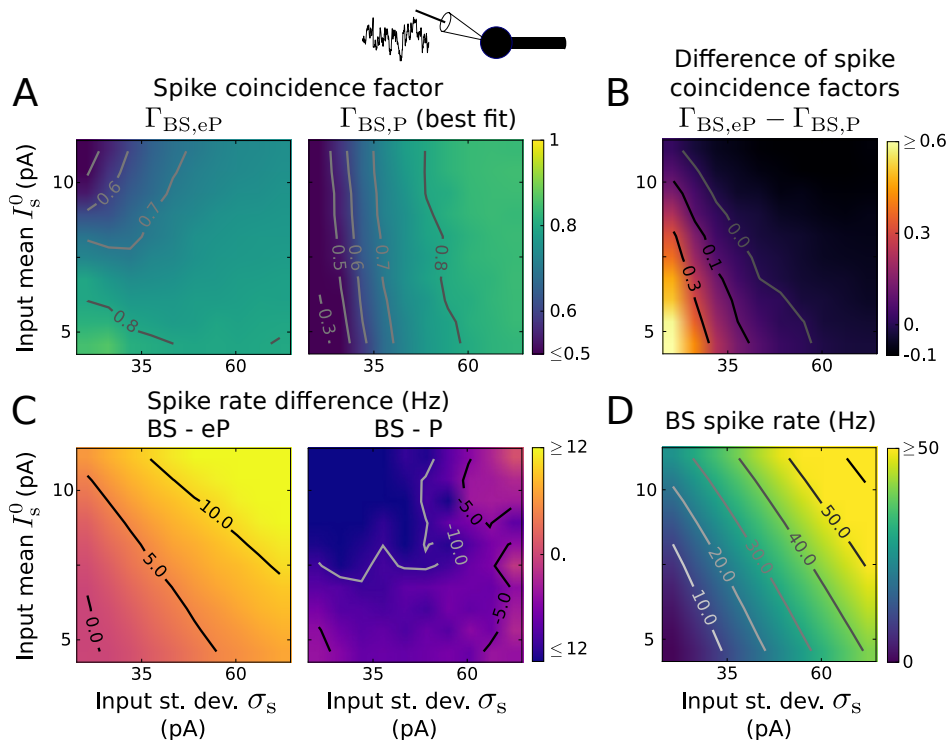


Figure 2.9: Reproduction of spiking activity for somatic inputs using EIF type models (A) Coincidence factor for the BS and eP model spike trains, $\Gamma_{BS,eP}$ (left), and for the BS and P model spike trains, $\Gamma_{BS,P}$ (right) as a function of input mean I_s^0 and standard deviation σ_s . The parameter values of the P model were optimized to maximize $\Gamma_{BS,P}$ for each input (i.e., (I_s^0, σ_s) -pair) independently. (B) Difference $\Gamma_{BS,eP} - \Gamma_{BS,P}$ between the coincidence factors shown in (A). (C) Spike rate difference of the BS and eP models (left) and of the BS and P models (right) as a function of I_s^0 and σ_s . (D) Spike rate of the BS neuron model. Results presented in (A)-(D) are averages over 6 noise realizations. The parameter values of the BS model are listed in Table C.1 in Appendix. Figure and caption adapted from (Aspart et al., 2016, CC BY 4.0)

¹⁰Several values were tested in the range $[V_r, V_s]$ (results not shown).

¹¹As for the LIF case, we choose the lower bound of I_s^0 to induce a somatic depolarization of 5mV in the absence of noise. We then adjust, through simulations, the range of σ_s and the higher bound of I_s^0 to obtain the same range of spike rate as for the LIF case.

fairly well reproduces the BS spike trains. Indeed, $\Gamma_{BS,eP} \geq 0.7$ for a wide range of input parameters. Similarly to the LIF case, $\Gamma_{BS,eP}$ is large for small spike rates (small I_s^0 and σ_s) and decreases when I_s^0 increases (towards mean dominated input), see Fig. 2.9A,D.

Overall, the eP model underestimates the firing rate of the BS model (Fig. 2.9C). Interestingly, this discrepancy is lower than the one observed for the LIF case.

As for the LIF case, the spike rate reproduction could probably be reduced through optimization of reset voltage, V_r' , of the point neuron model.

Here again, we compare the eP model to an usual EIF point neuron model, P. The parameters of the P model are optimized for each input realization in order to maximize the spike coincidence with the BS model. In spite of this best fit parametrization, the P model poorly reproduces the BS spike trains for small input noise intensity ($\Gamma \leq 0.6$ for $\sigma_s \leq 30$ pA, see Fig. 2.9A). In the small spike rates regime, the eP model clearly outperforms the simpler model ($\Gamma_{BS,eP} - \Gamma_{BS,P} \geq 0.3$ for small I_s^0 and σ_s); both models achieves a similar performance for high spiking activity (Fig. 2.9B).

Now, we test the reproduction of the BS spiking activity in case of distal dendritic inputs (Fig. 2.10). Again, we adjust the range of input parameters (I_d^0 and σ_d) to observe similar spike rates as for the LIF case. The reproduction performance of the eP model decreases compared to the previously observed somatic input case (Fig. 2.10A).

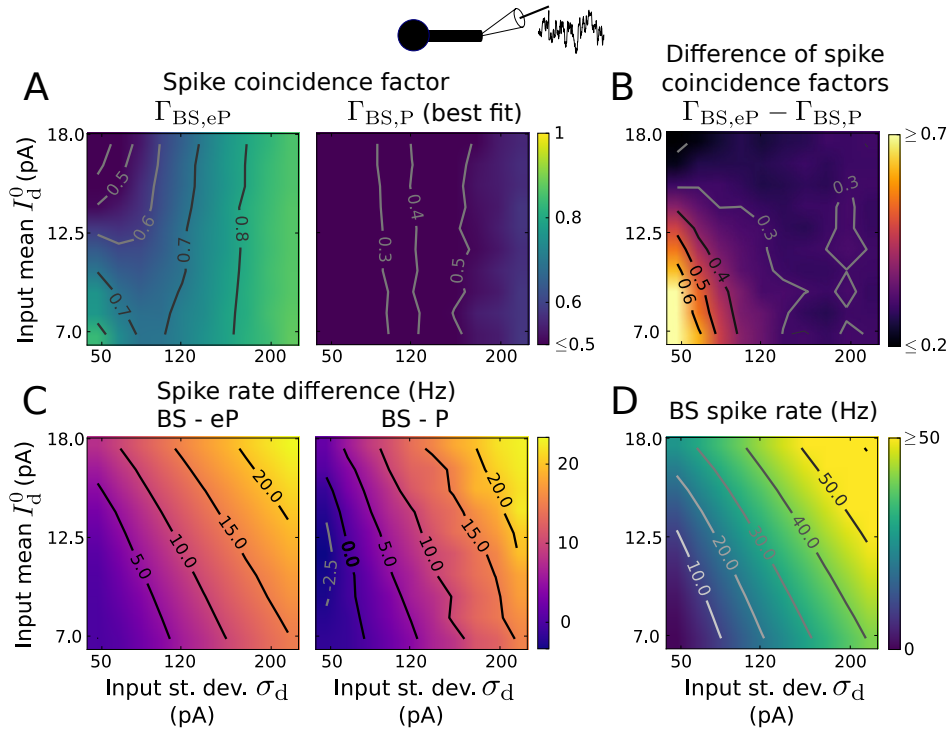


Figure 2.10: Reproduction of spiking activity for dendritic inputs using EIF type models (A) Coincidence factor for the BS and eP model spike trains, $\Gamma_{BS,eP}$ (left), and for the BS and P model spike trains, $\Gamma_{BS,P}$ (right) as a function of input mean I_d^0 and standard deviation σ_d . The parameter values of the P model were optimized to maximize $\Gamma_{BS,P}$ for each input (i.e., (I_d^0, σ_d) -pair) independently. (B) Difference $\Gamma_{BS,eP} - \Gamma_{BS,P}$ between the coincidence factors shown in (A). (C) Spike rate difference of the BS and eP models (left) and of the BS and P models (right) as a function of I_d^0 and σ_d . (D) Spike rate of the BS neuron model. Results presented in (A)-(D) are averages over 6 noise realizations. The parameter values of the BS model are listed in Table C.1 in Appendix. Figure and caption adapted from (Aspart et al., 2016, CC BY 4.0)

Nevertheless, it performs well for small spike rates or sufficiently noisy inputs. The eP model performances drop in the mean driven regime. Both the P and eP model tend to underestimate the BS model spike rate (Fig. 2.10C).

Finally, we analyze the spike rate modulation of the EIF neuron models due to an electric field. The simulation setup and the analysis are similar to the LIF case, with adjusted input parameters (mean input and noise intensity) though.

As in the LIF case, the spike rate modulation does not decrease monotonously with increasing field frequency (Fig. 2.11 and Fig. 2.12). If the stochastic background input is located at the soma (Fig. 2.11), the spike rate modulation exhibits a resonance with a peak in the beta/gamma frequency range, i.e. around 20-40Hz). This is similar to the LIF case. However, in case of distal dendritic inputs (Fig. 2.12), the spike rate modulation exhibits a resonance in the high gamma range (between 70Hz and 300Hz depending on the input parameters). The exact resonance frequency increases with the neuron spike rate, i.e. with increasing I_d^0 , and σ_d . This resonance frequency is much lower than in the LIF case, where the resonance peak was outside of the considered frequency range in case of distal dendritic synaptic input (see below, Section 2.5, for

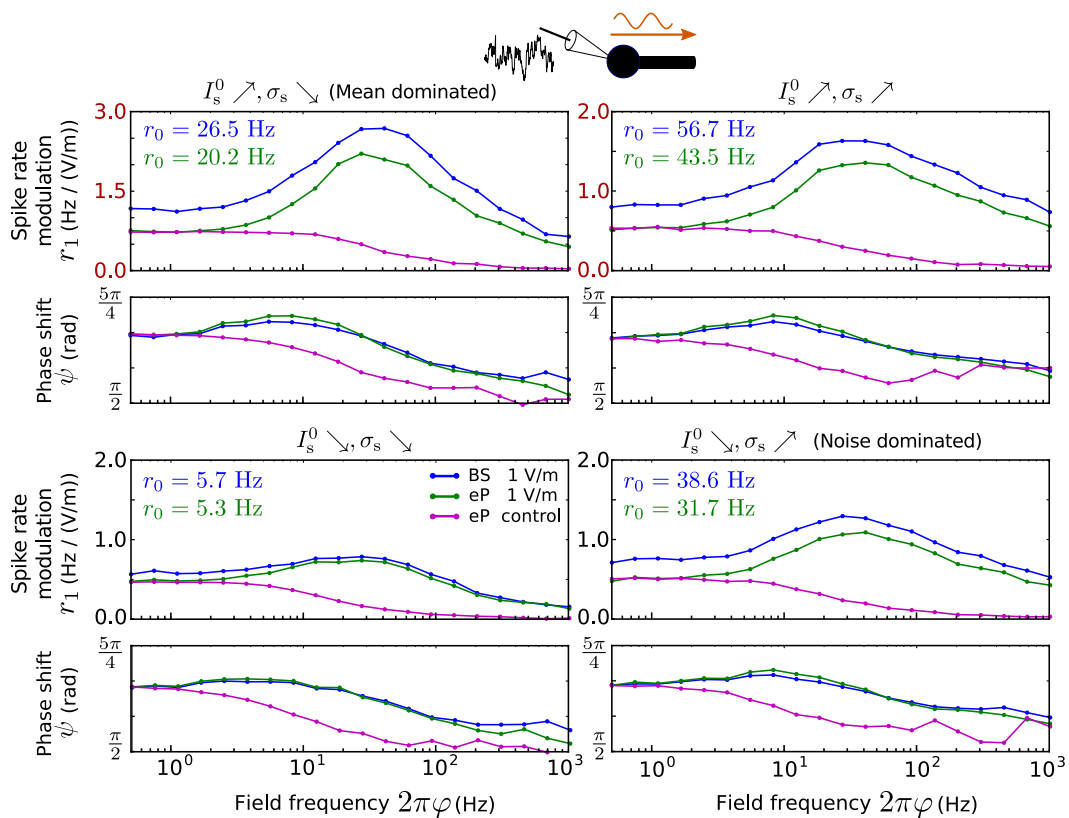


Figure 2.11: Spike rate modulation due to an electric field for somatic inputs using neuron models of the EIF type

Spike rate modulation of the BS (blue) and the eP (green) models due to an oscillating electric field ($E_1 = 1$ V/m) as a function of its frequency, for different somatic inputs: $I_s^0 = 10.61$ pA, $\sigma_s = 24.08$ pA (top left), $I_s^0 = 10.61$ pA, $\sigma_s = 68.21$ pA (top right), $I_s^0 = 5.05$ pA, $\sigma_s = 24.08$ pA (bottom left), and $I_s^0 = 5.05$ pA, $\sigma_s = 68.21$ pA (bottom right). Magenta lines show the spike rate modulation of the eP model for which I_E was given by $I_E(t) = I_1 \sin(\varphi t + \phi)$ with constant amplitude $I_1 = |B(0.5/(2\pi))|$ and phase shift $\phi = \arg(B(0.5/(2\pi)))$ with B from Eq. 21 and $E_1 = 10$ V/m. Note the different amplitude scales in the two top plots. The parameter values of the BS model are listed in Table C.1 in Appendix. Figure and caption adapted from (Aspart et al., 2016, CC BY 4.0)

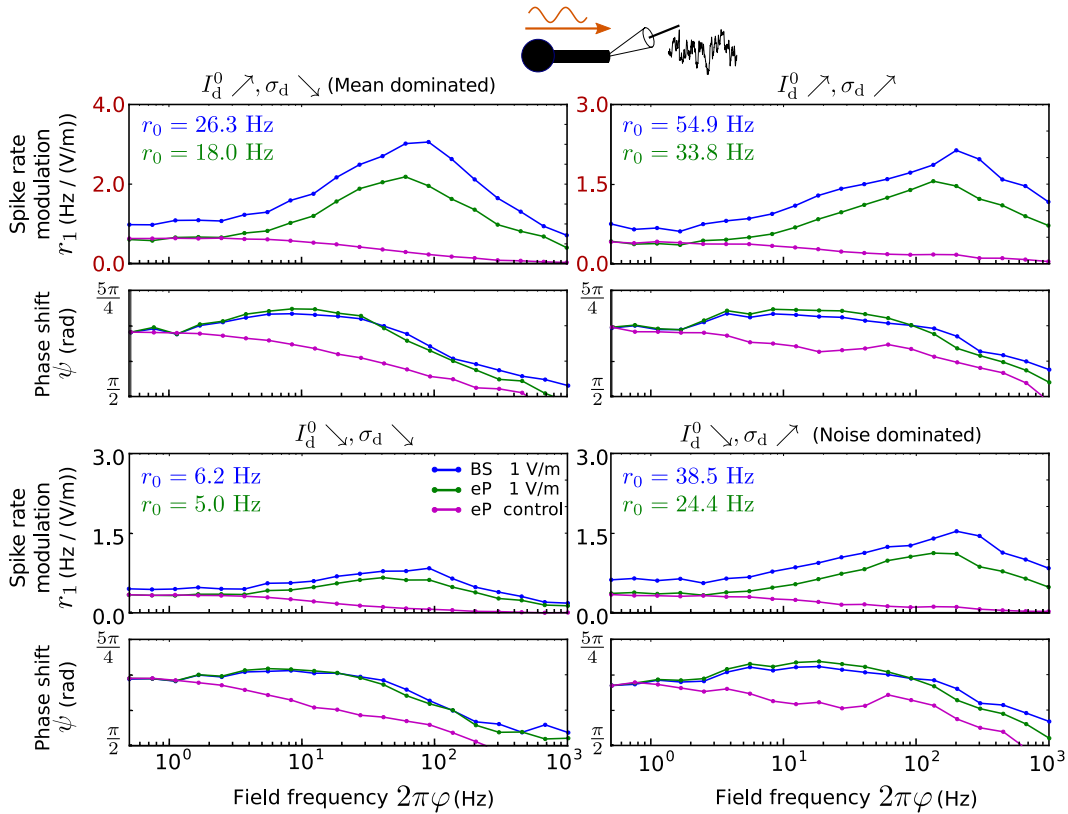


Figure 2.12: Spike rate modulation due to an electric field for distal dendritic inputs using neuron models of the EIF type

Spike rate modulation of the BS (blue) and the eP (green) models due to an oscillating electric field ($E_1 = 1$ V/m) as a function of its frequency, for different distal dendritic inputs: $I_d^0 = 16.73$ pA, $\sigma_d = 57.73$ pA (top left), $I_d^0 = 16.73$ pA, $\sigma_d = 203.41$ pA (top right), $I_d^0 = 7.56$ pA, $\sigma_d = 57.73$ pA (bottom left), and $I_d^0 = 7.56$ pA, $\sigma_d = 203.41$ pA (bottom right). Magenta lines show the spike rate modulation of the eP model for which I_E was given by $I_E(t) = I_1 \sin(\varphi t + \phi)$ with constant amplitude $I_1 = |B(0.5/(2\pi))|$ and phase shift $\phi = \arg(B(0.5/(2\pi)))$ with B from Eq. 21 and $E_1 = 10$ V/m. Note the different amplitude scales in the two top plots. The parameter values of the BS model are listed in Table C.1 in Appendix. Figure and caption adapted from (Aspart et al., 2016, CC BY 4.0)

an explanation).

For both input locations, the resonance amplitude is the strongest in the mean dominated regime (i.e., large I_x^0 , small σ_x , $x \in \{s, d\}$). In general, the rate modulation is stronger for large spike rates than in the low spike rate regime (i.e., small I_x^0 and small σ_x , $x \in \{s, d\}$).

For all considered inputs, e.g. locations and intensity, the eP model successfully reproduces the spike rate modulation observed in the BS model. The eP model tends to underestimate the spike rate modulation amplitude, though. In case of distal dendritic input, the eP model also underestimates the resonance frequency.

In summary, we derived an extended point neuron model for EIF neurons. The derived additional model components, i.e. the two input filters and the equivalent input current, are similar to the ones for LIF neurons. In spite of the linear approximation during the components derivation, the eP model well reproduces the sub- and suprathreshold activity of the BS model. In particular, the eP model outperforms the P model, i.e. usual EIF point neuron models. Furthermore, we found that the pres-

ence of an exponential spike mechanism lowers the resonance frequency of the spike rate modulation due to electric fields.

2.5 Discussion

In this chapter, we focused on the effects of tCS-induced electric fields at the soma. We looked for an efficient way to embed these effects in large simulations of neuronal population. To this end, we introduced an extension for IF point neuron models which accounted for the presence of a virtual dendritic cable. The model extension aimed at accurately reflecting (i) the synaptic inputs filtering depending on the inputs location and (ii) the effects of weak AC extracellular fields on neural activity, as observed in a canonical spatially extended neuron model: the ball-and-stick model.

The point neuron model extension consisted of additional model components, which we analytically derived to reproduce the somatic subthreshold membrane response of BS neuron model. These components included (i) two linear filters applied to synaptic inputs, one for each input location (soma or distal dendrite) and (ii) an additional input current accounting for the somatic polarization due to the field.

We successively extended point neuron models of the LIF and EIF type. In addition to the above mentioned components, the EIF point neuron model further required a scaling parameter to better match the BS membrane dynamics during spike initiation. We further demonstrated, through exhaustive evaluations with fluctuating inputs, that the extended point neuron model reproduced the spiking activity of the BS model accurately. On the contrary, standard LIF and EIF models, i.e. without the extension, were not able to reproduce the spiking activity of the BS model adequately.

In the following, we further summarize our results and relate them to existing literature.

Synaptic input filtering due to the dendrite

We showed that, due to the presence of the dendrite, synaptic signals were integrated differently at the soma, depending on the input location. The low-pass filtering of distal dendritic inputs (cf. Fig. 2.2A), which travel through the dendritic cable, has been known for some time (Koch, 2004). On the contrary, we found synaptic inputs located at the soma to be high-pass filtered by the presence of the dendritic cable (cf. Fig. 2.4B). Combining *in vitro* measurements and theoretical analysis, Ostojic et al. (2015) reported a similar change in somatic impedance due to the presence of a dendritic tree (Fig. 4 in Ostojic et al., 2015); this change was similar to the one we observed here (Fig. 2.2A). As a result, the presence of a dendrite could amplify the neuronal spiking response to high-frequency somatic inputs (Ostojic et al., 2015). Note that, this response may be further enhanced by the dendritic effect on the sharpness of spikes at the axon initial segment (Eyal et al., 2014).

Our aim was to take into account complex neuron morphologies in models whose numerical simulations are computationally efficient. To this end, two different strategies emerge from previous literature. The first option is to reduce the number of compartments while preserving important properties of the dendritic tree (Pinsky and Rinzel, 1994). The second alternative is to extend point neuron models with temporal kernels. These temporal kernels are calibrated to reproduce the somatic membrane dynamics of complex cells models in response to synaptic inputs (Dayan and Abbott, 2005;

Jolivet et al., 2004). In this chapter, we adopted the second approach, with the advantage that we analytically derived the temporal kernels, i.e. the filters, from the underlying morphological BS model. Note that, a similar extension for point neuron models has been developed to reproduce the dendritic input integration of cells with reconstructed morphologies (Wybo et al., 2013). Wybo et al. derived the temporal kernels using the Green’s function formalism. Nevertheless, the computational complexity of their kernel derivation only allows, in practice, for a limited number of synaptic input locations.

Thanks to the lower dimensionality of the BS model, we derived input filters for point neuron models only using the Fourier transform, in contrast to the more complex Green’s function. This results in filters which were easier to evaluate and to implement.

Despite being derived in the subthreshold regime, our extended model could, overall, accurately reproduce the spike trains of the BS model. Our model performed particularly well in case of weak (but still suprathreshold) distal and somatic inputs. As we mentioned in the results section, the performance of the extended model may be further improved through optimization of the reset voltage. This reset voltage could be adjusted to better reflect the membrane depolarization which remains after each spike in the dendritic cable of the BS model. Importantly, the extended model outperformed simpler point neuron models in terms of spike train reproduction.

In this chapter, we solely considered passive dendrites. Therefore, we ignored active membrane properties along the dendrite, which have been shown to cause nonlinear synaptic input integration (Migliore and Shepherd, 2002; Zhou et al., 2013; Zhang et al., 2013). It should be possible to incorporate such currents in our model extension using the “quasi-active” framework (see (Koch, 2004) and next chapter). In brief, this would involve linearizing the nonlinear components, e.g. the active ion channels, before solving the linearized cable equation, similarly as we did for the exponential terms in the boundary condition (EIF case).

Effects of weak electric fields on neuronal activity

Besides the point neuron model extension, the main objective of this chapter was to investigate the effects of weak electric fields on the activity of the BS neuron. This one-dimensional spatial model is a canonical representation for neurons with elongated (apical) dendrites. Here, we followed the somatic doctrine (Bikson et al., 2012b) and we focused exclusively on the effects of the field which result from the somatic membrane polarization.

We analytically calculated the field sensitivity at the soma, i.e. the somatic membrane polarization due to the field. Despite the simplicity of the BS model, its field sensitivity at the soma agreed with electrophysiological observations. First, the magnitude of the somatic membrane polarization scaled linearly with the field amplitude (Bikson et al., 2004). Furthermore, the field sensitivity was of the same order of magnitude as that measured in rats CA3 pyramidal cells (Deans et al., 2007): circa $0.3 \text{ mV} \cdot (\text{V/m})^{-1}$ for low frequency fields (see Fig. 2.5). The field sensitivity also decreased with increasing field frequency in a morphology-dependent manner (Radman et al., 2009).

Note that, this decrease is specific to the spatially uniform field we focused on. In case of non-uniform electric fields (such as generated by point source extracellular stimulation),

the field sensitivity can remain roughly constant for frequencies up to at least 100 Hz (Anastassiou et al., 2011). Nevertheless, we also observed this constant behavior with spatially uniform field when using rather short dendritic cables (cf. Fig. 2.5).

Whereas field sensitivity due to DC current has been extensively studied (Cartee and Plonsey, 1992; Plonsey and Altman, 1988; Tranchina and Nicholson, 1986), the polarization due to time-varying fields has received less attention. In previous studies, the field sensitivity has been analytically derived for a finite dendritic cable with a shunt end subject to uniform AC fields (Monai et al., 2010) and for a simple cable subject to spatially non-uniform DC fields (Anastassiou et al., 2010). However, previous studies did not consider a somatic compartment. Using the BS model, we showed that the somatic field sensitivity was modulated by the relative size of the soma compared to the dendritic cable. In the next chapter, we further analyze the impact of the morphology, e.g. electrotonic length or branching, on the field sensitivity at different locations.

Besides the subthreshold field sensitivity, we considered the ensuing spike rate modulation due to the electric field¹². Contrarily to the subthreshold field sensitivity, the spike rate modulation amplitude did not decrease monotonically with the field frequency; the exact relationship between the modulation and the field frequency depended on the synaptic input location and on the model type (LIF or EIF).

For a BS neuron subject to a somatic input, the spike rate modulation exhibited a resonance for fields in the 15-50Hz, i.e. in the beta and gamma frequency bands (cf Figs. 2.7 and 2.11). In comparison, the spike rate modulation amplitudes were the strongest at much higher field frequencies when the neuron was driven by distal dendritic inputs (cf. Figs. 2.8 and 2.12). This shift of the resonance towards higher frequencies can be explained by the low-pass filtering of distal dendritic inputs. This results in an equivalent fluctuating synaptic input at the soma with an increased autocorrelation time. This larger autocorrelation has been shown, analytically, to increase the response of single-compartment neuron models to high frequency inputs (Brunel et al., 2001).

Furthermore, the spike rate resonance frequencies in the EIF neurons were lower than for LIF neurons, this shift being the most prominent in case of distal dendritic input. This resonance frequency may be attributed to the presence of the exponential term, simulating the spike initiating sodium current. Indeed, this spike initiation current decreases the rate response to high frequency inputs (see (Fourcaud-Trocmé et al., 2003) and the analytical results in (Ostojic et al., 2015)).

For all considered model types and input locations, the amplitude of the modulation varied with the input strength (i.e. input mean and noise intensity), but the resonance frequency was little affected by the input parameters.

A similar spike rate resonance has been observed in Purkinje neurons (Ostojic et al., 2015) in response to synaptic input. Purkinje cells, due to their large dendritic trees, exhibited a spike rate resonance at rather high frequencies when subject to somatic input modulations and a noisy dendritic input (Ostojic et al., 2015, Fig. 5A). Nevertheless, a spatially uniform AC field corresponded to anti-phased oscillatory input currents at the soma and the distal dendrite, respectively (cf. Eqs. 2.2 and 2.3). Consequently, the effects of the field can not be directly inferred from those of an input current modulation at the soma alone (see also Discussion in next chapter).

More generally, our observation of a spike rate modulation due to weak AC fields is

¹²The spike rate modulation is a similar measure to the spike-field coherence.

in accordance with existing literature. Indeed, Radman et al. (2007) measured *in vitro* an increase in the spiking coherence of rats CA1 pyramidal cells in the presence of weak, 30 Hz, AC fields; this increase was proportional to the subthreshold field sensitivity of the cells. Nevertheless, while several experimental studies investigated the modulation of spiking activity due to AC fields, they only considered a small number of field frequencies (see Reato et al., 2013, for a review, in particular their Fig. 1E). In light of these studies, the spike rate resonance we reported here can not be confirmed; the resonance may be considered as a prediction. Nonetheless, Fröhlich and McCormick (2010) observed a stronger entrainment of multi-unit activity (MUA) due to extracellular electric fields with high-frequency components compared to fields with low-frequency components (see Fig. S6 in Fröhlich and McCormick, 2010)¹³. In summary, our results on spike rate modulation due to AC fields agree with current knowledge. These results are informative for future experimental studies and may be of interest for the design of tACS protocols.

We also extended point neuron models to include the effects of electric fields at the soma. This extension took the form of an additional input current derived analytically to reproduce the subthreshold response of the BS model. The amplitude and phase (relative to the field) of the equivalent input current depended on the parameters of the BS neuron and on the electric field.

Previous studies used similar model extensions, i.e. equivalent input currents, for simulating the effects of the field on neural population. The amplitude of these phenomenological input currents were either constant across frequencies (Fröhlich and McCormick, 2010; Ali et al., 2013) or fitted to electrophysiological data (Reato et al., 2010). Note that, in the latter study, the input current amplitude decreased monotonically with the field frequency. This contrasts with our equivalent input current whose magnitude increases with frequencies up to 10 kHz. Both studies, i.e. (Reato et al., 2010) and the one here, present similar subthreshold sensitivity. The discrepancy between the input currents of both studies may come from the impedances of their respective point neuron models, which influence the equivalent input current. In (Reato et al., 2010) the point neuron model parameters (and hence the impedance) were not fitted to real cells. It is therefore unlikely that the model impedance corresponded to the impedance of pyramidal cells from which the field sensitivity was recorded (Deans et al., 2007). Furthermore, our extended point neuron model successfully reproduced the spike rate modulation, e.g. the resonance, of the BS model. This accurate reproduction supports the frequency-dependent profile of the equivalent input current we presented here. Moreover, our equivalent input current agrees with the results of Cartee and Plonsey (1992), who reported a faster rate of rise of the membrane potential in response to a step extracellular field than in response to a step input current.

The derived IF model extension enables efficient analyses of the BS spike rate response to various the input currents and electric fields. A thorough analysis of the BS dynamics in case of coupled neuronal population is, however, out-of-the scope of this thesis. In fact, coauthors of the article corresponding to this chapter developed a further efficient reduction of the BS model (Ladenbauer and Obermayer, 2018). In brief, they considered a two-compartments model with input impedance fitted to the BS model and with the input current equivalent to the field we presented here. They then used moment closure to derive a mean field model of populations of this two-

¹³Fröhlich and McCormick (2010) measured the entrainment *in vitro* in ferrets V1

compartments model.

Additionally, the here-presented input current equivalent to the field is currently used in large-scale simulations of the effects of tCS on the brain dynamics (Cakan et al., 2017).

We presented an extension for point neuron models of the LIF and EIF types. More refined point neuron models include variables with slow dynamics (Brette and Gerstner, 2005) to account for spike rate adaptation and associated characteristic neuronal response properties (Ladenbauer et al., 2012, 2014). The presented extension approach could be adapted to such refined models by using a separation of timescales before performing the model extension.

In summary, using a canonical spatial neuron, we showed that weak extracellular fields polarized the somatic membrane. This somatic polarization then modulated the spike rate. Importantly, this spike rate modulation displayed a resonance which was not present in the subthreshold field sensitivity. Additionally, we derived a point neuron model extension to reproduce the somatic dynamics of the canonical neuron. While remaining computationally efficient, our extended model accounted for the effects of morphology on synaptic inputs and for the effects of weak extracellular fields. This model is well suited to be used in large scale simulations to investigate the effects of weak extracellular fields on neuronal population activity.

Chapter 3

The dendritic doctrine: Fields effects on cortical pyramidal cells

3.1 Overview

In the precedent chapter, we extended point neuron models to account for the sub-threshold membrane polarization due to extracellular fields. We also highlighted a modulation of the neuron spike rate through the polarization due to the field (see Fig. 2.7). We focused solely on the somatic doctrine and ignored the polarization of the dendritic tree due to the field. Yet, terminal, e.g. dendritic, polarization was recently found to modulate synaptic efficacy (Kronberg et al., 2017; Rahman et al., 2017).

The field sensitivity at the soma has been investigated in several experimental and theoretical works. For example, the somatic field sensitivity is known to be stronger for field orientations parallel to the somato-dendritic axis, to depend on cell morphology (Radman et al., 2009) and to decrease with the field frequency (Deans et al., 2007). On the contrary, little is known about the dendritic sensitivity to oscillating (AC) fields. Yet, the dendritic tree receives virtually all afferent synaptic inputs. The dendritic tree is also endowed with voltage-dependent currents (Major et al., 2013), which might be modulated by electric fields. As a result, understanding the dendritic tree field sensitivity could be of major importance when designing tCS protocols.

In the present chapter, we investigate the polarization of cortical pyramidal cells dendritic tree in response to an AC extracellular field. More specifically, we consider the frequency-dependent field sensitivity of cortical pyramidal cell using a biophysical model. To begin with, we compute the subthreshold field sensitivity of the passive model, i.e. with reconstructed morphology but without active membrane properties. We then explain the main properties of the field sensitivity observed in the passive model using simplified passive cable models. We further consider the field sensitivity of the pyramidal cell model with active conductances. Interestingly, we find a strong frequency resonance in the field sensitivity of the apical dendrites; this resonance is absent in the basal dendrites. We relate this resonance to both the cell passive properties and the presence of specific ion channels, in particular the I_h channel. Using a simplified model of active conductances, we generalize the relation between the active properties of a cell and its field sensitivity. Finally, we illustrate how weak electric fields can modulate the cell spiking activity both at the soma and at the dendritic tree.

Besides Section 3.4¹, the results presented in this chapter have been previously published (Aspart et al., 2018)² ³.

3.2 Impact of the morphology on the field sensitivity

To begin with, we investigate how the morphology of a neuron impacts its field sensitivity, i.e. its frequency-dependent polarization in response to an extracellular electric field. Specifically, we first consider the field sensitivity of a passive pyramidal neuron model with reconstructed morphology. Then, we explain the main characteristics of the reconstructed cell field sensitivity using simpler passive cable models.

Field sensitivity of a passive pyramidal neuron

We first consider the subthreshold response of a passive pyramidal cell model subject to an extracellular electric field. Specifically, we use the layer 5b pyramidal neuron model published by Hay et al. (2011) without active membrane properties. Unless stated otherwise, we use the reconstructed morphology *cell #1* from (Hay et al., 2011). We simulate the model with NEURON(Carnevale and Hines, 2006) and set the extracellular field, i.e. the gradient of extracellular potential, using the *extracellular* mechanism. As in the previous chapter, we focus on fields induced by transcranial current stimulation. These fields are of low amplitude (1 V/m) and spatially uniform, i.e. their spatial derivative is null (Bikson et al., 2012b). Furthermore, the fields are either constant in time, e.g. Direct Current (DC) fields, $E(x, t) = E_0$, or sinusoidal, e.g. Alternating Current (AC), $E(x, t) = E_0 \sin(2\pi f_t t)$ where f_t is the field frequency. We exclusively consider fields oriented parallel to the cell somato-dendritic axis (Fig. 3.1A), i.e. parallel to the vector formed by the soma and center of mass of the cell. This field orientation has been shown to result in the strongest somatic membrane polarization (Radman et al., 2009).

In presence of a DC field parallel to this axis, the apical dendrites get oppositely polarized compared to the soma and basal dendrites (Fig. 3.1BC). This is in accordance with reported *in vitro* measurements (Bikson et al., 2004). In this passive case, the apical end presents the strongest polarization amplitude. At the field onset, the basal and somatic regions display a slight overshoot. The passive model being linear, the polarization is reversed when the field has opposite sign.

We now consider AC fields. At each location, the resulting membrane polarization is sinusoidal (Fig. 3.1D), but the phases vary. For example the polarization at the apical end is anti-phased with the somatic polarization. Due to the linearity of the model, the polarization amplitude scales linearly with the field amplitude. Similarly

¹ The conceptualization, analysis and visualization of Section 3.4 were performed by F. Aspart. Joram Keijsers, under supervision of F. Aspart, implemented the code for evaluating the 3 neuron models (see first paragraph of that section).

² The authors contribution to the original article are (FA: Florian Aspart, MR: Michiel WH Remme, KO: Klaus Obermayer): Conceptualization: FA. Funding acquisition: KO. Resources: KO. Investigation: FA. Methodology: FA, MR. Formal analysis: FA, Software: FA. Supervision: MR, KO. Visualization: FA, MR. Writing – original draft: FA, MR. Writing – review & editing: FA, MR, KO.

³The article is published under the Creative Commons Attribution License (CC BY 4.0).

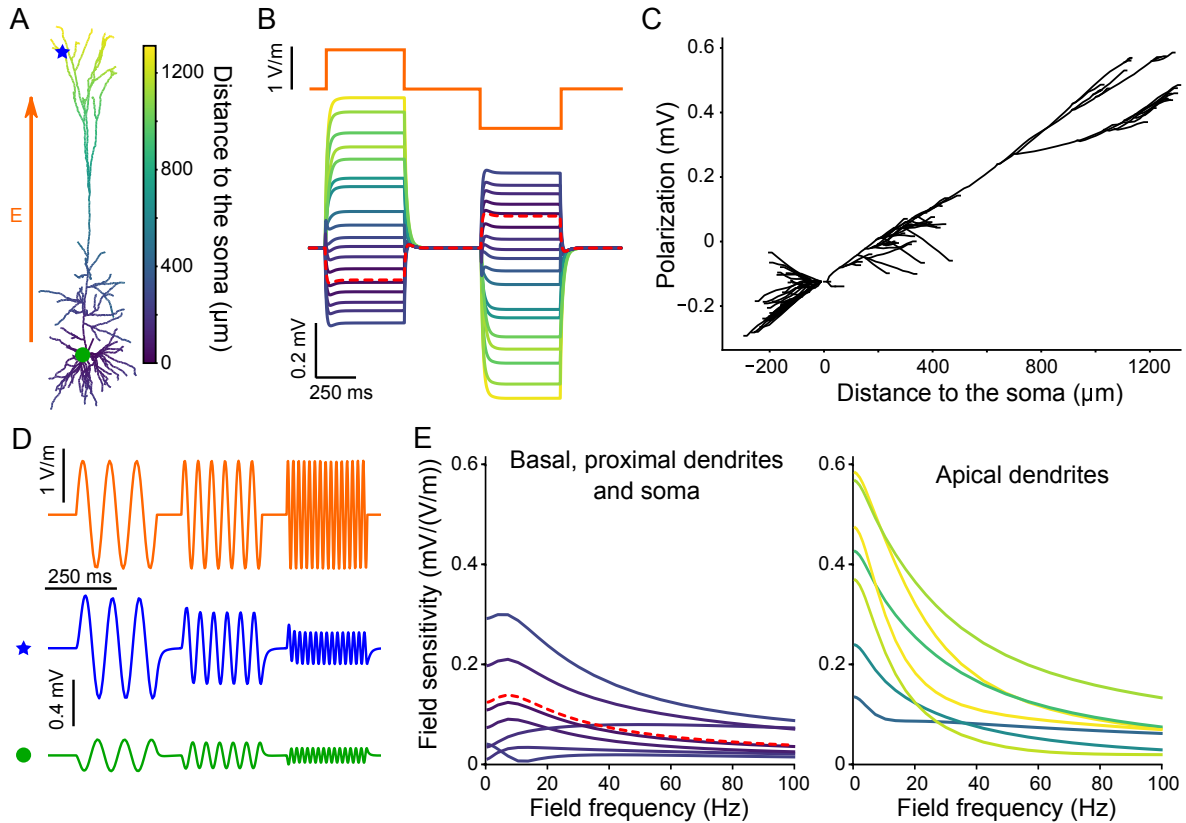


Figure 3.1: In a passive pyramidal cell model subject to an electric field, soma and basal dendrites get oppositely polarized than apical dendrites. This later are the most responsive to low frequency stimulations.

(A) Considered neuron morphology with color coding the distance of each segment to the soma. (B) (Bottom) Membrane polarization of the passive cell due to positive and negative steps of DC electric field (orange, top). (C) Polarization due to a positive 1 V/m field plotted as the function of the distance from the soma. For clarity basal dendrites are plotted with negative distance. (D) Example polarization at the apical dendrite (blue star, bottom) and soma (green circle, middle) due to an an oscillating field of diverse frequencies (orange, top). (E) Frequency-dependent sensitivity to AC fields of different cell segments, namely basal, proximal dendrites and soma (left panel) and distal apical dendrites (right). Colors of the polarization (B) and field sensitivity (E) correspond to the distance from the soma as depicted in A. The red dashed lines correspond to the soma. Figure and caption adapted from (Aspart et al., 2018, CC BY 4.0)

to the previous chapter, we define the field sensitivity as the ratio between membrane polarization and field amplitude (Deans et al., 2007). In practice, we compute the field sensitivity of the pyramidal cell model through simulation⁴.

The field sensitivity mostly decreases monotonously with the field frequency. While, the apical dendrites present the strongest field sensitivity to low frequency fields, their sensitivity decreases faster with increasing frequency. The field sensitivity at the soma and basal dendrites display a slight resonance around 5-10Hz. This resonance is due to the dendritic branches attached close to the soma (see below for further details). Interestingly, some proximal and basal dendrites exhibit a field sensitivity with a strong frequency resonance in the 20Hz to 50Hz range (Fig. 3.2). These locations correspond

⁴After waiting 700 ms to ensure that the cell is in its resting state, we apply a 1V/m field for 2 cycles or at least 400ms and use the last peak of polarization to compute the sensitivity. Using longer simulation does not affect the measured field sensitivity. Note that, contrarily to the original Hay et al. model, we initialize all variables in the model (see Section 3.4).

to proximal and basal branches whose tips, when projected on the field axis, are closer to the apical dendrites than their branching point. However, the maximum field sensitivity at this resonance is low compared to the maximum field sensitivity measured in the apical dendrites.

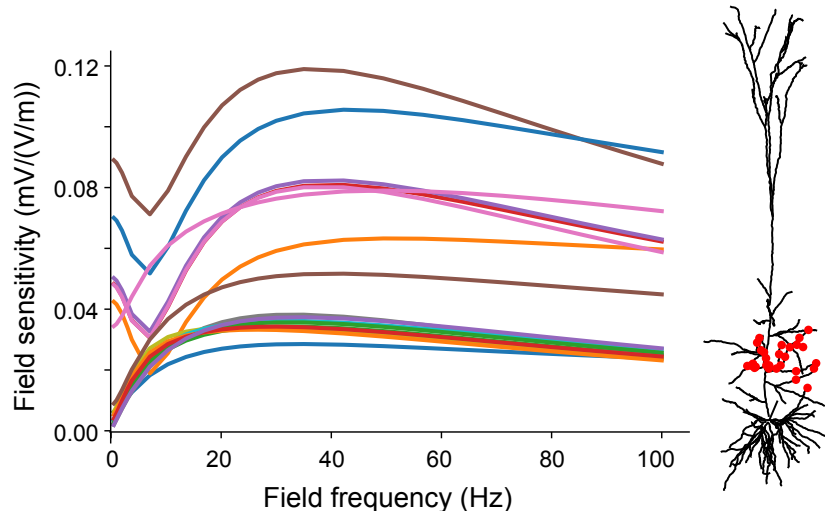


Figure 3.2: A passive pyramidal neuron exhibits a frequency resonance in its field sensitivity at the proximal dendrites

(Left) Frequency-dependent sensitivity of the passive cell, i.e. without any active ion channels, due to an AC field parallel to the somato-dendritic axis. (right) Locations of measurement of the sensitivities displayed in (left). Figure and caption adapted from (Aspart et al., 2018, CC BY 4.0)

In sum, the considered passive pyramidal cell model is more sensitive to low frequency fields at the apical dendrites than at the soma and basal dendrites. The field sensitivity mostly decreases with frequency. However, the field sensitivity at some proximal dendrites presents a strong frequency resonance. In the rest of this section, we will use simpler models, that is passive cable models with or without branches, to investigate (i) the origin of the disparity in the sensitivity to low frequency fields at the apical dendrites and at the soma/basal dendrites and (ii) the origin of the resonance at the proximal dendrites.

3.2.1 Field sensitivity of passive cable models

Sensitivity of a passive cable to an arbitrary extracellular electric field

We further consider a passive dendritic cable, to which we apply an extracellular field, E , parallel to its axis, \vec{x} :

$$E(x, t) = -\frac{\partial v_e}{\partial x}(x, t),$$

where v_e denotes the extracellular potential. For the sake of generality, we here do not restrain ourselves to spatially uniform electric fields but consider also non-uniform fields. We define the membrane potential v , as the difference between the intra- and extracellular potential $v(x, t) = v_i(x, t) - v_e(x, t)$. It is solution of the cable equation (Roth and Basser, 1990) (see Appendix A.1 for the full derivation):

$$\tau \frac{\partial v}{\partial t} - \lambda^2 \frac{\partial^2 v}{\partial x^2} + v = -\lambda^2 \frac{\partial E}{\partial x} \quad 0 < x < l \quad (3.1)$$

with the boundary conditions (sealed end):

$$\begin{aligned}\frac{\partial v}{\partial x} &= E, & x = 0 \\ \frac{\partial v}{\partial x} &= E, & x = l,\end{aligned}\tag{3.2}$$

where l , λ and τ denote respectively the cable length and the membrane space and time constants.

We solve this equation under the assumption that the spatial and temporal components of the extracellular potential, respectively $v_{x,e}(x)$ and $v_{t,e}(t)$ are independent, i.e. $v_e(x, t) = v_{x,e}(x)v_{t,e}(t)$. In this case, the field is equivalent to correlated inputs distributed according to the field spatial component, along the cable (right hand side of Eq. 3.1) and at the extremities (Eq. 3.2). The full expression of the solution and its derivation are not directly relevant for the following analysis and are, for the sake of clarity, described in Appendix A.3. In the following, all displayed field sensitivities of straight and bent passive cables are obtained through evaluation of this analytical solution.

In case of AC fields, the induced polarization is sinusoidal in time and of the form:

$$v(x, t) = \alpha(x, f_t) \sin(2\pi f_t t + \phi(x, f_t)),$$

where f_t is the field frequency, $\alpha(x, f_t)$ the amplitude of the polarization at the location x and $\phi(x, f_t)$ the phase shift between the field and the polarization. We further express the field sensitivity as:

$$\text{Field sensitivity}(x, f_t) = \alpha(x, f_t)/E_0,$$

E_0 being the field amplitude.

For given field spatial distribution and field frequency, the field sensitivity of the cable depends on its length l , its membrane time, τ , and length constants λ . In the following, we further decrease this parameter space by normalizing the lengths by the space constant, for example: $L = l/\lambda$. For clarity, we denote the normalized length units using upper case, and the unnormalized lengths using lower-case. We also express the field sensitivity in normalized units: $V/(V/\lambda)$.

The space constant λ corresponds to the distance over which the polarization due to a steady state input decreases by $1/e$ (Koch, 2004). In case of time dependent inputs, we can define the *generalized frequency-dependent space constant*, $\lambda_{gen}(f_t)$, as:

$$\lambda_{gen}(f_t) = \frac{\lambda}{\text{Re}(\sqrt{1 + 2i\pi f_t \tau})},\tag{3.3}$$

where $\text{Re}(z)$ is the real part of the complex number z .

$\lambda_{gen}(f_t)$ decreases with the frequency f_t . Consequently, the effects of high frequency inputs are more localized than the one of low frequency inputs (Koch, 2004, chapter 2.3). Transposed to the field, this means that the effects of high frequency fields depend more on their local spatial profile than for low frequency fields. The membrane time constant determines the influence of the field frequency on λ_{gen} : the higher τ is, the faster $\lambda_{gen}(f_t)$ decreases with f_t . In the ensuing sections, we will analyze the impact of the generalized frequency-dependent space constant on the field sensitivity of straight and bent cables. We then relate this impact to the field sensitivity observed in the reconstructed cell model.

Field sensitivity of straight cables

We now consider the effects of a spatially uniform field on a straight passive cable. Due to its spatial uniformity, the effect of the field along the cable is null (right hand side of Eq. 3.1 equals 0). The field is therefore equivalent to input currents injected at both cable ends (right hand sides of Eqs. 3.2). These inputs have opposite orientations: inward on one side, and outwards on the other. The resulting polarization is antisymmetric (Fig. 3.3B): both cable sides have the same field sensitivity and their AC polarization is antiphased.

For all frequencies, the field sensitivity is maximal at the cable ends and cancels at the center of the cable. The area of null sensitivity in the middle broadens with increasing frequencies. We explain this phenomenon through the decrease of λ_{gen} with increasing field frequencies. Consequently, with increasing frequencies, the influence of the cable ends on the cable center decreases; so does the influence of the input currents equivalent to the field (right hand side of Eq. 3.2) on the cable center. For high frequency fields (e.g. $f_t > 200Hz$), the cable is locally equivalent at its center to an infinite cable, which is not polarized by uniform fields.

The field sensitivity monotonously decreases with increasing frequencies (Fig. 3.3C). While the membrane time constant τ does not affect the sensitivity to low frequency fields, it determines the cutoff frequency, i.e. the frequency at which the field sensitivity starts to decrease. The higher the time constant, the higher the cutoff frequency. Intuitively, τ determines how fast the membrane reacts to perturbations and therefore up to which frequency it is able to get polarized.

Increasing the cable length, L , increases the field sensitivity at the cable ends (Fig. 3.3D). The inputs at both ends being opposite, they tend to cancel each other out. When the cable gets longer, each extremity is less impacted by the opposite input, the cancellation effect decreases and the extremity gets more polarized. At a given length, the increase in field sensitivity with field frequency saturates: the cable is long enough and the cable ends do not influence each other anymore. The cable is then locally semi-infinite. In this case, the field sensitivity is solely determined by the membrane time constant τ , i.e. how fast the membrane can integrate the input.

Field sensitivity of bent cables

While the straight cable model presents an opposite polarization at both ends, it fails to reproduce some characteristics of the field sensitivity of the passive pyramidal cell model. For example, unlike straight cables, the passive pyramidal cell exhibits an asymmetric polarization amplitude (at the apical and basal dendrites) and some proximal dendrites have an atypical field sensitivity profile.

We further consider a bent passive cable subject to a uniform field as depicted in Fig. 3.4A. We refer to the part of the cable parallel to the field as the *main branch*, and to the other part, i.e. the one forming an angle Θ with the main branch, as the *bent branch*.

This model is equivalent to a straight cable in a spatially non-uniform extracellular field. The spatial profile of the corresponding field is obtained through projection of the bent cable coordinates on the field axis:

$$v_{x,e}(x, t) = \begin{cases} E_0 x & 0 \leq x \leq h, \quad \text{"main branch"} \\ -E_0 \cos(\theta) * (x - h) & h < x \leq l, \quad \text{"bent branch"}, \end{cases} \quad (3.4)$$

where x is the position along the straight cable, l the total cable length and h the length of the main branch. $x = 0$ corresponds to the main branch extremity and $x = l$ to the extremity of the bent branch. We also note d the length of the bent branch. Sticking to the notation convention of the precedent section, L , H and D represent the normalized (using the space constant λ) lengths of (respectively) the total cable, the main and the bent branches.

The bent cable subject to a spatially uniform field is analog to a straight cable in a field with the spatial distribution defined in Eq. 3.4. We therefore compute the field sensitivity of the bent cables using the solution of the cable equation for straight cables

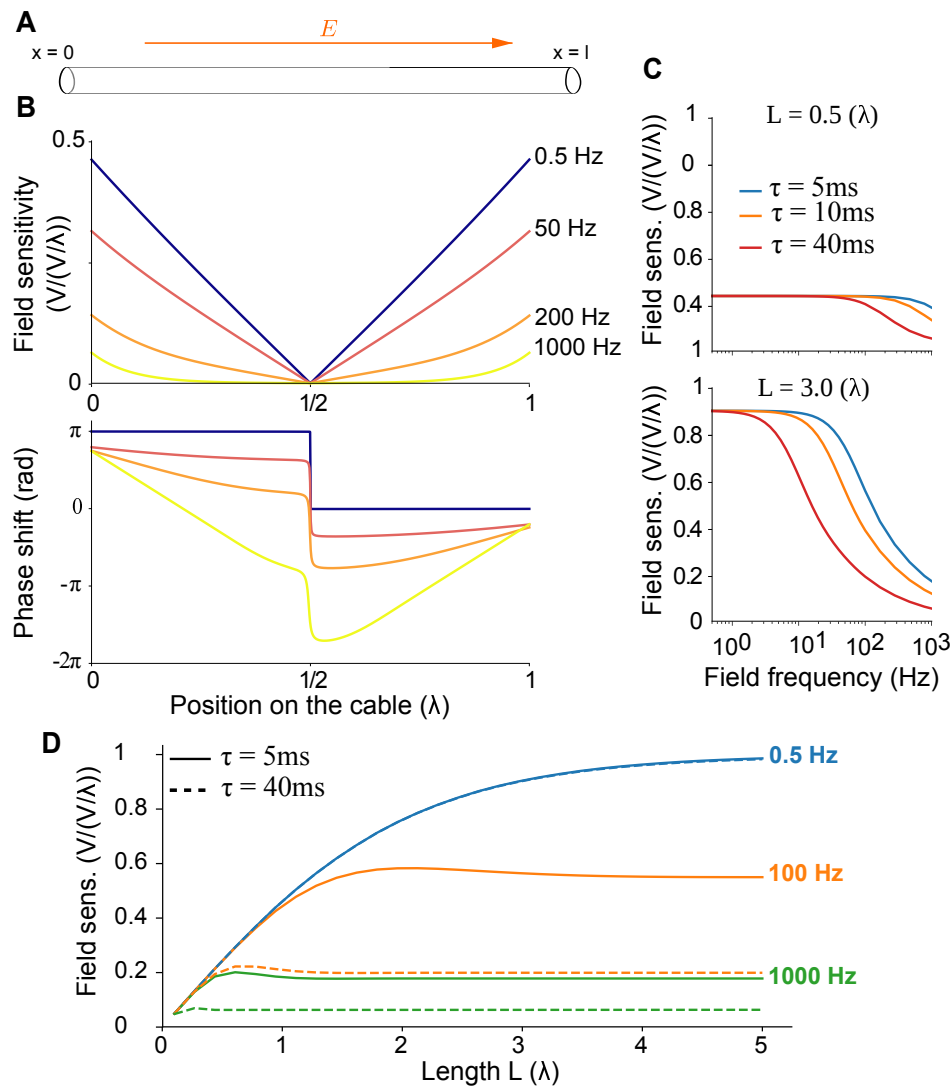


Figure 3.3: The polarization of a passive straight cable due to an extracellular field is anti-symmetric and decreases with the field frequency

(A) Schematic representation of a straight cable subject to a parallel electric field. (B) (top) Field sensitivity, i.e. ratio between membrane polarization and field amplitude, along the cable for different field frequencies (0.5, 50, 200 and 1000Hz, color coded) for $\tau = 40$ ms and $L = 1\lambda$. (bottom) Phase shift between the field and the membrane polarization oscillations. (C) Field sensitivity at the cable ends as a function of frequency (x axes), for various cable's electrotonic length L (top: 0.5λ , bottom: 3λ) and time constant τ (color coded). (C) Field sensitivity at the cable ends as a function of electrotonic length L , for various frequencies (color coded) and membrane time constants (solid lines: 5ms, dashed lines: 40ms). Figure and caption adapted from (Aspart et al., 2018, CC BY 4.0)

subject to field with arbitrary spatial profile (see Appendix A.3 for the solution and its full derivation). Note that in the following, we no longer mention this model analogy and refer solely to the field sensitivity of bent cables.

Unlike the straight cable case, the bent cable is not symmetric and its polarization is therefore not antisymmetric. Obtuse bending angles, i.e. $\Theta \leq \pi/2$, lower the field sensitivity at the cable ends but do not qualitatively change its frequency-dependent profile. For example a bending angle of $3\pi/4$ slightly decreases the field sensitivity at the bent end while the other side is even less affected (Fig. C.1 in Appendix). This effect on the field sensitivity is stronger when both branches get more orthogonal, reaching a maximum for a right bending angle, i.e. $\Theta = \pi/2$ (Fig. C.2 in Appendix). For all obtuse and right bending angles, the decrease of the field sensitivity due to the bending increases with the length of the bent cable part. If the main branch is sufficiently long, the field sensitivity at the end of the main branch is little affected by the bending.

In case of an acute bending angle ($\Theta < \pi/2$), the frequency-dependent profile of the field sensitivity at the bent end changes qualitatively. Indeed, the sensitivity to low frequency fields decreases and a resonance appears (see Fig. 3.4C for $\Theta = \pi/4$). This resonance is similar to the one we observed previously at proximal dendrites in the passive pyramidal cell model (Fig. 3.2). At the end of the main branch, the field sensitivity does not display any resonance (Fig. 3.4B).

For a fixed acute bending angle, the presence or not of the resonance at the bent end is determined by the relative lengths of the main and bent cable branches (Fig. 3.4E and Fig. C.4 in Appendix). The membrane time constant τ has no influence on the presence or not of a resonance. However, the time constant influences the frequency of the resonance. In fact, the time constant determines the range of frequencies affected by the decrease of sensitivity to low frequency fields at the bend end (Fig. C.3 in Appendix). The lower τ is, the higher is the cutoff frequency and therefore the higher is the resonance frequency (Fig. C.4 in Appendix).

The resonance frequency influences the amplitude of the resonance (Fig. 3.4C). As mentioned above, the resonance is due to a decrease in the sensitivity to low frequency fields; the sensitivity to high frequency field remains unchanged, that is very low. As a result, the amplitude of the resonance, i.e. the difference between the field sensitivities at the resonance and at very low frequency (0.5 Hz), depends both on the decrease of the sensitivity to low frequency fields and on the field sensitivity at the resonance frequency⁵.

To better understand the origin of this resonance, we now inspect the spatial distribution of the field sensitivity along the bent cable for various field frequencies (Fig. 3.4D). For all frequencies, the field sensitivity reaches a local minima on each branch, i.e. on each side of the bending. The location of this local minima is biased towards the bent end but its exact location depends on the field frequency. In fact, the higher the field frequency is, the closer to the branches centers the local minima are. Consequently, the minimal (at constant frequency) field sensitivity can be reached at the bent end for low frequency fields, but in the middle of the bent branch for high frequency fields. For example, in case of very low frequency fields (e.g. 0.5Hz), the local

⁵Note that, we do not use the standard Q-factor (i.e. the ratio between the peak and DC field sensitivity), since this measure explodes when the DC field sensitivity approaches 0.

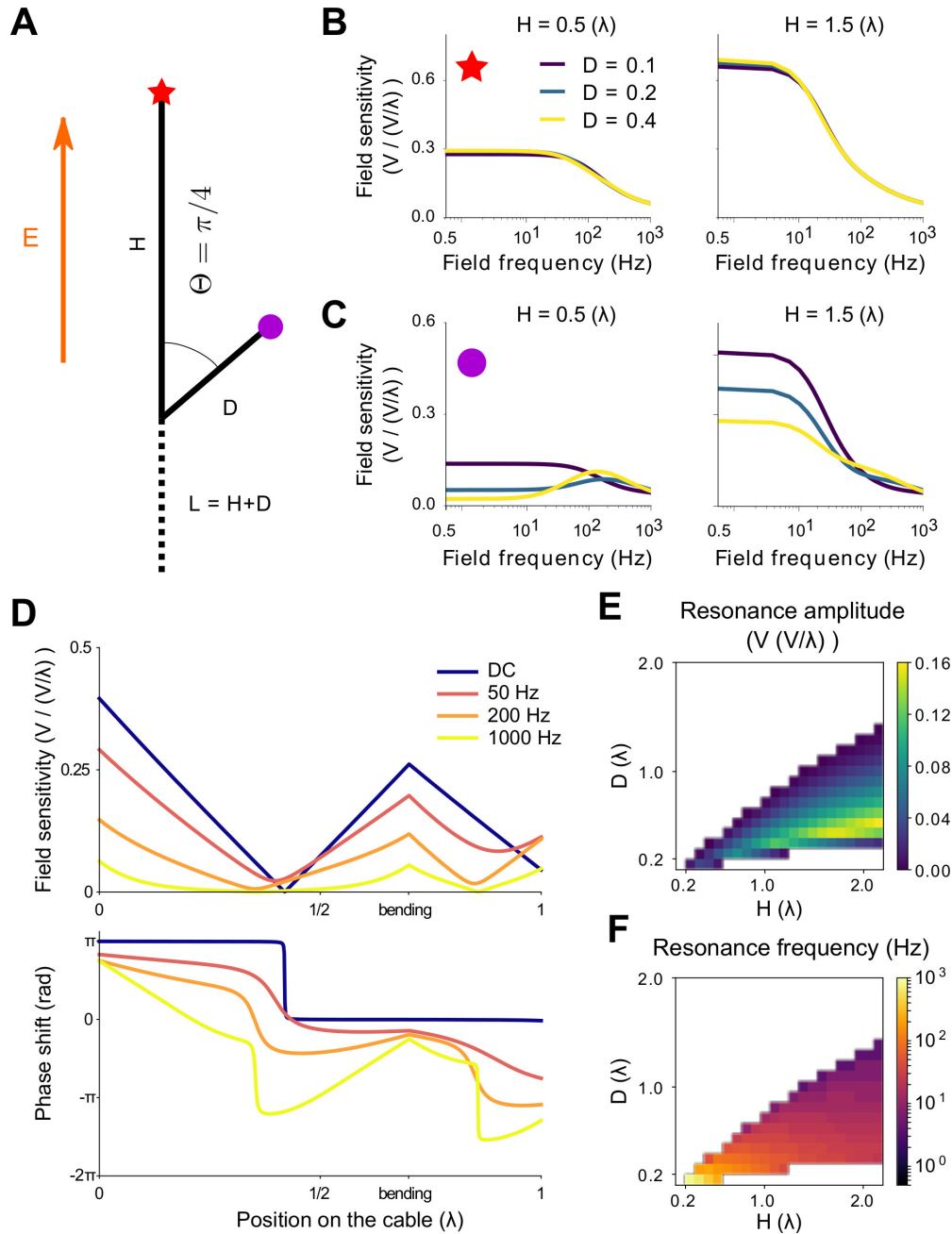


Figure 3.4: Passive cables with an acute bending angle can display a resonance in their sensitivity to spatially uniform fields

(A) Schematic representation of a bent cable. The unbent branch of the cable, of length H , is parallel to the field axis. The bent branch, of length D , has an angle Θ with the field. L is the total cable length. (B,C) Sensitivity (in $V/(V/\lambda)$) at both cable ends, i.e. at the main (B) and bent (C) branches ends, as function of the field frequency. The sensitivities are displayed for various main (H , columns) and bent (D color coded) branches lengths. (D) Distribution of the sensitivity (top) and phase (bottom) along the bent cable for different field frequencies (0.5, 50, 200 and 1000 Hz) for $H = 0.6(\lambda)$ and $D = 0.4(\lambda)$. (E) Resonance amplitude (sensitivity at the resonance minus sensitivity at 0.5 Hz) and (F) resonance frequency at the bent end depending on both branches length. The white area corresponds to the absence of resonance. In all the plots the bending angle is $\Theta = \pi/4$ (rad) and the membrane time constant $\tau = 40(ms)$. L , H and D are electrotonic lengths. Figure and caption adapted from (Aspart et al., 2018, CC BY 4.0)

minimum on the bent branch is located at its extremity while for very high frequency (1 kHz) it is located at its center. This results in a reduced sensitivity to low frequency fields and, therefore, in the observed resonance at the bent end.

We attribute this frequency-dependent phenomena to the generalized frequency-dependent space constant $\lambda_{gen}(f_t)$. The higher the field frequency is, the smaller is the generalized space constant and consequently the lower is the interplay between both branches. When $\lambda_{gen}(f_t)$ is very small, the branches are locally independent of each other and their field sensitivities cancel at their respective centers, as in straight cables. When the time constant decreases, $\lambda_{gen}(f_t)$ is less affected by changes in the field frequency f_t and both branches still have an impact on each other at high frequencies (Fig. C.5 in Appendix).

Field sensitivity of cables with several bending branches

In the preceding paragraph, we showed that a simple bent in a passive cable induces an asymmetric field sensitivity. Specifically, the bent end displays a reduced field sensitivity compared to the other cable end (Fig. C.2 in Appendix). Yet, this effect is limited in amplitude for obtuse bending angles and it therefore does not explain the strong asymmetry in the field sensitivity of the reconstructed cell, that is the soma and basal dendrites being 2-3 times less sensitive than the apical dendrites (see Fig. 3.1). To better understand the origin of this asymmetry, we now investigate the effects of adding several branches to the field sensitivity of a main cable.

To begin with, we consider a model composed of a main straight cable to which end several branching cables are attached. The extracellular field is parallel to the main cable (see Fig.3.5A for a schematic representation). By analogy, we refer to the main cable as the apical dendritic tree and to the branching cables as the basal dendrites; the soma is located at the branching point. The model includes at least one basal dendrite which is parallel to the apical axis, all additional basal branches form an angle of $\Theta \in [0, \pi]$ with that axis. We note N the number of non-parallel basal dendrites. We compute the field sensitivity of the model through numerical simulation as for the reconstructed pyramidal cell model⁶. The model parameters are the electrotonic lengths of the basal (D) and apical (H) branches, the membrane time constant τ and the number N and angle Θ of the additional basal branches.

The addition of basal branches increases the sensitivity to low frequency fields at the apical end (Fig. 3.5). The length of the apical cable modulates the exact range of affected frequencies. For longer apical cables (e.g. $H = 2\lambda$), the apical sensitivity to field of frequencies lower than 25Hz increases. This results in a stronger frequency dependence of the apical field sensitivity, comparable to the one observed in the passive pyramidal cell model (Fig. 3.1E). Oppositely, the field sensitivity at the soma and at the end of the parallel basal branch decreases with the number of additional basal branches N (Fig. 3.5).

The angle Θ has little impact on the changes of field sensitivity when adding new basal branches. The changes remain qualitatively the same for all considered angle Θ (result not shown), besides $\Theta = \pi$. In the virtual case where all basal dendrites are parallel to the apical dendrites ($\Theta = \pi$), the field sensitivity at the soma presents a

⁶To limit the computational cost of the simulations and enable a full parameter exploration, we focus on frequencies lower than 100Hz as in the reconstructed model.

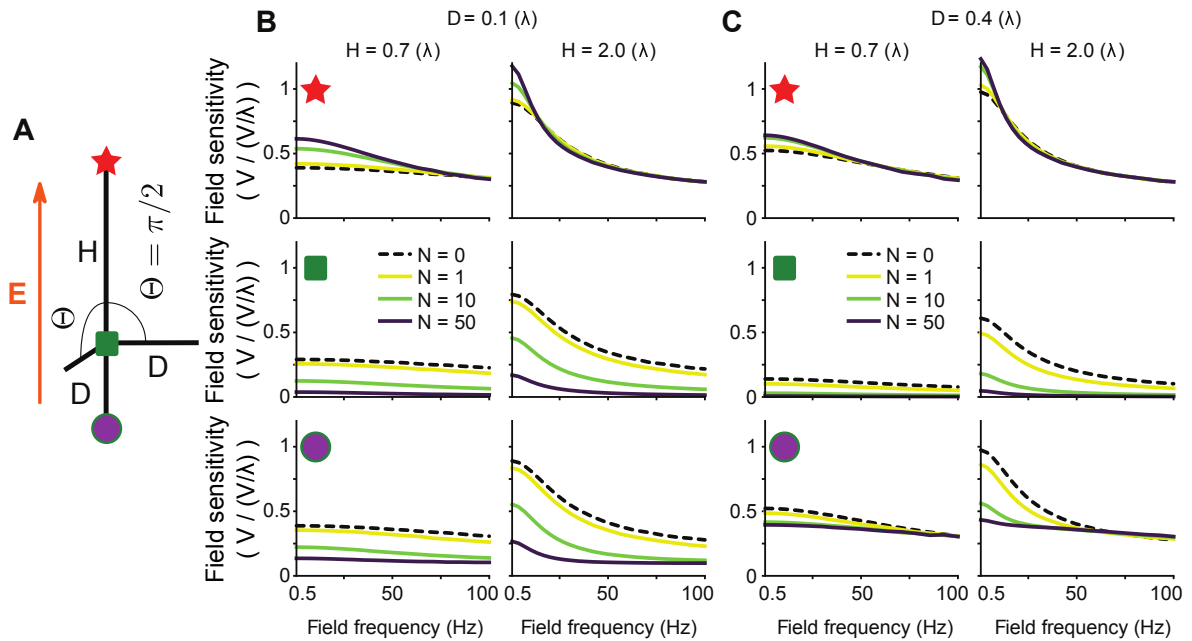


Figure 3.5: The presence of several basal dendrites increases the field sensitivity at the apical dendrites while decreasing the field sensitivities at the soma and basal dendrites

(A) Schematic representation of the simplified neuron model. The model consists of a main branch of length H , parallel to the extracellular field. Several branches of length D are attached to one end of the main cable. At least one of the attached branches is parallel to the main cable axis, the others form an angle Θ with that axis. (B,C) Sensitivity (in $V/(V/\lambda)$) at the end of the main cable (red star), at the branching point (green square) and at the end of the parallel branching cable (purple circle), as function of the field frequency. The field sensitivities are displayed for various number N (color coded) of branches with an angle of Θ and various main cable lengths (H , columns) and branch lengths (D , columns). In all the plots the bending angle is $\Theta = \pi/2$ (rad) and the membrane time constant $\tau = 40$ ms. H and D are electrotonic lengths. Figure and caption reproduced from (Aspart et al., 2018, CC BY 4.0)

resonance (Fig. C.6 in Appendix); nevertheless, the effect on the field sensitivity at the apical end remains the same.

The additional basal dendrites act as an electric shunt, i.e. a locally increased conductance, at the soma. This shunt is sufficient to explain the asymmetric field sensitivity (Monai et al., 2010). In fact, replacing the non-parallel basal branches with a simple shunt at the soma results in the same effects on the field sensitivity (see Fig. 3.6)⁷. The shunt due to the additional basal branches, therefore, accounts for the increased field sensitivity at the apical dendrites and for the decreased field sensitivity at the soma and basal dendrites. Furthermore, the shunt induces a slight resonance around 10Hz as observed in the field sensitivity of the soma and basal dendrites in the reconstructed cell (compare Fig. 3.1 and Fig. 3.6). Note that, using the simple model with several cables, we did not find any resonance at the soma, except for the virtual case where all basal dendrites were parallel to the apical cable ($\Theta = \pi$, Fig. C.6).

To summarize, in the absence of active membrane properties, the (passive) pyramidal cell model displays an asymmetric sensitivity to extracellular electric fields. The

⁷ We simulate the shunt through an increased passive conductance g_L at a single segment. The shunt conductances we report account for the membrane surface of the segment (using *area* function in NEURON).

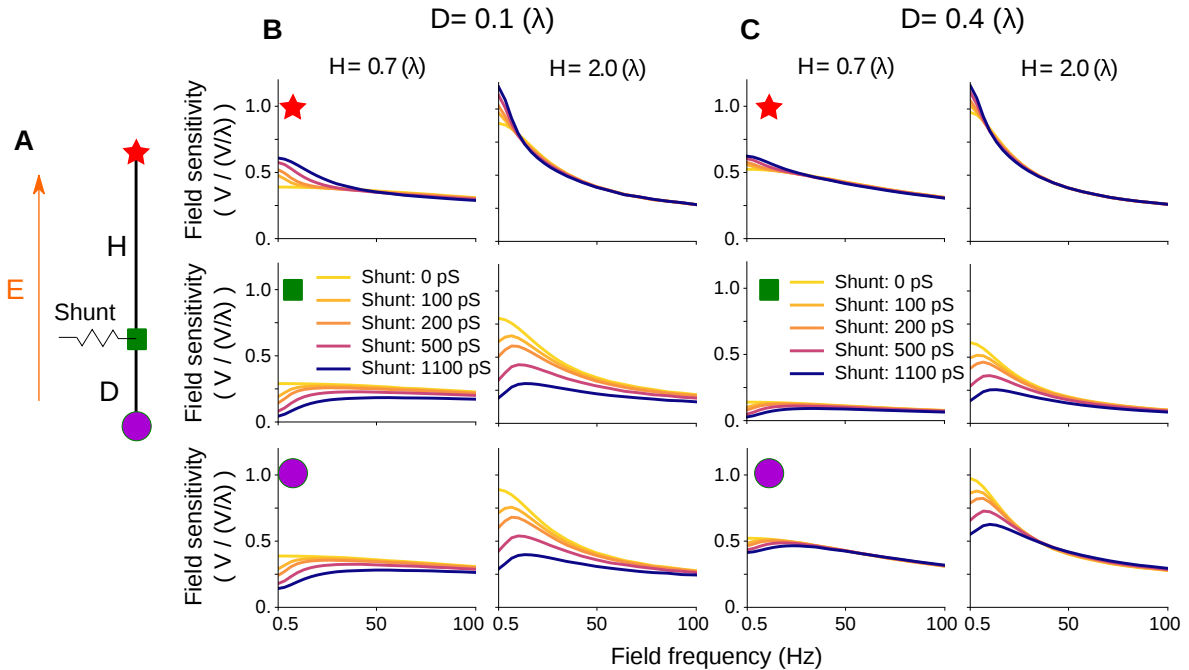


Figure 3.6: The presence of a shunt at the soma induces an asymmetric field sensitivity, the apical dendrites being more sensitive than the soma and basal dendrites

(A) Schematic representation of the simplified neuron model at use. The model consists of a passive cable with a local shunt (green square), i.e. an additional local conductance. The shunt is located at a distance H from one cable end and D from the other; H being longer than D . The cable is subject to an extracellular field parallel to it. (B,C) Sensitivity (in $V/(V/\lambda)$) at both cable ends (red star and purple circle) and at the location of the shunt (green rectangle), as function of the field frequency. The sensitivities are displayed for various shunt conductances (color coded) and various distances between the shunt and both extremities (H and D columns). In all the plots the membrane time constant is $\tau = 40(ms)$. H and D are electrotonic lengths. Figure and caption reproduced from (Aspart et al., 2018, CC BY 4.0)

apical dendrites are more sensitive to low frequency fields than the soma or basal dendrites; this difference in field sensitivity fades with increasing field frequencies. We explain this asymmetry through the multitude of basal branches and the associated increased conductance, i.e. shunt, at the soma. This shunt further results in a slight resonance around 5Hz at the basal dendrites and the soma. Finally, we observed a resonance in the field sensitivity of some oblique and basal dendrites which forms an obtuse branching angle with the apical dendrites. We attribute this "passive resonance" to the competition between the main branch (i.e. the apical cable) and the bent branches (the oblique and basal branches), both branches experiencing the extracellular field with opposite effective directions.

3.3 Impact of voltage-dependent membrane properties on the field sensitivity

In the precedent section, we analyzed the role of pyramidal cells morphology on their sensitivity to weak electric fields. We now investigate the effects of active, i.e. voltage-dependent, membrane properties on the field sensitivity. Specifically, we first consider a biophysical model of cortical pyramidal cells with experimentally constrained con-

ductances. Using this model we investigate how active membrane properties influence the field sensitivity of pyramidal cells. We then generalize our findings to any type of active channels using a simplified channel model, namely a quasi-active current.

3.3.1 Field sensitivity of a biophysical pyramidal cell model with experimentally constrained conductances

Let us consider the full Hay et al. (2011) model, i.e the same reconstructed morphology as for the passive case above with additional voltage-dependent conductances. This state-of-the-art model of a thick-tufted layer 5b pyramidal cell includes nine ionic channels, which were constrained using experimental data. Specifically, the authors used a multi-objective evolutionary algorithm to fit the ion channels parameters, e.g. the spatial distribution of the conductance. The model reproduces the perisomatic response to current step input and back-propagating action potential-activated calcium spikes as reported experimentally (see Section 3.4 for more details about the fitting procedure). Note that, the conductance distribution of the hyperpolarization-activated inward current, I_h , was not fitted but set according to electrophysiological evidences (Nevian et al., 2007; Kole et al., 2006). In brief, the I_h conductance was distributed uniformly in the basal dendrites and with an exponential increase with distance from the soma in the apical dendrites.

Similarly to the passive case, we investigate the subthreshold sensitivity of this biophysical model to an extracellular electric field. The field is spatially uniform and parallel to its somato-dendritic axis. We consider solely the field sensitivity of the cell at rest, i.e. at its steady state in absence of synaptic inputs⁸. In the following, the field sensitivities are computed with 1V/m electric fields; using fields with higher amplitude (but still weak) does not qualitatively change the results.

In the absence of field, the original model has a spatially non-uniform membrane potential at rest due to the active conductances distribution: the membrane in the apical dendrite is more depolarized than the basal dendrites and the soma (Fig. C.7A in Appendix). This gradient of rest membrane potential agrees with experimental *in vitro* recordings (Kole et al., 2006; Larkum and Zhu, 2002).

Weak DC fields slightly polarize the membrane, but not sufficiently to qualitatively counterbalance the gradient of resting membrane potential (Fig. C.7B in Appendix). In the following, we consider the effective membrane polarization due to a DC field, i.e. the membrane polarization around the resting potential of each location (Fig. 3.7A).

Unlike in the passive model, the soma and basal dendrites are more sensitive to DC fields than the apical dendrites. Besides, the membrane potential at the apical dendrites display a strong overshoot at the field onset. Looking at the membrane response to AC fields (Fig. 3.7B and Fig. C.8 in Appendix), the apical dendrites sensitivity to low frequency fields is decreased compared to the passive case (see Fig. 3.8 red and black traces for a comparison). This decrease induces a strong frequency resonance of the field sensitivity in the 10-20Hz range.

This resonance is only present in the apical dendrites; the soma or basal dendrites

⁸In the original Hay et al. (2011) model, the mechanism *CaDynamics.E2* is lacking of an initialization block "INITIAL"; the internal calcium concentration *cai* is therefore not initialized (see Section 3.4 and Fig. 3.20). We use version of this mechanism corrected by Ness et al. (2016), in order to ensure that our neuron is simulated at steady state.

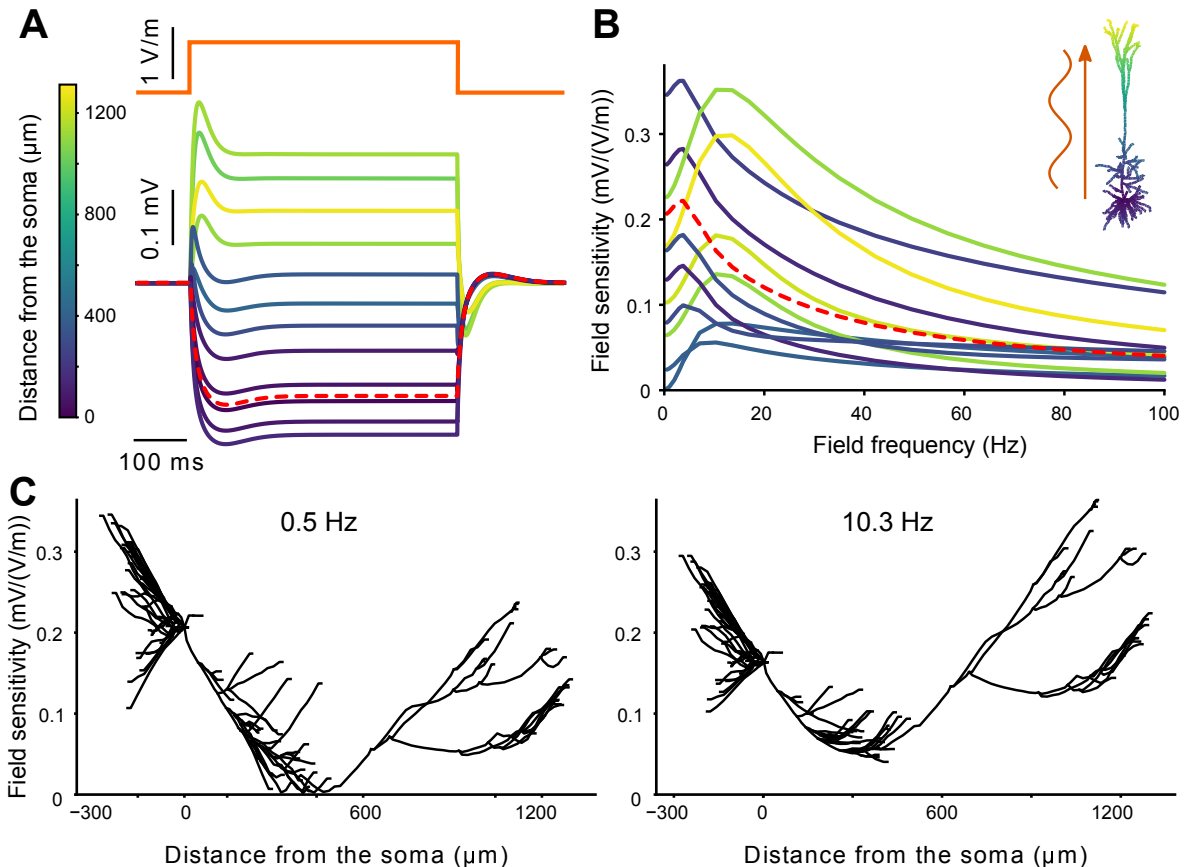


Figure 3.7: Unlike the soma and basal dendrites, the apical dendrites of an active cell have an increased subthreshold response to AC fields of 10-20Hz

We consider a pyramidal cell model of Hay et al. (2011) with all active channels. (A) Membrane polarization around the resting state due to a positive step current electric field (orange). (B) Frequency-dependent sensitivity of the cell to AC fields measured at different location on the whole cell. (C) Sensitivity to sinusoidal fields of frequency 0.5Hz (left) and 10.3Hz (right) as a function of distance to the soma. For clarity basal dendrites are plotted with negative distance. Colors of the polarization (A) and field sensitivity (B) correspond to the distance from the soma as depicted in A. The red dashed lines correspond to the soma. Figure and caption adapted from (Aspart et al., 2018, CC BY 4.0)

still exhibit a slight resonance around 5Hz as in the passive case. While the sensitivity to low frequency fields is the highest at the soma and the basal dendrites, the apical dendrites are the most sensitive to fields at the resonance frequency (Fig. 3.7C,D).

The resonances present at some locations in the passive model, e.g. at some proximal dendrites, remain qualitatively the same in this biophysical model.

To better understand the role of voltage-dependent ion channels on the field sensitivity profile of the cell, we further consider the effects of the three main differences between the passive and active models: (i) the non-uniform distribution of the resting membrane potential, (ii) the increased resting conductance due to the presence of additional active channels and (iii) the dynamics of the active channels themselves.

We first consider the impact of the non-uniform membrane potential at rest on the field sensitivity. We set the rest membrane potential uniformly to arbitrary values by adjusting the reversal potential of the leak current along the membrane (Carnevale and Hines, 2006, Chapter 8). In all considered model variations, i.e. values

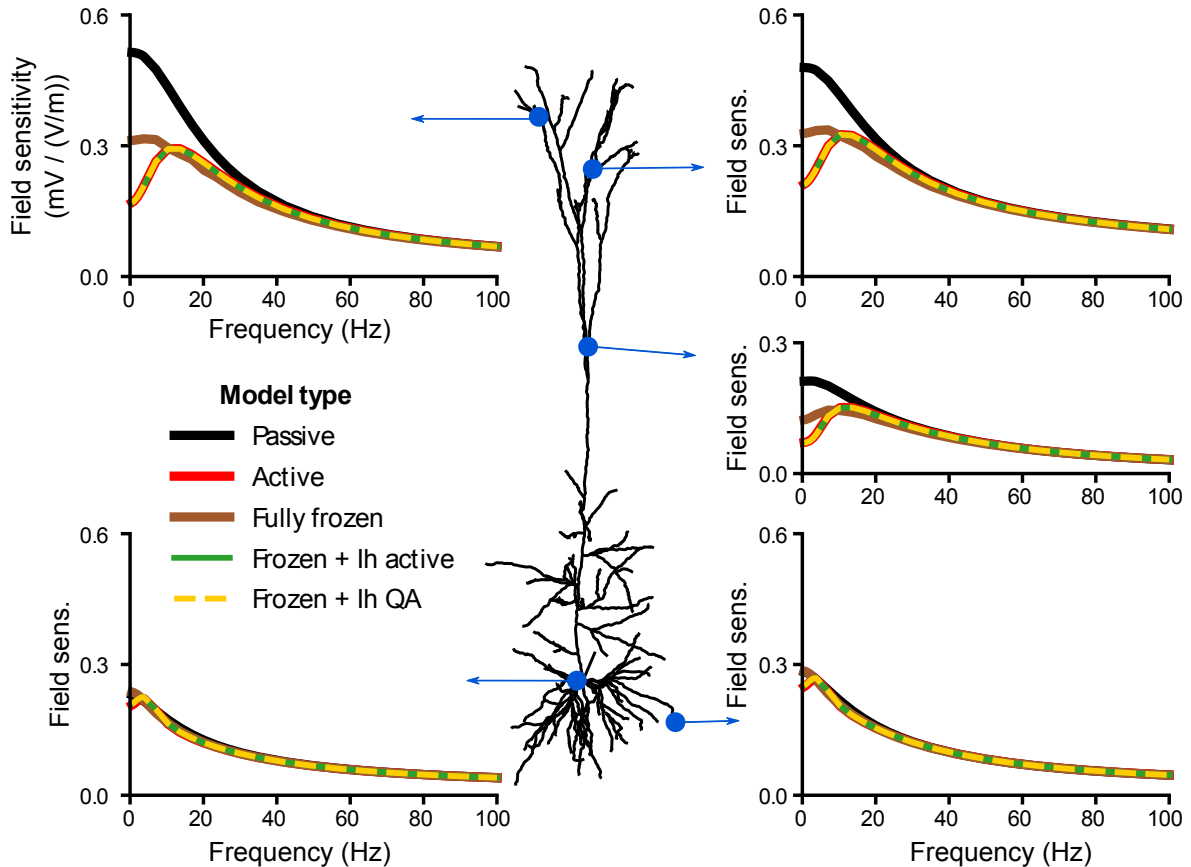


Figure 3.8: The hyperpolarization-activated inward current, I_h , is responsible for the frequency resonance in the sensitivity of apical dendrites to AC fields

The subplots display the field sensitivity (in $\text{mV}/(\text{V}/\text{m})$) of the cell at given locations depending on the channels included in the model: without any active channels (*passive*) or with all active channels present in the model of Hay et al. (2011) active (*Active*). We also consider the model with frozen channels, i.e. their gating variable is fixed to their resting value. We freeze either all the channels (*Fully frozen*) or all except the I_h which is fully active (*Frozen + I_h active*) or linearized following the quasi-active approximation (*Frozen + I_h QA*). Figure and caption adapted from (Aspart et al., 2018, CC BY 4.0)

of uniform rest potential, the field sensitivity exhibits a resonance at the apical tuft (Fig. 3.9). Nevertheless the frequency and amplitude of the resonance change with the rest membrane potential. The field sensitivity at the soma and basal dendrites is little affected by the rest membrane potential, except for highly depolarized values (60mV), where the somatic and basal sensitivity to low frequency fields increase drastically.

We then disentangle the role of the local, i.e. at the location of measurement, rest membrane potential against the global, i.e. at the whole cell level, rest membrane distribution. For each measurement location, we consider a model in which the rest membrane potential is set uniformly to the same value as the local membrane potential in the original Hay et al. (2011) model. In this case (Fig. 3.9, red line), the field sensitivity is the same as the field sensitivity in the original model (black line). This indicates that the local rest membrane potential determines the resonance amplitude and frequency of the field sensitivity.

We further evaluate the impact of the increased resting conductance in the biophysical model (compared to the passive one) due to the presence of active ion channels. To this aim, we freeze some of or all the active channels present in the full biophysical

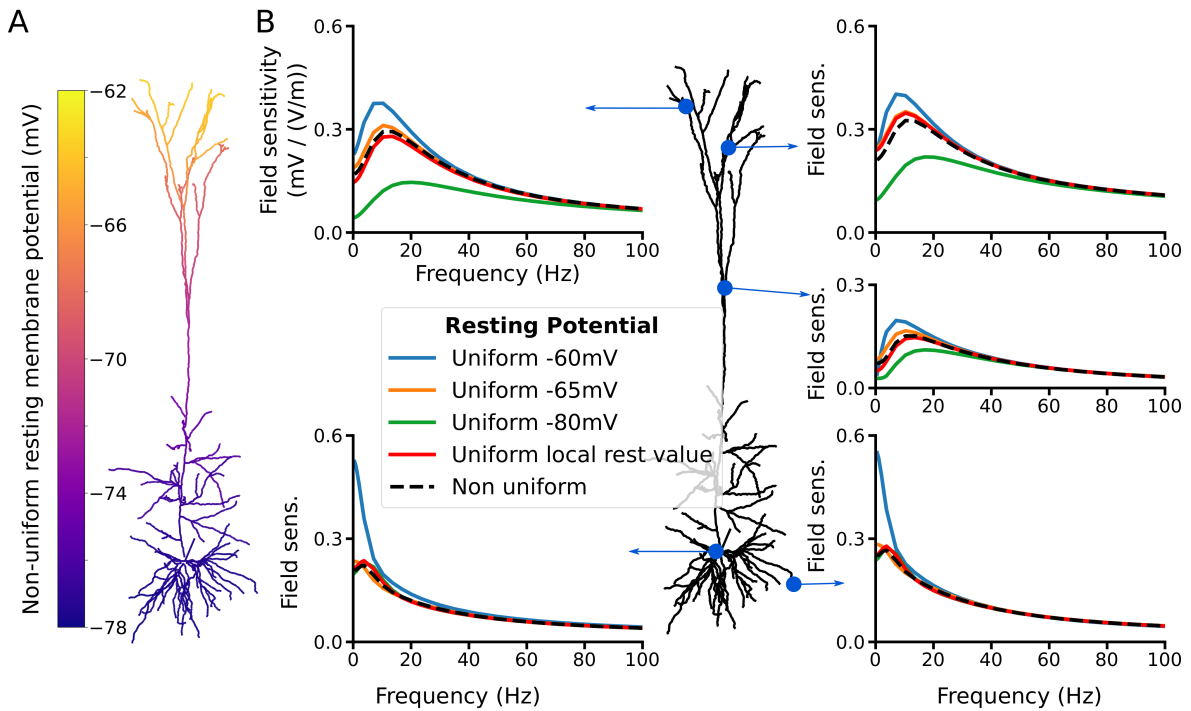


Figure 3.9: The distribution of the resting membrane potential does not qualitatively affects the field sensitivity profile of the active cell at the apical dendrites

(A) Distribution of the membrane potential at rest, i.e. in absence of electrical fields, in the fully active Hay et al. (2011) model. (B) Field sensitivity of the fully active model in case of non-uniform (black dashed line) and uniform resting membrane potential (solid lines). The uniform distribution of the resting membrane was set to an arbitrary value by adjusting the passive leak reversal potential at each dendritic segment independently. The red line traces are measured with a different value of uniform rest membrane potential in each subplots. In this case, the rest membrane potential is set uniformly to the local (i.e. at the location of measurement) value of the rest membrane potential in the non-uniform case. In other words, in each subplot the red line and the dashed black line correspond to sensitivity with a same local rest membrane potential. The local rest potentials in the red line and the black dashed line are (from left to right, top to bottom): -65.5 mV, -67.8 mV, -71.1 mV, -77.3 mV and -77.8 mV. Figure and caption adapted from (Aspart et al., 2018, CC BY 4.0)

model. In other words, we fix the channels conductances and gating variables to their rest values (Ness et al., 2016). We refer to these channels as "frozen". The dynamics of frozen channels are blocked and therefore they simply act as additional leak conductances. We first consider the fully frozen (Fig. 3.8, brown curve) model in which all active conductances of the biophysical model are presents and frozen. Compared to the passive model (black curve), the addition of frozen channels reduces the apical dendrites sensitivity to fields with frequencies up to 40 Hz. The active model (red curve) and the fully frozen model display the same sensitivity to fields of frequency higher than the resonance frequency of the active model. However, the fully frozen model does not exhibit any strong resonance and its sensitivity to low frequency fields is halfway between the one of the passive and active models. The addition of frozen channels, has little effects on the field sensitivity at the soma and basal dendrites.

To examine the role of single channels dynamics on the resonance, we further starts from the fully frozen model and unfreeze each channel separately. Reactivating the hyperpolarization-activated inward current (I_h) is sufficient to recover the resonance. In fact, the model with all channels frozen except I_h (Fig. 3.8, green curve) displays

the same field sensitivity as the fully active model. Keeping I_h frozen and reactivating other channels does not yield any resonance. We therefore conclude that the I_h channel is responsible for the field sensitivity resonance in the apical dendrites.

In vivo, neurons are constantly bombarded with background synaptic activity. This additional synaptic conductance results in a “high-conductance state” (Destexhe et al., 2003; Chance et al., 2002; Mishra and Narayanan, 2015). The increased conductance could prevail over the active membrane properties and lower their effects. To assess the effects of such conductance changes on the field sensitivity, we consider a model with a uniformly increased membrane conductance. The increased membrane conductance results in a decreased field sensitivity of the model (Fig. 3.10). Actually, increasing the membrane conductance, reduces the frequency-dependence of the field sensitivity and, consequently, the resonance amplitude. The resonance frequency remains unaltered when varying the membrane conductance (see the normalized field sensitivities in Fig. C.9 in Appendix).

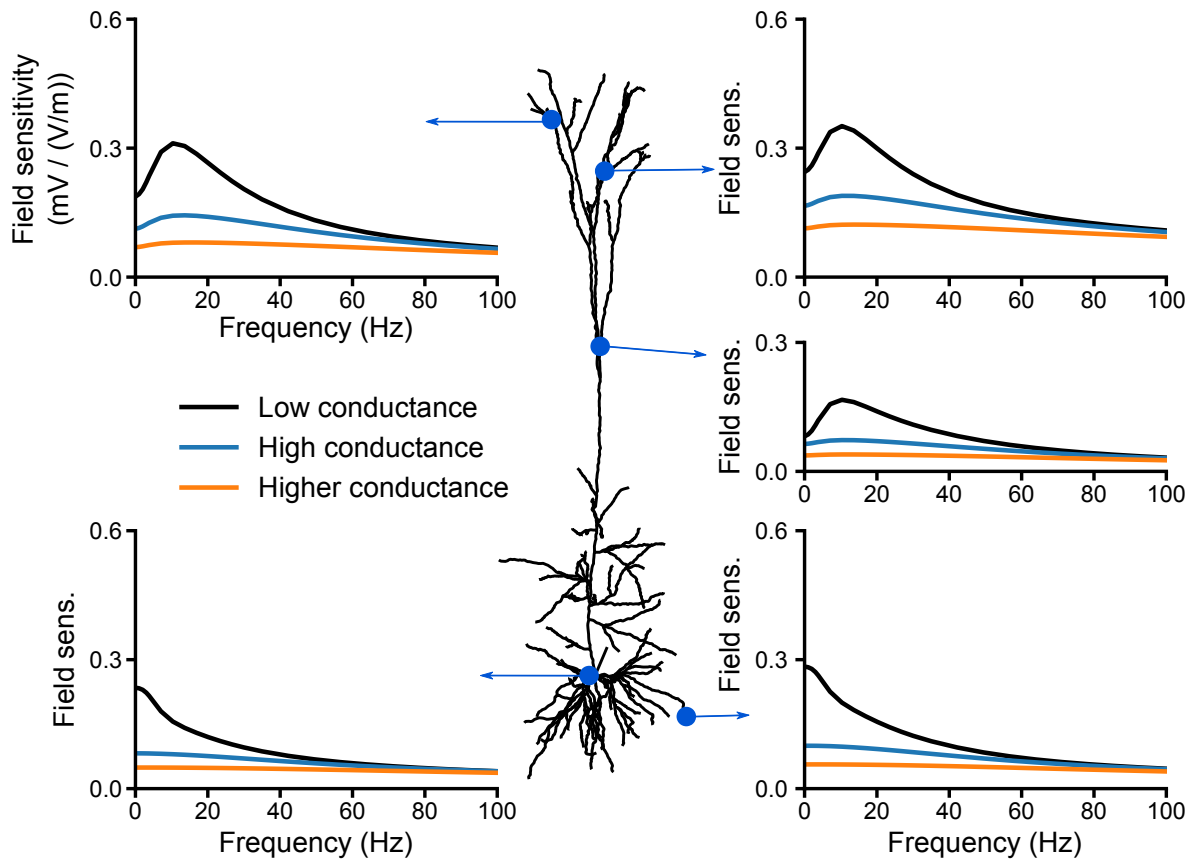


Figure 3.10: The field sensitivity of a pyramidal cell decreases in a high-conductance state

The subplots display the field sensitivity (in $\text{mV}/(\text{V}/\text{m})$) of the pyramidal cell model in different conductance states. The low-conductance state corresponds to the model with the same leak conductance as the original Hay et al. (2011) model. In the high- (blue lines) and higher-conductance (orange lines) states, we uniformly increased the passive conductance of the original model by adding respectively $350\mu\text{S}/\text{cm}^2$ and $900\mu\text{S}/\text{cm}^2$ uniformly throughout the model. To remove the effects of changes in resting membrane potential, we uniformly set the resting membrane potential of all 3 models to -65 mV by adjusting the leak reversal potential. The somatic input resistances of the low-, high- and higher-conductance state model are respectively: $53\text{ M}\Omega$, $15.62\text{ M}\Omega$, and $9.05\text{ M}\Omega$. Figure and caption adapted from (Aspart et al., 2018, CC BY 4.0)

To summarize, the field sensitivity of the passive pyramidal neuron model mostly decreases with field frequency (with the exception of some proximal dendritic branches). Adding active conductances lower the apical dendrites sensitivity to low frequency fields; this decrease in field sensitivity results in a resonance. We explain this phenomenon by (i) the increased membrane conductance due to the additional channels and (ii) the intrinsic dynamics of the I_h channel. The exact resonance frequency and amplitude are determined by the resting membrane potential.

3.3.2 Field sensitivity of a pyramidal cell model with quasi-active channels

The above findings, e.g. the resonance at the apical dendrites, depend on the ion channels present in the Hay et al. (2011) model. We now would like to generalize these results to any kind of subthreshold currents included in a model. To this aim, we consider a simpler channel model and systematically study the effects of its parametrization on the model field sensitivity. Concretely, we use the quasi-active (QA) approximation (Koch, 1984; Remme and Rinzel, 2011; Remme, 2013; Ness et al., 2016), which consists in linearizing active currents around the membrane potential at rest. The QA framework lowers the parameter space of active currents, while still keeping their active properties. The linear approximation is, in our case, justified due to the low amplitude of the considered extracellular fields and of the resulting membrane polarization.

Presentation of the quasi-active approximation Let us consider a neuron with a leak current and a voltage-dependent current I_w , which has a single gating variable $w(t)$. At a given segment of the cell, the membrane potential $V(t)$ is determined by the equation:

$$\begin{aligned} c_m \frac{dV(t)}{dt} &= -g_L(V(t) - E_L) - g_w w(t)(V(t) - E_w) + I_{\text{axial}}(t) \\ \tau_w(V) \frac{dw(t)}{dt} &= (w_\infty(V) - w(t)) \end{aligned} \quad (3.5)$$

where c_m denotes the membrane capacitance. E_α , g_α (with $\alpha \in \{L, w\}$) are respectively the reversal potentials and conductances of the leak (subscript L) and active (subscript w) currents. I_{axial} corresponds to axial (intracellular) currents flowing from neighboring segments. In this description, the current conductance g_w is static and the active current dynamics are contained in the gating variable w , with activation function $w_\infty(V)$ and time constant $\tau_w(V)$.

We now linearize the active current by taking the first order term of the Taylor expansion of Eq. 3.5 around rest, i.e. around the rest membrane potential V_R and the rest gating variable $w_\infty(V_R)$ (see Appendix B for a detailed derivation of the equation):

$$c_m \frac{dV(t)}{dt} = -g_L (\gamma_R(V(t) - V_R) + \mu m(t)) + I_{\text{axial}}(t) \quad (3.6)$$

$$\tau_w(V_R) \frac{dm(t)}{dt} = V(t) - V_R - m(t) \quad (3.7)$$

with:

$$\begin{aligned}
 \gamma_R &= 1 + \frac{g_w}{g_L} w_\infty(V_R) \\
 \mu &= \frac{g_w}{g_L} (V_R - E_w) \frac{\partial w_\infty}{\partial V}(V_R) \\
 m(t) &= (w(t) - w_\infty(V_R)) / \frac{\partial w_\infty}{\partial V}(V_R)
 \end{aligned} \tag{3.8}$$

This quasi-active approximation can also be performed in models including several active channels. Each of them would then be linearized separately.

Before further analysis, we need to assess the validity of the quasi-active approximation in our case of study. We therefore simulate the field sensitivity of the pyramidal model with all channels of the Hay et al. (2011) model frozen except the I_h one, which we linearize following the QA approximation. This quasi-active model perfectly reproduces the field sensitivity of the fully active model (Fig. 3.8, yellow dashed curve). Regarding the weakness of the applied extracellular field, this result is not surprising. Indeed, the induce membrane polarization is of low amplitude and the active channels operate in a near linear regime.

A key asset of the QA framework is that it strongly reduces the parameter space of the model. Indeed, the dynamics of the quasi-active membrane (Eq. 3.6) is now fully described by the scalars γ_R , μ and $\tau_w(V_R)$ which do not depend on the current membrane potential. Most importantly the sign of μ determines the behavior of the QA channel in the low frequencies (Remme and Rinzel, 2011; Remme, 2013; Ness et al., 2016):

1. $\mu < 0$: the channel provides a positive feedback to modulations of the membrane. The current is *regenerative*.
2. $\mu = 0$: the dynamics of the normalized gating variable m has no influence on the membrane. The quasi-active current acts as a passive (leak) current.
3. $\mu > 0$: the channel provides a negative feedback to membrane modulations. The current is *restorative*.

It is worth noting that this classification of quasi-active currents is valid for membrane modulations of shorter timescale than the QA current time constant $\tau_w(V_R)$. For faster variations, the gating variables have no time to adapt and to provides their feedback to the modulation. In case of modulations with a timescale comparable to $\tau_w(V_R)$, some phase shift between m and V may occur and this classification would break.

Effect of quasi-active currents on the field sensitivity Three factors can determine the impact of a QA current on the field sensitivity of a cell: (i) the QA conductance distribution along the cell, (ii) the channel type (i.e. the sign of μ), and (iii) the channel activation time constant $\tau_w(V_R)$. In the following, we assess the importance of each of these factors using a pyramidal cell model with a leak current and a quasi-active current.

In particular, we consider three different distributions of the QA conductance over the whole cell: 1) uniform, 2) linearly increasing and 3) linearly decreasing with distance from the soma; we distribute the leak conductance g_L uniformly to $50\mu S/cm^2$

in all models. In case of the linear distributions, we set the difference in conductance between the soma and the most distal apical point to be 60-fold (Ness et al., 2016). This relates to empirical measurement of the I_h conductance distribution in the apical dendrites of cortical pyramidal cell (Kole et al., 2006). For simplification, we consider a linear distribution of QA channel over both basal and apical dendritic trees in our models⁹.

We calibrate all conductance distributions to have an equal amount of total, i.e. summed over the whole cell, quasi-active g_w and leak conductance g_L ¹⁰. As a result, the linearly increasing and decreasing distributions are respectively $g_w(x) = 0.117x + 2.60$ ($\mu S/cm^2$) and $g_w(x) = -0.0539x + 71.9$ ($\mu S/cm^2$), x (μm) being the distance along the dendritic tree separating a given cell segment and the soma. Unless specified otherwise, the QA channel activation time constant is 50 ms. We further fix uniformly the membrane capacitance c_m to 1 $\mu F/cm^2$, the axial resistance $R_{axial} = 100(\Omega cm)$ and $w_\infty(V_R) = 0.5$. We also set the rest membrane potential V_R uniformly.

The channel type is defined by μ which, by definition (Eq. 3.8), depends on the local QA conductance $g_w(x)$. To set the type of QA current independently of the local QA channel conductance, we use μ^* instead. μ^* is defined as:

$$\mu^*(x) := \mu(x)g_L/g_w(x) = (V_R - E_w)\frac{\partial}{\partial V}w_\infty(V_R) \quad (3.9)$$

To begin with, we investigate the effects of the QA channel conductance distribution on the field sensitivity. To this end, we consider a pyramidal neuron model with the uniformly distributed leak conductance and a passive (i.e. $\mu = 0$) QA channel. The QA conductance is distributed according to one of the three above mentioned distributions. Changing the conductance distribution mainly alters the sensitivity to low frequency fields (below 80Hz) (Fig. 3.11). In general, increasing the local passive QA conductance decreases the local field sensitivity. For example, compared to the uniform case, the model with a linearly increasing conductance distribution has a higher QA conductance at the apical dendrites and a lower one at the basal dendrites and at the soma. This leads to a lower field sensitivity (still compared to the uniform distribution) at the apical dendrites and a stronger one at the basal dendrites and the soma (Fig. 3.11, blue and orange lines). Using the linearly decreasing distribution induces the opposite effect. The range of affected frequencies is higher at the apical dendrites (up to 80Hz) than at the soma and the basal dendrites (up to 30Hz). Moreover, using a linearly increasing conductance distribution results in a slight resonance at the apical dendrites.

We next study the effect of the channel type on the field sensitivity. We consider a uniformly distributed QA channel with various channel type, i.e. various values of μ ¹¹. Restorative QA currents ($\mu > 0$) provide a negative feedback to membrane modulations and therefore decrease the sensitivity to low frequency fields compared to passive QA channels ($\mu = 0$) (Fig. 3.12 blue and black lines). Consequently, a resonance appears in the field sensitivity. The resonance is similar to the one previously observed due to I_h in the Hay et al. (2011) model. In fact, I_h is a restorative current (see below).

⁹Actually, I_h is known to be uniformly distributed in the basal dendritic tree of rats cortical pyramidal cells (Nevian et al., 2007).

¹⁰Note that, when computing the total QA conductance, we need to multiply it by its activation function at rest $w_\infty(V_R)$

¹¹By definition, in case of a uniform distribution $g_L(x) = g_w(x)$ and $\mu(x) = \mu^*(x)$

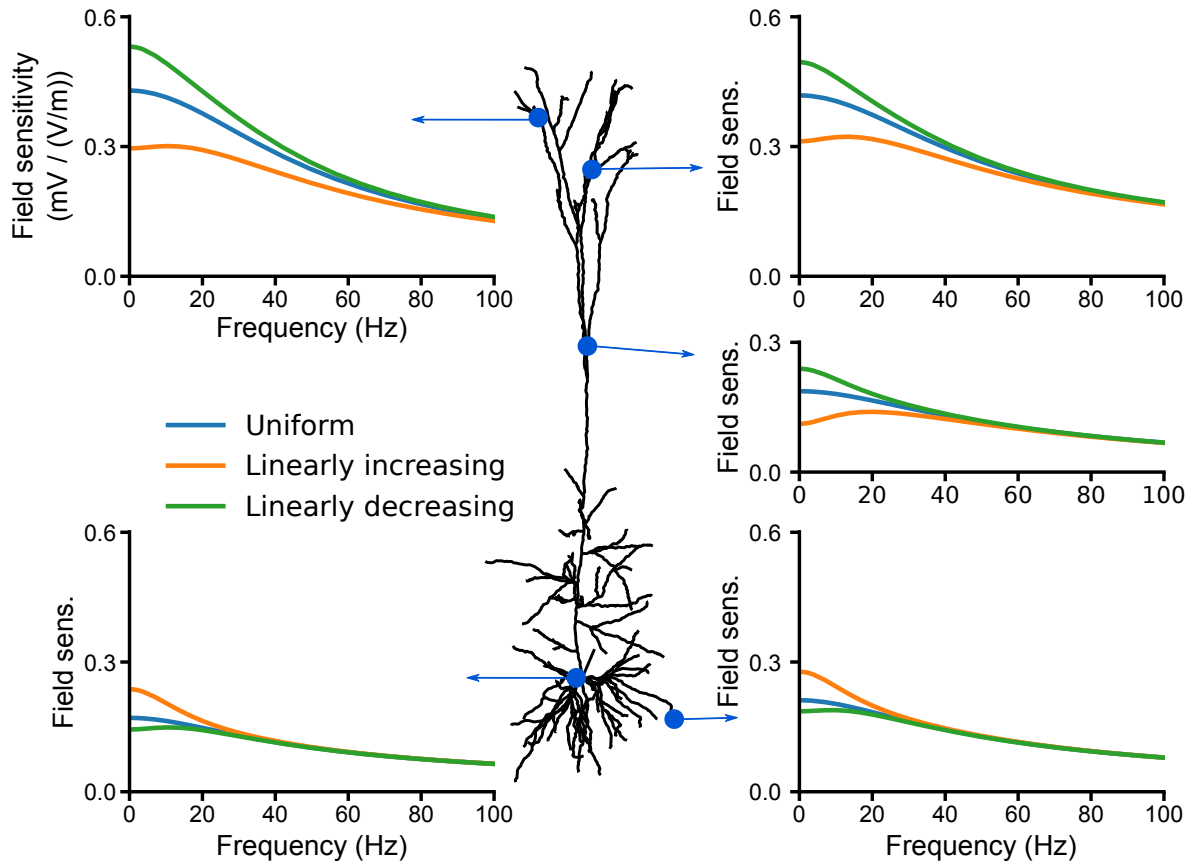


Figure 3.11: The quasi-active channel conductance distribution affects the cell field sensitivity depending of the local conductance at the considered location

We consider a neuron model which includes solely a leak conductance and a single quasi-active channel (QA). The QA channel have no active dynamics ($\mu = 0$) and acts as an additional leak current. We consider 3 different QA conductance distributions: uniform and linearly increasing/decreasing with distances from the soma. For each distribution, the sum over the whole cell of the QA conductances at rest is equal to the sum of the leak conductances. Figure and caption reproduced from (Aspart et al., 2018, CC BY 4.0)

On the contrary, regenerative currents provide a positive feedback to membrane modulations and, thus, increase the cell sensitivity to low frequency fields (Fig. 3.12 red and black lines). In this case no resonance appears. This is similar to what we observed at the soma of the Hay et al. (2011) model in case of highly depolarized membrane at rest (Fig. 3.9, blue line).

The QA conductance being uniformly distributed, we observe the effects of the restorative and regenerative currents at all considered locations (soma, basal and apical dendrites).

We further consider the effects of the channel type in case of non uniform QA conductance distribution, i.e. linearly increasing or decreasing. For both distributions, the effects of the QA channel type on the field sensitivity remains qualitatively the same as in the uniform case. Regenerative currents increase the sensitivity to low frequency fields and restorative currents decrease it, inducing a resonance.

In case of linearly increasing distribution (Fig. 3.13), the impact on field sensitivity is the strongest in the apical tree, while the field sensitivity at the soma and basal dendrites is only slightly affected by the channel type. In comparison, for linearly decreasing distribution (Fig 3.14), the modulation of the field sensitivity by the channel

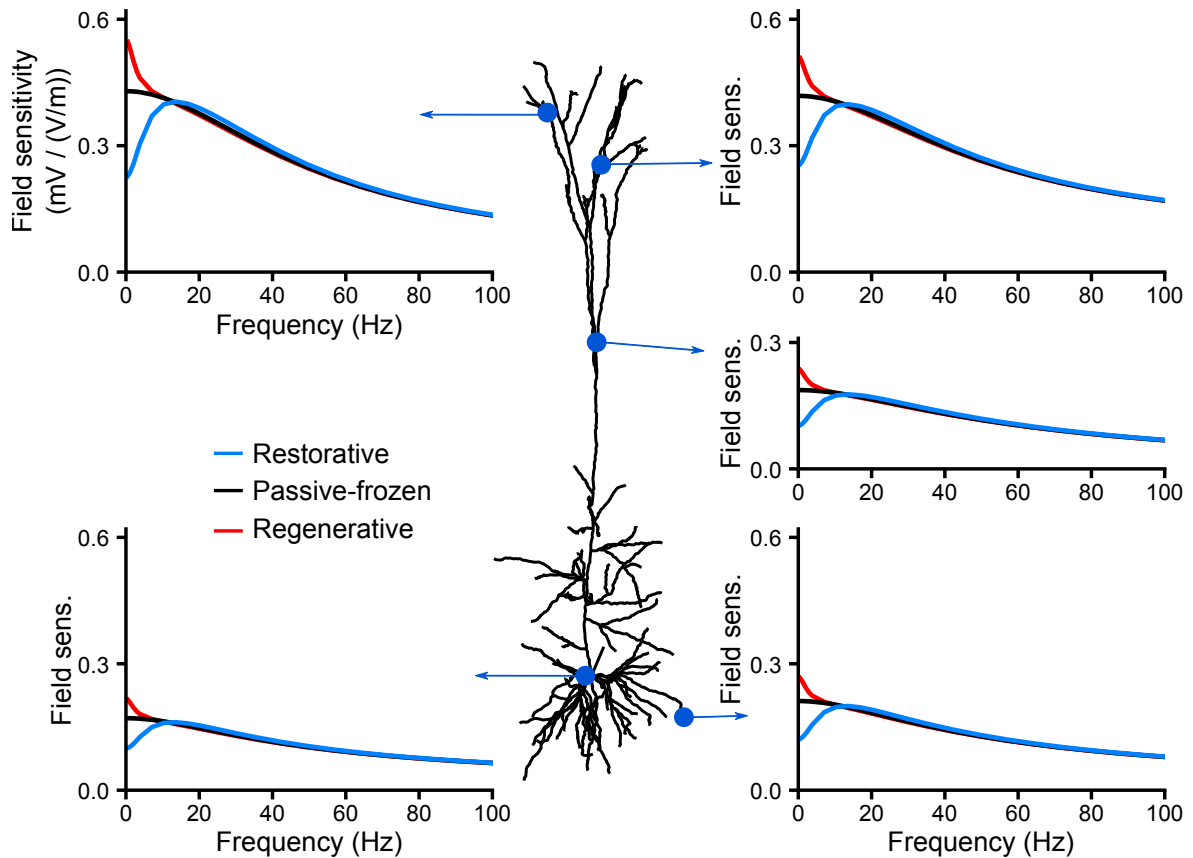


Figure 3.12: While regenerative currents increase the cell sensitivity to low frequency fields, restorative currents decrease it and induce a resonance

We consider a neuron model which includes solely a leak conductance and a single uniformly distributed quasi-active channel (QA). The plots display the sensitivity (in $\text{mV}/(\text{V}/\text{m})$) of the cell to AC fields at different location in case of restorative (blue, $\mu^* = 2$), passive (black, $\mu^* = 0$) and regenerative (red, $\mu^* = -1$) quasi-active currents. Figure and caption adapted from (Aspart et al., 2018, CC BY 4.0)

type, i.e. μ^* , is weakened at the apical dendrites and is enhanced at the soma and basal dendrites. In sum, these observations support a local effects of the QA channels: the field sensitivity is the most affected by the channel dynamics at locations with the highest channel density.

Finally, we study the impact of the activation time constant $\tau_w(V_R)$ on the field sensitivity profile of the cell (Fig. 3.15). The faster the channels (i.e. the lower the time constants), the broader the range of affected frequencies. In other words, channels with a shorter $\tau_w(V_R)$, modulate the field sensitivity up to higher frequencies. Consequently, the activation time constant of restorative QA currents determines the cut-off frequency of the low-pass filtering effect on the field sensitivity. The time constant therefore modulates the resonance frequency: the smaller the activation time constant $\tau_w(V_R)$, the higher the resonance frequency. For very short $\tau_w(V_R)$, e.g. 1 ms, the channel attenuates the field sensitivity over the whole range of frequencies and the resonance disappears.

We further assess if the above effects of QA channels on field sensitivity also transpose to other pyramidal cell morphologies. To this end, we consider other reconstruction of cortical pyramidal cells (specifically the morphologies referred as cell #2 and

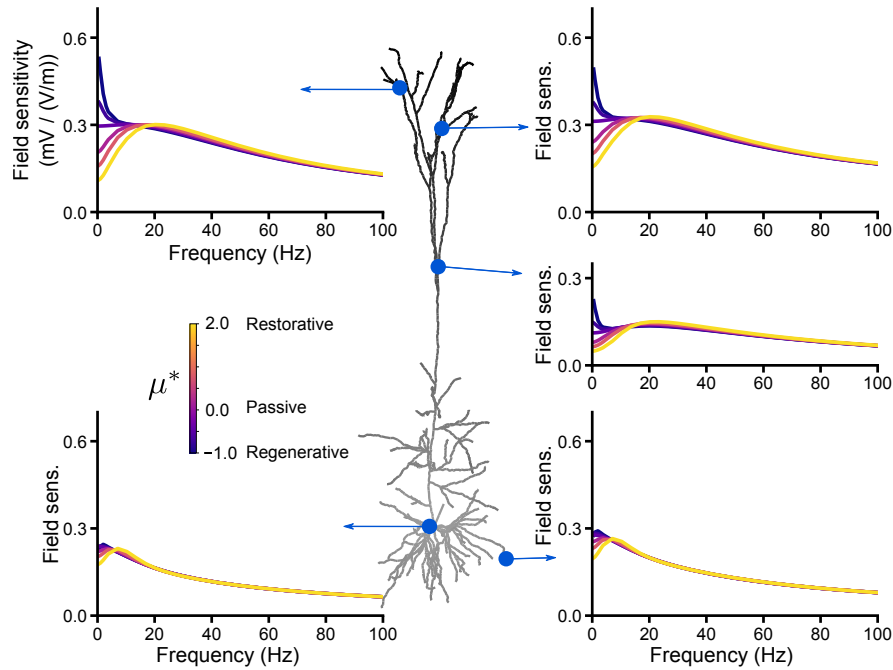


Figure 3.13: The type of QA channel, with conductance distributed increasingly from the soma, affects more strongly the field sensitivity at apical dendrites than at the soma and basal dendrites

The neuron model includes a leak current and a single QA channel, whose conductance distribution increases linearly with distance from the soma. The shades of grey in the cell plot represent this distribution. μ^* determines the type of the QA channel. The plots display the sensitivity of the cell to AC fields at different locations depending on the values of μ^* (color coded). Figure and caption adapted from (Aspart et al., 2018, CC BY 4.0)

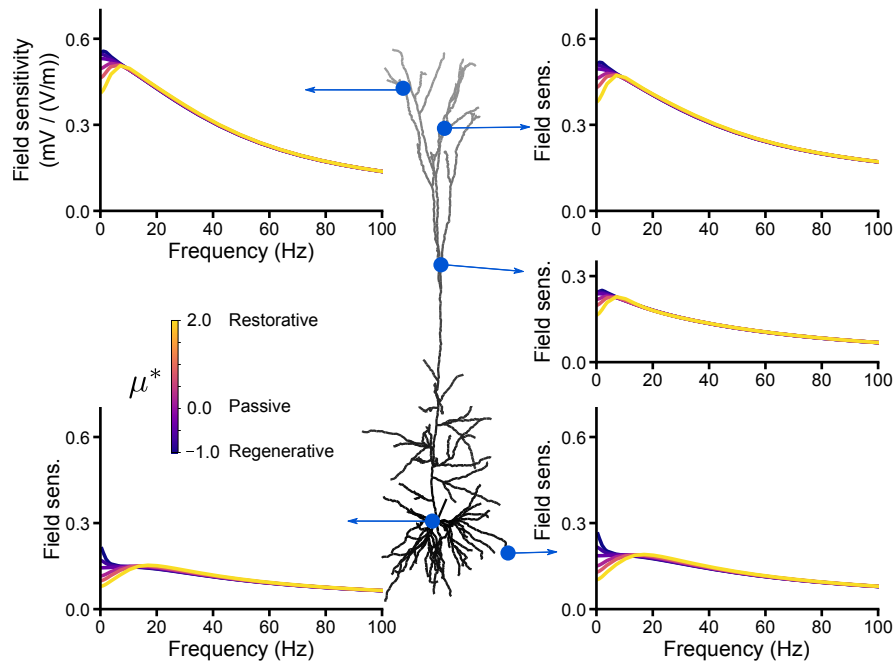


Figure 3.14: The type of QA channel, with conductance distributed decreasingly from the soma, affects the field sensitivity at the soma, apical and basal dendrites

The neuron model includes a leak current and a single QA channel, whose conductance distribution decreases linearly with distance from the soma. The shades of grey in the cell plot represent this distribution. μ^* determines the type of the QA channel. The plots display the sensitivity of the cell to AC fields at different locations depending on the values of μ^* (color coded). Figure and caption adapted from (Aspart et al., 2018, CC BY 4.0)

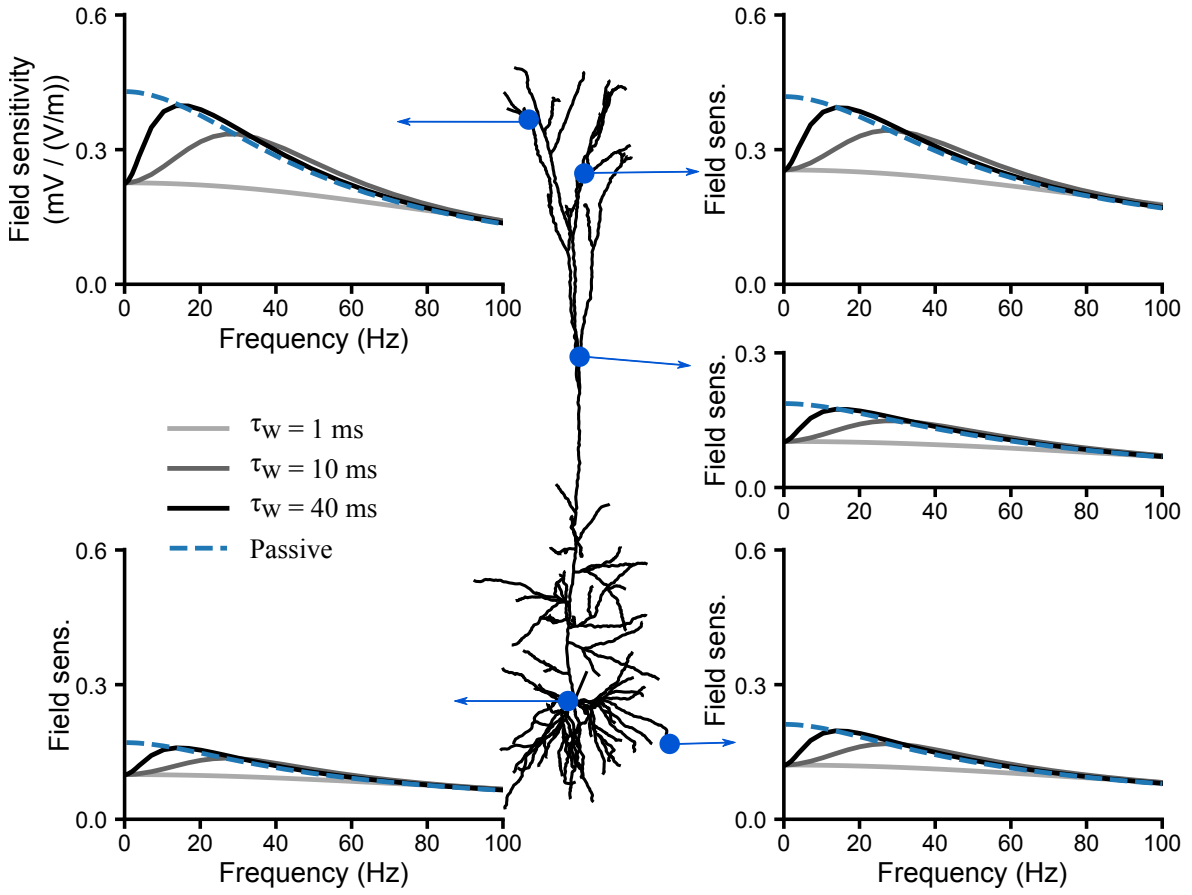


Figure 3.15: The time constant of restorative currents determines the resonance frequency of the sensitivity to AC fields

We consider a neuron model which includes solely a leak conductance and a single uniformly distributed quasi-active channel (QA). The plots display the cell’s sensitivity (in $\text{mV}/(\text{V}/\text{m})$) to AC fields at different locations in case of a passive ($\mu^* = 0$, dashed line) or a restorative ($\mu^* = 2$, dashed lines) quasi-active current. The shades of grey encode the restorative QA channel time constant, $\tau_w(V_R)$. Figure and caption reproduced from (Aspart et al., 2018, CC BY 4.0)

cell #3 in (Hay et al., 2011). Similarly to the precedent case, each cell has a leak current and a QA current, whose distribution is uniform or linearly increasing/decreasing. The exact distribution is recomputed for each morphology following the same constraints as for the precedent morphology. As expected, for both morphologies and all three QA conductance distributions, restorative currents decrease the sensitivity to low frequency fields, while regenerative currents increase it (Fig.3.16,3.17 and Fig.C.10-C.13 in Appendix).

Furthermore, at a given location, the field sensitivity decreases with increased local conductance independently of the morphology. For example, in case of a passive QA channel ($\mu^* = 0$), the field sensitivity at the apical dendrites is lower when the QA conductance is distributed linearly increasingly with distance from the soma (Fig. C.10 or Fig. C.12 in Appendix) than when the QA conductance is uniformly distributed (Fig. 3.16 or Fig. 3.17).

Interestingly, we observe a resonance around 20Hz at the center of the apical tuft in case of a linearly increasing QA conductance distribution (Fig. C.10 and Fig. C.12, middle subplot right). This resonance occurs independently of the QA channel type, i.e. independently of μ^* and is not present in the first considered morphology (Fig. 3.13).

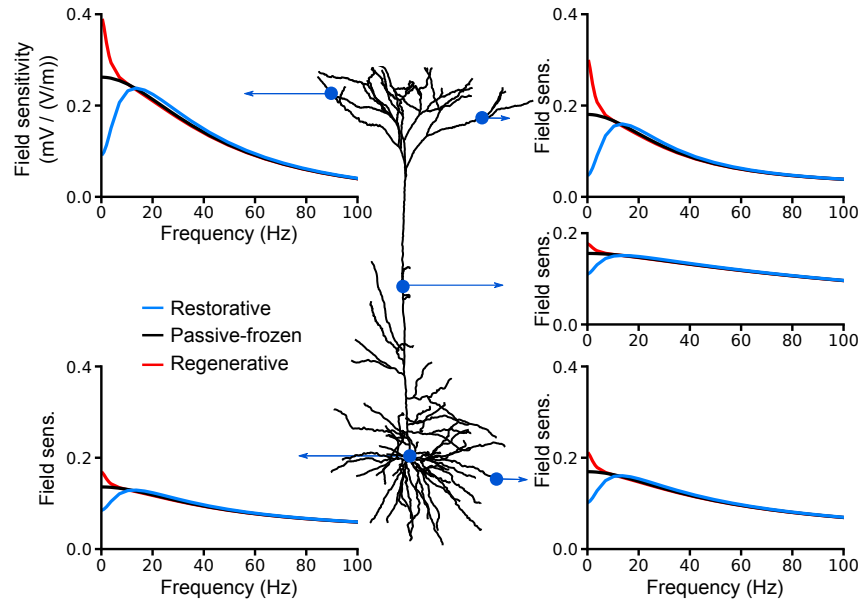


Figure 3.16: The effects of the channel type on the field sensitivity are transposable to other pyramidal cell morphologies, cell 2

We consider a neuron model which includes solely a leak conductance and a single uniformly distributed quasi-active channel (QA). We use the reconstructed morphology corresponding to cell 2 in the Hay et al. (Hay et al., 2011) paper. The plots display the sensitivity (in $\text{mV}/(\text{V}/\text{m})$) of the cell to AC fields at different locations in case of restorative (blue, $\mu^* = 2$), passive (black, $\mu^* = 0$) and regenerative (red, $\mu^* = -0.5$) quasi-active currents. Figure and caption adapted from (Aspart et al., 2018, CC BY 4.0)

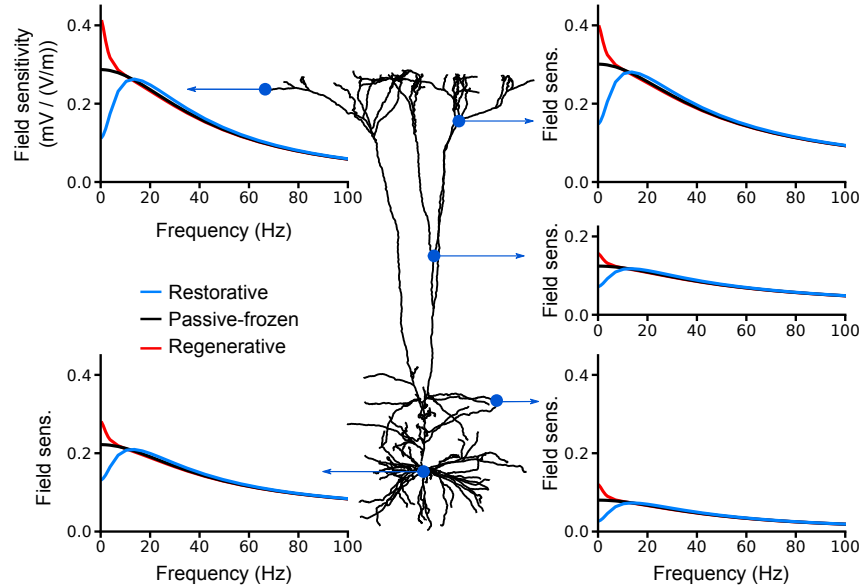


Figure 3.17: The effects of the channel type on the field sensitivity are transposable to other pyramidal cell morphologies, cell 3

We consider a neuron model which includes solely a leak conductance and a single uniformly distributed quasi-active channel (QA). We use the reconstructed morphology corresponding to cell 3 in the Hay et al. (2011) paper. The plots display the sensitivity (in $\text{mV}/(\text{V}/\text{m})$) of the cell to AC fields at different locations in case of restorative (blue, $\mu^* = 2$), passive (black, $\mu^* = 0$) and regenerative (red, $\mu^* = -0.5$) quasi-active currents. Figure and caption adapted from (Aspart et al., 2018, CC BY 4.0)

This resonance being also observed with the passive QA channel, it may have a similar origin as the one observed at some proximal dendrites of the passive cell with the first morphology (Fig 3.2); the non-uniform conductance distribution could play the role of the non-uniform field as in the bent cable.

To summarize, we used in this section the quasi-active approximation to investigate the effects of voltage-dependent channels on the field sensitivity. We first found that, independently on the channel intrinsic dynamics, the field sensitivity at a given location decreases with increasing local conductance (Fig. 3.11). This explains the decrease of field sensitivity at the apical dendrites observed when adding frozen channels to the passive model (Fig. 3.8). Furthermore, the intrinsic channels dynamics alter the cell sensitivity to lower frequency fields. While regenerative currents increase this field sensitivity, restorative ones decrease it, which results in a resonance (Fig. 3.12). The range of affected field frequencies, and therefore the resonance frequency, is determined by the channel activation time constant: the lower the time constant, the wider the range of affected frequencies (Fig. 3.15). All these results are independent of the exact neuron morphology.

In the light of these results, we can explain the effects of I_h on the field sensitivity of the full Hay et al. (2011) model, in case of varying rest membrane potential (Fig. 3.9). Fig. 3.18 displays the parameters of the quasi-active, i.e. linearized, I_h currents as a function of the rest membrane potential V_R . For all considered rest membrane potential, I_h is a restorative current ($\mu^* < 0$). Furthermore, μ^* decreases when the membrane at rest gets more hyperpolarized. Therefore, I_h impacts the sensitivity to low frequency fields more strongly in case of lower rest membrane. (Fig. 3.9). Furthermore the activation time constant τ_w decreases with increasing membrane potential. This results in the shift of resonance frequency towards higher frequencies observed when considering more hyperpolarized rest membrane potential (Fig. 3.9, resonance of the green versus blue curves).

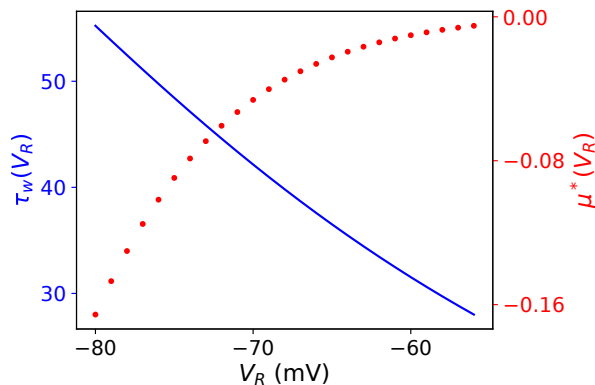


Figure 3.18: I_h is a restorative current whose time constant increases with increasing rest membrane potential

Parameters of the quasi-active approximation of the I_h current depending on the rest membrane potential. The displayed parameters are the QA time constant, τ_w , (blue line) and μ^* (red dots). These parameters are independent on the local conductance distribution of I_h . The QA approximation is derived from the full description of I_h as used in Hay et al. (2011) and Kole et al. (2006).

3.4 Modulation of pyramidal cells spiking activity by weak electric fields

In the beginning of this chapter, we focused on the subthreshold polarization of L5b pyramidal cells due to weak extracellular electric fields. Importantly, we highlighted a resonance in the subthreshold field sensitivity at the apical dendrites which is absent at the soma and basal dendrites.

In this section, we now investigate the modulation of suprathreshold, i.e. spiking, activity of pyramidal cells through weak extracellular fields. In particular, we want to study whether the subthreshold resonance observed at the apical dendrites (Fig. 3.7) translates to a resonance in the modulation of spiking activity.

In the following, we first provide more details about the Hay et al. (2011) pyramidal cell model to better understand to which extent it can be used for further analysis. Then we investigate how weak electric fields can modulate the somatic spiking activity and the firing of calcium spikes in the apical dendrites.

Assessing the pyramidal cell model quality So far, we used the Hay et al. (2011) pyramidal cell model. As mentioned above, the biophysical properties of the model were fitted to reproduce empirical measurements of L5 pyramidal cells (Hay et al., 2011). These properties include the conductance distribution of 10 ionic channels, notably calcium currents. The distributions were adjusted to reproduce (i) the pyramidal cells response to somatic step current injections (Fig. 3.19E), (ii) the back-propagation of action potential (BAP) in the apical tree (Fig. 3.19B) and (iii) the backpropagating action potential-activated calcium (BAC) firing (Fig. 3.19D), as measured *in vitro*.

The response to somatic step current injections were measured for 3 different input current amplitudes: low (0.619 nA), reference (0.793 nA) and high (1.507 nA). Hay et al. chose the reference amplitude as the average amplitude (across 11 pyramidal cells) eliciting a 15Hz spike rate. Low and high amplitudes correspond to respectively 78% and 190% of the reference amplitude. The step input current lasted for 2s (see Table 3.1 for a full list of the stimulation parameters).

The BAC firing corresponds to a burst of action potentials (AP) at the soma in

Step input current at the soma	Low amplitude	0.619 nA
	Reference amplitude	0.793 nA
	High amplitude	1.507 nA
	Duration	2 s
BAP stimulus: brief step current injected at the soma (pulse)	Pulse amplitude	1.9 nA
	Pulse duration	5 ms
BAC stimulus: brief step current injected at the soma (pulse) followed by an EPSP at the distal apical tuft ($620\mu\text{m}$ from the soma)	Pulse amplitude	1.9 nA
	Pulse duration	5 ms
	EPSP amplitude	0.5 nA
	EPSP rise time constant	0.5 ms
	EPSP decay time constant	5 ms
	Delay (ΔT) between somatic pulse and EPSP	5 ms

Table 3.1: Stimuli parameters used to fit the Hay et al. (2011) model

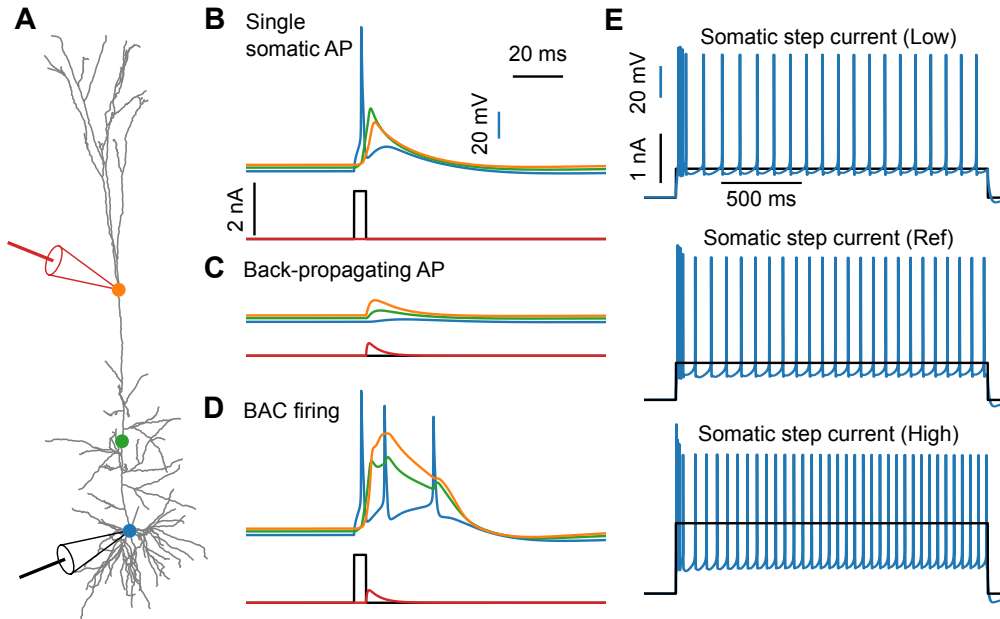


Figure 3.19: The Hay et al. model is fitted to reproduce BAC firing and responses to somatic step current injection as recorded *in vitro*

(A) Location of the current injection (black and red electrodes) and of the recording locations, i.e. at the soma (blue), at $420\mu\text{m}$ (green) and $600\mu\text{m}$ (orange) from the soma. (B,C,D) Cell response to (B) an impulse current at the soma, (C) an EPSP at $600\mu\text{m}$ from the soma and (D) both the somatic impulse and the EPSP with a 5ms delay. (E) Somatic membrane response (blue) to (from top to bottom) low, reference and high DC input currents injected at the soma. The colors of all traces in (B,C,D,E) are matched to the schematic representation in (A). The black traces correspond to the somatic input current and the red traces (if present) to the apical input current, i.e. the EPSP.

response to concurrent somatic current impulse and a synaptic excitatory input at the distal dendrites. When subject to a suprathreshold current impulse at the soma (Fig. 3.19B), pyramidal cells fire an AP at the soma. This AP backpropagates along the apical dendritic tree, increasing the apical membrane potential. If the cell receives a concurrent excitatory post synaptic potential (EPSP) at the apical dendrites (Fig. 3.19D, red trace), a plateau-shaped calcium spike is triggered in the apical dendrites (green and orange traces). This calcium spike, in turn, induces further APs at the soma (blue traces). Note that, the somatic current impulse or the EPSP alone do not induce this calcium spike and the subsequent burst at the soma (Fig. 3.19B and C). In the following, we will refer to the pulse current at the soma followed by an EPSP at the apical dendrites as the BAC stimulus. Similarly, we refer to the sole somatic pulse current as the back-propagating action potential (BAP) stimulus. The BAC and BAP stimuli parameters are listed in Table 3.1.

During the fitting procedure, Hay et al. (2011) characterized the model reproduction performance using a set of features for each kind of stimuli. For instance, in case of somatic step current injections, these features include the neuron spike rate, the latency of the first spike after stimulus onset or measures of the interspike interval (ISI). In case of BAC firing, these features include the ISI at the soma or the calcium spike width and height. In case of BAP stimuli, the features consist of measures of the membrane voltage along the apical dendrites. The full list of features is summarized in Table C.3 (in Appendix C) in case of somatic step input current and in Table C.2 (in Appendix C) for the BAP and BAC stimuli.

Among the BAC features Hay et al. (2011) used to characterize the model, the authors put a particular emphasis on having a burst of exactly 3 action potentials (AP). In fact, all pyramidal cells they recorded fired 3 APs in response to the BAC stimuli. Yet, this hard constraint is not fully achieved by the fitted model the authors provided¹².

During the fitting procedure, the authors applied to their model a BAC stimulus at 295ms after the beginning of the simulation; this results in a burst of 3 APs as required (Fig. 3.20B). Nevertheless, applying a BAC stimulus at a later time (see Fig. 3.20C for a stimulus 2s later), no longer induces a burst of 3 APs but only 2. In brief, the model response depends on the stimulus onset time. This dependence is due to an incorrect initialization in the original Hay et al. (2011) model. Specifically, the internal calcium

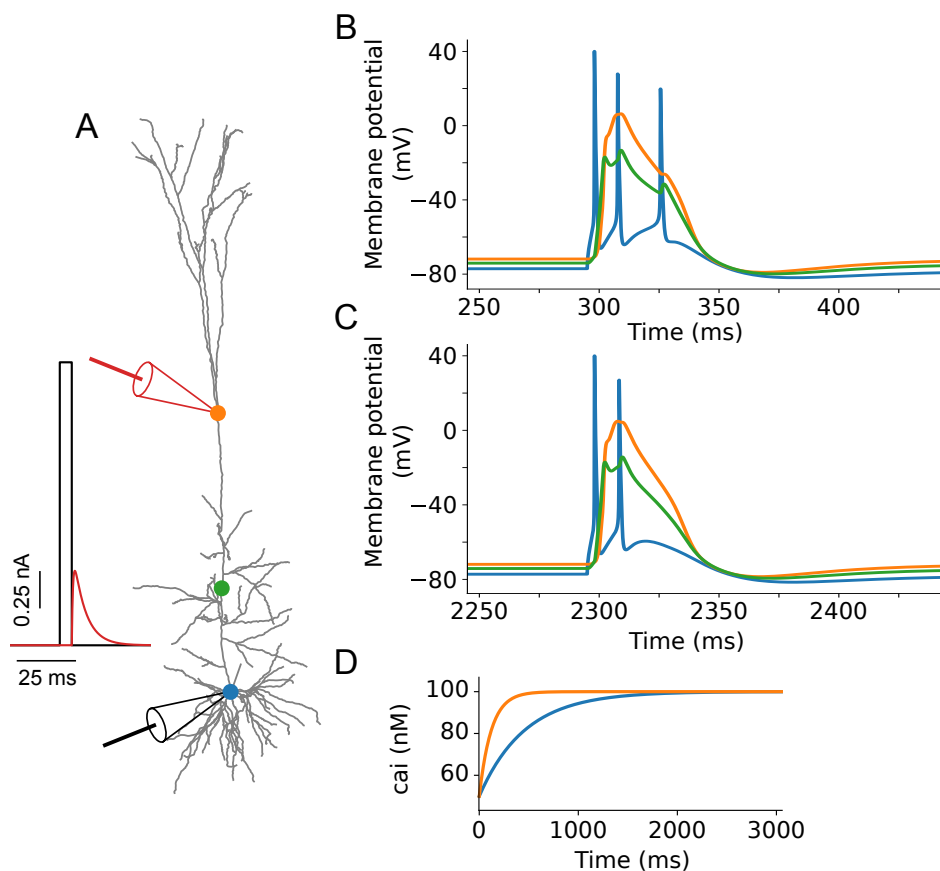


Figure 3.20: Stimulus onset-dependent BAC firing behavior of the Hay et al. model due to non-initialized internal calcium concentration

(A) Schematic of the BAC stimulus applied to the neuron model. A pulse current is applied at the soma, followed by an EPSP-like input current at the apical tuft. The parameters of the stimulation are summarized in Table 3.1. (B) Membrane voltage response of the original Hay et al. model when the BAC stimulus is applied at 295ms. (C) Membrane voltage response of the original Hay et al. model when the BAC stimulus is applied at 2295ms. (D) Internal calcium concentration over time in the absence of BAC stimulus. In all plots, the blue traces correspond to measurement at the soma, the green and orange traces to measurement at the apical dendrites at, respectively, 400 μm and 620 μm from the soma (see locations of blue, green and orange dots in (A)).

¹²Hay et al. (2011) published their model on ModelDB (McDougal et al., 2016), accession number 139653

concentration (namely the variable *cai* from the *Ca_dynamics_E2* NEURON mechanism¹³) is not initialized. This concentration reaches its steady state only after 2s, i.e. later than the stimulus onset time used by Hay et al. (2011) (295ms) (see Fig. 3.20D). This bug in the original Hay et al. model is particularly problematic when comparing the cell response to stimuli occurring at various times, e.g. at various phases of the extracellular AC fields.

To circumvent this issue, we perform an *ad hoc* fix of the model in order to always get 3 APs independently of the BAC stimulus onset time. Specifically, we adjust the minimum internal calcium concentration to obtain a steady state internal calcium concentration equal to the concentration of the original model at 295ms¹⁴. In the following, we refer to this model as the "fixed model" in contrast to the original Hay et al. (2011) model.

We now assess the changes in reproduction accuracy of the model induced by the *ad hoc* fix. We successively simulate (i) the original Hay et al. model in its fitting condition, i.e. not at its steady state, (ii) the original Hay et al. model at its steady state and (iii) the fixed model. We measure the response of the 3 models to all kind of stimuli used for the fitting procedure (cf Fig. 3.19). Fig. 3.21 summarizes the deviations of the feature values obtained with the 3 models from the *in vitro* measurements. Overall, the introduced fix does not drastically reduce the reproduction performance of the model. The fixed model tends to overestimate the spike frequency in response to low and reference step input currents (Fig. 3.21B and C) though. The original model does not perfectly reproduce the features as measured *in vitro*. In fact, these measurements were not reported by Hay et al. (2011) in their original article; the authors simply presented this model as the best performing model.

In the following, we use exclusively the fixed model to investigate the effects of weak extracellular fields on the spiking activity of pyramidal cells. Note that the subthreshold field sensitivities of the original Hay et al. model and of the fixed model do not differ.

Modulation of somatic firing due to extracellular fields We now investigate the modulation of the somatic firing due to extracellular electric fields. We use the fixed pyramidal cell model described above. Except otherwise mentioned, we apply fields of 1 V/m.

To begin with, we consider how DC fields modulate the cell response to step currents of low amplitude injected at the soma. The extracellular field being weak, they do not qualitatively alter the cell response to step currents. The cell first fires 4 to 5 action potentials (AP) in a burst mode before firing further APs more temporally spaced (Fig. 3.22).

In presence of a positive DC field, the APs in the spike train are delayed compared to the no field case (Fig. 3.22). This agrees with the subthreshold modulation: in our convention positive fields hyperpolarize the soma. Furthermore, the intervals between

¹³In the precedent sections, we used a version of the mechanism corrected by Ness et al. (2016) to initialize these concentrations; the reported subthreshold field sensitivities were therefore computed at steady state.

¹⁴We set the *minCai* variable of the *CaDynamics_E2* to 0.737e-4 mM at the soma and 0.955e-4 mM uniformly at the apical dendrite. Obviously, we further initialize the *cai* variable to its steady state with the new *minCai* values.

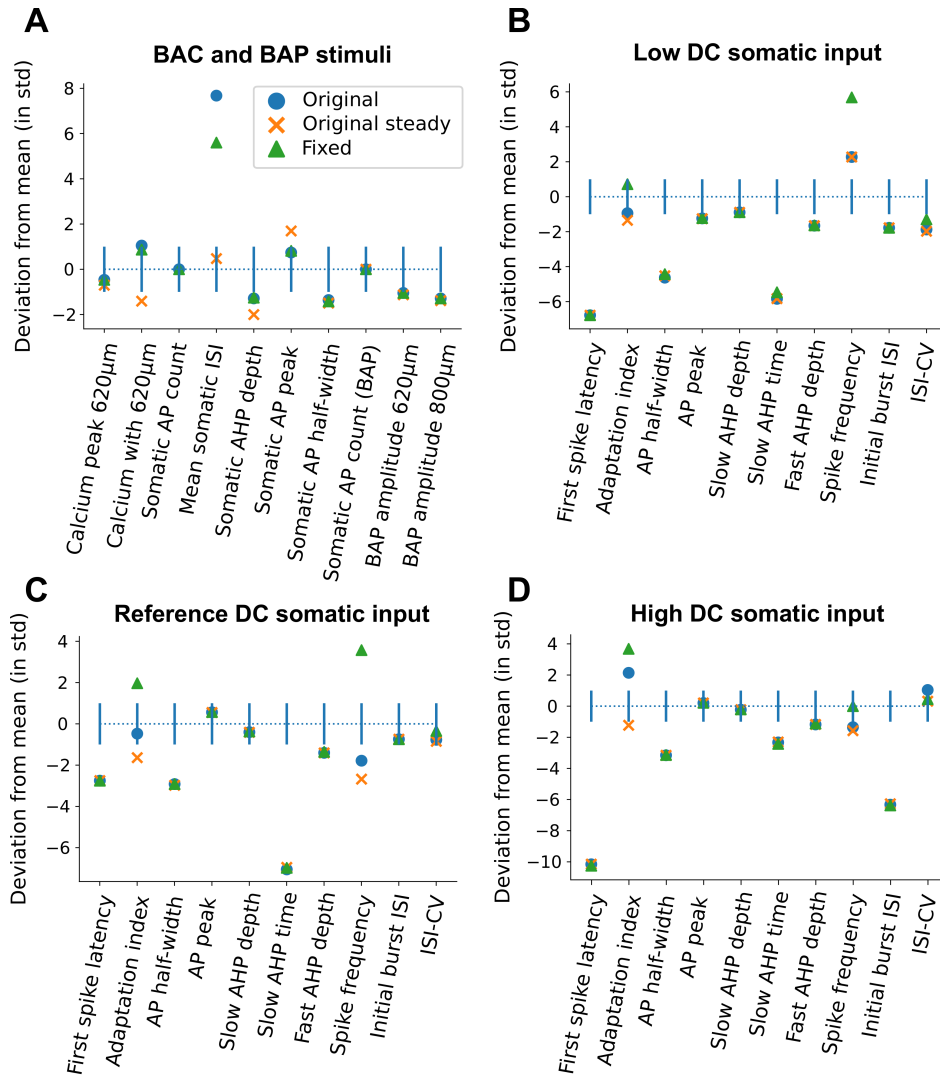


Figure 3.21: Fixing the Hay et al. model does not strongly lower the reproduction accuracy of the original model

The plots display how accurately different pyramidal cell models reproduce the response of cortical pyramidal cells measured *in vitro*. The four plots correspond to the response to different kind of stimuli: to (A) the BAC and BAP stimuli and to step currents of (B) low, (C) reference and (D) high amplitude injected at the soma. The stimulation parameters are listed in Table 3.1. For each stimulus, the reproduction accuracy is quantified through the set of features (x-axis) used for fitting the Hay et al. (2011) model. The models reproduction are plotted in term of deviation from the empirical mean, as measured *in vitro*. The deviations are expressed in empirical standard deviations. The features and the experimental values are listed in Tables C.2 and C.3 in Appendix C. The three compared pyramidal cell models are (blue dot) the original Hay et al. (2011) model in the same condition as during the fitting procedure, (orange cross) the original Hay et al. model at steady state at the stimuli onset and (green triangle) the fixed model, i.e. with an internal calcium concentration initialized to obtain 3 spikes during BAC firing (see text). The AP count in (A) for the original model at steady state would be equal to $-\infty$ and is therefore not displayed here.

two spikes in the steady state (i.e. after the burst) are increased.

Interestingly, in case of a negative field, the first AP after the initial burst is also delayed compared to the "no field" case (see Fig. 3.23, 5th spike in middle plot). At first sight, this delay may seem counterintuitive: negative fields depolarize the soma and should facilitate the trigger of an AP. In fact, zooming in the initial burst, the

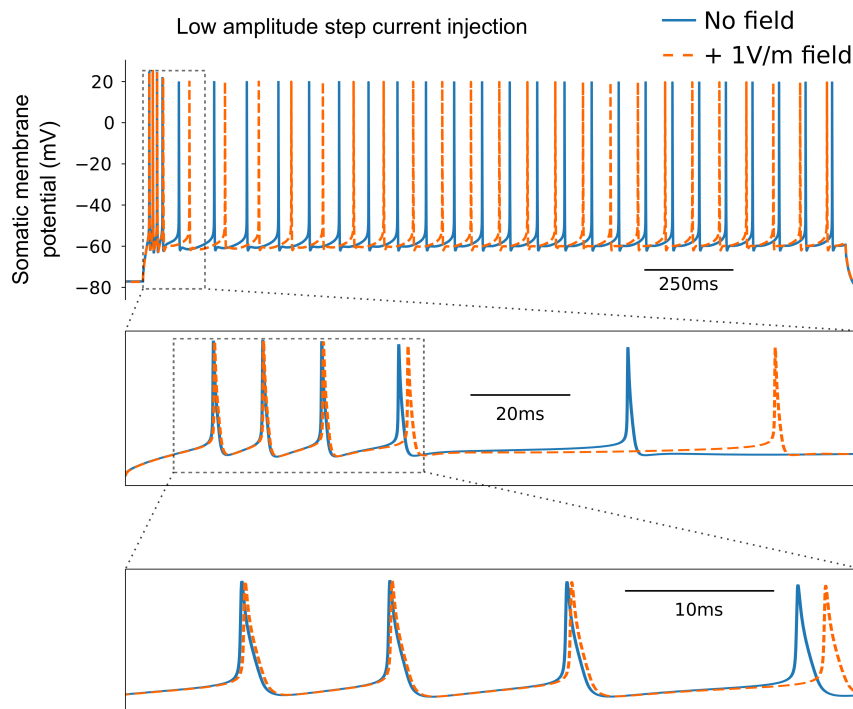


Figure 3.22: Positive electric fields delay the cell response to low amplitude step currents injected at the soma

Somatic membrane response to a low amplitude step current injected at the soma in presence (orange dashed lines) or absence (blue line) of a positive (+1 V/m) extracellular field. The middle and bottom plots are zoomed version of the top one. The stimulation parameters are described in Table 3.1.

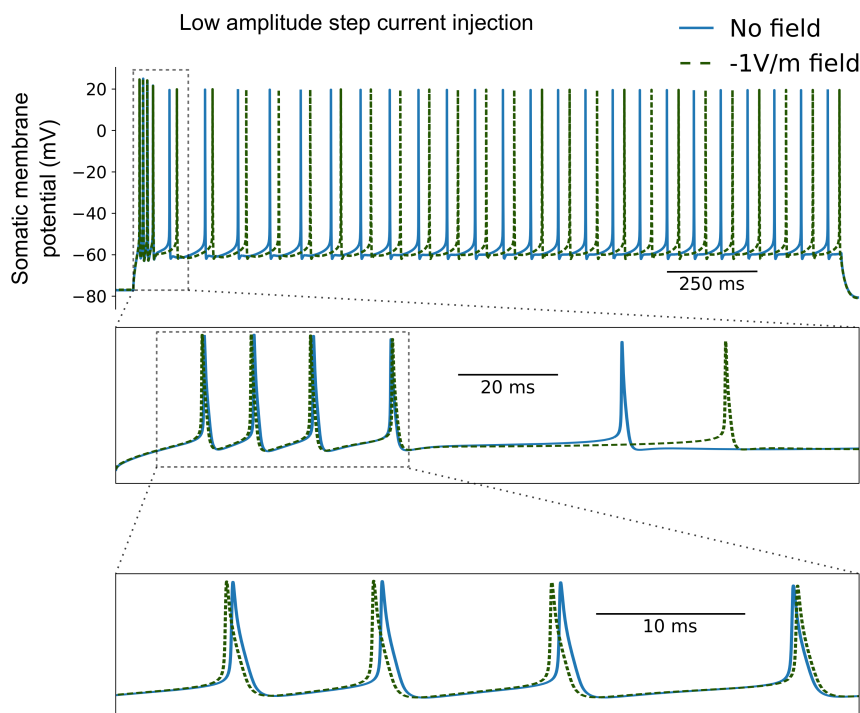


Figure 3.23: Negative electric fields advance the initial spiking response of the cell to low amplitude step currents injected at the soma, resulting in a delayed spike after the initial burst

Somatic membrane response to a low amplitude step current injected at the soma in presence (orange dashed lines) or absence (blue line) of a negative (-1 V/m) extracellular field. The middle and bottom plots are zoomed version of the top one. The stimulation parameters are described in Table 3.1.

negative DC field advances the timing of the first 4 spikes; this advance then induces a delay in the AP after burst, probably due to intrinsic dynamics of the cell.

DC fields have a lower effect on the response to step input current with higher amplitude (Fig. 3.24). Indeed, the change in spike timing between the field and no field case is smaller (compare top plots of Fig. 3.22 and Fig. 3.24A). Importantly, negative fields no longer induce a delay of the first spike after the burst at stimulus onset. Instead negative fields advance this first spike, in agreement with the depolarization of the somatic membrane. In case of a step input of reference amplitude, the results are similar as for the high amplitude step current (not shown).

We further investigate the modulation of the cell response due to time varying fields. As for DC fields, we examine the cell response to a step input current at the soma in presence of an AC field (Fig. 3.25). The modulation can depend on both the field frequency and the field phase at the input stimulus onset. For each frequency, we

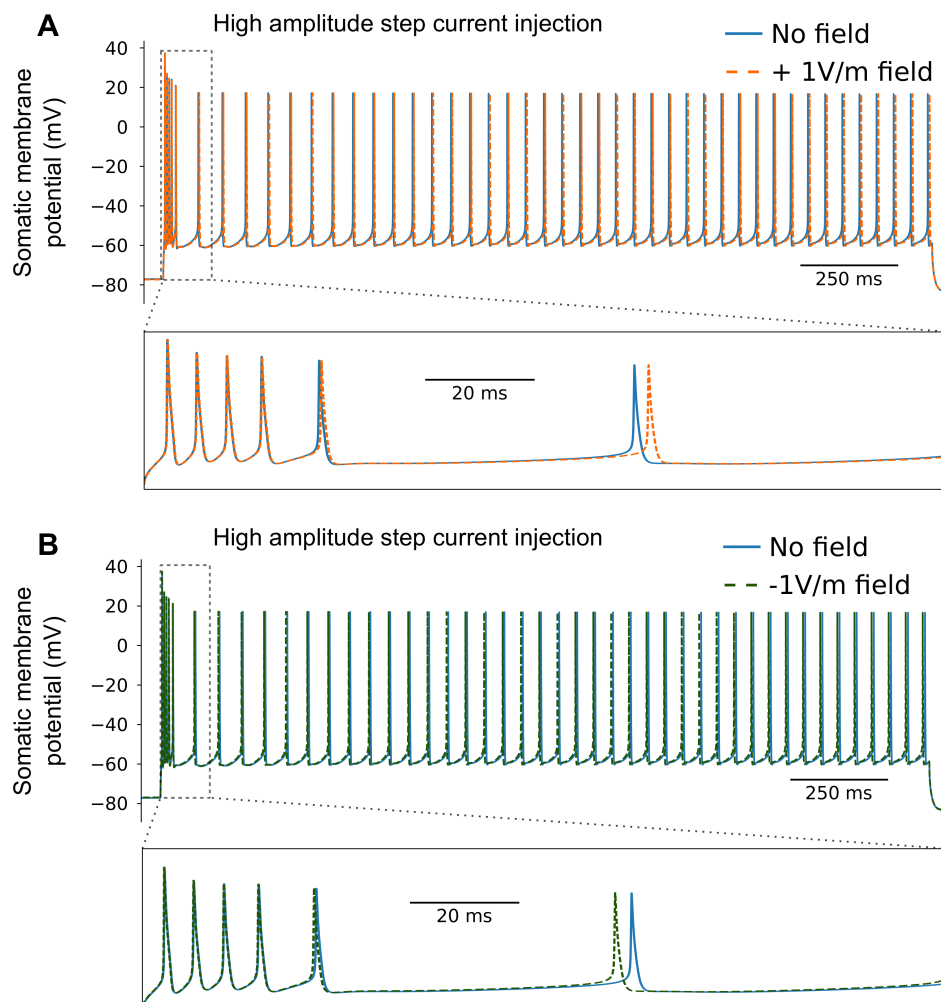


Figure 3.24: In case of a somatic step input current of high amplitude, positive DC fields delay the first spike after the initial burst and negative fields advance it

Somatic membrane response in response to a step current of high amplitude injected at the soma, in absence (solid blue lines) and presence (dashed orange and green lines) of a DC extracellular field. (A) Response in case of a positive DC field (+1 V/m). (B) Response in case of a negative DC field (-1 V/m). The bottom plots in (A) and (B) are zoomed version of the top ones. The stimulation parameters are described in Table 3.1.

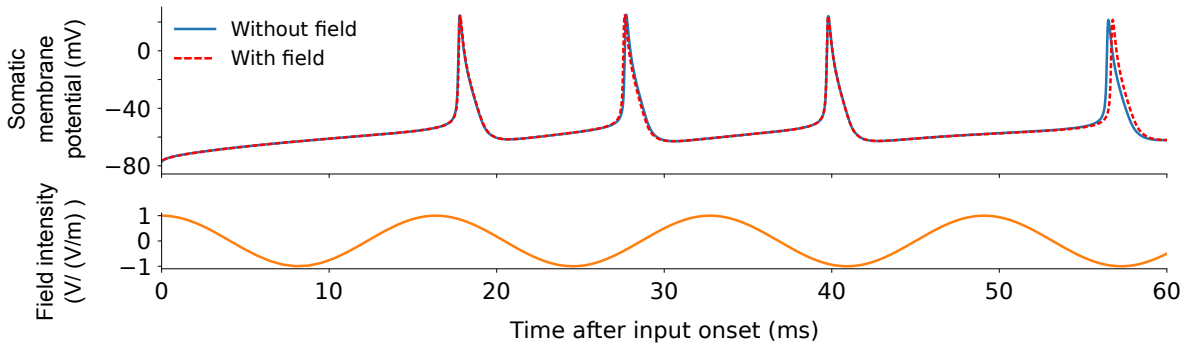


Figure 3.25: The modulation of the first interspike interval after stimulus onset by AC fields is very weak

(Top) Somatic membrane potential in response to a step current of low amplitude injected at the soma in presence (blue solid line) and absence (red dashed line) of an oscillating extracellular electric field. (Bottom) Oscillating intensity of the extracellular field applied to the neuron model. The field parametrization, i.e. frequency and phase at the stimulus onset, is the one inducing the smallest initial interspike interval. The input stimulus parameters are summarized in Table 3.1. The origin of the displayed time ($t = 0\text{ms}$) corresponds to the onset of the somatic step input current.

test 16 different field phases (ranging from 0 to 2π) at the stimulus onset¹⁵.

AC fields modulate the latency of the first spike, i.e. the delay between the stimulus onset and the first spike (Fig. 3.26, left column). The modulation depends on the field frequency and phase and on the amplitude of the step input current. Overall, the amplitude of the modulation, i.e. the maximal and minimal latency over the field phases, decreases with the field frequency. This agrees with the subthreshold field sensitivity at the soma. Furthermore, the modulation of the first spike latency is weaker in case of higher amplitude input currents.

AC fields also modulate the first interspike interval (ISI), i.e. the delay between the first 2 spikes after the stimulus onset (Fig. 3.26, right column). Interestingly, the modulation of the first ISI presents a resonance. The frequency of the resonance depends on the amplitude of the step input current. While the resonance frequency is around 60Hz in case of a low amplitude input current, it becomes higher than 100Hz for high amplitude current. Nevertheless, the modulation is very weak, see for instance the traces corresponding to the lowest first ISI in Fig. 3.25.

Finally, we investigate how weak electric fields modulate the somatic suprathreshold sensitivity to input currents. To this aim, we consider the cell response to a single pulse current (5ms) injected at the soma. Over a given amplitude threshold, this pulse triggers an action potential (AP); below this threshold, no AP is fired (Fig. 3.27 A). DC fields modulate this input current amplitude threshold to fire an AP (Fig. 3.27 B). Consistently with the subthreshold polarization, negative DC fields lower the threshold, making the cell more sensitive to somatic input current. Positive fields increases this threshold. The change in amplitude threshold scales linearly with the field amplitude. Similarly to DC fields, AC fields also modulate the pulse amplitude threshold necessary to trigger an AP (Fig. 3.28). The modulation depends on the field frequency and the phase of the field at the input current onset (Fig. 3.28A). Overall, the threshold modulation decreases with the field frequency. Yet, the modulation presents a slight resonance in the very low field frequencies, as observed in the subthreshold field sen-

¹⁵In practice, the electric field is applied from the beginning of the simulation and we vary the stimulus onset to be triggered at a given phase of the field

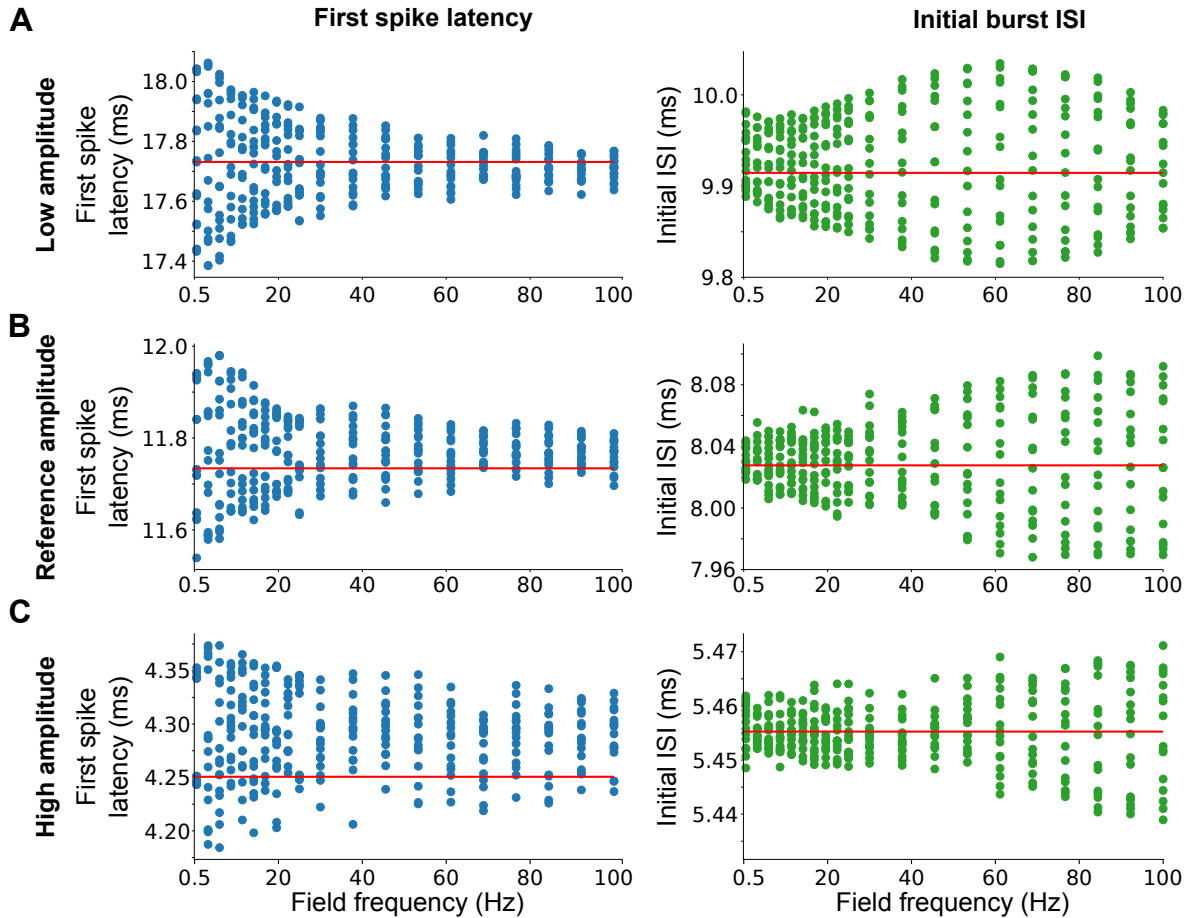


Figure 3.26: Weak AC fields modulate the response to onset of somatic step input currents in a field frequency- and phase-dependent manner

The plots quantify the modulation through weak (1 V/m) AC fields of the cell initial response to step current injected at the soma. Specifically, the plots display the latency of the first spike (left column, blue points) and the interval between the two first spikes (right column, green points) after onset of step current. Each dot represents a field at a given frequency and at a given phase at onset of the somatic stimulus. We consider 16 different field phases ($2\pi n/16, n \in \{0, \dots, 15\}$). The rows correspond to step input currents of different amplitudes, namely (A) low, (B) reference and (C) high amplitudes (see Table 3.1). The red lines correspond to the feature values in the absence of field. All simulations are performed with the fixed pyramidal cell model.

sitivity at the soma (Fig. 3.7B). In fact, the change in AP threshold is related to the somatic polarization due to the field at the pulse onset (Fig. 3.28B). Nonetheless, for a given somatic polarization, the phase of the field at the pulse onset further determines the change in pulse amplitude threshold. Fields in a raising phase (within $[-\pi/2, \pi/2]$) will increase the threshold, while fields in a descending phase ($[\pi/2, 3\pi/2]$) decreases the threshold and facilitate the firing of an action potential. Note that, this phase effects take place for higher frequency fields (i.e. lower somatic polarization). In this case, the field phase will have changed before the AP is actually fired, which may explains this phase effect.

To summarize, we showed that weak extracellular electric fields can modulate the response of pyramidal cells to somatic input currents. For example, electric fields modulate the cell response to step input currents. The field shifts the timing of the

Figure 3.27: DC fields modulate the somatic pulse amplitude threshold to trigger an action potential

(A) Somatic membrane voltage responses (top) to an impulse current injected at the soma (bottom). The response is plotted for two different impulse amplitudes: one suprathreshold (1.9 nA, dashed lines), i.e. triggering an action potential, and one subthreshold (1.3 nA, solid lines). The pulse current lasts 5ms. (B) Minimum pulse amplitude required to trigger an action potential in presence of a DC field, depending on the field amplitude. The minimum pulse amplitude is computed by dichotomy; action potentials are detected using a somatic membrane voltage threshold of 0mV.

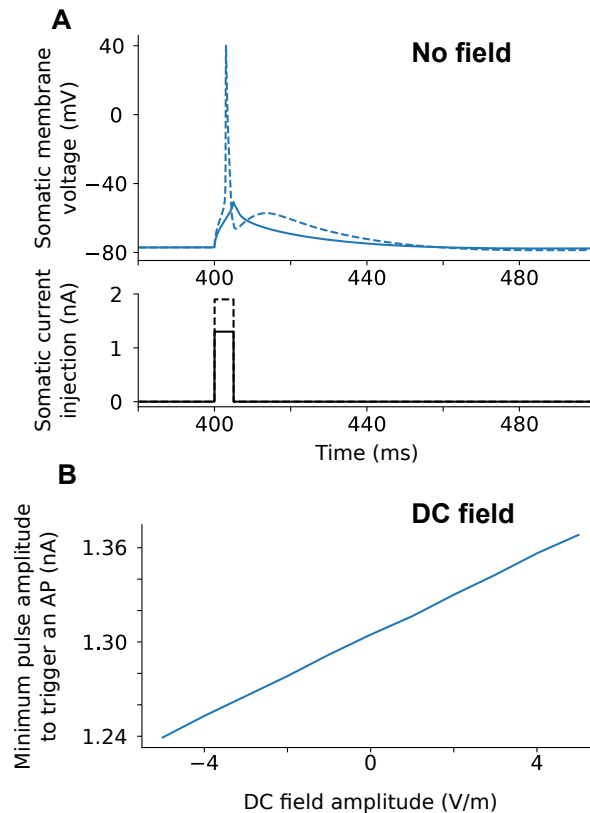
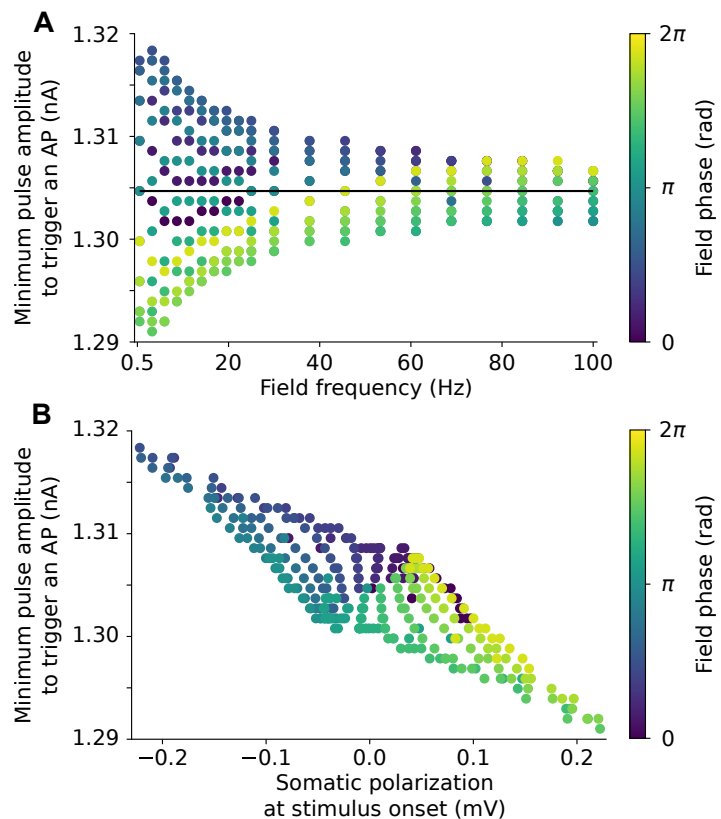


Figure 3.28: The modulation of the somatic pulse amplitude threshold by AC fields depends on the subthreshold somatic polarization and therefore on the field frequency

(A,B) Pulse amplitude threshold, i.e. minimum amplitude of the pulse current injected at the soma, to trigger an action potential, in presence of an AC extracellular field. Each dot corresponds to a field parametrization, i.e. field frequency (x-axis) and phase at the current stimulus onset (color coded). (A) Pulse amplitude threshold as a function of the field frequency. The black line corresponds to the minimal pulse amplitude in the absence of an extracellular field. (B) Pulse amplitude threshold as a function of the somatic polarization at the pulse onset. In both plots, the pulse current lasts 5ms. The amplitude of the AC field is 1V/m. The amplitude thresholds are computed as described in Fig. 3.27.



spikes in the response spike trains. This modulation does not solely depend on the field parameters but also on the input current amplitude. The stronger the step current, the lower the effects of the fields. Weak electric fields also affect the cell sensitivity to pulse

input currents: the fields modulate the input amplitude threshold to trigger an action potential. Importantly, this threshold modulation is consistent with the subthreshold field sensitivity at the soma.

Modulation of BAC firing due to extracellular fields After investigating the impact of weak electric fields on the response of pyramidal cells to somatic input currents, we further consider the modulation of the firing of calcium spikes through weak electric fields. Specifically, we study how electric fields modulate the backpropagating action potential-activated calcium (BAC) firing of the fixed pyramidal cell model. The BAC firing is triggered in response to a somatic pulse input current followed by an EPSP injected at the apical dendrite.

During BAC firing, DC fields mainly modulate the timing of the third action potential in the burst (Fig. 3.29). In agreement with the somatic subthreshold polarization, positive fields delay the firing of the action potentials and negative fields advance it. For strong positive fields, e.g. 5 V/m, the field even inhibits the firing of the third action potential. The time shift of the third action potential depends on the DC field amplitude in a nonlinear manner (Fig. 3.30, green curve).

AC fields can modulate the BAC firing of the pyramidal cell too. In particular, AC fields modulate the backpropagation of action potentials (BAP) along the apical dendrites (Fig. C.16A in Appendix). This modulation depends on the field frequency and phase at the onset of the BAP stimulus (that is an impulse current injected at

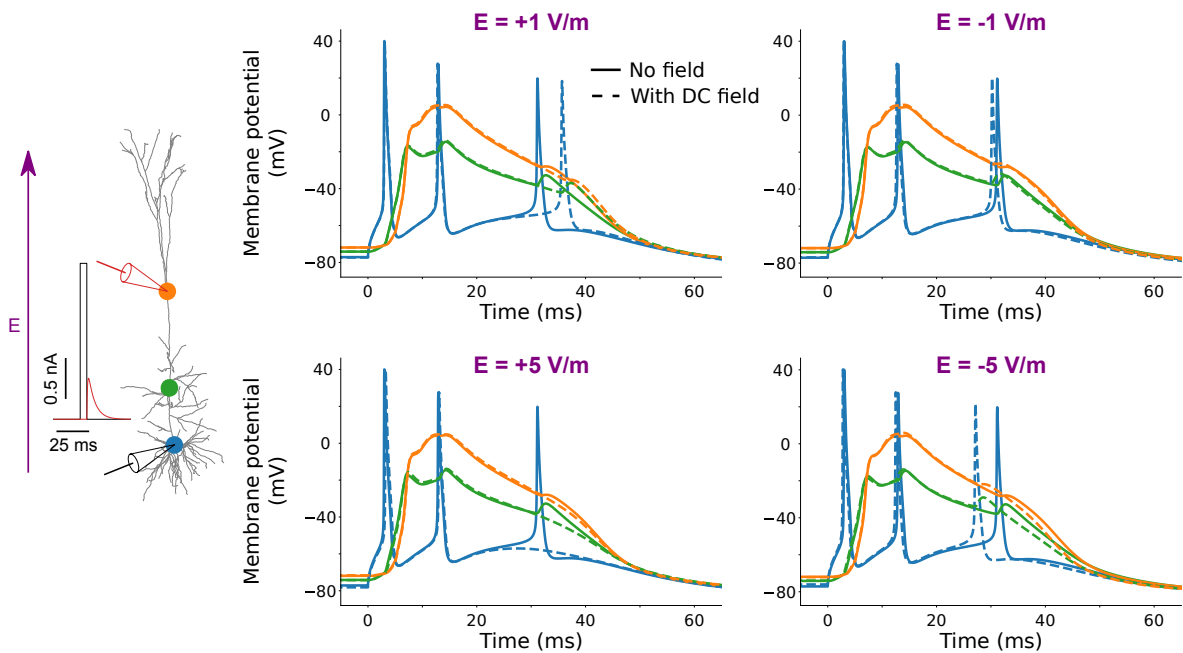
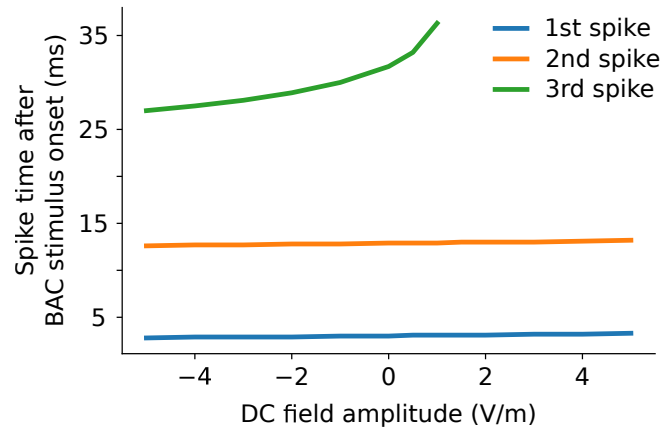


Figure 3.29: DC fields modify the timing of action potentials during BAC firing

All four plots display the membrane potentials at different locations during BAC firing, in presence (solid lines) and absence (dashed lines) of DC fields. The different plots correspond to different field amplitudes (top plots: ± 1 V/m, bottom plots: ± 5 V/m) and different field orientations (left plots: positive fields, right plots: negative fields). The field amplitude is written as title of the 4 different subplots. The membrane voltages are measured at three different locations: soma (blue lines), and at $400\mu\text{m}$ (green lines) and $600\mu\text{m}$ (orange lines) from the soma on the apical dendrites (see colored dots in the schema on the left). The BAC stimulation parameters are summarized in Table 3.1). The simulation were performed with the fixed neuron model.

Figure 3.30: DC fields mainly affect the timing of the last spike during BAC firing

Timing of the 3 action potentials (AP) during BAC firing in presence of a DC field. The AP times are plotted as a function of the field amplitude. The BAC firing was simulated in the fixed neuron model with stimulus parameters defined in Table 3.1 and with a spatially uniform DC field of various amplitude. Note that the third somatic spike disappears for too strong positive fields; consequently the green curve stops where the third AP disappears.



the soma). Interestingly, the strength of the modulation does not decrease with the field frequency. AC fields also modulate the amplitude of calcium spikes during BAC firing (Fig. C.16B in Appendix). Here again, this modulation does not decrease with increasing field frequencies.

More interesting is the modulation of the cell sensitivity to BAC stimulus. In other words, do electric fields modulate the cell ability to detect coincident somatic pulse input current and EPSP at the apical dendrites? For instance, do electric fields alter the minimum EPSP amplitude or the maximal delay between the EPSP and the somatic impulse which triggers BAC firing?

To begin with, we consider the EPSP amplitude required to trigger BAC firing. In brief, we stimulate the cell with the BAC stimulus, i.e a pulse current injected at the soma and an EPSP at the apical dendrite (see Table 3.1), with various EPSP amplitudes. Over a given EPSP amplitude, a calcium spike is triggered (Fig. 3.31A). To determine the EPSP amplitude threshold for BAC firing, we measure the peak membrane voltage at different locations along the apical dendrites for the various EPSP amplitudes. Over a given EPSP amplitude, the peaks of the membrane voltages at distal apical locations, e.g. $620\mu\text{m}$ and $800\mu\text{m}$ from the soma (respectively orange and magenta lines), become higher than at proximal locations, e.g. $400\mu\text{m}$ from the soma (green line)(Fig. 3.31B). In the following, we consider the point where the peaks of the membrane voltages at $400\mu\text{m}$ and $620\mu\text{m}$ cross as the EPSP amplitude threshold to trigger BAC firing. This transition point is affected by the presence of a field (see dashed line in Fig. 3.31B for a positive 5V/m field). In fact, weak DC fields modulate the EPSP amplitude threshold (Fig. 3.31C). While positive fields decrease the EPSP amplitude threshold for BAC firing, negative fields increase it, making the cell less sensitive to the presence of an EPSP concurrent to the action potential. The change in EPSP amplitude threshold scales linearly with the field amplitude.

We further investigate how AC fields modulate the sensitivity of the cell to the EPSP amplitude. In this case, the modulation depends on the field frequency and the phase of the field at the BAC stimulus onset (Fig. 3.32). Interestingly, the strength of the threshold modulation does not decrease with the field frequency. Instead, the modulation presents a resonance around 10-20Hz similar to the precedently observed subthreshold field sensitivity at the apical dendrites. Then the modulation decreases a bit until

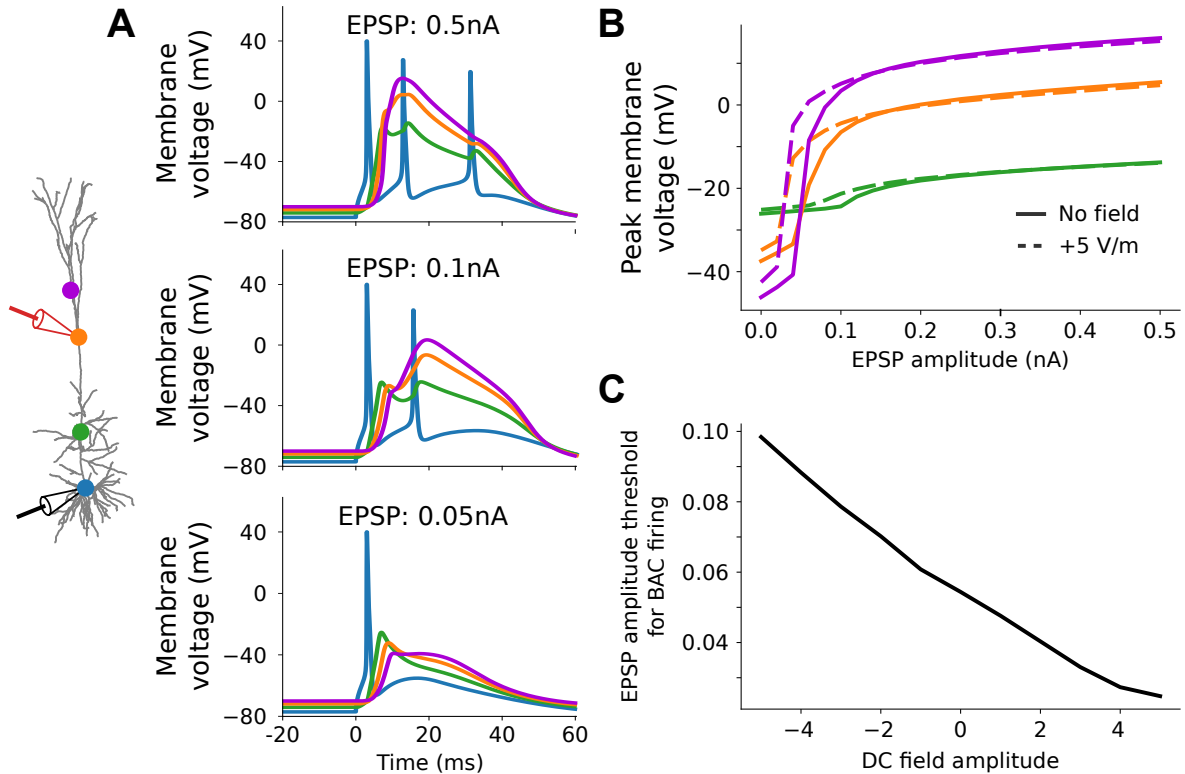


Figure 3.31: Weak DC fields modulate the EPSP amplitude threshold to trigger BAC firing

(A) Example membrane voltage traces in response to a BAC stimulus with various EPSP amplitudes: 0.5nA (top), 0.1nA (middle) and 0.05nA (bottom). (B) Peak membrane voltage in response to BAC stimulus depending on the EPSP amplitude. The peak membrane voltage are displayed in the presence (dashed lines) and in the absence (solid lines) of a 5V/m extracellular field parallel to the somato-dendritic axis. (C) EPSP amplitude threshold, i.e. minimal EPSP amplitude, to trigger BAC firing. The BAC firing is detected if the peak membrane voltage on the apical dendrites is higher at $620\mu\text{m}$ than at $400\mu\text{m}$ from the soma. In (A) and (B), the colors code the different locations of measurement: at the soma (blue) and at the apical dendrite, $400\mu\text{m}$ (green), $620\mu\text{m}$ (orange) and $800\mu\text{m}$ (magenta) from the soma (see dots on the left schema). Besides the varying EPSP amplitude, the parameters of the BAC stimulus are listed in Table 3.1.

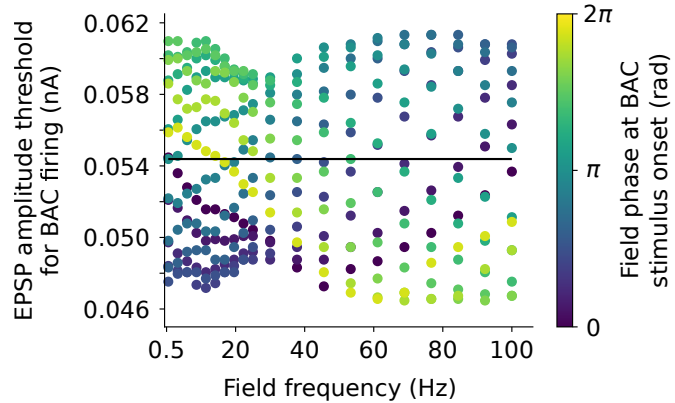
30Hz before increasing again. Note that this last increase over 30Hz cannot be inferred directly from the subthreshold field sensitivity.

In addition to the EPSP amplitude, the delay ΔT between the EPSP and the somatic impulse current influences whether a backpropagating action potential-activated calcium spike (BAC) is fired or not (Fig. 3.33A). The EPSP needs to arrive in a given time window around the somatic pulse current in order to trigger BAC firing. If the EPSP arrives too early before the somatic input current or too late after it, no dendritic calcium spike is triggered. For simplicity, we refer in the following to an EPSP arriving after the somatic stimulus as a positive delay ($\Delta T > 0$), and to an EPSP arriving before the somatic input as a negative delay ($\Delta T < 0$).

We want to determine the maximum (positive) and minimum (negative) delays between both stimuli, which still trigger BAC firing. As for the EPSP amplitude, we measure the peak membrane voltage at different locations along the apical dendrites (Fig. 3.33B). For delays in a given range around 0, the peak membrane voltage is higher at the distal apical dendrites (620 and $800\mu\text{m}$ from the soma, orange and magenta lines) than at proximal locations ($400\mu\text{m}$, green lines); beyond this range, the

Figure 3.32: The modulation of the EPSP amplitude threshold through AC fields does not decrease monotonically with the field frequency

Each dot represents the minimal EPSP amplitude necessary to trigger BAC firing, depending on the field frequency (x-axis) and on the field phase at the BAC stimulus onset (color coded). The black line corresponds to the EPSP amplitude threshold in the absence of an extracellular field. Besides the varying EPSP amplitude, the parameters of the BAC stimulus are listed in Table 3.1.



peak membrane is the strongest at proximal locations. In practice, this range of delays corresponds to delays triggering BAC firing. In other words, this is the time window during which the pyramidal cell model detects a coincidence between the EPSP and the somatic pulse stimuli.

In the following, we consider the points where the curves of the peak membrane potentials at $400\mu\text{m}$ and at $620\mu\text{m}$ cross as the threshold delays to trigger a BAC firing. There are two thresholds: one for negative and one for positive delays. Note that the time window is not symmetric. Indeed, the negative delay threshold is shorter than the positive one.

Consistently with a depolarization of the apical membrane, positive DC fields enlarge this detection time window (Fig. 3.33B dashed lines). In other words, positive fields decrease the temporal precision for the coincidence detection: they decrease the negative delay threshold and increase the positive threshold (Fig. 3.33C). Negative DC fields induce the opposite effects. Overall, the shift in delay threshold scales with the field amplitude. Unexpectedly, fields between 1.5 and 3V/m have the same negative delay threshold for BAC firing. It is noteworthy that, compared to the negative delay threshold, the positive delay threshold is much more affected by the fields.

We then look at the modulation of the delay thresholds through AC fields depending on the field frequency and phase at the somatic stimulus onset. Interestingly, the modulations of the negative and positive delay thresholds do not present the same dependence on the field frequency (Fig. 3.34). The modulation of the negative delay threshold reaches its peak for fields with frequency in the 10-20Hz range (Fig. 3.34A), it then decreases monotonically with field frequencies higher than 20Hz. Moreover, the modulation at the resonance frequency is not symmetric around the "no field" case (red line). Indeed, for field with frequency in the 10-20Hz range, the maximal increase of the negative delay is weaker than the maximal decrease of this delay.

The modulation of the positive delay threshold also displays a resonance in the 10-20Hz range (Fig. 3.34B). The modulation strength then decreases until 30Hz before increasing again in the 40Hz range. This increase of the modulation in the high frequency cannot be directly inferred from the subthreshold field sensitivity. The modulation of the positive delay threshold is not symmetric either. Consistently with the negative delay, AC fields tend to more strongly increase the positive delay threshold. Note that, the field phases which enlarge the negative delay also enlarge the positive delay.

To summarize, we have shown that weak extracellular fields can modulate the

firing of backpropagating action potential-activated calcium spikes (BAC) by cortical pyramidal cells. For example, the fields can alter the timing of the action potentials in the BAC burst or the amplitude of the back-propagating action potential. Moreover, the fields can alter the sensitivity of the cell to the BAC stimulus (a somatic impulse input current concurrent with an EPSP at the apical dendrite). Indeed, the field can modulate the EPSP amplitude thresholds or the delay threshold (between the somatic stimulus and the EPSP) to trigger the BAC firing.

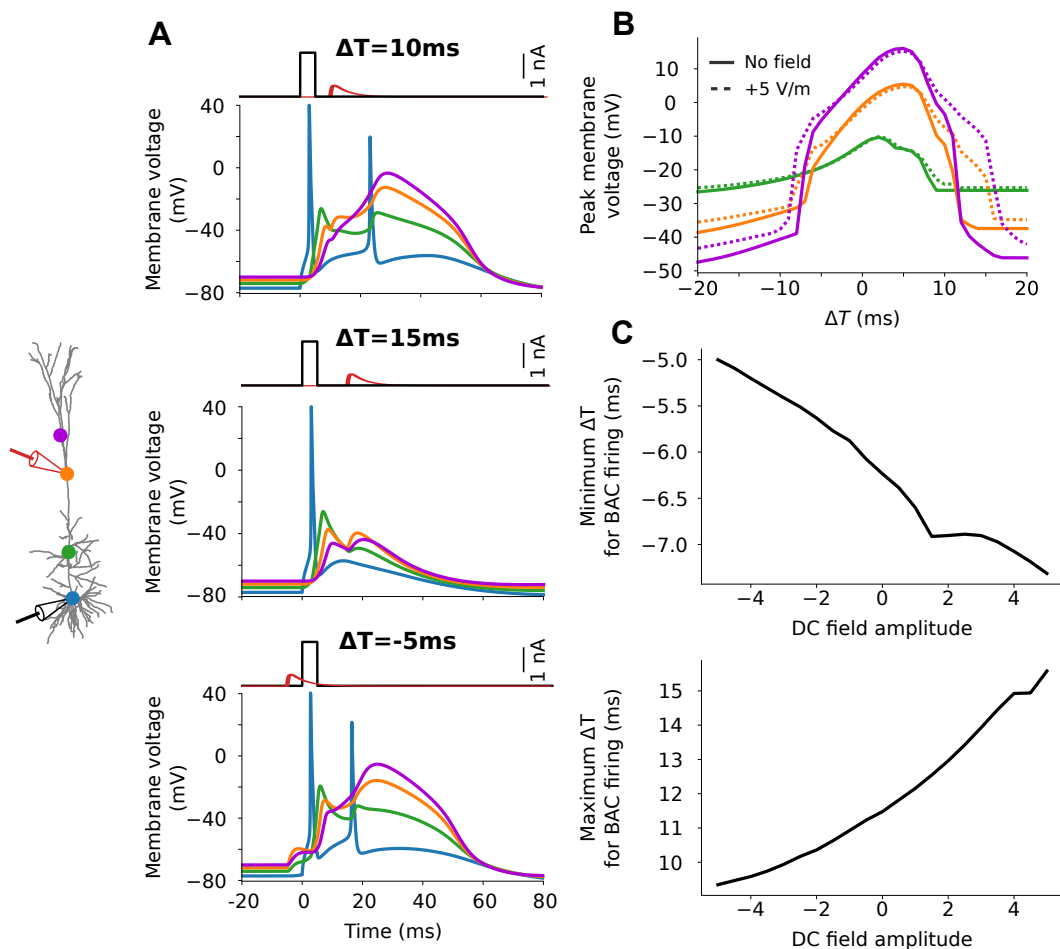
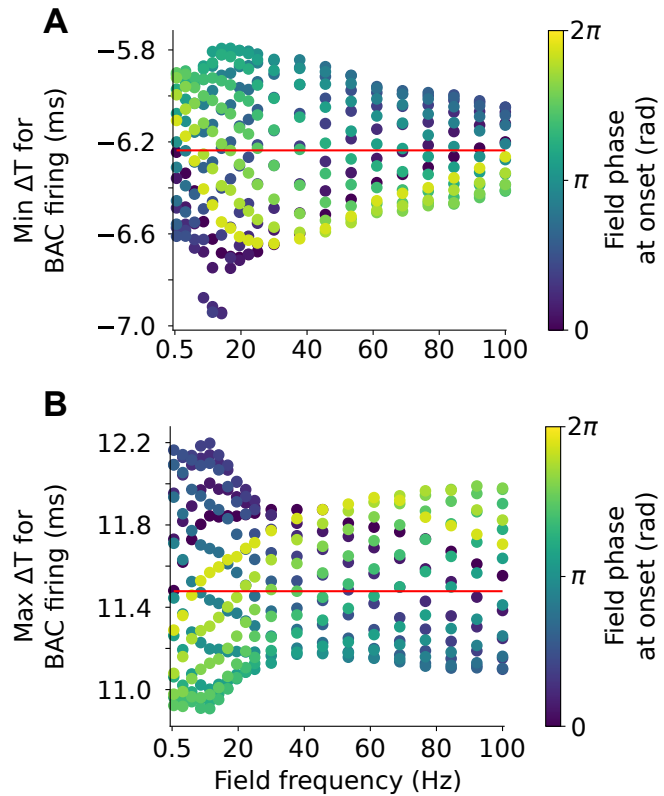


Figure 3.33: Weak DC fields modulate the temporal precision for detecting coincidence between action potentials and afferent EPSPs

(A) Example membrane voltage traces in response to the BAC stimulus for various delay between the somatic input current and the EPSP: 10ms (top), 15ms (middle) and -5ms (bottom). Positive delay corresponds to an EPSP arriving after the somatic impulse. (B) Peak membrane voltage in response to BAC stimulus depending on the delay between the two stimuli. The peak membrane voltage are displayed in presence (dashed lines) and in absence (solid lines) of a 5V/m extracellular field parallel to the somato-dendritic axis. (C) Threshold delays between the stimuli to trigger BAC firing. The thresholds are given for (top) negative delays, i.e. minimum ΔT , and for (bottom) positive delays, i.e. maximum ΔT . The BAC firing is detected if the peak membrane voltage on the apical dendrites is higher at $620\mu\text{m}$ than at $400\mu\text{m}$ from the soma. In (A) and (B), the colors code the different locations of measurement: at the soma (blue) and at the apical dendrite, $400\mu\text{m}$ (green), $620\mu\text{m}$ (orange) and $800\mu\text{m}$ (magenta) from the soma (see dots on the left schema). Besides the varying EPSP amplitude, the parameters of the BAC stimulus are listed in Table 3.1.

Figure 3.34: Weak AC fields modulate the temporal precision for detecting BAC stimuli in a field frequency-dependent manner

Modulation through AC fields of the delay thresholds between BAC stimuli, i.e. between the somatic pulse current and the EPSP, which still triggers BAC firing. (A) corresponds to the minimal, e.g. negative, delay and (B) to the maximal, e.g. positive delay. In (A) and (B), each dot represents the longer delay which still triggers BAC firing, depending on the field frequency (x-axis) and on the field phase at the BAC stimulus onset (color coded). The red line corresponds to the delay threshold in the absence of an extracellular electric field. Besides the varying delay between the stimuli, the parameters of the BAC stimulus are listed in Table 3.1.



3.5 Discussion

In the present chapter, we investigated the effects of weak extracellular electric fields on the activity of cortical pyramidal neurons. We considered solely electric fields parallel to the somato-dendritic axis. To begin with, we assessed the field sensitivity of pyramidal neurons, that is their subthreshold frequency-dependent sensitivity to weak electric fields. Importantly, we found a strong frequency resonance in the field sensitivity of the apical dendrites. This resonance, located in the 10-20 Hz range, was absent at the basal dendrites and at the soma. We explained this differential frequency-dependence of the field sensitivity through the intrinsic properties of the cell. Specifically, we attributed this spatial profile of the field sensitivity to the interplay between the morphology and the active properties of the pyramidal cells. While the presence of numerous basal dendrites increased the field sensitivity at the apical dendrites, the presence of active channels, notably the h-type current, decreased the apical sensitivity to low frequency fields. Furthermore, we thoroughly analyzed the mechanism behind the observed resonance. We therefore provided a better understanding of the relative role of a pyramidal cell membrane properties and morphology on its sensitivity to weak electric fields. Finally, we illustrated how weak extracellular fields may modulate the suprathreshold neural activity of the pyramidal cells, e.g.. their firing of somatic action potentials and dendritic calcium spikes. Below, we further detail our findings and relate them to previous studies.

Impact of the morphology We first considered a passive pyramidal cell model, i.e. with all active conductances removed. In agreement with previous studies (Bikson et al., 2004; Radman et al., 2009), this model exhibited, in presence of spatially uniform fields,

an opposite polarization in the apical dendrites compared to the soma and basal dendrites. At most locations, the field sensitivity of this passive model decreased monotonically with the field frequency. Deans et al. (2007) measured, *in vitro* a similar frequency-dependent field sensitivity profile at the soma (Deans et al., 2007); this field sensitivity profile may therefore be explained by a purely passive effect.

Importantly, the sensitivity of the passive cell model to low frequency fields was not symmetrical. The apical dendrites were more sensitive to low frequency fields than the basal dendrites and the soma were. We attributed this asymmetry to the presence of numerous dendrites radial from (or close to) the soma, namely the basal and oblique dendrites. These branches acted as a local shunt, lowering the field sensitivity close to their branching points (see Fig. 3.5). This shunting effect agrees with a study of Monai et al. (2010). Analyzing mathematically a single cable with a shunt at one end, Monai et al. showed that the shunt broke the symmetry of the field sensitivity. In addition, the authors observed a resonance in the field sensitivity close to the shunted endpoint; this resonance is similar to the one we reported at the soma in a simplified model (see Fig. 3.6) and in the reconstructed cell (see Fig 3.1). We further showed In the reconstructed cell that the effects of the shunt were not restricted to the branching point, i.e. the soma, instead the shunt lowered the field sensitivity of the oblique and basal dendrites too.

Surprisingly, the field sensitivity at some oblique and basal branches exhibited a frequency resonance. We observed this resonance for branches pointing in the apical direction. Due to its relatively small amplitude, this resonance would probably have only a limited effect on the cell response to tACS. However, similar resonances could possibly occur at different locations in presence of spatially non-uniform fields, e.g. endogeneous fields.

We considered a simpler model to explain this passive resonance at the proximal dendrites. Using Fourier transforms and the Green’s function (that is, the impulse response function), we derived analytically the polarization of a passive cable subject to time-dependent and spatially non-uniform fields (see also Anastassiou et al., 2010). To begin with, we exposed how the sensitivity of a straight cable depended on the cable length and on the field frequency (see Fig. 3.3; see also (Malik, 2011)); we explained these dependence using the generalized frequency-dependent space constant, $\lambda_{gen}(f_t)$ (Eq. 3.3). This generalized space constant further accounted for the frequency resonance in the field sensitivity of passive cables with an acute bending angle (see Fig. 3.4). In that case, the bending resulted in a change in the field orientation experienced locally by the cable. This change in effective field orientation strongly reduced the sensitivity to DC fields; the sensitivity to alternating fields with high frequency, i.e. associated to a shorter generalized space constant, depended mostly on the local effective field orientation. Importantly, similar effects may take place in presence of spatially non-uniform fields. Indeed, these effects could potentially explain the “passive resonance” Malik (2011) observed in the sensitivity of a straight cable to a field generated by a point source.

The presence of dendritic spines alters the membrane surface area and can therefore modulate the field sensitivity. The membrane properties of the Hay et al. (2011) model already accounts for the presence of dendritic spines. In brief, the membrane surface area was increased by 100% at the apical and basal dendrites (Sterratt et al., 2011). In general, increasing the membrane surface results in a reduced field sensitivity (see

Fig. C.14 in Appendix for an example in case of a DC field). While a further uniform increase of the cell surface does not affect the asymmetry in the field sensitivity, a non-uniform distribution of spines could potentially affect the spatial shape of the field sensitivity.

Impact of the active currents After the passive case, we studied the polarization of a pyramidal cell neuron model with voltage-dependent ion channels. In agreement with *in vitro* recordings (Bikson et al., 2004; Deans et al., 2007), the polarization amplitude of this neuron model scaled linearly with the field amplitude. Also in accordance with *in vitro* measurements in CA1 pyramidal cells (Bikson et al., 2004), our active model displayed a stronger sensitivity to DC fields at the soma and basal dendrites than in the apical dendrites. The polarization at the apical dendrites exhibited a strong overshoot at the DC field onset, still in accordance with Bikson et al. (2004) measurements. We observed a slight resonance (around 5Hz) in the somatic sensitivity to AC fields; this resonance cannot be confirmed or challenged in hands of published *in vitro* data (see Fig. 10 in Deans et al., 2007). Importantly, the field sensitivity of our model displayed a strong resonance in the 10-20 Hz range at apical dendrites. No experimental studies have, to our knowledge, investigated the sensitivity of the dendritic tree to weak AC fields; this resonance at the apical dendrites cannot be confirmed or excluded by electrophysiology data yet. Nonetheless, we explained this resonance by the presence of the I_h channel, whose conductance were distributed in the model according to *in vitro* measurements (Kole et al., 2006; Nevian et al., 2007). The presence of h-type current in pyramidal cell has been long known to induce resonances in the impedance profile, i.e. in the subthreshold membrane response to injected current (Hutcheon and Yarom, 2000; Ulrich, 2002; Narayanan and Johnston, 2008; Kalmbach et al., 2013; Dembrow et al., 2010). Nevertheless, the field sensitivity cannot be easily inferred from the membrane impedance (see Fig. 6 in Monai et al., 2010, for an explicit demonstration of the difference between impedance and field sensitivity). During the last writing stage of our manuscript (Aspart et al., 2018), Toloza et al. (2017) reported, using computational models, a similar resonance due to I_h in the field sensitivity of pyramidal cells.

To systematically study the effects of active properties on the field sensitivity, we next used a simplified model of voltage-dependent ion channels: the quasi-active approximation (Koch, 1984; Remme and Rinzel, 2011). Given the low amplitude of the considered field and of the resulting membrane polarization, this linear approximation was particularly well suited for our purposes. Under the quasi-active approximation, voltage-dependent currents can be divided in two classes: regenerative and restorative currents. The restorative currents provide negative feedback to slow voltage fluctuations and, hence, reduce the sensitivity to low frequency fields. In practice, this reduction induced a frequency resonance as observed with the I_h channel; I_h is indeed a restorative current. Oppositely, regenerative currents (e.g., a persistent sodium current) amplified the sensitivity to low-frequency fields without leading to resonances. This effect of the channel type remained qualitatively the same with other pyramidal cell morphologies (see Fig. 3.16 and Fig. 3.17 for example).

The amplitude of the channel effects on the field sensitivity depended on the density of the active conductance (relative to other currents) and on the channel activation function at rest. The cutoff frequency, and therefore the resonance frequency in case of

restorative currents, were determined by the channel activation time constant at rest. Using these relationships, we explained the variation of field sensitivity at rest through the variation of the I_h properties at rest.

Effect of the polarization on spiking activity After focusing on the subthreshold membrane polarization resulting from extracellular fields, we illustrated how this subthreshold polarization can modulate the neuron suprathreshold response to input currents. To this end, we first had to fix the Hay et al. (2011) neuron model without actually refitting it on experimental data. The ensuing explorations should therefore be taken as a proof-of-concept rather than accurate predictions of the modulation due to weak electric fields of pyramidal cells suprathreshold responses.

We showed that weak extracellular fields could modulate the cell response to step current inputs injected at the soma. In accordance with Radman et al. (2007), we found that the fields shifted the timing of single spikes in the spike train response. The exact modulation depended on the step current amplitude: the stronger the current, the lower the modulation. Counterintuitively, in case of low amplitude step currents, both DC fields directions induced a delay of the first spike after the initial burst (see Fig. 3.22 and Fig. 3.23). This effect illustrates the importance of the cell intrinsic dynamics in their response to electric fields. AC fields further modulated the cell sensitivity to impulse currents. Depending on their phase at the pulse onset, AC fields lowered or increased the pulse amplitude threshold to trigger an action potential. This modulation of threshold displayed the same frequency profile as the subthreshold field sensitivity at the soma.

The strong frequency resonance we found in the subthreshold field sensitivity was exclusively present in the apical dendrites. Hence, questions remained: can this subthreshold polarization of the apical dendrites modulate the output spiking activity? Does the subthreshold resonance translate into the suprathreshold modulation? In fact, most of the modelling and experimental studies followed the “somatic doctrine” (Bikson et al., 2012b): these studies solely considered the impact of the somatic polarization on neural output activity (see Reato et al., 2013, for a review).

Recent studies observed, *in vitro*, a modulation of synaptic efficacy through the polarization of dendritic endings (Rahman et al., 2013, 2017; Lafon et al., 2017). The reported modulation was very subtle ($\pm 1.17\%$ of EPSP amplitude change per $\text{V}\cdot\text{m}^{-1}$). Nevertheless, each neuron being subject to the same field, the modulation could be amplified at the network scale. Additionally, using CA1 rat hippocampal slices, Kronberg et al. (2017) highlighted a modulation of plasticity, specifically long term potentiation (LTP) and depression (LTD), at Schaffer collaterals by weak DC fields. Whether the fields reduced or enhanced the plasticity depended on the synapse location and on the fields orientation. Note that, these studies were limited to DC fields; given our results on the subthreshold field sensitivity, AC fields at the resonance frequency may achieve stronger modulations.

The dendritic arbor is the locus of non-linear events such as NMDA, calcium and sodium spikes (Major et al., 2013; Moore et al., 2017). These events greatly increase the importance of distal dendritic inputs compared to proximal inputs. Interestingly, these events present a voltage-dependent threshold, which could be modulated by the polarization due to the field. In fact, we showed that weak extracellular electric fields could modulate the firing of backpropagating action potential-activated calcium spikes

(BAC). This BAC firing, generated exclusively in the apical dendrite, is crucial for the integration of feedback inputs from higher level cortical areas (Larkum, 2012). Therefore, weak electric fields may be able to interfere with the integration of these feedback inputs.

In particular we showed that weak fields modulated both the EPSP amplitude threshold and the time window during which an EPSP can trigger the BAC firing. In agreement with the subthreshold polarization, DC fields had opposite effects on the threshold for somatic spikes than on the threshold for BAC firing. While positive DC fields increased the threshold for somatic action potentials, they facilitated the BAC firing, and vice-versa (see Fig. 3.27B and Fig. 3.31C). This could be of interest when trying to modulate the balance between feedforward and feedback inputs, which arrive respectively at the basal and apical dendrites (Larkum, 2012). Interestingly, unlike the subthreshold field sensitivity, the modulation of the threshold for BAC firing by AC fields did not decrease monotonously with the field frequency. This suggests the presence of some temporal effects which require further investigation.

Note that, while we considered only the BAC firing, the firing of dendritic NMDA and Sodium spikes may be similarly modulated by the weak electric fields. This would increase the importance of the dendritic arbor polarization in response to the field.

To conclude, the modelling work presented in this chapter provides a better understanding on the sensitivity of cortical pyramidal cells to weak extracellular fields. In particular, we highlighted the relative role of a cell morphology and active membrane properties on its frequency-dependent sensitivity to subthreshold electric fields. Importantly, we predicted a strong resonance in the sensitivity of apical dendrites to AC fields. We further illustrated how weak extracellular fields could modulate the suprathreshold activity, e.g. the firing of somatic action potentials and dendritic calcium spikes, of cortical pyramidal cells.

Chapter 4

Conclusion

In this thesis, I investigated the response of single cells to weak electric fields as induced by tCS.

First, I concentrated on the somatic doctrine using a spatially extended canonical model: the ball-and-stick model (Chapter 2). Specifically, I investigated the effects of the somatic polarization, induced by sinusoidal weak electric fields, on the cell activity. Interestingly, I identified a resonance in the modulation of spike rate due to sinusoidal fields which was absent in the subthreshold field sensitivity at the soma. Based on this canonical model, I derived an extension of point neuron models which accounted for different locations of input currents and for the somatic polarization due to the field. The extended model successfully reproduced the dynamics of the canonical model while being computationally efficient to simulate.

In the next step, following the dendritic doctrine, I extended my focus from the somatic polarization to the polarization of the whole dendritic tree in response to electric fields. In particular, I studied the field sensitivity of L5 cortical pyramidal cells, using a biophysical model with reconstructed morphology. I found the frequency-dependence of the field sensitivity to differ at the basal and apical dendrites. Importantly, I explained this difference through intrinsic pyramidal cell properties, that is their morphology and the distribution of ion channels. Finally, I illustrated how the subthreshold polarization of pyramidal cells may induce a change in spiking neural activity.

Based on these results, future research may take two directions. On one hand, the effects of weak fields on large neuron populations still need to be investigated. This would be an important step in understanding how tCS modulates neural activity. In fact, the investigation of the population response to the field is already the subject of ongoing works, based on the model extension presented here (Cakan et al., 2017; Ladenbauer and Obermayer, 2018, see Section 2.5 for more details). On the other hand, how weak extracellular fields modulate the spike response of single pyramidal cell is still not fully understood. For example, the same modelling approach as in chapter 3 could be used to investigate the impacts of the field-induced subthreshold polarization on the synaptic integration or on the triggering of dendritic spikes.

Overall, the modelling work I presented provides an improved understanding on the mechanisms underlying the modulation of neural activity through weak extracellular electric fields. I focused solely on spatially uniform fields, as induced by tCS. Nonetheless, my approach could easily be extended to spatially non-uniform extracellular fields, e.g. endogenous fields, to study ephaptic coupling or invasive electric stimulation.

Importantly, my results predict resonances in the cell response to weak extracellular fields. These modelling predictions still require to be confirmed experimentally, which could be achieved *in vitro* using the experimental setup developed in earlier studies (Bikson et al., 2004; Deans et al., 2007; Radman et al., 2007, 2009; Reato et al., 2010). Nevertheless, the resonances I exhibited in this thesis suggest that the response of single neurons to extracellular fields might not decrease monotonically with increasing field frequencies, unlike previously hypothesized (see Reato et al., 2013, for a review). In this respect, this thesis adds substantially to our understanding of the effects of weak electric fields on neural activity and provides insight towards improving the design of tCS protocols.

Appendix A

Cable equation subject to an electric field: derivation and solutions

In this appendix, we first present the derivation of the cable equation in presence of an extracellular field, and of the boundary conditions for a sealed end (for simple passive cables) and a lumped soma (for the ball-and-stick model) (Section A.1). We then solve the cable equation for the ball-and-stick neuron model in presence of a spatially uniform electric field (Section A.2). Finally, we solve the cable equation for a simple passive cable model (with sealed end) in presence of a spatially non-uniform electric field (Section A.3).

A.1 Derivation of the equation for passive cables subject to an extracellular electric field

A.1.1 Cable equation

We derive in this section the cable equation subject to the field as expressed by Roth and Bassar (1990).

We consider a passive straight cable of length l (mm) and of cable radius r (mm). The cable is subject to an extracellular electric field, $E(x, t)$, defined as the spatial derivative of the extracellular potential, $v_e(x, t)$, along the cable axis x :

$$E(x, t) = -\frac{\partial v_e}{\partial x}(x, t) \quad (\text{A.1})$$

We note c (F.mm²), ρ_i (S/mm) and ρ_m (S/mm²) the specific membrane capacitance, the axial conductance and the membrane conductance of the cable. We assume these values to be uniform along the cable. We further define the membrane capacitance per unit length $c_m = 2\pi r c$ (F/mm), as well as the internal (axial) and membrane conductances per unit length respectively $g_m = 2\pi r \rho_m$ (S/mm) and $g_i = \rho_i \pi r^2$ (S.mm). These variables are depicted in Fig. A.1. The membrane potential, $v(x, t)$, is defined as the difference between the intracellular (v_i) and extracellular (v_e) potentials:

$$v(x, t) = v_i(x, t) - v_e(x, t) \quad (\text{A.2})$$

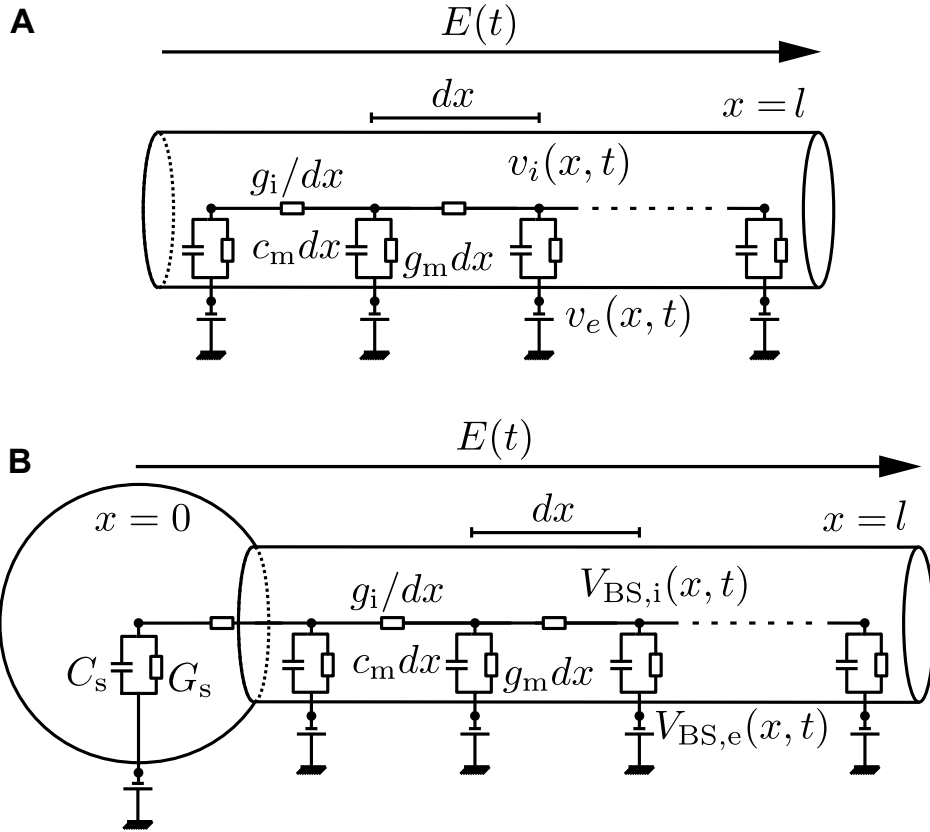


Figure A.1: Schematic description of a passive cable and a ball-and-stick models subject to an extracellular electric field

(A) Passive cable model and its associated electric circuit. At both cable ends, the boundary conditions are sealed ends, i.e. no axial current is flowing at the cable end. v_i and v_e refer to the intracellular and extracellular potential of the passive model. (B) Ball-and-stick (BS) model and its associated electric circuit. The BS model has a lumped soma ($x=0$) and a sealed end ($x=l$) boundary conditions. $V_{BS,i}$ and $V_{BS,e}$ are the intracellular and extracellular potential of the BS model. In both models, c_m , g_m and g_i denote respectively the membrane capacitance and the membrane (leak) conductance and the axial conductance per unit length. Both models are of length l . dx corresponds to a small length. C_s and G_s are the capacitance and conductance of the lumped soma in the BS model.

For simplicity, we assume that the rest membrane potential, i.e. in the absence of an extracellular field, is null.

Writing the Kirchoff's law of conservation of current at a given location x , we have:

$$I_a(x - dx, t) + I_m(x, t) - I_a(x, t) = 0 \quad (\text{A.3})$$

where I_a and I_m are respectively axial and transmembrane currents, which can be expressed using the Ohm's law and the expression for the capacitive current:

$$I_a(x, t) = \frac{g_i}{dx} (v_i(x + dx, t) - v_i(x, t))$$

$$I_m(x, t) = c_m dx \frac{\partial v}{\partial t}(x, t) + g_m dx v(x, t)$$

Injecting these expressions in Eq. A.3, we obtain:

$$-\frac{g_i}{dx} (v_i(x + dx, t) - v_i(x - dx, t)) + c_m dx \frac{\partial v}{\partial t}(x, t) + g_m dx v(x, t) = 0$$

Dividing by dx and taking the limit $dx \rightarrow 0$:

$$-g_i \frac{\partial^2 v_i}{\partial x^2}(x, t) + c_m \frac{\partial v}{\partial t}(x, t) + g_m v(x, t) = 0$$

Using the definitions of the membrane potential Eq. A.2 and of the field Eq. A.1:

$$-g_i \frac{\partial^2 v}{\partial x^2}(x, t) + c_m \frac{\partial v}{\partial t}(x, t) + g_m v(x, t) = -g_i \frac{\partial E}{\partial x}(x, t)$$

We further express the cable equation subject to the field using the cable membrane time constant $\tau = c_m/g_m$ (s) and electrotonic length scale $\lambda = \sqrt{g_i/g_m}$ (mm):

$$\tau \frac{\partial v}{\partial t}(x, t) - \lambda \frac{\partial^2 v}{\partial x^2}(x, t) + v(x, t) = -\lambda \frac{\partial E}{\partial x}(x, t) \quad (\text{A.4})$$

A.1.2 Boundary conditions

The partial differential equation of the cable (Eq. A.4) fully determines the membrane potential response to the field when "associated" to the boundary conditions. In this thesis we solely consider two kind of cable ends: the *sealed end* and the *lumped soma* (used in the ball-and-stick model). Depending on the analysis we perform, these cable ends can be subject to synaptic input currents; in all considered cases, they are subjects to an extracellular field. In the following, we briefly derive the different boundary conditions encountered in this thesis.

Sealed-end In the sealed end condition, no axial current is allowed to flow at the boundary:

$$\frac{\partial v_i}{\partial x}(x, t) = 0, \quad x \in \{0, l\}$$

and therefore, in presence of an electric field:

$$\frac{\partial v_i}{\partial x}(x, t) = E(x, t), \quad x \in \{0, l\} \quad (\text{A.5})$$

We now consider a sealed end at the cable end ($x = l$) subject to both an extracellular field and a synaptic input current $I(t)$. The intracellular voltage is determined by (Tuckwell, 1988):

$$\frac{\partial v_i}{\partial x}(x, t) = \frac{I(t)}{g_i} \quad x \in l,$$

This yields for the membrane voltage:

$$\frac{\partial v}{\partial x}(x, t) = \frac{I(t)}{g_i} + E(l, t) \quad x = l. \quad (\text{A.6})$$

Lumped soma In the lumped soma condition, we consider a soma attached to the cable at $x = 0$. Given the relative size of the soma compared to the cable length, we assume the soma is an equipotential surface with a capacitance C_s and resistance R_s (Tuckwell, 1988). Applying Kirchhoff's law of current conservation at $x = 0$, we have:

$$C_s \frac{\partial v}{\partial t}(0, t) + G_s v(0, t) = \frac{g_i}{dx} (v_i(dx, t) - v_i(0, t))$$

Taking the limit $dx \rightarrow 0$, using the definitions of the membrane ($v = v_i - v_e$) and of the field (Eq. A.1), we obtain the lumped soma boundary condition at $x = 0$ in presence of an extracellular field:

$$C_s \frac{\partial v}{\partial t}(0, t) + G_s v(0, t) - g_i \frac{\partial v}{\partial x}(0, t) = -g_i E(0, t) \quad (\text{A.7})$$

If subject to a synaptic input current $I(t)$ in addition to the field, the lumped soma boundary condition is expressed as:

$$C_s \frac{\partial v}{\partial t}(0, t) + G_s v(0, t) - g_i \frac{\partial v}{\partial x}(0, t) = I(t) - g_i E(0, t) \quad (\text{A.8})$$

Finally, we consider the case where the lumped-soma includes voltage dependent currents $I_{\text{ion}}(V, t)$. When subject to both an extracellular field E and an input current I , this lumped soma corresponds to the boundary condition:

$$C_s \frac{\partial v}{\partial t}(0, t) + G_s v(0, t) - g_i \frac{\partial v}{\partial x}(0, t) - I_{\text{ion}}(t) = I(t) - g_i E(0, t) \quad (\text{A.9})$$

where, for example:

$$I_{\text{ion}}(t) = G_s \Delta_T e^{\frac{V_{\text{BS}} - V_T}{\Delta_T}} \quad (\text{A.10})$$

in case of an exponential integrate-and-fire neuron (EIF) (see Table C.1 for a description of the parameters).

A.2 Derivation of the BS somatic membrane potential in response to synaptic inputs and a spatially uniform extracellular electric field

In this section, we analytically derive the subthreshold membrane response of the Ball-and-stick (BS) neuron model in response to synaptic input currents located at the model ends and to a spatially uniform extracellular field.

The Ball-and-stick neuron (BS) model consists of a lumped somatic compartment attached to a finite passive dendritic (Fig. A.1B). The BS morphology is defined by the cable length l , the cable diameter D_d and the soma diameter D_s . The BS cable is oriented along the x axis, the lumped soma being at $x = 0$ and the sealed end at the cable extremity $x = l$. We note V_{BS} the deviation from rest, V_{rest} , of the membrane potential of the BS model¹. By definition:

$$V_{\text{BS}}(x, t) := V_{\text{BS},i}(x, t) - V_{\text{BS},e}(x, t) - V_{\text{rest}}$$

where $V_{\text{BS},i}$ and $V_{\text{BS},e}$ denote respectively the intra- and extracellular potentials. We are interested in the BS model response to synaptic inputs and to an electric field. The synaptic inputs are located at the soma $I_s(t)$ and at the distal dendritic end $I_d(t)$. Here, we consider solely electric fields, $E(t) = -\frac{\partial V_{\text{BS},e}}{\partial x}(x, t)$, which are spatially uniform, i.e. their spatial derivative is null, at the scale of the neuron.

¹ Note that, we use a different notation than for the membrane potential of a simple passive cable to emphasize the distinction between both models.

Furthermore, we consider a BS model including an exponential mechanism (Eq. A.10) at the soma which corresponds to spike initiating currents.

Using the cable equation Eq. A.4 and the boundary conditions of Eqs. A.6, A.9 and A.10, we express the cable equation corresponding to the EIF BS neuron model:

$$c_m \frac{\partial V_{BS}}{\partial t} - g_i \frac{\partial^2 V_{BS}}{\partial x^2} + g_m V_{BS} = -g_i \frac{\partial E}{\partial x} = 0 \quad 0 < x < l, \quad (\text{A.11})$$

and the boundary conditions:

$$C_s \frac{\partial V_{BS}}{\partial t} - g_i \frac{\partial V_{BS}}{\partial x} + G_s V_{BS} - G_s \Delta_T e^{\frac{V_{BS}-V_T}{\Delta_T}} = I_s(t) - g_i E(t) \quad x = 0, \quad (\text{A.12})$$

$$\frac{\partial V_{BS}}{\partial x} = \frac{I_d(t)}{g_i} + E(t), \quad x = l. \quad (\text{A.13})$$

$c_m = cD_d\pi$ refers to the membrane capacitance per unit length. $g_i = \varrho_i(D_d/2)^2\pi$ and $g_m = \varrho_m D_d\pi$ are respectively the internal (axial) and the membrane conductances, per unit length, of the cable. c still denotes the specific membrane capacitance (in F/m²), ϱ_m the specific membrane conductance (in S/m²) and ϱ_i the specific internal conductance (in S/m). $G_s = \varrho_m D_s^2\pi$ and $C_s = cD_s^2\pi$ are the somatic membrane leak conductance and capacitance.

The rightmost equality in Eq. A.11 results from the assumption of the field spatial uniformity.

In the following we solve an approximation of this BS cable equation (Eq. A.11-A.13) for the subthreshold regime. In brief, we first linearize the exponential term around a baseline membrane potential, then separate the temporal and spatial variables, apply the temporal Fourier transform and finally solve the resulting complex second order differential equation with respect to the spatial variable (see the following for more details).

Assuming the variations of the synaptic inputs $I_s(t)$, $I_d(t)$ and the amplitude of the weak oscillatory electric field $E(t)$ are small, we linearize the exponential term in the boundary condition at the soma ($x=0$, Eq. A.12) around a baseline voltage value V_0 . This yields:

$$C_s \frac{\partial V_{BS}}{\partial t} - g_i \frac{\partial V_{BS}}{\partial x} + G_s \left(1 - e^{\frac{V_0-V_T}{\Delta_T}}\right) V_{BS} = G_s e^{\frac{V_0-V_T}{\Delta_T}} (\Delta_T - V_0) + I_s(t) - g_i E(t) \quad (\text{A.14})$$

This results in a partial differential equation A.11 and associated boundary conditions A.14 and A.13 which are linear. This system of differential equations can be solved using, successively, the separation of variables $V_{BS}(x, t) = W(x)U(t)$ and the Fourier transform in the temporal domain:

$$\hat{V}_{BS}(x, \omega) = W(x)\hat{U}(\omega) = W(x) \int_{-\infty}^{\infty} U(t)e^{i\omega t} dt,$$

where $\omega = 2\pi f$ indicates angular frequency and $\hat{\cdot}$ the temporal Fourier transform. The

system of differential equations becomes:

$$c_m i \omega \hat{V}_{BS} - g_i \frac{\partial^2 \hat{V}_{BS}}{\partial x^2} + g_m \hat{V}_{BS} = 0 \quad 0 < x < l, \quad (\text{A.15})$$

$$C_s i \omega \hat{V}_{BS} - g_i \frac{\partial \hat{V}_{BS}}{\partial x} + G_s \left(1 - e^{-\frac{V_0 - V_T}{\Delta_T}} \right) \hat{V}_{BS} = 2\pi \delta(\omega) G_s e^{-\frac{V_0 - V_T}{\Delta_T}} (\Delta_T - V_0) + \hat{I}_s(\omega) - g_i \hat{E}(\omega) \quad x = 0, \quad (\text{A.16})$$

$$\frac{\partial \hat{V}_{BS}}{\partial x} = \frac{\hat{I}_d(\omega)}{g_i} + \hat{E}(\omega) \quad x = l, \quad (\text{A.17})$$

where $\delta(\cdot)$ denotes the Dirac delta function.

Eq. A.15 is a second order linear differential equation whose solution is of the form:

$$\hat{V}_{BS}(x, \omega) = a_1(\omega) e^{z(\omega)x} + a_2(\omega) e^{-z(\omega)x} \quad (\text{A.18})$$

$\pm z(\omega)$ correspond to the roots of the characteristic polynomial $g_i \lambda^2 = g_m + c_m i \omega$ of Eq. A.15:

$$z(\omega) = \sqrt{\frac{g_m + \sqrt{g_m^2 + \omega^2 c_m^2}}{2g_i}} + \text{sign}(\omega) i \sqrt{\frac{-g_m + \sqrt{g_m^2 + \omega^2 c_m^2}}{2g_i}}, \quad (\text{A.19})$$

The boundary conditions Eq. A.16, A.17 of the differential system constrain its general solution Eq. A.18. Specifically, the coefficients $a_1(\omega)$ and $a_2(\omega)$ are derived by inserting $\hat{V}_{BS}(x, \omega)$ from Eq. A.18 in Eqs. A.16 and A.17. This yields the subthreshold somatic membrane response of the BS model to synaptic inputs and an extracellular field:

$$\hat{V}_{BS}(0, \omega) = \hat{V}_{BS}^{I_s}(0, \omega) + \hat{V}_{BS}^{I_d}(0, \omega) + \hat{V}_{BS}^{\Delta_T}(0, \omega) + \hat{V}_{BS}^E(0, \omega) \quad (\text{A.20})$$

with

$$\hat{V}_{BS}^{I_s}(0, \omega) = \frac{\hat{I}_s(\omega)}{X(\omega)}, \quad \hat{V}_{BS}^{\Delta_T}(0, \omega) = \frac{2\pi \delta(\omega) G_s e^{-\frac{V_0 - V_T}{\Delta_T}} (\Delta_T - V_0)}{X(\omega)}, \quad (\text{A.21})$$

$$\hat{V}_{BS}^{I_d}(0, \omega) = \frac{\hat{I}_d(\omega) \text{sech}(z(\omega)l)}{X(\omega)}, \quad \hat{V}_{BS}^E(0, \omega) = \frac{\hat{E}(\omega) g_i [\text{sech}(z(\omega)l) - 1]}{X(\omega)}, \quad (\text{A.22})$$

and

$$X(\omega) = C_s i \omega + G_s \left(1 - e^{-\frac{V_0 - V_T}{\Delta_T}} \right) + z(\omega) g_i \tanh(z(\omega)l). \quad (\text{A.23})$$

The function $\text{sech}(x) = \cosh(x)^{-1}$ indicates the hyperbolic secant.

$V_{BS}^{I_s}$, $V_{BS}^{I_d}$ and V_{BS}^E are respectively the membrane response components to I_s , I_d and E . $V_{BS}^{\Delta_T}$ is the membrane ‘‘response’’ to the (linearized) exponential term, i.e. the spike initiation mechanism.

Furthermore, the membrane response to a sinusoidal field, $E(t) = E_1 \sin(\varphi t)$, can be expressed in the time domain as

$$V_{BS}^E(0, t) = |A(\varphi)| \sin(\varphi t + \arg(A(\varphi))), \quad (\text{A.24})$$

$$A(\varphi) = \frac{E_1 g_i [\text{sech}(z(\varphi)l) - 1]}{C_s i \varphi + G_s \left(1 - e^{-\frac{V_0 - V_T}{\Delta_T}} \right) + z(\varphi) g_i \tanh(z(\varphi)l)}. \quad (\text{A.25})$$

A.3 Derivation of the membrane polarization of a straight passive cable due to a spatially non-uniform electric field

In this section, we analytically derive the membrane polarization of a straight passive cable in response to an extracellular electric field. Unlike for the ball-and-stick case in the precedent section, we do not assume that the field is spatially uniform.

We consider a straight cable of radius r (mm) and length l (mm). The cable electronic properties are characterized by its membrane time constant $\tau = c_m/g_m$ (s) and electrotonic length scale $\lambda = \sqrt{g_i/g_m}$ (mm), $c_m = 2\pi r c$ (F/mm) being the membrane capacitance per unit length and $g_m = 2\pi r \rho_m$ (S/mm), $g_i = \rho_i \pi r^2$ (S.mm) respectively the internal (axial) and membrane (radial) conductances per unit length. c (F.mm²), ρ_i (S/mm), ρ_m (S/mm²) denote respectively the specific membrane capacitance, the axial conductance and the membrane conductance. We define the membrane potential along the cable as $v(x, t) = v_i(x, t) - v_e(x, t)$. We assume that the rest membrane potential is null. Note that, the cable being passive, this later assumption does not change the results.

We apply an extracellular electric field $E(x, t)$ parallel to the cable axis, x :

$$E(x, t) = -\frac{\partial v_e}{\partial x}(x, t)$$

In the following computation, we do not assume the field to be stationary or spatially non-uniform but we do assume that its spatial and temporal components are independent:

$$v_e(x, t) = v_{e,x}(x)v_{e,t}(t) \quad (\text{A.26})$$

As derived in section A.1, the membrane potential along the cable is governed by the cable equation:

$$\tau \frac{\partial v}{\partial t} - \lambda^2 \frac{\partial^2 v}{\partial x^2} + v = -\lambda^2 \frac{\partial E}{\partial x} \quad 0 < x < l$$

Or, in terms of v_i and v_e :

$$\tau \frac{\partial v_i}{\partial t} - \lambda^2 \frac{\partial^2 v_i}{\partial x^2} + v_i = v_e + \tau \frac{\partial v_e}{\partial t} \quad 0 < x < l \quad (\text{A.27})$$

and the sealed end boundary conditions:

$$\begin{aligned} \frac{\partial v_i}{\partial x} &= 0, & x &= 0 \\ \frac{\partial v_i}{\partial x} &= 0, & x &= l \end{aligned}$$

To solve Eq. A.27, we first apply the separation of variables (for which the assumption of Eq. A.26 is necessary) and the temporal Fourier transform:

$$v_\alpha(x, t) = v_{x,\alpha}(x)v_{t,\alpha}(t) = v_{x,\alpha}(x) \int_{-\infty}^{\infty} \hat{v}_{t,\alpha}(\omega_t) e^{i\omega_t t} d\omega_t \quad (\text{A.28})$$

$$\hat{v}_\alpha(x, \omega_t) = v_{x,\alpha}(x) \hat{v}_{t,\alpha}(\omega_t) = v_{x,\alpha}(x) \int_{-\infty}^{\infty} v_{t,\alpha}(t) e^{-i\omega_t t} dt \quad (\text{A.29})$$

$$(\text{A.30})$$

with $\alpha \in \{i, e\}$. $\hat{\cdot}$ denotes the temporal Fourier transform and $\omega_t = 2\pi f_t$ the temporal angular frequency.

We consider each angular frequency separately and rewrite Eq. A.27 in the temporal Fourier domain, for a fixed ω_t , :

$$-\lambda^2 \frac{\partial^2 \hat{v}_i}{\partial x^2} + (1 + i\omega_t \tau) \hat{v}_i = (1 + i\omega_t \tau) \hat{v}_e \quad 0 < x < l \quad (\text{A.31})$$

We further define the complex *frequency-dependent space constant*, $\lambda_{eq}(f_t)$:

$$\lambda_{eq}^2 = \frac{\lambda^2}{1 + i\omega_t \tau}$$

As a side note, in the results of Chapter 3, we use the real component of λ_{eq} , that is the *generalized frequency-dependent space constant* (Koch, 2004, Chapt. 2.3), λ_{gen} :

$$\lambda_{gen}(f_t) = \text{Re}(\lambda_{eq}(f_t)) = \frac{\lambda}{\text{Re}(\sqrt{1 + 2i\pi f_t \tau})}$$

Using the frequency dependent space constant, Eq. A.31 becomes:

$$-\lambda_{eq}^2 \frac{\partial^2 \hat{v}_i}{\partial x^2} + \hat{v}_i = \hat{v}_e, \quad 0 < x < l \quad (\text{A.32})$$

After the temporal Fourier transform, we now apply the Fourier transform in the spatial domain. To avoid confusion between imaginary terms resulting from Fourier transforms in the temporal and spatial domains, we use the cosine transform for the spatial domain:

$$\begin{aligned} v_{x,\alpha}(x) &= \int_{-\infty}^{\infty} \tilde{v}_{x,\alpha}(\omega_x) e^{i\omega_x x} d\omega_x = \int_{-\infty}^{\infty} |\tilde{v}_{x,\alpha}(\omega_x)| e^{i(\omega_x x + \arg(\tilde{v}_{x,\alpha}(\omega_x)))} d\omega_x \\ &= \int_{-\infty}^{\infty} |\tilde{v}_{x,\alpha}(\omega_x)| \sin(\omega_x x + \arg(\tilde{v}_{x,\alpha}(\omega_x)) + \pi/2) d\omega_x \\ \tilde{v}_{x,\alpha}(\omega_x) &= \int_{-\infty}^{\infty} v_{x,\alpha}(x) e^{-i\omega_x x} dx \end{aligned}$$

with $\alpha \in \{i, e\}$. $\tilde{\cdot}$ denotes the spatial Fourier transform and $\omega_x = 2\pi f_x$ the spatial frequency of the extracellular potential. This cosine notation is valid since $v_{x,\alpha}$ is real, i.e. $\forall x, v_{x,\alpha}(x) \in \mathbb{R}$.

We consider each spatial component separately. For a fixed ω_x , and after setting $\bar{v}_\alpha(\omega_x, \omega_t) = \tilde{v}_{x,\alpha}(\omega_x) \hat{v}_{t,\alpha}(\omega_t)$, $\alpha \in \{i, e\}$ Eq. A.32 becomes:

$$-\lambda_{eq}^2 \frac{\partial^2 \bar{v}_i}{\partial x^2} + \bar{v}_i = v_0 \sin(2\pi f_s x + \phi_s), \quad 0 < x < L \quad (\text{A.33})$$

with $v_0(\omega_x, \omega_t) = \hat{v}_{t,e}(\omega_t) |\tilde{v}_{x,e}(\omega_x)|$ and $\phi_s(\omega_x) = \arg(\tilde{v}_{x,e}(\omega_x)) + \pi/2$.

For fixed temporal (ω_t) and spatial (ω_x) field frequencies, we normalize the length units using the frequency-dependent space constant:

$$\Omega_x = \omega_x \lambda_{eq}, \quad X = \frac{X}{\lambda_{eq}}, \quad V_\alpha = \frac{\bar{v}_\alpha}{v_0}, \alpha \in \{e, i\}$$

Eq. A.33 becomes:

$$-\frac{\partial^2 V_i}{\partial X^2} + V_i = \sin(\Omega_x X + \phi_s), \quad 0 < X < L = l/\lambda_{eq}$$

and the boundary conditions:

$$\begin{aligned} \frac{\partial V_i}{\partial X} &= 0, & X &= 0 \\ \frac{\partial V_i}{\partial X} &= 0, & X &= L \end{aligned}$$

This differential system has already been solved by Anastassiou et al. (2010, Supporting Information) using the Green's function derived in (Tuckwell, 1988):

$$\begin{aligned} V_i(X) &= -\frac{\Omega_x}{\Omega_x^2 + 1} \sin(\Omega_x X + \phi_s) \\ &+ \frac{\Omega_x^2}{\Omega_x^2 + 1} \left(\frac{\cosh(X)}{\tanh(L)} \cos(\phi_s) - \frac{\cosh(X)}{\sinh(L)} \cos(\Omega_x L + \phi_s) - \sinh(X) \cos(\phi_s) \right) \end{aligned}$$

In terms of membrane potential, i.e. $V = V_i - V_e$:

$$\begin{aligned} V(X) &= -\frac{\Omega_x^2}{\Omega_x^2 + 1} \sin(\Omega_x X + \phi_s) \\ &+ \frac{\Omega_x^2}{\Omega_x^2 + 1} \left(\frac{\cosh(X)}{\tanh(L)} \cos(\phi_s) - \frac{\cosh(X)}{\sinh(L)} \cos(\Omega_x L + \phi_s) - \sinh(X) \cos(\phi_s) \right) \end{aligned} \quad (\text{A.34})$$

$V(X)$ is a complex function which corresponds to the subthreshold cable membrane polarization due to an electrical field with given spatial and temporal frequencies. Indeed, the dependence of $V(X)$ in the field spatial, ω_x , and temporal, ω_t , angular frequencies is hidden in the variables Ω_x , ϕ_s and λ_{eq} . To obtain the full membrane modulation, i.e. for an arbitrary field, we need to integrate V over these angular frequencies. The full equation for the membrane polarization due to an arbitrary extracellular field is:

$$v(x, t) = \int \int v_0(\omega_x, \omega_t) V(x/\lambda_{eq}) e^{i\omega_t t} d\omega_x d\omega_t \quad (\text{A.35})$$

where V is given by Eq. A.34 and also depends on ω_x . Note that, $v_0(\omega_x, \omega_t)$ corresponds to the spatial and temporal Fourier coefficients of the extracellular field for the respective frequencies ω_x and ω_t .

In the above derivation, we solely assumed that the spatial and temporal components of the extracellular field are independent (Eq. A.26). Since we consider only fields whose spatial component does not vary in time, this assumption is not restricting the present work but it could be in case of endogenous fields. Nevertheless, this limitation can be easily by-passed by considering each spatial components separately and using the linearity of the cable equation.

Appendix B

Derivation of the quasi-active approximation

For completeness, we present here the derivation of the cable equation with a quasi-active current (Remme and Rinzel, 2011; Remme, 2013).

We consider a neuron with a leak current I_L and a voltage-dependent current I_w . The cable equation governing the membrane dynamics is:

$$c_m \frac{\partial V}{\partial t}(x, t) = g_i \frac{\partial^2}{\partial x^2} V(x, t) + I_L(x, t) + I_w(x, t) \quad (\text{B.1})$$

where $V(t) = V_i(t) - V_e(t)$ the membrane potential, i.e. the difference between intra- and extracellular potentials. c_m denotes the membrane capacitance.

The leak and voltage-dependent current are expressed as:

$$I_L(x, t) = -g_L(V(x, t) - E_L) \quad (\text{B.2})$$

$$I_w(x, t) = -g_w w(x, t)(V(x, t) - E_w), \quad (\text{B.3})$$

E_α, g_α (with $\alpha \in \{L, w\}$) being respectively the reversal potentials and conductances of the leak (subscript L) and active (subscript w) currents. In this description, the current conductance g_w is static and the voltage-dependent dynamics of the active current are contained in the gating variable w . The gating variable w is determined by:

$$\frac{\partial w}{\partial t}(x, t) = \frac{1}{\tau_w(V(x, t))} (w_\infty(V(x, t)) - w(x, t)) \quad (\text{B.4})$$

where $w_\infty(V)$ and $\tau_w(V)$ are the activation function and time constant of the gating variable w .

We are interested by the variation of the membrane potential and gating variables around rest, we therefore set:

$$U(x, t) = V(x, t) - V_R(x)$$

$$W(x, t) = w(x, t) - w_\infty(V_R(x))$$

where V_R is the rest membrane potential. We do not assume a spatial uniformity of the rest membrane potential: $V_R(x)$ depends on x .

For the sake of readability, we omit writing down the dependence in x and t of the variables V , U , W and w in the following derivation.

We now linearize the dynamics of the active current around the rest state. To this end we take the first order term of the Taylor expansion of the right hand sides of Eq. B.3 and of Eq. B.4.

Beginning with the current I_w :

$$\begin{aligned} I_w(x, t) &\approx I_w \Big|_R + \frac{\partial I_w}{\partial V} \Big|_R U + \frac{\partial I_w}{\partial w} \Big|_R W \\ &= -g_w w_\infty(V_R)(V_R - E_w) - g_w w_\infty(V_R)U - g_w(V_R - E_w)W \end{aligned} \quad (\text{B.5})$$

We now linearize the right hand side of Eq. B.4, which we note $F(x, t)$:

$$\begin{aligned} F(x, t) &\approx F \Big|_R + \frac{\partial F}{\partial V} \Big|_R U + \frac{\partial F}{\partial w} \Big|_R W \\ &= 0 + \left[\frac{1}{\tau_w(V_R)} \frac{\partial w_\infty}{\partial V}(V_R) - \frac{1}{\tau_w(V_R)^2} \frac{\partial \tau_w}{\partial V}(V_R)(w_\infty(V_R) - w_\infty(V_R)) \right] U - \frac{1}{\tau_w(V_R)} W \\ &= \frac{1}{\tau_w(V_R)} \frac{\partial w_\infty}{\partial V}(V_R)U - \frac{1}{\tau_w(V_R)} W \end{aligned} \quad (\text{B.6})$$

Combining Eq. B.2, B.3 and B.5 into Eq. B.1:

$$\begin{aligned} c_m \frac{\partial V}{\partial t} &= g_i \frac{\partial^2}{\partial x^2} V - g_L(V - E_L) - g_w w_\infty(V_R)(V_R - E_w) \\ &\quad - g_w w_\infty(V_R)(V - V_R) - g_w(V_R - E_w)(w - w_\infty(V_R)) \\ &= g_i \frac{\partial^2}{\partial x^2} V_R - g_L(V_R - E_L) - g_w w_\infty(V_R)(V_R - E_w) \\ &\quad + g_i \frac{\partial^2}{\partial x^2} (V - V_R) - g_L(V - V_R) \\ &\quad - g_w w_\infty(V_R)(V - V_R) - g_w(V_R - E_w)(w - w_\infty(V_R)) \end{aligned}$$

Using the fact that the right hand side of Eq. B.1 is null at rest and setting:

$$\begin{aligned} \gamma_R &= 1 + \frac{g_w}{g_L} w_\infty(V_R) \\ \mu &= \frac{g_w}{g_L} (V_R - E_w) \frac{\partial w_\infty}{\partial V}(V_R) \\ m(t) &= (w(t) - w_\infty(V_R)) / \frac{\partial w_\infty}{\partial V}(V_R) \end{aligned}$$

The cable equation and the dynamics of the gating variable become:

$$c_m \frac{\partial V}{\partial t}(x, t) = g_i \frac{\partial^2 (V - V_R)}{\partial x^2}(x, t) - g_L \left(\gamma_R (V(x, t) - V_R(x)) + \mu m(x, t) \right) \quad (\text{B.7})$$

$$\tau_w(V_R(x)) \frac{\partial m}{\partial t}(x, t) = V(x, t) - V_R(x) - m(x, t) \quad (\text{B.8})$$

It is noteworthy that after the linearization, no term involving the derivative of τ_w remain.

In this thesis, we consider only quasi-active membrane with spatially uniform membrane potential at rest. For commodity, we note:

$$I_{axial} = g_i \frac{\partial^2(V - V_R)}{\partial x^2}(x, t) = g_i \frac{\partial^2 V}{\partial x^2}(x, t)$$

Appendix C

Supplementary information

C.1 Supplementary information for chapter 2

Parameter (Unit)	Value (range)	Description
c (F/m ²)	10^{-2} (Migliore et al., 2005; Mainen and Sejnowski, 1996)	Specific membrane capacitance
ϱ_m (S/m ²)	1/2.8 (Migliore et al., 2005)	Specific membrane conductance
ϱ_i (S/m)	1/1.5 (Migliore et al., 2005; Mainen and Sejnowski, 1996)	Specific internal (axial) conductance
D_s (m)	$\{5, 10^*, 15\} \cdot 10^{-6}$ (Rattay, 1999)	Soma diameter
D_d (m)	$\{0.6, 1.2^*, 1.8\} \cdot 10^{-6}$ (Major et al., 1994)	Dendritic cable diameter
l (m)	$\{3.5, 7^*, 10.5\} \cdot 10^{-4}$ (Spruston, 2009)	Dendritic cable length
C_s (F)	$cD_s^2\pi$	Somatic membrane capacitance
G_s (S)	$\varrho_m D_s^2\pi$	Somatic membrane conductance
c_m (F/m)	$cD_d\pi$	Dendritic membrane capacitance per unit length
g_m (S/m)	$\varrho_m D_d\pi$	Dendritic membrane conductance per unit length
g_i (S · m)	$\varrho_i (D_d/2)^2\pi$	Internal (axial) conductance per unit length
V_s (mV)	{10, 20}	Spike (or cutoff) voltage
V_r (mV)	0	Reset voltage of BS model
V_T (mV)	10 (Badel et al., 2008)	Threshold voltage
V_0 (mV)	V_r	Baseline voltage for EIF model extension
Δ_T (mV)	1.5 (Badel et al., 2008)	Threshold slope factor
T_{Ref} (ms)	1.5	Duration of refractory period
C_{eP} (F)	C_s	Membrane capacitance of eP model
G_{eP} (S)	G_s	Membrane conductance of eP model
V_r' (mV)	5	Reset voltage of eP and P models
I_s^0 (pA)	[4.254, 11.407]	Mean input current at the soma
σ_s (pA)	[8.887, 74.512]	Somatic input noise intensity
I_d^0 (pA)	[6.255, 13.214]	Mean input current at the dendrite
σ_d (pA)	[21.875, 122.363]	Dendritic input noise intensity
τ (ms)	0.5	Synaptic current correlation time
E_1 (V/m)	{1, 10}	Amplitude of electric field
φ (rad)	$[0, 10^4] \cdot 2\pi$	Angular frequency of electric field
Δ (ms)	3	Spike coincidence precision

* indicates default values.

Table C.1: Description of parameters and applied values for the simulations

Table and caption adapted from (Aspart et al., 2016, CC BY 4.0).

C.2 Supplementary information for chapter 3

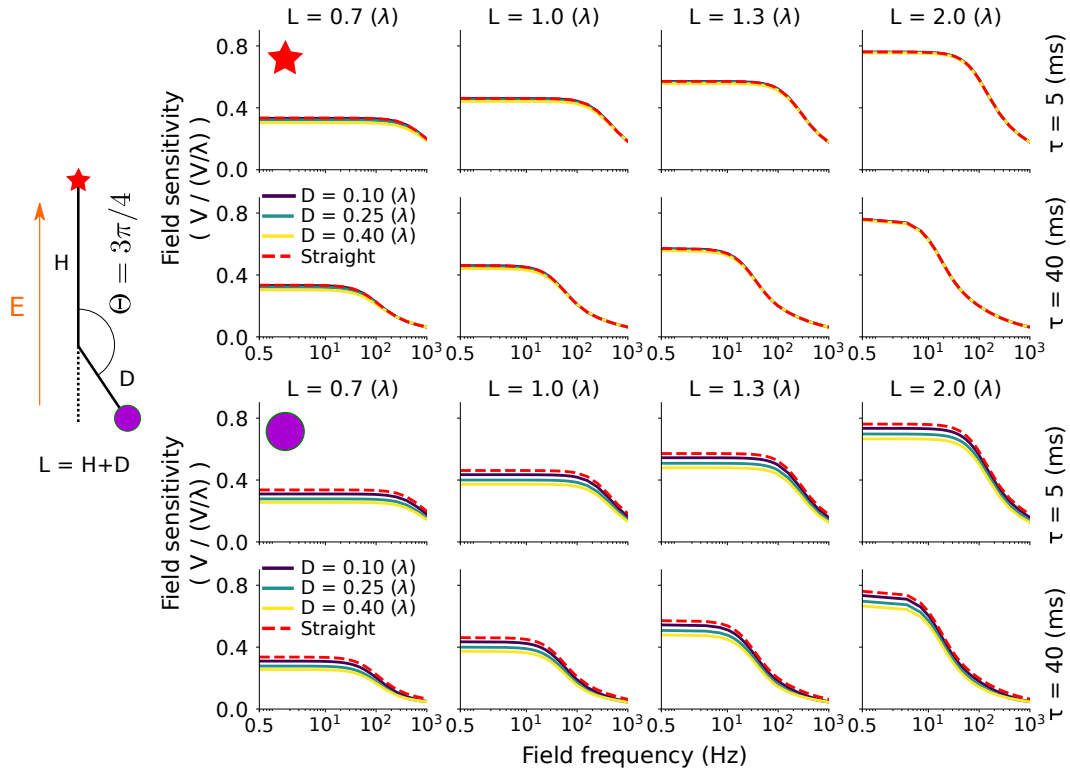


Figure C.1: In a passive cable with an obtuse bending angle, the length of the bent branch has little effects on the field sensitivity at both ends

The subplots represent the field sensitivity (in $V / (V/\lambda)$) at both cable ends: (top, red star) the unbent branch and (bottom, violet circle) the bent one, as function of the field frequency (x axis). The field sensitivity are displayed for various membrane time constants τ (rows for each location), total cable lengths L (increasing from left to right) and bent branch lengths D (color coded). The bending angle is $\Theta = 3\pi/4$ (rad). The red dashed lines correspond to the sensitivity of a straight cable of length L (i.e. $D = 0$). Figure and caption adapted from (Aspart et al., 2018, CC BY 4.0)

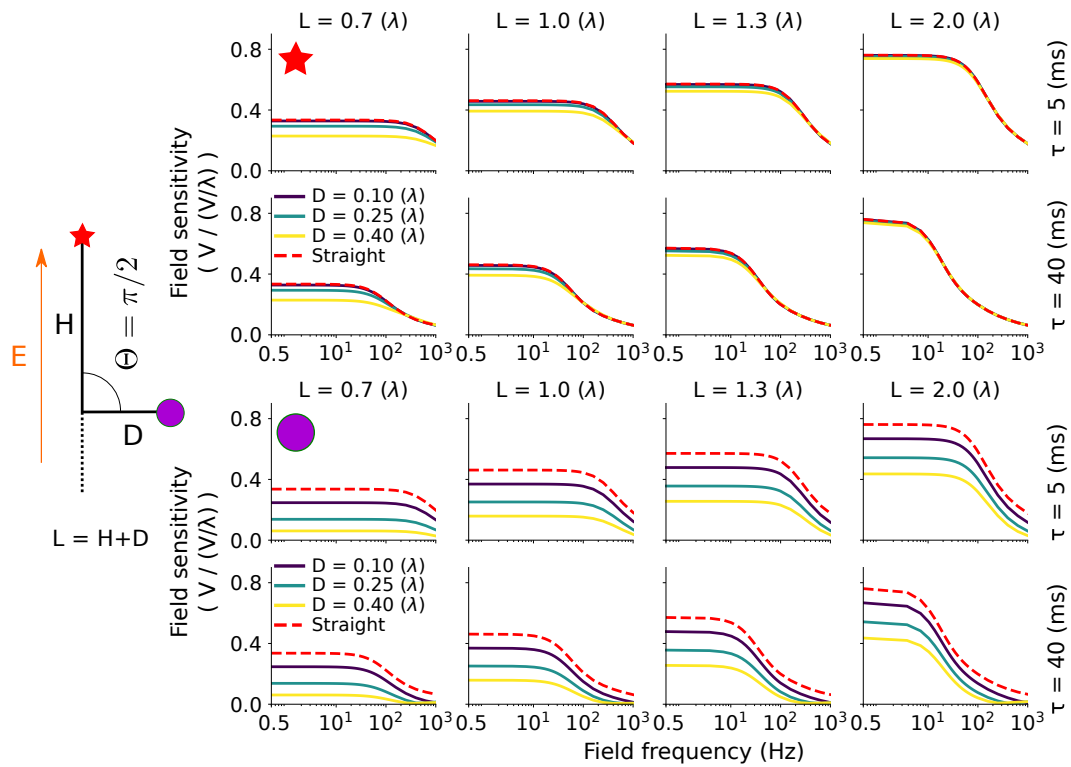


Figure C.2: In a passive cable with a right bending angle, the length of the bent branch mainly affects the field sensitivity at its end, without inducing a resonance

The subplots represent the field sensitivity (in $V / (V/\lambda)$) at both cable ends: (top, red star) the unbent branch and (bottom, violet circle) the bent one, as function of the field frequency (x axis). The field sensitivity are displayed for various membrane time constants τ (rows for each location), total cable lengths L (increasing from left to right) and bent branch lengths D (color coded). The bending angle is $\Theta = \pi/2$ (rad). The red dashed lines correspond to the sensitivity of a straight cable of length L (i.e. $D = 0$). Figure and caption adapted from (Aspart et al., 2018, CC BY 4.0)

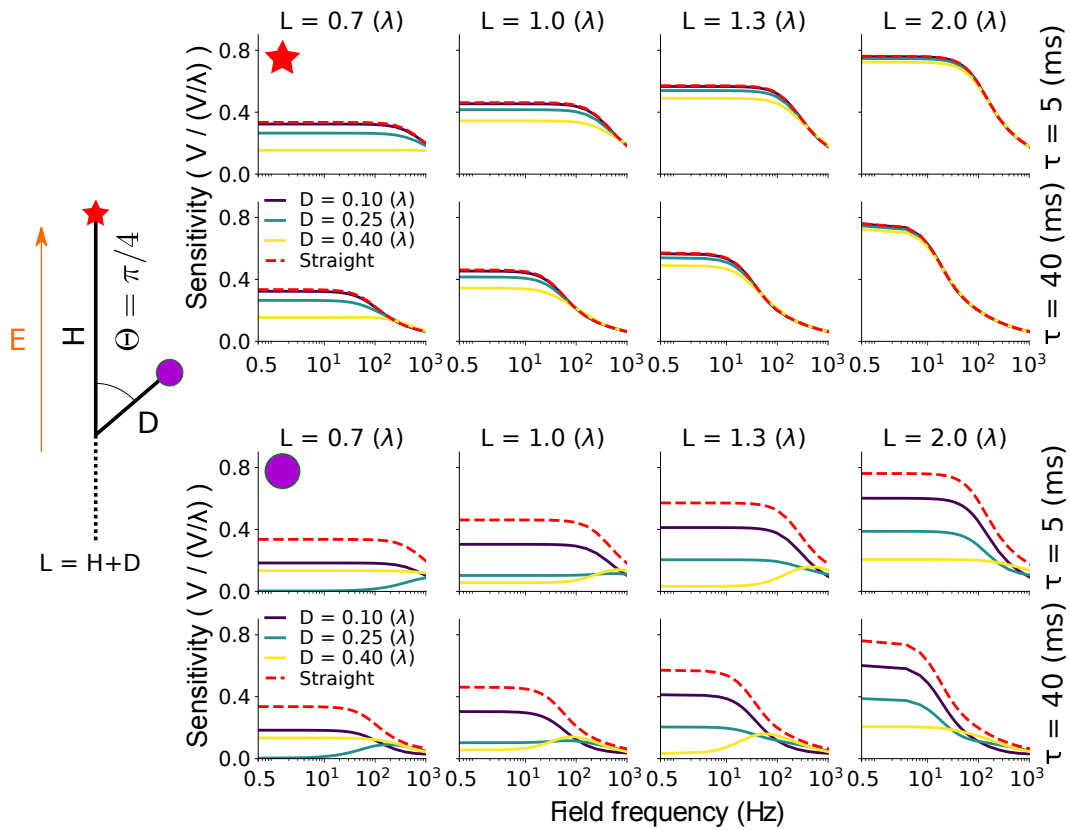


Figure C.3: In a passive cable with an acute bending angle, the membrane time constant τ determines the resonance frequency

The subplots represent the field sensitivity (in $V / (V/\lambda)$) at both cable ends: (top, red star) the unbent branch and (bottom, violet circle) the bent one, as function of the field frequency (x axis). The field sensitivity is displayed for various membrane time constants τ (rows for each location), total cable lengths L (increasing from left to right) and bent branch lengths D (color coded). The bending angle is $\Theta = \pi/4$ (rad). The red dashed lines correspond to the sensitivity of a straight cable of length L (i.e. $D = 0$). Figure and caption adapted from (Aspart et al., 2018, CC BY 4.0)

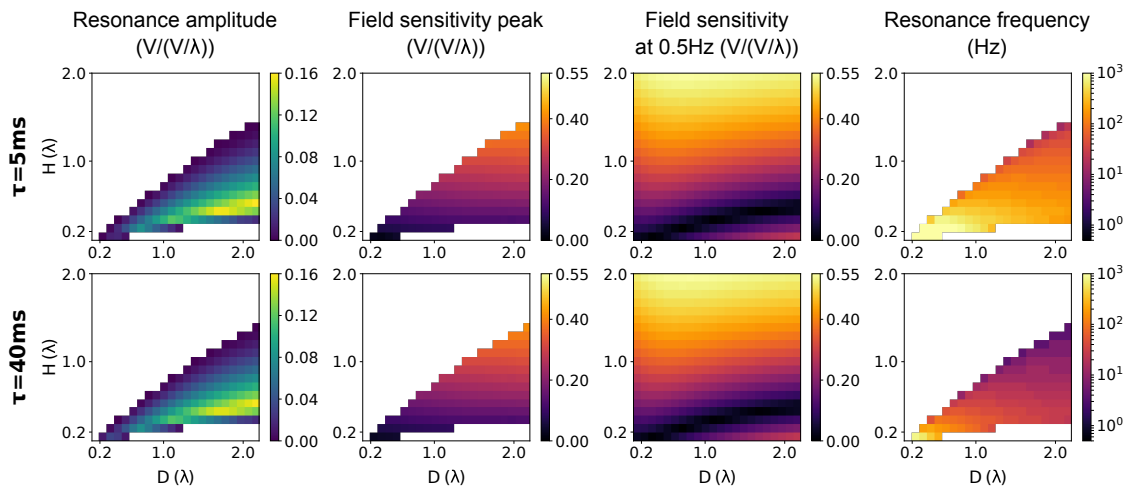


Figure C.4: In a passive cable with an acute bending angle, the relative lengths of the main and bent branches determine the presence of a resonance; the membrane time constant determines the resonance frequency

We consider the sensitivity to AC fields of a cable with an acute bending angle ($\Theta = \pi/4$). The field sensitivity is measured at the bent end. From left to right, the plots represent the resonance amplitude (peak field sensitivity, i.e. at the resonance, minus the field sensitivity at 0.5Hz), the peak field sensitivity, the field sensitivity at 0.5 Hz and the resonance frequency. Each of these measures is plotted for various electrotonic lengths of (vertical axis) the main branch, H , and of (horizontal axis) the bent branch, D . The white areas correspond to the absence of resonance. The rows correspond to different membrane time constants (top: $\tau = 5$ ms, bottom: $\tau = 40$ ms). Figure and caption adapted from (Aspart et al., 2018, CC BY 4.0)

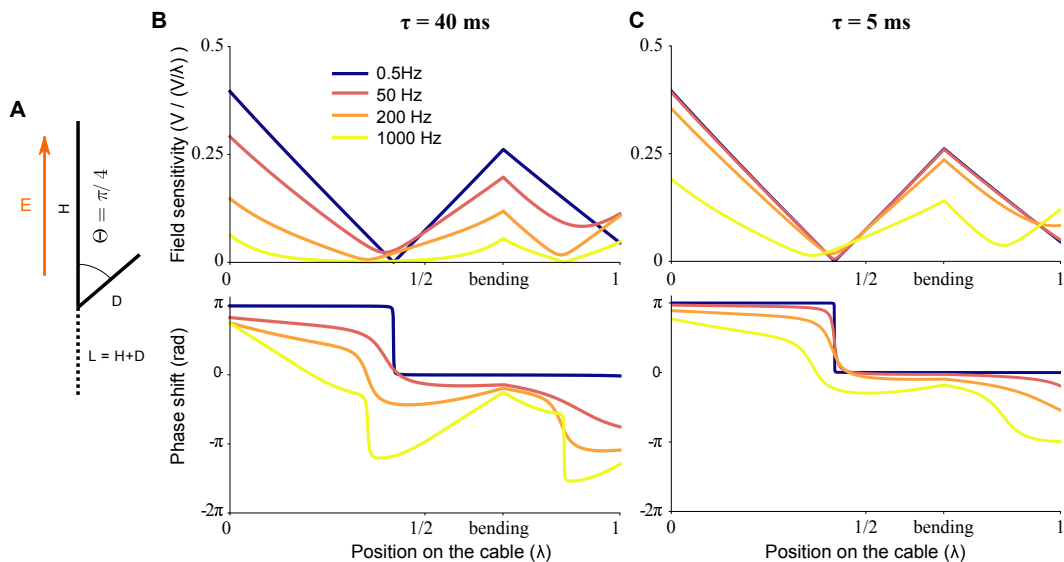


Figure C.5: Decreasing the membrane time constant reduces the frequency-dependence of the field sensitivity along bent cables

(A) Schematic representation of a bent cable. The unbent branch of the cable, of length H , is parallel to the field axis. The bent branch, of length D , have an angle Θ with the field. L is the total cable length. (B,C) Distribution of the sensitivity (top) and phase (bottom) along the bent cable for different field frequencies (0.5, 50, 200 and 1000Hz) in case of a slow (B, $\tau = 40$ (ms)) and a fast (C, $\tau = 40$ (ms)) membrane time constant. In all the plots the bending angle is $\Theta = \pi/4$ (rad), $H = 0.6(\lambda)$ and $D = 0.4(\lambda)$. Figure and caption adapted from (Aspart et al., 2018, CC BY 4.0)

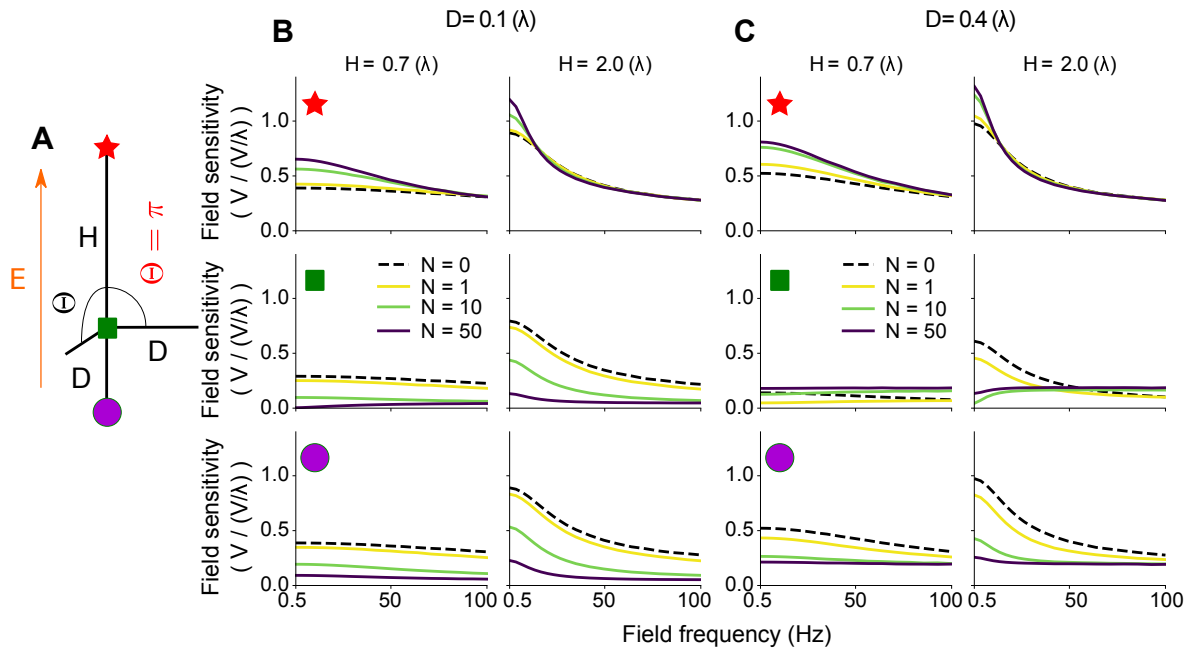


Figure C.6: The presence of several basal dendrites parallel to apical dendrites increases the field sensitivity at the apical dendrites and can induce a resonance at the soma

(A) Schematic representation of the simplified neuron model at use. The model consists of a main branch of length H , parallel to the extracellular field. Several branches of length D are attached to one end of the main cable. At least one of the attached branch is parallel to the main cable axis, the others form an angle Θ with that axis. (B,C) Sensitivity (in $V/(V/\lambda)$) at the end of the main cable (red star), at the branching point (green square) and at the end of the parallel branching cable (purple circle), as function of the field frequency. The field sensitivities are displayed for various number N (color coded) of branches with an angle of Θ and various electrotonic lengths of the main cable (H , columns) and of the branches (D , columns). In all the plots the bending angle is $\Theta = \pi$ (rad) and the membrane time constant $\tau = 40$ (ms). H and D are electrotonic lengths. Figure and caption reproduced from (Aspart et al., 2018, CC BY 4.0)

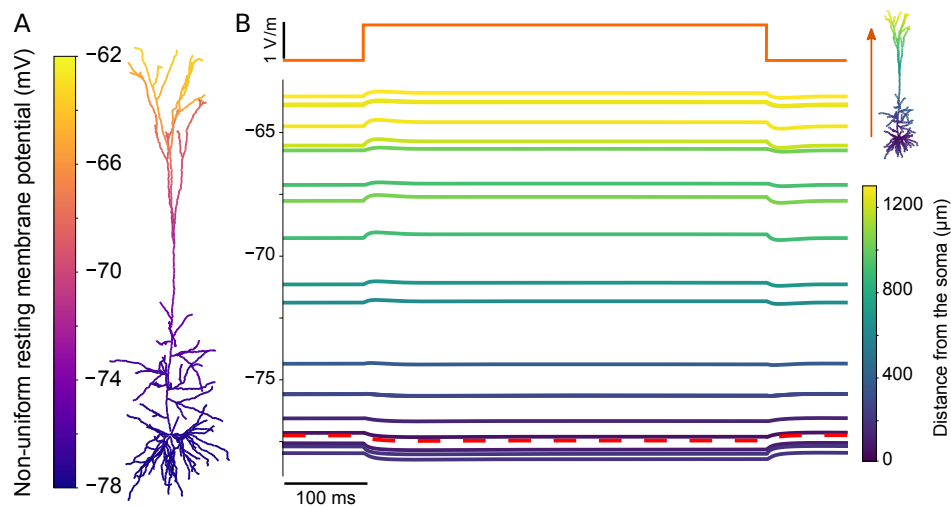


Figure C.7: Pyramidal cells present, at rest, a gradient of membrane potential which is not counterbalanced by the polarization due to weak DC fields.

(A) Membrane potential (color coded) at rest, i.e. in the absence of electric fields or synaptic inputs, of the Hay et al. pyramidal cell model. (B) Membrane voltage in presence of a DC extracellular field (orange trace). Colors of the polarization correspond to the distance from the soma (see top right schema). The red dashed red line corresponds to the soma.

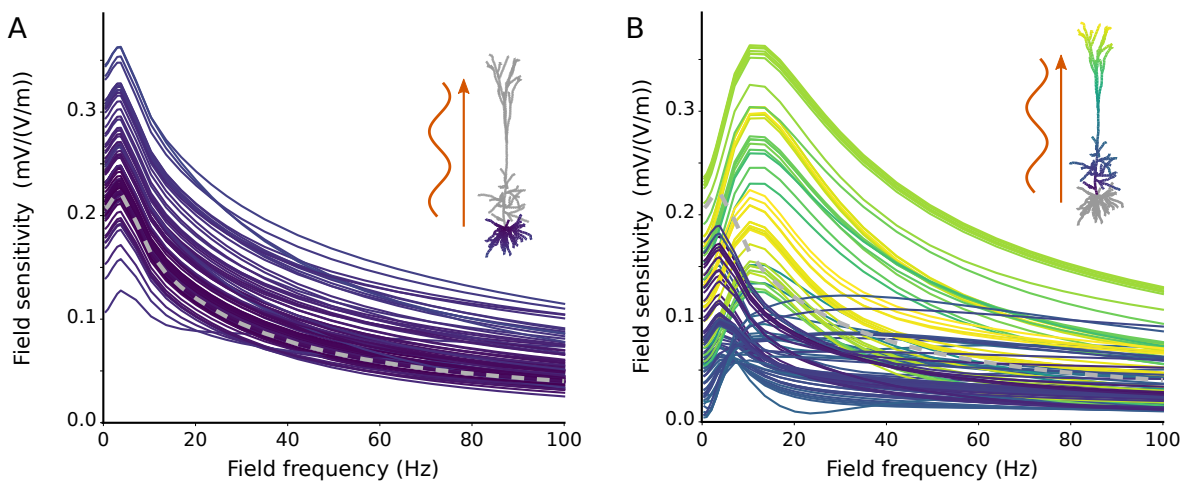


Figure C.8: In an active pyramidal cell model, the field sensitivity presents a strong resonance around 10-20Hz at the apical dendrites but not at the soma or the basal dendrites

Frequency-dependent sensitivity of the cell to AC fields measured at different locations at the basal (A) or apical (B) dendrites. Colors code the distance to the soma of the considered segment. Figure and caption adapted from (Aspart et al., 2018, CC BY 4.0)

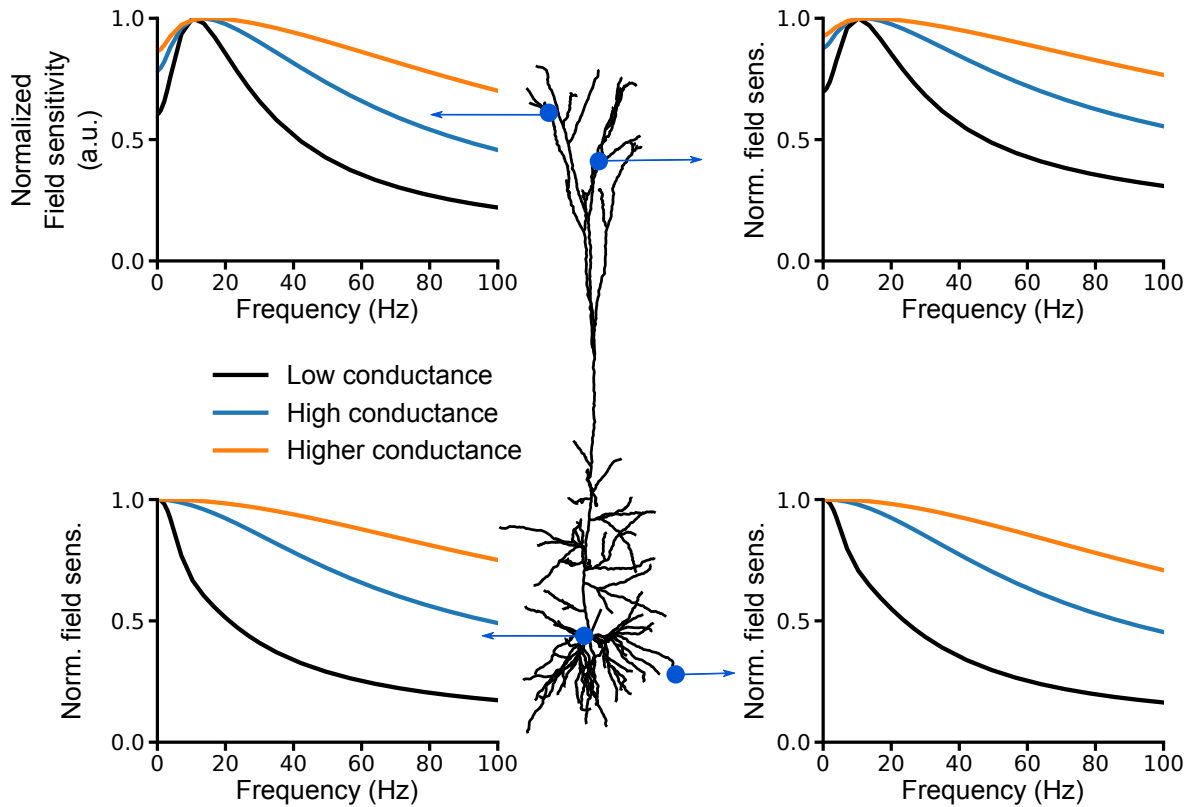


Figure C.9: The field sensitivity of a pyramidal cell is less frequency-dependent in an high-conductance state

We consider the field sensitivity of a neuron model in different conductance states. The low-conductance state corresponds to the model with the same leak conductance as the original Hay et al. (2011) model. In the high- (blue lines) and higher-conductance (orange lines) state, we uniformly increased the passive conductance of the original model by adding respectively $350\mu S/cm^2$ and $900\mu S/cm^2$. To remove the effects of changes in resting membrane potential, we uniformly set the resting membrane potential of all 3 models to $-65mV$ by adjusting the leak reversal potential. The resistance to somatic input current of the low-, high- and higher-conductance state models are respectively: $53 M\Omega$, $15.62 M\Omega$, and $9.05 M\Omega$. The subplots display the normalized field sensitivity (in fraction of the local peak sensitivity) for the models in different conductance state. Figure and caption adapted from (Aspart et al., 2018, CC BY 4.0)

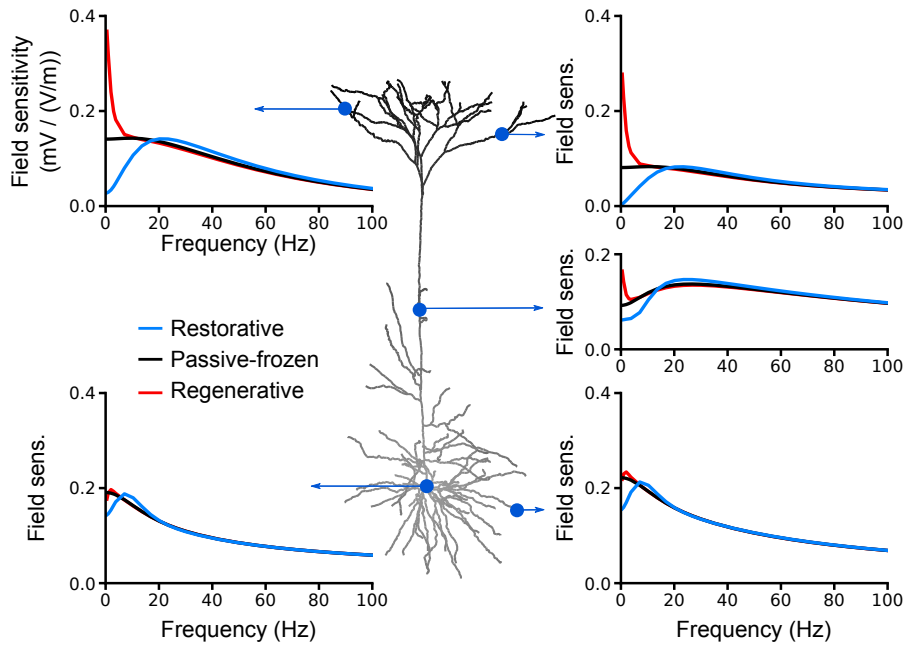


Figure C.10: Results with a QA channel conductance distributed linearly increasingly with distance from the soma are transposable to the cell 2 morphology.

The neuron model includes a leak current and a single QA channel, whose conductance distribution increases linearly with distance from the soma. The shades of grey in the cell plot represent this distribution. We use the reconstructed morphology corresponding to cell 2 in the Hay et al. (2011) paper. μ^* determines the type of the QA channel. The plots display the sensitivity (in mV/(V/m)) of the cell to AC fields at different locations in case of restorative (blue, $\mu^* = 2$), passive (black, $\mu^* = 0$) and regenerative (red, $\mu^* = -0.5$) quasi-active currents.

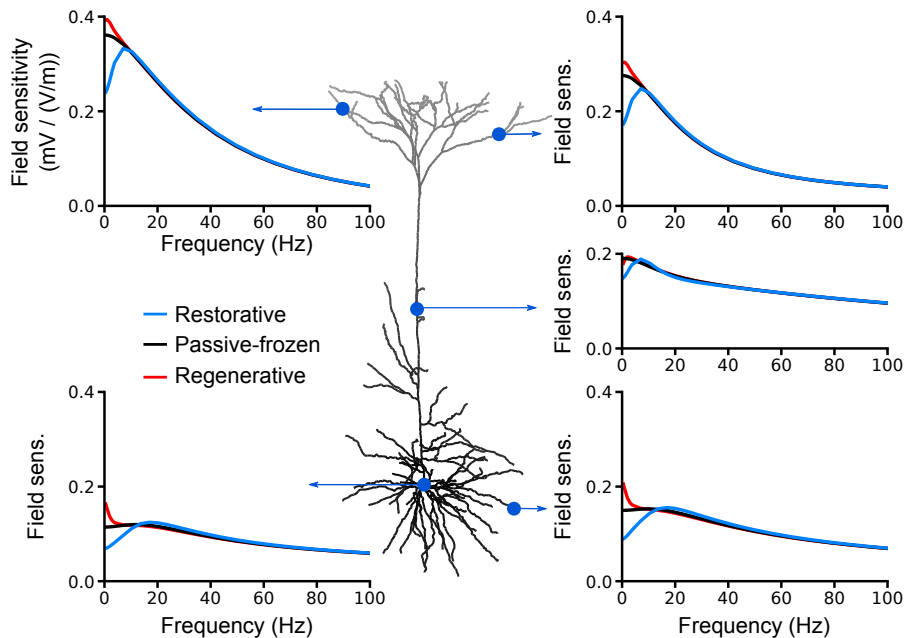


Figure C.11: Results with a QA channel conductance distributed linearly decreasingly with distance from the soma are transposable to the cell 2 morphology.

The neuron model includes a leak current and a single QA channel, whose conductance distribution decreases linearly with distance from the soma. The shades of grey in the cell plot represent this distribution. We use the reconstructed morphology corresponding to cell 2 in the Hay et al. (2011) paper. μ^* determines the type of the QA channel. The plots display the sensitivity (in mV/(V/m)) of the cell to AC fields at different locations in case of restorative (blue, $\mu^* = 2$), passive (black, $\mu^* = 0$) and regenerative (red, $\mu^* = -0.5$) quasi-active currents.

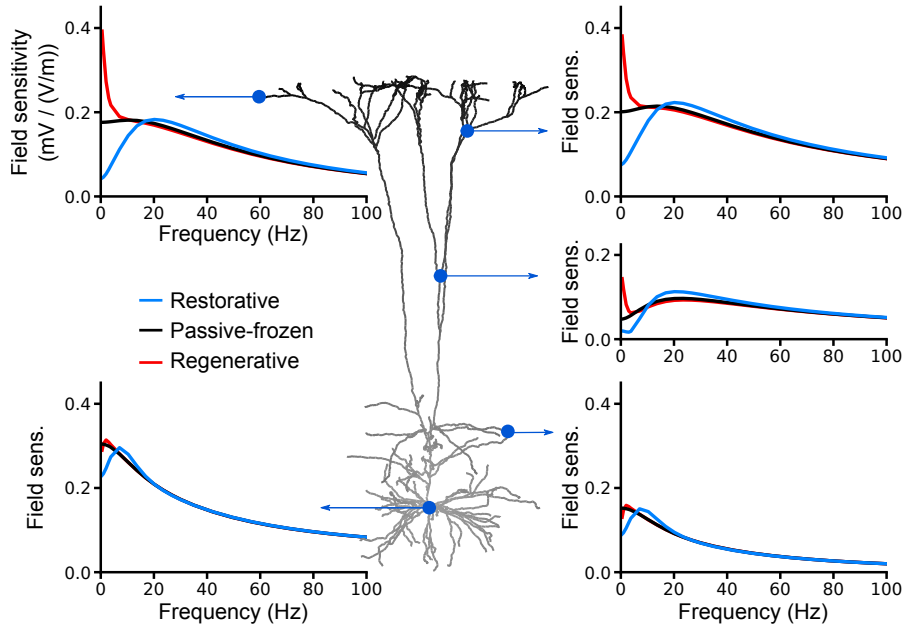


Figure C.12: Results with a QA channel conductance distributed linearly increasingly with distance from the soma are transposable to the cell 3 morphology.

The neuron model includes a leak current and a single QA channel, whose conductance distribution increases linearly with distance from the soma. The shades of grey in the cell plot represent this distribution. We use the reconstructed morphology corresponding to cell 3 in the Hay et al. (2011) paper. μ^* determines the type of the QA channel. The plots display the sensitivity (in mV/(V/m)) of the cell to AC fields at different locations in case of restorative (blue, $\mu^* = 2$), passive (black, $\mu^* = 0$) and regenerative (red, $\mu^* = -0.5$) quasi-active currents.

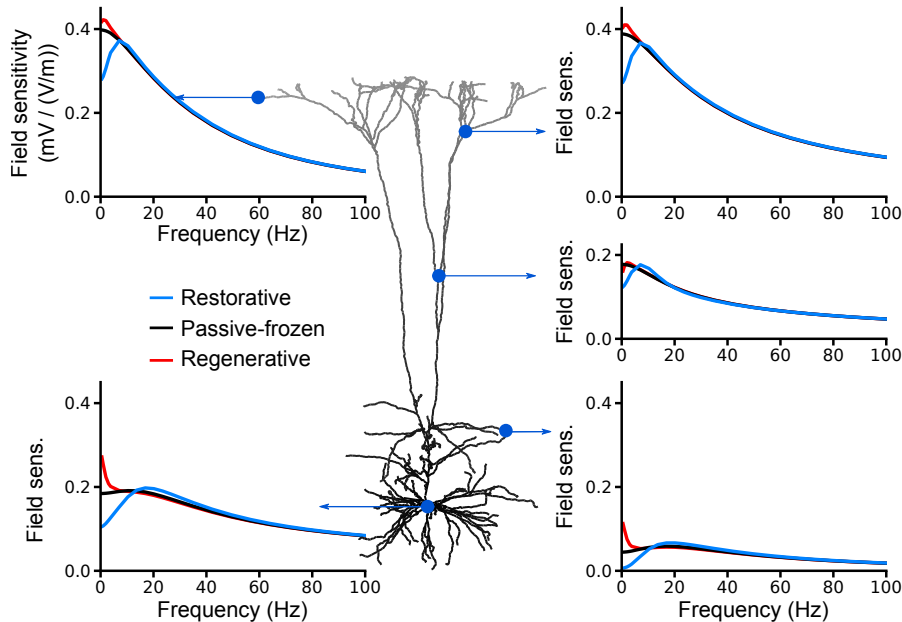


Figure C.13: Results with a QA channel conductance distributed linearly decreasingly with distance from the soma are transposable to the cell 3 morphology.

The neuron model includes a leak current and a single QA channel, whose conductance distribution decreases linearly with distance from the soma. The shades of grey in the cell plot represent this distribution. We use the reconstructed morphology corresponding to cell 3 in the Hay et al. (2011) paper. μ^* determines the type of the QA channel. The plots display the sensitivity (in mV/(V/m)) of the cell to AC fields at different locations in case of restorative (blue, $\mu^* = 2$), passive (black, $\mu^* = 0$) and regenerative (red, $\mu^* = -0.5$) quasi-active currents.

Figure C.14: Increasing the neuron membrane surface reduces the sensitivity to DC fields

Polarization of passive pyramidal cell models due to a positive 1 V/m field plotted as the function of the distance from the soma. For clarity basal dendrites are plotted with negative distance. The polarization is plotted for original cell (green) and for a cell with an increased membrane surface (black). The passive cell properties of the original cell, e.g. membrane conductance and capacitance, are the one reported in (Hay et al., 2011). In the other cell, we mimic a further 40% increase of the membrane surface by adjusting the membrane conductance and capacitance (Sterratt et al., 2011, Chapter 4.3.2). Figure and caption adapted from (Aspart et al., 2018, CC BY 4.0)

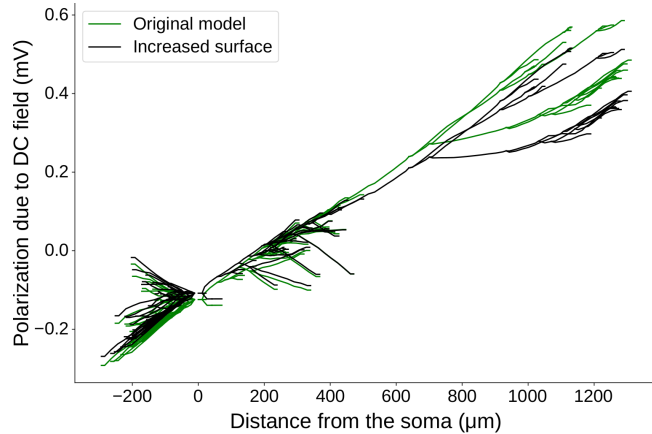
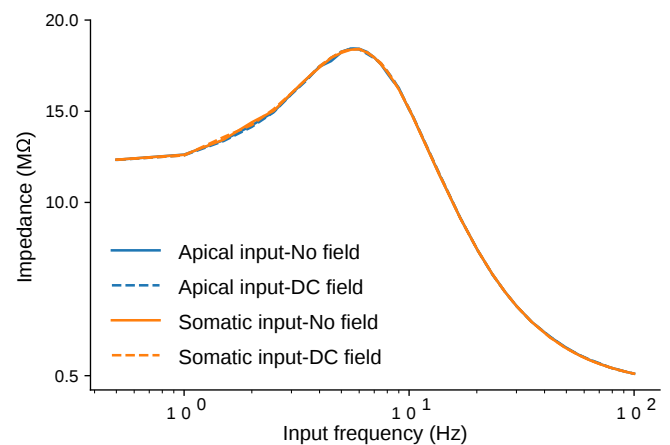


Figure C.15: The transfer impedances between the apical dendrites and the soma are symmetric and are not affected by DC fields

Transfer impedances from the apical dendrites to the soma (blue lines) and in the opposite direction (orange lines). The impedances are displayed in the absence of field (solid lines) and in the presence of a positive DC field of 1 V/m (dashed lines). The impedances are computed through the injection of a low amplitude sinusoidal current at one location and measuring the membrane potential response at the other. The amplitude of the injected current is 0.05 nA for an injection at the soma and 0.01 nA for a dendritic injection. The apical location is located at 620 μm from the soma. Figure and caption reproduced from (Aspart et al., 2018, CC BY 4.0)



Features of BAP and BAC firing	Description	Mean \pm SD
Ca ²⁺ peak (mV)	Peak membrane voltage at the distal apical trunk 620 μ m from the soma	6.73 \pm 2.54
Ca ²⁺ width (ms)	Width of the calcium spike at 620 μ m, computed at the base of the spike (-55mV)	37.43 \pm 1.27
Somatic AP spike count (during somatic + dendrite current injection)	Number of APs during the BAC firing	3 \pm 0
Mean somatic AP ISI (ms)	Mean interspike interval	9.9 \pm 0.85
Somatic AHP depth (mV)	Averaged minimum somatic voltage between 2 APs	-65 \pm 4
Somatic AP peak (mV)	Averaged peak somatic membrane potentials during an AP	25 \pm 5
Somatic AP half-width (ms)	Average AP width at the middle point between its onset and peak	2 \pm 0.5
Somatic AP spike count (during somatic current injection only)	Number of APs in the absence of a concurrent EPSP	1 \pm 0
BAP amplitude at 620 μ m (mV)	Peak membrane voltage in the apical tuft (620 μ m from the soma) in response to a sole somatic impulse current (no EPSP)	45 \pm 10
BAP amplitude at 800 μ m (mV)	Peak membrane voltage in the apical tuft (800 μ m from the soma) in response to a sole somatic impulse current (no EPSP)	36 \pm 9.33

Table C.2: List of features characterizing the backpropagation of AP and the BAC firing of pyramidal cells.

The table summarizes the list of features used by Hay et al. (2011) to fit the back-propagation of Action Potential (BAP) along the apical dendrite and the ensuing backpropagating action potential-activated calcium (BAC) firing. The features values were measured *in vitro* and reported in Hay et al. (2011). The BAP features were measured after the injection of a 1.9nA impulse current (5ms) at the soma. In case of BAC, an EPSP was injected in the apical tuft 5ms after the impulse onset. The simulation parameters are summarized in Table 3.1. See also Hay et al. (2011) for more details.

Somatic Feature	firing	Description	Mean \pm SD, Low	Mean \pm SD, Reference (15Hz)	Mean \pm SD, High
Spike frequency (Hz)		Neuron spike rate	9 ± 0.88	14.5 ± 0.56	22.5 ± 2.22
Adaptation Index		Average of the difference between two consecutive interspike intervals divided by their summed duration (Druckmann et al., 2007) ^a ISI coefficient of variation:	$3.6e-3 \pm 9.1e-3$	$2.3e-3 \pm 5.6e-3$	$4.6e-3 \pm 2.6e-3$
ISI-CV		$\frac{\text{ISI mean}}{\text{ISI SD}}$	0.1204 ± 0.0321	0.1083 ± 0.0368	0.0954 ± 0.0140
Initial Burst (ms)	ISI	ISI between the first two spikes	57.5 ± 33.48	6.625 ± 8.65	5.38 ± 0.83
First spike latency (ms)		Time between the stimulus onset and the first spike ^b	43.25 ± 7.32	19.13 ± 7.31	7.25 ± 1
AP peak (mV)		Peak voltage value averaged over all APs	26.23 ± 4.97	16.52 ± 6.11	16.44 ± 6.93
Fast AHP depth (mV)		Fast After-spike Hyperpolarization (AHP) depth, i.e. average minimum membrane voltage within the first 5ms after an AP	-51.95 ± 5.82	-54.19 ± 5.57	-56.56 ± 3.58
Slow AHP depth (mV)		Average minimum membrane voltage between 5ms after an AP and the next one	-58.04 ± 4.58	-60.51 ± 4.67	-59.99 ± 3.92
Slow AHP time		Average time of the minimum membrane voltage between 5ms after an AP and the next one	0.238 ± 0.030	0.279 ± 0.027	0.213 ± 0.037
AP half-width (ms)		Average AP width at the middle point between its onset and peak	1.31 ± 0.17	1.38 ± 0.28	1.86 ± 0.41

Table C.3: List of features characterizing the cell response to step input currents at the soma.

The table summarizes the list of features used by Hay et al. (2011) to fit the model response to step currents injected at the soma. The features values correspond to the feature measured *in vitro*, as reported in (Hay et al., 2011). For each cell, the features were measured for three different input intensities: a reference amplitude which by definition elicit a 15Hz spike rate, a low and high amplitude corresponding to 78% and 190% of the reference input intensity. Each input lasted 2s. The simulation parameters are summarized in Table 3.1. See also Hay et al. (2011) for more details.

^aThe first 4 spikes or at least 20% of the total number of spikes are skipped for computing this feature

^bThe spike onset is defined as the maximum of the second temporal derivate of the membrane voltage

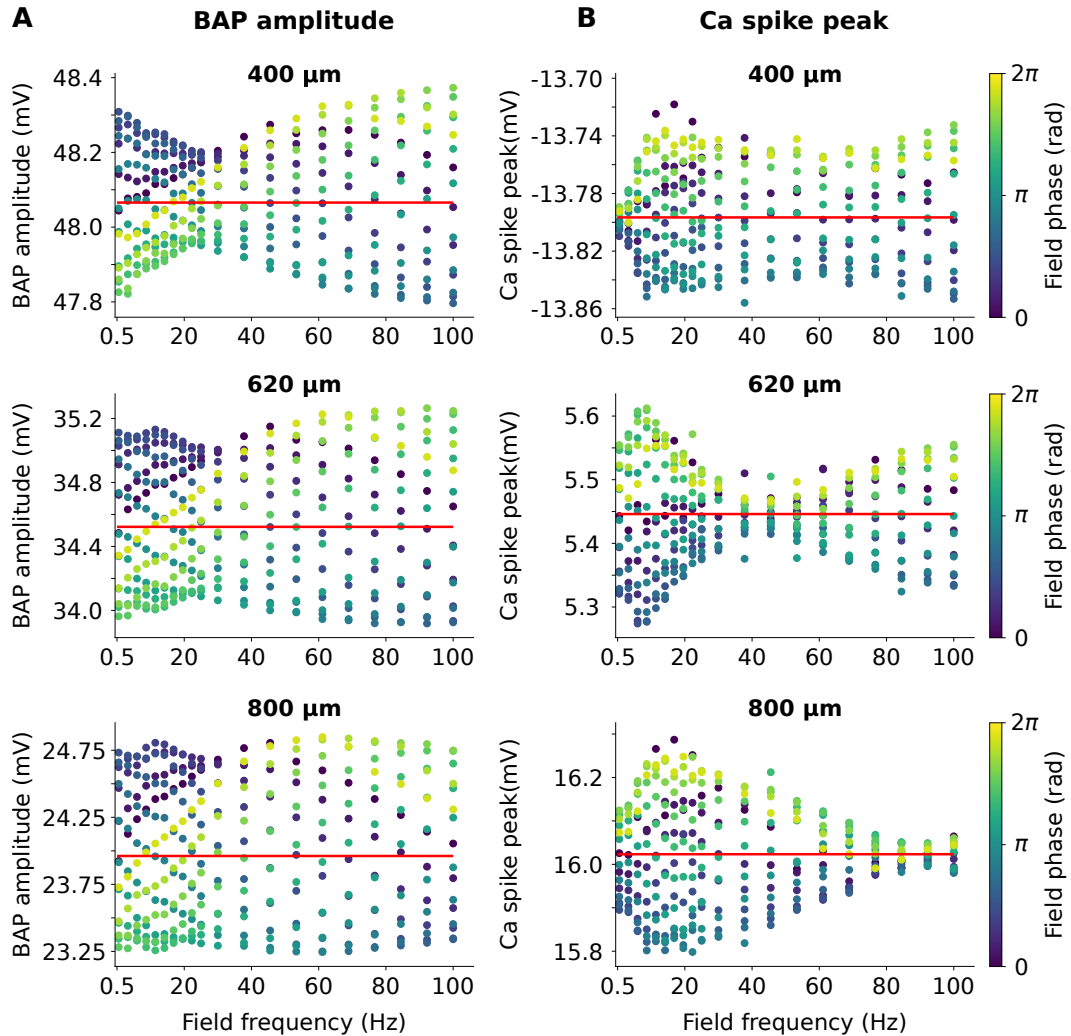


Figure C.16: Weak AC fields modulate the back-propagation of action potentials along the apical dendrite, as well as the peak of the calcium spike during BAC firing.

(A) Modulation of the action potential back-propagation (BAP), i.e. the peak membrane voltage, in response to the BAP stimulus by weak 1 V/m AC fields. The BAP stimulus consists in the injection of a brief pulse current at the soma. (B) Modulation of the calcium spike peak, i.e. the peak membrane voltage, in response to the BAC stimulus, by weak 1V/m AC fields. The BAC stimulus consists in the injection of a brief pulse current at the soma followed by an EPSP at the apical dendrite. In (A) and (B) the features are measured along the apical dendrites at 400 μm (top), 620 μm (middle) and 800 μm (bottom) from the soma. Each dot corresponds to the feature value in presence of an AC field, depending on the field frequency (x-axis) and the field phase at the stimuli onset (color coded). The red lines correspond to the features values in the absence of field.

Bibliography

- Aldini. 1804. *Essai théorique et expérimental sur le galvanisme, avec une série d'expériences faites en présence des commissaires de l'Institut national de France, et en divers amphithéâtres anatomiques de Londres*. Imprimerie de Fournier Fils.
- Ali, Sellers, and Fröhlich. 2013. Transcranial alternating current stimulation modulates large-scale cortical network activity by network resonance. *J. Neurosci.* doi: 10.1523/JNEUROSCI.5867-12.2013.
- Anastassiou, Montgomery, Barahona, Buzsaki, and Koch. 2010. The effect of spatially inhomogeneous extracellular electric fields on neurons. *J. Neurosci.* doi: 10.1523/JNEUROSCI.3635-09.2010.
- Anastassiou, Perin, Markram, and Koch. 2011. Ephaptic coupling of cortical neurons. *Nat. Neurosci.* doi: 10.1038/nn.2727.
- Aspart, Ladenbauer, and Obermayer. 2016. Extending integrate-and-fire model neurons to account for the effects of weak electric fields and input filtering mediated by the dendrite. *PLoS Comput. Biol.* doi: 10.1371/journal.pcbi.1002107.
- Aspart, Remme, and Obermayer. 2018. Differential polarization of cortical pyramidal neuron dendrites through weak extracellular fields. *PLoS Comput. Biol.* doi: 10.1371/journal.pcbi.1006124.
- Badel, Lefort, Brette, Petersen, Gerstner, and Richardson. 2008. Dynamic i-v curves are reliable predictors of naturalistic pyramidal-neuron voltage traces. *J. Neurophysiol.* doi: 10.1152/jn.01107.2007.
- Bédard and Destexhe. 2013. Generalized cable theory for neurons in complex and heterogeneous media. *Phys. Rev. E.* doi: 10.1103/PhysRevE.88.022709.
- Bikson, Inoue, Akiyama, Deans, Fox, Miyakawa, and Jefferys. 2004. Effects of uniform extracellular dc electric fields on excitability in rat hippocampal slices in vitro. *J. Physiol.* doi: 10.1113/jphysiol.2003.055772.
- Bikson, Dmochowski, and Rahman. 2012a. The "quasi-uniform" assumption in animal and computational models of non-invasive electrical stimulation. *Brain Stimul.* doi: 10.1016/j.brs.2012.11.005.
- Bikson, Reato, and Rahman. 2012b. Cellular and network effects of transcranial direct current stimulation. In Miniussi, Paulus, and Rossini, editors, *Transcranial Brain Stimulation*. CRC Press. ISBN 978-1-4398-7571-1. doi: 10.1201/b14174-5.

- Brette and Gerstner. 2005. Adaptive exponential integrate-and-fire model as an effective description of neuronal activity. *J. Neurophysiol.* doi: 10.1152/jn.00686.2005.
- Brunel. 2000. Dynamics of sparsely connected networks of excitatory and inhibitory spiking neurons. *J. Comput. Neurosci.* doi: 10.1016/S0925-2312(00)00179-X.
- Brunel, Chance, Fourcaud, and Abbott. 2001. Effects of synaptic noise and filtering on the frequency response of spiking neurons. *Phys. Rev. L.* doi: 10.1103/PhysRevLett.86.2186.
- Cakan, Aspart, Ladenbauer, and Obermayer. 2017. Effects of weak electric fields on neural activity. Conference: Bernstein Conference 2017. doi: 10.13140/rg.2.2.24378.29128.
- Carnevale and Hines. 2006. *The NEURON Book*. Cambridge University Press. ISBN 0521843219. doi: 10.1017/CBO9780511541612.
- Cartee and Plonsey. 1992. The transient subthreshold response of spherical and cylindrical cell models to extracellular stimulation. *IEEE Trans. Biomed. Eng.* doi: 10.1109/10.108130.
- Chakraborty, Truong, Bikson, and Kaphzan. 2017. Neuromodulation of axon terminals. *Cereb. Cortex.* doi: 10.1093/cercor/bhx158.
- Chance, Abbott, and Reyes. 2002. Gain modulation from background synaptic input. *Neuron.* doi: 10.1016/s0896-6273(02)00820-6.
- Datta, Bansal, Diaz, Patel, Reato, and Bikson. 2009. Gyri-precise head model of transcranial direct current stimulation: improved spatial focality using a ring electrode versus conventional rectangular pad. *Brain Stimul.* doi: 10.1016/j.brs.2009.03.005. Gyri.
- Datta, Truong, Minhas, Parra, and Bikson. 2012. Inter-individual variation during transcranial direct current stimulation and normalization of dose using mri-derived computational models. *Front. Psychiatry.* doi: 10.3389/fpsy.2012.00091.
- Dayan and Abbott. 2005. *Theoretical Neuroscience: Computational and Mathematical Modeling of Neural Systems*. MIT Press. ISBN 0262541858.
- Deans, Powell, and Jefferys. 2007. Sensitivity of coherent oscillations in rat hippocampus to ac electric fields. *J. Physiol.* doi: 10.1113/jphysiol.2007.137711.
- Dembrow, Chitwood, and Johnston. 2010. Projection-specific neuromodulation of medial prefrontal cortex neurons. *J. Neurosci.* doi: 10.1523/jneurosci.3644-10.2010.
- Destexhe, Rudolph, and Paré. 2003. The high-conductance state of neocortical neurons in vivo. *Nat. Rev. Neurosci.* doi: 10.1038/nrn1198.
- Druckmann, Banitt, Gidon, Schürmann, Markram, and Segev. 2007. A novel multiple objective optimization framework for constraining conductance-based neuron models by experimental data. *Front. Neurosci.* doi: 10.3389/neuro.01.1.1.001.2007.

- Einevoll, Kayser, Logothetis, and Panzeri. 2013. Modelling and analysis of local field potentials for studying the function of cortical circuits. *Nat. Rev. Neurosci.* doi: 10.1038/nrn3599.
- Eyal, Mansvelder, de Kock, and Segev. 2014. Dendrites impact the encoding capabilities of the axon. *J. Neurosci.* doi: 10.1523/JNEUROSCI.5431-13.2014.
- Fourcaud-Trocmé, Hansel, van Vreeswijk, and Brunel. 2003. How spike generation mechanisms determine the neuronal response to fluctuating inputs. *J. Neurosci.* doi: 23/37/11628[pii].
- Fröhlich and McCormick. 2010. Endogenous electric fields may guide neocortical network activity. *Neuron.* doi: 10.1016/j.neuron.2010.06.005.
- Fröhlich, Sellers, and Cordle. 2014. Targeting the neurophysiology of cognitive systems with transcranial alternating current stimulation. *Expert Rev. Neurother.* doi: 10.1586/14737175.2015.992782.
- Gerstner and Kistler. 2002. *Spiking Neuron Models: Single Neurons, Populations, Plasticity.* Cambridge University Press, Cambridge, UK. ISBN 9780521813846.
- Gillespie. 1996. Exact numerical simulation of the ornstein-uhlenbeck process and its integral. *Phys. Rev. E.* doi: 10.1103/PhysRevE.54.2084.
- Hay, Hill, Schürmann, Markram, and Segev. 2011. Models of neocortical layer 5b pyramidal cells capturing a wide range of dendritic and perisomatic active properties. *PLoS Comput. Biol.* doi: 10.1371/journal.pcbi.1002107.
- Herrmann, Rach, Neuling, and Strüber. 2013. Transcranial alternating current stimulation: a review of the underlying mechanisms and modulation of cognitive processes. *Front. Hum. Neurosci.* doi: 10.3389/fnhum.2013.00279.
- Hines and Carnevale. 2001. Neuron: a tool for neuroscientists. *Neurosci.* doi: 10.1177/107385840100700207.
- Hutcheon and Yarom. 2000. Resonance, oscillation and the intrinsic frequency preferences of neurons. *Trends Neurosci.* doi: 10.1016/s0166-2236(00)01547-2.
- Jolivet, Lewis, and Gerstner. 2004. Generalized integrate-and-fire models of neuronal activity approximate spike trains of a detailed model to a high degree of accuracy. *J. Neurophysiol.* doi: 10.1152/jn.00190.2004.
- Kalmbach, Chitwood, Dembrow, and Johnston. 2013. Dendritic generation of mGluR-mediated slow afterdepolarization in layer 5 neurons of prefrontal cortex. *J. Neurosci.* doi: 10.1523/jneurosci.2018-13.2013.
- Kar, Duijnhouwer, and Krekelberg. 2017. Transcranial alternating current stimulation attenuates neuronal adaptation. *J. Neurosci.* doi: 10.1523/jneurosci.2266-16.2016.
- Koch. 1984. Cable theory in neurons with active, linearized membranes. *Biol. Cybern.* doi: 10.1007/BF00317936.

- Koch. 2004. *Biophysics of Computation: Information Processing in Single Neurons*. Oxford University Press. ISBN 9780199760558.
- Kole, Stefan, and Stuart. 2006. Single ih channels in pyramidal neuron dendrites: Properties, distribution, and impact on action potential output. *J. Neurosci.* doi: 10.1523/JNEUROSCI.3664-05.2006.
- Kronberg, Bridi, Abel, Bikson, and Parra. 2017. Direct current stimulation modulates ltp and ltd: Activity dependence and dendritic effects. *Brain Stimul.* doi: 10.1016/j.brs.2016.10.001.
- Ladenbauer and Obermayer. 2018. Weak electric fields promote resonance in neuronal spiking activity: analytical results from two-compartment cell and network models. *Under review*.
- Ladenbauer, Augustin, Shiau, and Obermayer. 2012. Impact of adaptation currents on synchronization of coupled exponential integrate-and-fire neurons. *PLoS Comput. Biol.* doi: 10.1371/journal.pcbi.1002478.
- Ladenbauer, Augustin, and Obermayer. 2014. How adaptation currents change threshold, gain and variability of neuronal spiking. *J. Neurophysiol.* doi: 10.1152/jn.00586.2013.
- Ladenbauer, Ladenbauer, Külzow, de Boor, Avramova, Grittner, and Flöel. 2017. Promoting sleep oscillations and their functional coupling by transcranial stimulation enhances memory consolidation in mild cognitive impairment. *J. Neurosci.* doi: 10.1523/jneurosci.0260-17.2017.
- Lafon, Rahman, Bikson, and Parra. 2017. Direct current stimulation alters neuronal input/output function. *Brain Stimul.* doi: 10.1016/j.brs.2016.08.014.
- Larkum. 2012. A cellular mechanism for cortical associations: an organizing principle for the cerebral cortex. *Trends Neurosci.* doi: 10.1016/j.tins.2012.11.006.
- Larkum and Zhu. 2002. Signaling of layer 1 and whisker-evoked ca²⁺ and na⁺ action potentials in distal and terminal dendrites of rat neocortical pyramidal neurons in vitro and in vivo. *J. Neurosci.* doi: 10.1523/JNEUROSCI.22-16-06991.2002.
- Mainen and Sejnowski. 1996. Influence of dendritic structure on firing pattern in model neocortical neurons. *Nature.* doi: 10.1038/382363a0.
- Major, Larkman, Jonas, Sakmann, and Julian. 1994. Detailed passive cable models of whole-cell recorded ca3 pyramidal neurons in rat hippocampal slices. *J. Neurosci.* doi: 10.1523/jneurosci.14-08-04613.1994.
- Major, Larkum, and Schiller. 2013. Active properties of neocortical pyramidal neuron dendrites. *Annu. Rev. Neurosci.* doi: 10.1146/annurev-neuro-062111-150343.
- Malik. 2011. *Frequency-Dependent Response of Neurons to Oscillating Electric Fields*. PhD thesis, University of Warwick Coventry, UK.

- Marshall, Helgadóttir, Mölle, and Born. 2006. Boosting slow oscillations during sleep potentiates memory. *Nature*. doi: 10.1038/nature05278.
- McDougal, Morse, Carnevale, Marenco, Wang, Migliore, Miller, Shepherd, and Hines. 2016. Twenty years of ModelDB and beyond: building essential modeling tools for the future of neuroscience. *J. Comput. Neurosci.* doi: 10.1007/s10827-016-0623-7.
- McNickle and Carson. 2015. Paired associative transcranial alternating current stimulation increases the excitability of corticospinal projections in humans. *J. Physiol.* doi: 10.1113/jphysiol.2014.280453.
- Migliore and Shepherd. 2002. Emerging rules for the distributions of active dendritic conductances. *Nat. Rev. Neurosci.* doi: 10.1038/nrn810.
- Migliore, Ferrante, Ascoli, and Signal. 2005. Signal propagation in oblique dendrites of ca1 pyramidal cells signal propagation in oblique dendrites of ca1 pyramidal cells. *J. Neurophysiol.* doi: 10.1152/jn.00521.2005.
- Miranda, Wendling, Merlet, Molaee-Ardekani, Ruffini, Dunne, Soria-Frisch, and Whitmer. 2009. Review of state-of-the-art in currents distribution and effects. Deliverable for HIVE: Brain Stimulation: models, experiments and open questions, 2009. URL http://wiki.neuroelectronics.com/images/4/4d/HIVE-D1.1_State-of-the-art-V1.3withcovers-small.pdf.
- Mishra and Narayanan. 2015. High-conductance states and a-type k⁺ channels are potential regulators of the conductance-current balance triggered by hcn channels. *J. Neurophysiol.* doi: 10.1152/jn.00601.2013.
- Monai, Omori, Okada, Inoue, Miyakawa, and Aonishi. 2010. An analytic solution of the cable equation predicts frequency preference of a passive shunt-end cylindrical cable in response to extracellular oscillating electric fields. *Biophys. J.* doi: 10.1016/j.bpj.2009.10.041.
- Moore, Ravassard, Ho, Acharya, Kees, Vuong, and Mehta. 2017. Dynamics of cortical dendritic membrane potential and spikes in freely behaving rats. *Science*. doi: 10.1126/science.aaj1497.
- Narayanan and Johnston. 2008. The h channel mediates location dependence and plasticity of intrinsic phase response in rat hippocampal neurons. *J. Neurosci.* doi: 10.1523/jneurosci.0835-08.2008.
- Ness, Remme, and Einevoll. 2016. Active subthreshold dendritic conductances shape the local field potential. *J. Physiol.* doi: 10.1113/JP272022.This.
- Neuling, Wagner, Wolters, Zaehle, and Herrmann. 2012. Finite-element model predicts current density distribution for clinical applications of tdc_s and tacs. *Front. Psychiatry*. doi: 10.3389/fpsyt.2012.00083.
- Nevian, Larkum, Polsky, and Schiller. 2007. Properties of basal dendrites of layer 5 pyramidal neurons: a direct patch-clamp recording study. *Nat. Neurosci.* doi: 10.1038/nn1826.

- Nitsche and Paulus. 2000. Excitability changes induced in the human motor cortex by weak transcranial direct current stimulation. *J. Physiol.* doi: 10.1111/j.1469-7793.2000.t01-1-00633.x.
- Ostojic, Szapiro, Schwartz, Barbour, Brunel, and Hakim. 2015. Neuronal morphology generates high-frequency firing resonance. *J. Neurosci.* doi: 10.1523/JNEUROSCI.3924-14.2015.
- Ozen, Sirota, Belluscio, Anastassiou, Stark, Koch, and Buzsáki. 2010. Transcranial electric stimulation entrains cortical neuronal populations in rats. *J. Neurosci.* doi: 10.1523/JNEUROSCI.5252-09.2010.
- Paulus. 2011. Transcranial electrical stimulation (tes - tdc, trns, tacs) methods. *Neuropsychol. Rehabil.* doi: 10.1080/09602011.2011.557292.
- Pinsky and Rinzel. 1994. Intrinsic and network rhythmogenesis in a reduced traub model for ca3 neurons. *J. Comput. Neurosci.* doi: 10.1007/bf00962717.
- Plonsey and Altman. 1988. Electrical stimulation of excitable cells-a model approach. *Proc. IEEE.* doi: 10.1109/5.9658.
- Radman, Su, An, Parra, and Bikson. 2007. Spike timing amplifies the effect of electric fields on neurons: implications for endogenous field effects. *J. Neurosci.* doi: 10.1523/JNEUROSCI.0095-07.2007.
- Radman, Ramos, Brumberg, and Bikson. 2009. Role of cortical cell type and morphology in subthreshold and suprathreshold uniform electric field stimulation in vitro. *Brain Stimul.* doi: 10.1016/j.brs.2009.03.007.
- Rahman, Reato, Arlotti, Gasca, Datta, Parra, and Bikson. 2013. Cellular effects of acute direct current stimulation: Somatic and synaptic terminal effects. *J. Physiol.* doi: 10.1113/jphysiol.2012.247171.
- Rahman, Lafon, Parra, and Bikson. 2017. Direct current stimulation boosts synaptic gain and cooperativity in vitro. *J. Physiol.* doi: 10.1113/JP273005.
- Rattay. 1986. Analysis of models for external stimulation of axons. *IEEE Trans. Biomed. Eng.* doi: 10.1109/TBME.1986.325670.
- Rattay. 1998. Analysis of the electrical excitation of cns neurons. *IEEE Trans. Biomed. Eng.* doi: 10.1109/10.678611.
- Rattay. 1999. The basic mechanism for the electrical stimulation of the nervous system. *Neuroscience.* doi: 10.1016/S0306-4522(98)00330-3.
- Reato, Rahman, Bikson, and Parra. 2010. Low-intensity electrical stimulation affects network dynamics by modulating population rate and spike timing. *J. Neurosci.* doi: 10.1523/JNEUROSCI.2059-10.2010.
- Reato, Rahman, Bikson, and Parra. 2013. Effects of weak transcranial alternating current stimulation on brain activity-a review of known mechanisms from animal studies. *Front. Hum. Neurosci.* doi: 10.3389/fnhum.2013.00687.

- Reato, Bikson, and Parra. 2015. Lasting modulation of in vitro oscillatory activity with weak direct current stimulation. *J. Neurophysiol.* doi: 10.1152/jn.00208.2014.
- Remme. 2013. *Encyclopedia of Computational Neuroscience*, chapter Quasi-active approximation of onlinear dendritic cables, pages 2553–2556. Springer. ISBN 978-1-4614-7320-6. doi: 10.1007/978-1-4614-7320-6_34-1.
- Remme and Rinzel. 2011. Role of active dendritic conductances in subthreshold input integration. *J. Comput. Neurosci.* doi: 10.1007/s10827-010-0295-7.
- Roth and Basser. 1990. A model of the stimulation of a nerve fiber by electromagnetic induction. *IEEE Trans. Biomed. Eng.* doi: 10.1109/10.55662.
- Schmidt, Scholz, Obermayer, and Brandt. 2013. Patterned brain stimulation, what a framework with rhythmic and noisy components might tell us about recovery maximization. *Front. Hum. Neurosci.* doi: 10.3389/fnhum.2013.00325.
- Spruston. 2009. Pyramidal neuron. *Scholarpedia*. doi: 10.4249/scholarpedia.6130.
- Sterratt, Graham, Gillies, and Willshaw. 2011. *Principles of Computational Modelling in Neuroscience*. Cambridge University Press. doi: 10.1017/cbo9780511975899.
- Tiganj, Chevallier, and Monacelli. 2014. Influence of extracellular oscillations on neural communication: a computational perspective. *Front. Comput. Neurosci.* doi: 10.3389/fncom.2014.00009.
- Tolozza, Negahbani, and Frohlich. 2017. Ih interacts with somato-dendritic structure to determine frequency response to weak alternating electric field stimulation. *J. Neurophysiol.* doi: 10.1152/jn.00541.2017.
- Tranchina and Nicholson. 1986. A model for the polarization of neurons by extrinsically applied electric fields. *Biophys. J.* doi: 10.1016/S0006-3495(86)83558-5.
- Tuckwell. 1988. *Introduction to theoretical neurobiology - volume 1*. Cambridge University Press. ISBN 9780521350969. doi: 10.2277/052101932X.
- Ulrich. 2002. Dendritic resonance in rat neocortical pyramidal cells. *J. Neurophysiol.* doi: 10.1152/jn.2002.87.6.2753.
- Vatta, Meneghini, Esposito, Mininell, and Di Salle. 2010. Realistic and spherical head modeling for eeg forward problem solution: A comparative cortex-based analysis. *Comput. Intell. Neurosci.* doi: 10.1155/2010/972060.
- Wybo, Stiefel, and Torben-Nielsen. 2013. The green’s function formalism as a bridge between single and multi-compartmental modeling. *Biol. Cybern.* doi: 10.1007/s00422-013-0568-0.
- Xu, Wolff, and Wu. 2014. Low-intensity electric fields induce two distinct response components in neocortical neuronal populations. *J. Neurophysiol.* doi: 10.1152/jn.00740.2013.

Zaghi, Acar, Hultgren, Boggio, and Fregni. 2010. Noninvasive brain stimulation with low-intensity electrical currents: putative mechanisms of action for direct and alternating current stimulation. *Neuroscientist*. doi: 10.1177/1073858409336227.

Zhang, Li, Rasch, and Wu. 2013. Nonlinear multiplicative dendritic integration in neuron and network models. *Front. Comput. Neurosci.* doi: 10.3389/fncom.2013.00056.

Zhou, Li, hui Zhang, and Cai. 2013. Phenomenological incorporation of nonlinear dendritic integration using integrate-and-fire neuronal frameworks. *PLoS One*. doi: 10.1371/journal.pone.0053508.